Diss. ETH No. 14474

Identification and Automated Controller Design for Active Magnetic Bearing Systems

Florian Lösch

Swiss Federal Institute of Technology

ETH Zürich

2002

Diss. ETH No. 14474

Identification and Automated Controller Design for Active Magnetic Bearing Systems

Dissertation submitted to the

Swiss Federal Institute of Technology

Zurich

for the degree of

Doctor of Technical Sciences

presented by

Florian Lösch

Dipl.-Math. (techn.) University of Kaiserslautern

born February 11, 1971

citizen of Germany

accepted on the recommendation of

Prof. Dr. Gerhard Schweitzer, examiner

Prof. Dr. Rainer Nordmann, co-examiner

Zurich, 2002

Seite Leer /
Blank leaf

Acknowledgments

This thesis is the result of research work I carried out at the Institute of Robotics at the Swiss Federal Institute of Technology (ETH) in Zurich. I would like to express my sincere gratitude to those who made this project possible:

- Professor Gerhard Schweitzer: for giving me the opportunity to work at his institute, for providing me with challenging tasks to grow on, for scientific freedom, and for what I learned from him about life and diplomacy.

- Professor Rainer Nordmann: for arousing my interest in engineering applications, his guidance and support during the last decade, his interest in my work, and for being co–examiner of this thesis.

- Philipp Bühler: for co-supervising many student projects, for designing tricky electronics for the test rig, for his advice, and for countless stunning ideas and remarks.

- Ulrich Schönhoff: for making available his toolbox for uncertainty modeling and for many helpful comments.

- Alfons Traxler, Raoul Herzog and René Larsonneur: for their help in redesigning the test rig, their encouragement, and countless interesting discussions and valuable comments.

- Coni Gähler: for his pioneering work in the field, for his interest in my work, for proofreading this thesis, for hiking and snow shoe tours and numerous Sunday morning breakfasts.

- Edi Randak and Ruedi Borer: for their support with the test rig hardware.

- Beat Peyer, Philippe Cattin, and Patrick Mesquida: for providing a stable computer environment and efficient crisis management.

- All the students who contributed to this work, particularly Christoph Haugstetter, Urs Muntwyler, and Stefan Suter: for their interest, their ideas, and for what I learned about motivating people.

- The colleagues and guests from all over the world, in particular Letian Wang and Marcelo Becker: for sharing their views on life and for making the last years a truly international experience.

- Gabriel Gruener, Alexander Bartha and Markus Müller: for their companionship with many interesting discussions, for nights spent working at the institute and for days spent skiing in the mountains.

- My parents: for their loving support throughout three decades and for giving me the opportunity to attend university.

- My grandmother Änne: for giving me hope in life by proving that with enough determination a high morale can be maintained and incredible things can be achieved.

- Stephanie Bolling: for her love, her support, and for being the sunshine of my life.

Zurich, November 2001   Florian Lösch

Contents

Abstract

Contact–free levitation of rotors by means of active magnetic bearings has been a research topic for more than two decades. During this time, active magnetic bearings have evolved into an industry product that due to its numerous advantages over conventional bearing technology is used in many practical applications.

For the operation of active magnetic bearing (AMB) systems, adequate controllers are indispensable. The design of such controllers is a challenging task since they must compensate for the instability inherent to the magnetic bearings and at the same time avoid destabilization of any flexible eigenmodes the rotor may exhibit. This is a particularly delicate problem since damping is extremely weak due to the contactless levitation and since the poles are displaced by gyroscopic effects when the rotor is rotating.

Traditionally, AMB controllers are designed by well–trained engineers. The existing design techniques are either not standardized and hence depend on the designer's intuition and experience or they rely on highly accurate system models that must be manually fine tuned.
In any case, AMB controller design is a time–consuming task that requires considerable amounts of expertise from different fields.

The purpose of the present work is to contribute to controller design for AMB rotor systems by improving this situation. To this end research in two directions is presented.

The first area of investigation is that of *identification of AMB rotor systems.* In this context identification algorithms for obtaining accurate system models directly from the AMB system under consideration are presented. Identification is achieved by means of a step–wise procedure. First, a rigid body model of the rotor is extracted based on measured system re-

sponses to current steps applied to the bearings. Then a simple preliminary stabilizing controller that avoids destabilization of any high frequency flexible modes is designed. With the rotor levitated, the complete open loop model including the flexible rotor modes is identified based on measurements of the system's open–loop transfer function.
In addition to this, an algorithm for identifying the gyroscopic matrix G from the rotating system is introduced.

The second research topic is *automated controller design for AMB systems.* The first problem addressed in this context is the stabilization of flexible rotors of which only the rigid body dynamics are known. The problem is solved by means of a μ-synthesis based procedure automatically adapting the system's bias current such that maximum robustness to additive high frequency uncertainty is achieved.
Then automated controller design for flexible rotors is addressed. Based on an analysis of the state of the art methods in AMB controller design, the method best suited for automation is identified. Also based on μ–synthesis, this method is then adapted to meet the special requirements of gyroscopic rotor systems. The analysis of the resulting controllers is refined, and finally an automated version of the procedure is formulated.

The identification and controller design algorithms are integrated into an *automated procedure* that requires only little user interaction and expert knowledge on the part of the designer. This procedure consists of three parts, the first two of which comprise the identification of the rotor system at standstill. The third part consists in a sequence of steps in which controller design for the flexible rotor, controller performance tests on the system, and identification of the gyroscopic matrix are iterated at increasing speeds until the system's top operating speed has been reached or no improvements to the last controller can be made anymore.
The procedure has been tested on different configurations of a test rig with a highly flexible rotor and showed good performance even in presence of strong gyroscopic effects.

Kurzfassung

Die berührungsfreie Lagerung von Rotoren mit Hilfe von aktiven Magnetlagern ist seit über zwanzig Jahren Gegenstand der Forschung. In dieser Zeitspanne haben sich Magnetlager zu einem Industrieprodukt entwickelt, das aufgrund seiner vielfältigen Vorteile gegenüber herkömmlichen Lagertechniken in einer Vielzahl von praktischen Anwendungen zum Einsatz kommt.

Für den Betrieb von aktiven Magnetlagern sind geeignete Regler unverzichtbar. Die Auslegung solcher Regler ist eine herausfordernde Aufgabe, da diese die den Magnetlagern eigene Instabilität kompensieren müssen ohne dabei etwaige elastische Eigenmoden des Rotors zu destabilisieren. Dies ist besonders schwierig, da die Systemdämpfung aufgrund der kontaktlosen Lagerung nur sehr schwach ist und sich die Pole zudem infolge gyroskopischer Effekte verschieben sobald der Rotor rotiert.

Regler für aktive Magnetlagersysteme werden üblicherweise von erfahrenen Ingenieuren ausgelegt. Die heute existierenden Entwurfsverfahren sind entweder nicht standardisiert und bauen damit auf die Intuition und Erfahrung des Benutzers oder benötigen sehr genaue Systemmodelle, die Feinanpassung von Hand erfordern.
Unabhängig von der gewählten Entwurfsmethode benötigt der Reglerentwurf für aktive Magnetlagersysteme viel Zeit und beachtliches Expertenwissen aus verschiedenen Fachgebieten.

Ziel der vorliegenden Arbeit ist es durch Verbesserung dieser Situation einen Beitrag zur Regelung aktiver Magnetlagersysteme zu leisten. Dazu werden Forschungsergebnisse aus zwei Bereichen präsentiert.

Das erste Forschungsgebiet ist die *Identifikation von Magnetlagersystemen.* Hier werden Identifikationsalgorithmen präsentiert, mit deren Hilfe ausschliesslich aus Messungen, die am realen Magnetlagersystem durchgeführt

werden, genaue Systemmodelle gewonnen werden können. Die Identifika-
tion erfolgt dabei in mehreren Schritten. Zunächst wird die Systemantwort
auf Stromschritte, die auf die Magnetlager aufgegeben werden, gemessen
und daraus ein Starrkörpermodell des Rotors extrahiert. Dann wird ein
erster einfacher Regler entworfen, der das System zu stabilisieren vermag,
ohne etwaige hochfrequente elastische Eigenmoden zu destabilisieren. So-
bald der Rotor schwebt, wird basierend auf Frequenzgangmessungen der
Strecke das gesamte Modell mit allen elastischen Moden identifiziert.
Darüberhinaus wird ein Algorithmus zur Identifikation der gyroskopischen
Matrix G aus dem rotierenden System vorgestellt.

Der zweite Forschungsgegenstand ist der *automatisierte Reglerentwurf für
Magnetlagersysteme.* Hier wird zunächst die Frage der Stabilisierung elas-
tischer Rotoren untersucht, von denen lediglich ein Starrkörpermodell be-
kannt ist. Dieses Problem wird mit Hilfe eines μ–Synthese basierten Pro-
zedur gelöst, die automatisch den Vormagnetisierungsstrom so einstellt,
dass maximale Robustheit gegenüber hochfrequenter additiver Unsicher-
heit erreicht wird.
Dann wird der automatisierte Reglerentwurf für elastische Rotoren behan-
delt. Ausgehend von einer Analyse des Stands der Technik wird die am
besten zur Automatisierung geeignete Reglerentwurfsmethode ermittelt.
Dieses ebenfalls auf μ–Synthese basierende Verfahren wird dann angepasst,
um den besonderen Anforderungen von Systemen mit gyroskopischen Ro-
toren gerecht zu werden. Verfeinerte Analyseverfahren für die entworfenen
Regler werden vorgestellt, und schliesslich wird ein automatisierter Reg-
lerentwurfsalgorithmus formuliert.

Die Identifikations- und Reglerentwurfsalgorithmen werden in eine *auto-
matisierte Prozedur* eingebettet, die dem Anwender nur wenig aktives Ein-
greifen und geringes Expertenwissen abverlangt. Diese Prozedur ist in drei
Teile gegliedert, von denen die ersten beiden die Identifikation des Ma-
gnetlagersystems im Stillstand umfassen. Der dritte Teil besteht aus einer
Folge von Schritten in denen Reglerentwurf für den elastischen Rotor, Re-
gelgütetests am System und Identifikation der gyroskopischen Matrix bei
steigenden Drehzahlen wiederholt werden bis die Maximaldrehzahl erreicht
ist oder der letzte Regler nicht mehr weiter verbessert werden kann.
Die Prozedur ist an verschiedenen Konfigurationen eines Prüfstandes mit
sehr elatischem Rotor getestet worden. Auch für stark gyroskopische Ro-
toren wurden gute Ergebnisse erzielt.

Chapter 1

Introduction

In this chapter, a short overview of the operating principle and the basic structure of active magnetic bearing (AMB) rotor systems is given. The necessity of controllers is elaborated, and the state of the art of AMB controller design is outlined. Based on this analysis, the objectives of this thesis are formulated. Finally, an overview of the thesis is given.

1.1 AMB Rotor Systems

1.1.1 Principle of Operation

The first bearing has been invented together with the first wheel. Although no historical records describing this event are available, this can be concluded from the fact that whenever a rotating object (e.g. a wheel) is to be held in a fixed position with respect to a certain frame of reference (e.g. a cart), a suitable mechanism (bearing) is required.
While the invention of the wheel has in our understanding become a milestone in the history of mankind, its counterpart, the bearing, has not found its way into the history books. Considering the fact that there is little use to a wheel without a bearing, this is rather remarkable.

Although the ball bearing has already been conceived by Leonardo da Vinci when he studied friction in 1485, it is only in the last two centuries that durability and performance have become issues of interest and that specific attention has been paid to the design of bearings.
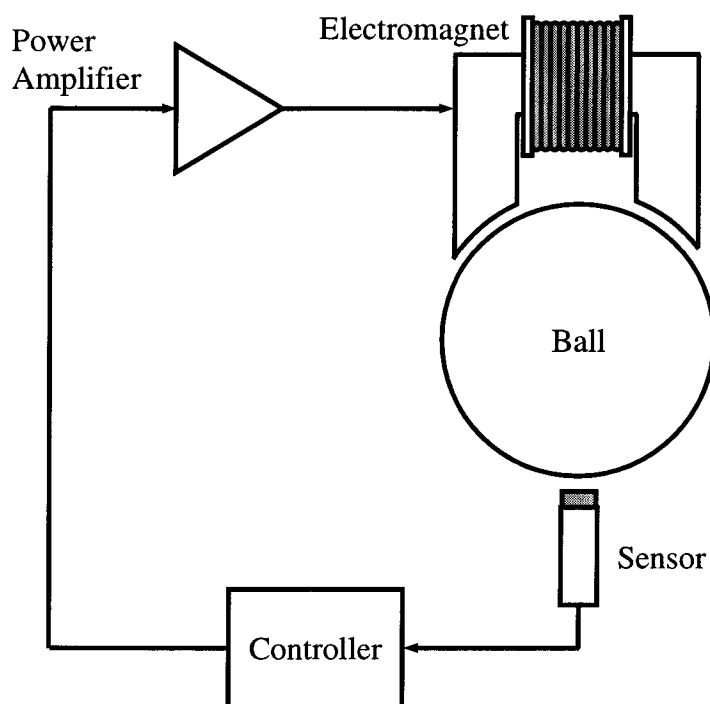
Figure 1.1: *Operating principle of a 1-dof AMB*

The first ball bearing was employed in 1795 in a French military cart [Rachline90]. While this invention and the improvements made later constitute a significant improvement over ancient technology, friction and therefore losses and wear can never be entirely eliminated in these conventional bearing designs. As a result, the achievable rotational velocities remain limited by the bearing temperature.

Due to the demand for higher velocities, new concepts for holding rotating bodies in place without friction were developed. Today the most widely spread concept for contact–less levitation is that of magnetic levitation. The basic operating principle of such systems is illustrated in Figure 1.1 for a one degree of freedom system.

The core of this system is formed by an electromagnet that exerts magnetic forces on a ferromagnetic ball that is to be supported without contact. If a current is passed through the magnet, it exerts an attractive force on the ball that opposes the gravitational force which pulls the ball downward. If the current is kept constant and the ball moves downward from the equilibrium position, the restoring magnetic force on the ball decreases as the distance to the magnet increases. This leads to the ball falling down. If on the other hand the ball moves upwards, the attractive magnetic force increases, and the ball will inevitably be accelerated towards the magnet.
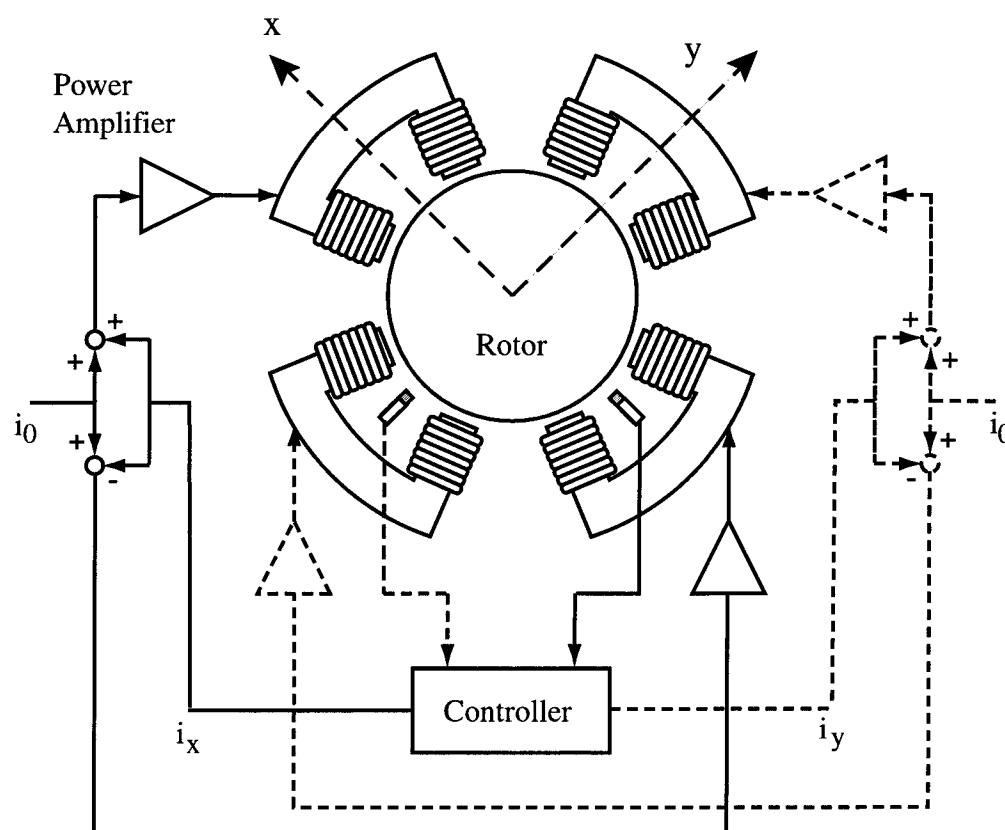
Figure 1.2: *Scheme of a radial Active Magnetic Bearing operated with current control and in differential driving mode.*

To avoid this unstable behavior, the electric current must be permanently adjusted. To do this in an appropriate manner, a sensor permanently measures the ball's deviation from its reference position. Based on this measurement, a controller (microprocessor) computes what current should be applied to the magnet. A power amplifier generates this current and passes it through the electromagnet. With an appropriately designed controller the ball can be held at its reference position, and the dynamics of the suspension can be adjusted in a wide range.

In technical applications the concept outlined above is extended as shown in Figure 1.2. For each of the two degrees of freedom, there are two opposing electromagnets that are operated in differential driving mode. In this configuration, forces can be exerted on the rotor in arbitrary directions in the plane and the gravitational force is no longer required to keep the rotor in position.

In the above system, the magnetic flux and therefore the magnetic force F_d exerted by the magnets depends on the coil current i_d and the rotor
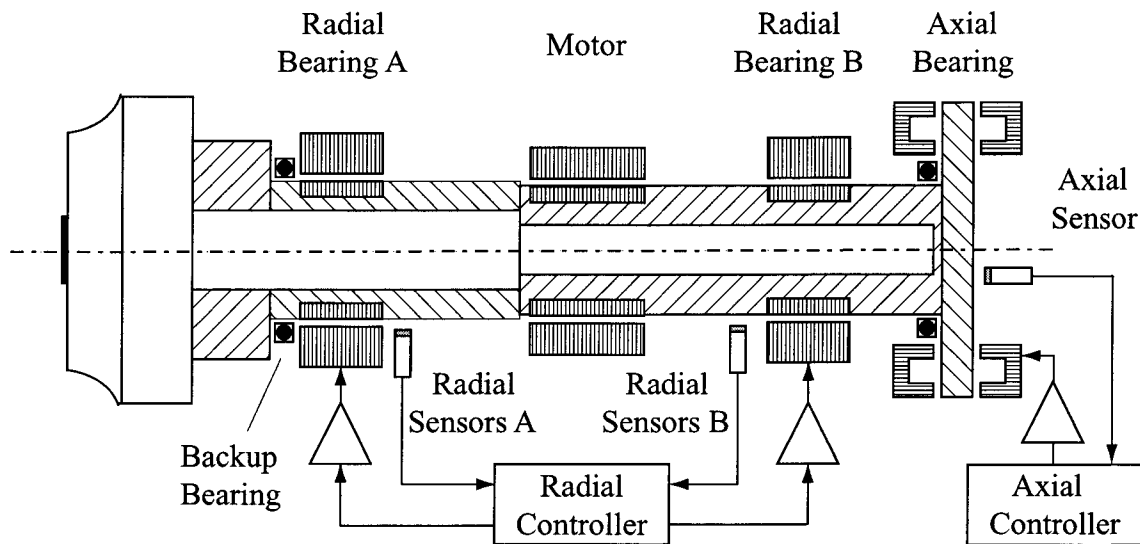
Figure 1.3: *AMB Rotor System with Axial and Radial Bearings and Motor Drive*

position d, where d represents any of the bearing axes x and y from Figure 1.2. For each axis, this relationship can be linearized with good accuracy to:

$$F_d = k_{i_d} + k_s d, \qquad d = x, y \qquad (1.1)$$

In the above, the coefficient k_i is denoted force–current factor, and k_s is called force–displacement factor.

The standard configuration for AMB rotor systems is shown in Figure 1.3. It consists of a rotor supported by two radial bearings like the one shown in Figure 1.2 and one axial bearing. Besides the AMBs, there are additional retainer bearings — usually roller bearings or solid rings — that support the rotor when the system is switched off and during overload conditions. The air gap width between the rotor and the electromagnets is typically in the range of 0.2–2mm, that between the rotor and the retainer bearings 0.05–1mm.

The above configuration allows to support of the rotor in five degrees of freedom. The design with the motor on the shaft enables rotation of the shaft without any contact between fixed and rotating parts. This has the following advantages:

Higher rotational speeds. The achievable velocity is no longer limited by the bearings. The new limit is imposed by the mechanical properties of the rotor materials, and circumferential speeds up to 200m/s and more can be reached at the bearing locations.

Lower energy consumption. The absence of bearing friction greatly reduces losses and permits the use of less powerful drives.

Cleanliness. As no lubricants are involved the system can be operated in conditions where no contamination can be tolerated (e.g. vacuum, clean–rooms, food industry).

Reliability. Due to the contact–less operation there is no mechanical wear. Maintenance intervals and the life time of the system are significantly prolonged.

New machinery designs. Systems can be designed in such a way that the rotor is entirely submerged in the operating medium (canned pumps).

Adjustable rotordynamics. By means of different controllers, the dynamic properties of the system can be varied within a wide range. In particular, rotor vibrations can be actively damped.

Unbalance compensation. By taking advantage of the air gap the rotor can be allowed to spin about its principal axis of inertia instead of its axis of geometric symmetry. This eliminates housing vibrations.

System monitoring and smartness. With only little additional cost a system for observing the operating conditions and for fault compensation can be added. The system can use the sensor signals from the AMBs as inputs and use the AMBs as actuators to counteract faults [Schweitzer98], [IMP01].

These advantages have led to employment of AMBs in a variety of applications, among them:

- compressors
- turbines
- tooling machines
- centrifuges
- textile spindles
- turbo molecular pumps
- clean room applications
- space applications

1.1.2   Controller Design for AMB Systems

A suitable controller is a prerequisite for the operation of any AMB system. In the following we will clarify what 'suitable' means in this context by listing typical requirements for AMB controllers.

Stability. The controller must stabilize the nominal system at standstill.

Performance. The controller must satisfy certain application dependent criteria concerning the behavior of the suspended rotor, e.g minimum stiffness and rejection of disturbances.

Robustness. Stability must be preserved if the system changes slightly with respect to the nominal model (modeling errors, thermal effects).

Robust performance. The performance criteria should also be met in face of small system changes.

Gyroscopic effects. During rotation, the rotor's system dynamics change due to gyroscopic effects, which must be dealt with by the controller. Although a special case of robustness, this is stated separately due to the great demands made.

Flexible rotors. Slender rotor structures typically show very weakly damped high–frequency eigenmodes (damping factor $\xi \approx 0.001$). These modes should be actively damped by the controller. In any case destabilization must be avoided.

Non–collocation. In typical applications, the rotor displacement is not measured in the bearing but next to it. It is therefore desired that controllers can deal with this situation.

Discrete control. For implementation on microprocessors, digital controllers are required. Discretization of continuous time controllers may degrade performance and robustness.

Low computational cost. Due to restricted computing power and minimum requirements on sampling time, the allowable computational complexity is limited. This has consequences for the admissible controller order.

Besides these requirements on the controller, there are additional demands on the design method:

Low modeling effort. The method should require as little modeling and model tuning effort as possible on behalf of the control engineer.

Ease of application. Little expert knowledge should be required for the design, and manual hand tuning after the design should be minimized.

Design Time. For short development cycles, controller design times should be short.

Design Flexibility. Performance and robustness requirements should be includable in a flexible and clear manner.

Transparency. The design method should provide information on the extent to which the stated goals were achieved without practical tests.

Over the last 15 years, large efforts have been made to develop methods for systematic AMB controller design. In the following, a brief overview of the developed methods will be given. Then, the methods will be compared with respect to the criteria formulated above.

In the early days of AMBs, computing power was very limited. At this time researchers were working on the development of design procedures for controllers with a low computational burden. Bleuler developed a method for designing decentralized PD controllers for rigid rotors [Bleuler84]. Salm introduced a control procedure for flexible rotors with collocation and gave stability guarantees for the case of continuous time control [Salm88]. Herzog identified this to be a special case of passive control[1] and showed that the stability guarantee does not hold for sampled systems as passivity is lost due to the sampling operation. Furthermore, he found passive controllers to generally have poor disturbance rejection capabilities. He also investigated the issue of theoretically achievable AMB controller performance in an $\mathcal{H}_\infty$ setting [Herzog91].

With Larsonneur's SPOC–D algorithm the design of optimal, low order digital controllers with predefined structure became possible [Larsonneur90]. This method is applicable to flexible rotors and shows better results than PID, but does not allow explicit consideration of gyroscopic effects.

In 1994, Gähler was confronted with the problem of finding a stabilizing controller for a highly flexible, highly gyroscopic rotor with non–collocated

---

[1]Recall that this term is unrelated to passive magnetic bearings, whose name comes from their operation based on permanent magnets, i.e. without control.

sensors. He developed a computer based design tool for phase–shaping of transfer functions by manual pole placement. By means of this tool he designed a controller for the system, making explicit use of non–collocation [Gähler98].

$\mathcal{H}_\infty/\mu$-synthesis control was first applied to AMB systems around 1990. While the pioneering work focused on applicability of the method [Fujita90], [Cui92], later work aimed at disturbance attenuation [Namerikawa96], [Yamashita96]. Performance–oriented implementations of μ-synthesis controllers for rigid tool spindles were realized by Fittro and Knospe [Fittro98]. Systematic lumped uncertainty modeling was addressed in [Lösch98]. An uncertainty model for the bearing itself was derived in [Namerikawa98]. Recently, [Schönhoff00b] has successfully implemented a μ-synthesis controller based on the four–block problem framework on an energy storage flywheel supported by AMBs.

Table 1.1 gives an overview over the capabilities and shortfalls of the individual approaches. Besides the methods listed in the table, other linear controller design methods have been applied to AMB systems, among them Gain Scheduling, Quantitative Feedback Theory (QFT), Linear Quadratic Ricatti (LQR), Decoupling Control, $\mathcal{H}_\infty$ –Loop Shaping, and others. However, these approaches either were of experimental nature, difficult to use, similar to other methods, or expensive to implement. None of them had prospects of becoming a standard design method for AMB controllers. Therefore these methods have not been considered in the table.

Additionally, a variety of non–linear and adaptive control algorithms have been applied to magnetic bearings. However, most of these applications were of experimental nature with extremely simplified hardware setups and did not aim at real–world application, [Bleuler90], [Costic00]. In particular, these methods have not been applied to rotors, not to mention flexible rotors. Other approaches have focused on sub–problems like unbalance attenuation rather than stabilization of the rotor [Knospe97].

Furthermore, sliding mode control has been investigated in conjunction with zero power operation of AMBs by several authors [Nonami96], [Allaire98], [Ariga00]. This research has aimed at operating AMBs without bias current, i.e. in a nonlinear mode of operation. The benefit of this approach is a significantly reduced power consumption. This could be a promising approach for future AMB systems, although many issues are left to be resolved — for example, the question of how excitation of weakly damped uncertain flexible poles can be avoided in the nonlinear setting is still to be resolved.

As a consequence, nonlinear methods have also not been included in the collection of application oriented controller design methods presented in Table 1.1.

As can be seen from this table, only two design methods, Gähler's phase shaping method and μ–synthesis, cover the full scope of problems and explicitly allow gyroscopic effects. A deeper analysis shows that both methods have strong points, but also considerable shortfalls.

The phase shaping method can be used to design low-order discrete controllers based on a relatively simple system model. However, the method fully relies on expertise of the user who has the responsibility to design the controller by placing poles and zeroes in the complex plane based on his own judgement. Performance requirements cannot be formulated directly, but must be considered by the designer, which often poses considerable problems. Furthermore, introduction of high order filters causes stability problems in many cases [Gähler98], which imposes additional constraints on the controllers that can be designed by this method. Despite these drawbacks, and although yielding only SISO controllers without any cross coupling between the channels, this method can be considered the state of the art method for AMB controller design.

The μ-synthesis method on the other hand relies on powerful algorithms that are commercially available [Balas95a]. It allows to explicitly include robustness and performance requirements formulated in the frequency domain, and the achievement of robust performance can be directly validated after the design. However this method yields high order controllers in continuous time. A further disadvantage is the need for sensible selection of weighting functions which is not intuitive. The biggest drawback, however, consists in the need for a very precise model of the AMB system. This may be surprising when considering that μ-synthesis is known as a design technique for robust controllers that can compensate for plant uncertainties. However, the special type of uncertainty encountered in AMB systems — uncertain high frequency poles with very weak damping — constitutes an exception here since small movements of poles may incur very large changes of transfer functions in the $\mathcal{H}_\infty$-sense.

Table 1.1: *Comparison of AMB controller design methods*

Design Method	Scope			Design Criteria		Controller Properties		Practical (User) Aspects			
	Non-Colloc.	Flexible Rotors	Gyros-copy	Robust-ness	Perfor-mance	Discrete	Low Com-plexity	Ease/ Speed of Use	Flexi-bility	Low Modeling Effort	Transpa-rency
PID/Bleuler	−	−	−	−	−	$-^3$	$+^1$	+	−	$+^{11}$	$-^{15}$
Passivity/Salm	−	+	−	o^4	−	$-^3$	o	o	−	o^{12}	$-^{15}$
LQG	+	+	−	−	+	$-^3$	$-^2$	o^8	o	$-^{13}$	$-^{15}$
SPOC-D	+	+	−	−	+	$+^5$	$+^1$	o^8	o	o^{12}	$-^{15}$
Phase Shaping	+	+	+	o^6	o^6	$+^5$	$+^1$	$-^9$	o	$+^{11,14}$	$-^{15}$
μ-synthesis	+	+	+	$++^7$	$++^7$	$-^3$	$-^2$	o^{10}	$+^7$	$-^{13}$	$+^{16}$

1: Decentralized design of low order controllers
2: High order controllers ($\geq$ plant order)
3: Controller must be discretized after design
4: Theoretical stability guarantee for continuous time controllers
5: Direct design of discrete controllers
6: Cannot be specified but achieved by skillful user
7: Requirements can be precisely specified in frequency domain
8: Adequate performance criteria must be determined and formulated

9: Many skills required, manual layout
10: Selection of adequate weighting functions required
11: Information on pole locations required
12: State space description required
13: Very precise, validated model required
14: Sign of flexible modes and effect of gyroscopics on poles req.
15: Robust performance can only be assessed with difficulty
16: Standardized tests inform about achievements and shortfalls

As a consequence, it is a prerequisite for application of the method that the control engineer creates a finite element model of the rotor, adds a model of the bearings and the foundation, and tunes this compound model by comparison to measurement data until it matches the real structure. In particular the fine–tuning of the model often takes a long time, rendering controller design by μ-synthesis just as difficult and time–consuming a task as the phase shaping procedure.

Summarizing the above it can be stated that with the methods available today, controller design for AMB systems with flexible rotors and non-negligible gyroscopic effects is a difficult and time–consuming task that requires expert knowledge from both the field of electrical and mechanical engineering.

1.2 Motivation and Objectives of this Thesis

1.2.1 Motivation

Active Magnetic Bearings have been subject of scientific study for more than two decades and are now increasingly used in industrial applications. For their operation, a stabilizing controller is a prerequisite. In the past, much research on controller design for magnetic bearings has been carried out. However, this early research focuses mainly on application of different control laws to specific test rotors, while only little work on systematic design approaches has been done. To date, controller design for AMB systems remains a complex and time–consuming task that is based on complex modeling and/or strongly relies on expert knowledge on behalf of the control engineer.

In industrial applications, the trend goes towards more compact systems with higher integration and lower power consumption. This often leads to rotors that have elastic eigenmodes within the system bandwidth. In particular for these flexible rotor systems, a large percentage of the time required for system development is spent on the design and tuning of a controller for the system, rendering controller design an important cost factor in the development of AMB systems.

1.2.2   Objectives of this Thesis and Approach

The goal of this thesis is to alleviate the task of the control engineer by reducing the amount of expert knowledge and manual work required in the controller design process. To this end, research in two directions will be presented:

1. Minimization of system modeling and model updating requirements. This will be done by basing the design of a suitable controller on a system model that is directly identified from the structure to be controlled instead of a hand made FE–model that requires lengthy fine–tuning. To this end, new identification algorithms will be developed and existing algorithms will be applied and extended where necessary.

2. Automation of the controller design process. An iterative self tuning algorithm that designs a stabilizing controller for flexible rotors based on identified models will be developed. Controller design criteria and suitable tests to verify the designed controllers' conformity with the specifications will be derived together with updating rules for the design criteria, if improvements are required.

The two components mentioned above will be combined to an automated start–up procedure for AMB systems with flexible rotors as follows. With the unknown rotor only supported by the retainer bearings, the first step of the procedure consists in an algorithm that identifies a rigid body model of the rotor. In a second step, this model will be used to design a low–gain controller for barely levitating the rotor without exciting any elastic modes. With the rotor levitated by this controller, a new rotor model including the flexible modes will be identified. The final controller design will then be based on this identified model of the elastic rotor.

Throughout this work the bearing characteristics are assumed to be known, whereas no a priori knowledge of the rotor is assumed. This perspective accommodates both the view of the bearing manufacturer distributing the new algorithm described above together with his bearings as well as that of the control engineer designing a new application based on a standard AMB.

1.3 Structure of this Thesis

1.3.1 Outline

This thesis is structured as follows. In Chapter 2, an overview of modeling techniques and model descriptions for AMB systems and their components is given.

In Chapter 3, an overview of robust controller design methods and principles is given. Being quite extensive, it contains the background information required to justify and understand the design approaches chosen and decisions taken in Chapter 5. Together with Chapter 2, this chapter provides a basis for the developments in the following chapters.

In Chapter 4, identification algorithms for rigid and flexible rotors are presented and their applicability to the given problem is discussed. The issue of gyroscopic effects receives special attention in this chapter, and an algorithm for identification of the gyroscopic matrix is presented.

In Chapter 5, the issue of controller design for AMB systems is addressed. In the first part of the chapter this problem is solved for rotors of which only the rigid body dynamics are known. Restrictions imposed by the unknown high frequency dynamics (flexible modes) are discussed, and an algorithm for the design of stabilizing controllers for soft bearing settings is derived. In the second part, controller design for flexible rotor AMB systems is addressed, the goal being a controller for operating the system under normal conditions. The state of the art methods are analyzed with respect to their potential for automation, and the most promising method is adapted and extended to fit the specific requirements. Special attention is paid to the question of physical meaning of weighting functions required for the μ-synthesis controller design and the sensible selection of these functions.

In Chapter 6, the overall concept of the automated controller design procedure is described. Furthermore, criteria for evaluation of the controller are discussed and measures for iterative adaptation of weighting functions are given. In addition, a number of useful tools for efficiently performing the required tests is presented.

In Chapter 7, experimental results are presented. To this end the procedure is applied to different configurations of a test rig with a reconfigurable rotor. The thesis ends with Chapter 8, where conclusions are formulated and an outlook on possible future work is given.

1.3.2   Finding Your Way through this Thesis

On the way towards the goals formulated above, this thesis touches topics from a variety of fields: robust control theory, identification, AMB controller design, AMB modeling, rotor dynamics, and signal processing. Since readers can be expected to be more inclined towards some of these topics than towards others, a quick overview on which parts of the present thesis might be of specific interest to whom is given here.

Readers with interest in *robust control* and its applications are referred to Chapter 5. In the first part of this chapter, μ–synthesis is applied to solving the problem of stabilizing an unstable plant with unknown, non-negligible high frequency dynamics. The second part deals with application of μ–synthesis to unstable structures with weakly damped, uncertain flexible poles. In both parts, the selection of the weighting functions involved is explicitly addressed, and the decisions taken are justified by links to the underlying theory presented in Chapter 3. Further interest may arise from the automation of the algorithms that is also presented in Chapter 5.
Readers with specific interest in *AMB control* might in addition find the overview over the state of the art in Chapter 1.1.2 interesting.

Readers *generally interested in AMBs* are referred to Chapter 5.1.4, where some amendments to the standard linear AMB model are made. Persons with deeper interest in the *modeling of AMB systems* may also find the new approach to amplifier modeling provided in Chapter 2.1.3 to be of interest.

For the reader mainly interested in *rotor dynamics*, the new algorithm for identification of the gyroscopic matrix presented in Chapter 4.3 could be of interest. This section and the other sections of Chapter 4 contain all information on *identification*, including a new algorithm for identification of rigid body model data from AMB rotors without control.

Finally, Chapter 6.2 contains some tools for efficient transfer function extraction that may be of interest to *AMB practitioners*.

For all readers who first wish to get a *quick survey* over the approach taken in this thesis, the overview over the developed algorithm provided in Chapter 6.1.2 may be a good point of entry from which it is easy to follow the provided links to the sections containing the technical details.

Chapter 2

Modeling of AMB Rotor Systems

The systems under consideration in this thesis are rotors supported by two radial and one axial AMB. The model of these systems is orientation independent (up to gravity) and consists of the combination of the models for the bearings (including amplifiers) and the rotor. Two types of rotors are typically distinguished. Rotors with all flexible eigenfrequencies beyond the bandwidth of the control system and the maximum rotational speed of the system are referred to as *rigid rotors*. In contrast to this, thin rotors typically have flexible eigenfrequencies in a low frequency range where they can be affected by control and/or are passed during run-up and run-down. These rotors require explicit modeling of their elastic behaviour and are referred to as *flexible rotors*.

In this chapter, a brief overview of the typical modeling approaches for AMB rotor systems is given. The concepts rolled out in the following will later be taken up in the chapters on identification and controller design. First, the modeling of the bearings is discussed, followed by modeling techniques for other components of active magnetic bearing systems. Then, the model description for a rigid rotor supported by AMBs is presented. Finally, the modeling technique for flexible rotors is described and a description of gyroscopic behavior is formally introduced into the model.

2.1   Modeling of Active Magnetic Bearings

2.1.1   Single-Sided Bearings

In the introduction (Chapter 1), the basic operating principle of active magnetic bearings has already been outlined. The simplest type of AMB is that levitating a ferromagnetic body by means of a single magnet, see Figure 1.1. For this setup, the force exerted on the rotor is (neglecting the magnetization of the iron) [Schweitzer94]

$$f = \frac{1}{4}k\frac{i^2}{s^2},\tag{2.1}$$

where s is the air gap between rotor and magnet and $k = \mu_0 n_c{}^2 A_c \cos(\alpha_p)$, where μ_0 is magnetic field constant of the vacuum ($\mu_0{=}4\pi{\times}10^{-7}$ Vs/Am), n_c is the number of windings in the electromagnet's coil, A_c is the cross section of the iron and α is the angle under which the magnetic forces affect the rotor for each of the poles (in the case of a radial bearing with four pole pairs, $\alpha = 22.5°$.

The above equation can be linearized around a nominal operating point with air gap s_0 and a corresponding current i_0 that holds the ball at position s_0. The above equation can then be rewritten with the definitions $i_x = i - i_0$ and $x = s_0 - s$ (positive x in upward direction) as

$$f = \frac{1}{4}k\frac{(i_0 + i_x)^2}{(s_0 - x)^2}\tag{2.2}$$

Linearization then yields

$$f = k_s x + k_i i_x\tag{2.3}$$

with

$$k_s = \frac{k}{2}\frac{i_0{}^2}{s_0{}^3}, \text{ and } k_i = \frac{k}{2}\frac{i_0}{s_0{}^2}\tag{2.4}$$

2.1.2   Two-Sided Bearings

In technical applications, single sided bearings are rarely used. Instead of using a single magnet to position the rotor in one axis, a second magnet identical to the first one but exerting forces exactly in the opposite direction is added. This makes the bearing independent from gravity and improves the achievable dynamics since now forces on the rotor can be

exerted in both directions of each axis. An example for this configuration can be found in Figure 1.2, where a radial bearing with two axes (and hence four magnets) is shown.

In the majority of applications, the magnets of each axis are operated in *differential driving mode*, which means that a constant current i_0 called *premagnetization current* or *bias current* is passed through both coils, and the control current i_x is added to the coil exerting forces in the positive direction and subtracted from the opposite coil. Based on Equation (2.2), the non-linear relationship describing the force that is exerted on the rotor in the two sided configuration can be written for each axis as

$$f = \frac{1}{4}k\left(\frac{(i_0 + i_x)^2}{(s_0 - x)^2} - \frac{(i_0 - i_x)^2}{(s_0 + x)^2}\right) \tag{2.5}$$

with $k = \mu_0 n_c^2 A_c \cos(\alpha_p)$.

Again, this relationship can be linearized to

$$f = k_s x + k_i i_x \tag{2.6}$$

with, assuming that the rotor nominally is centered between the magnets,

$$k_s = \left.\frac{\partial}{\partial x}f\right|_{x,i_x=0} = k\frac{i_0^2}{s_0^3} \tag{2.7}$$

and

$$k_i = \left.\frac{\partial}{\partial i_x}f\right|_{x,i_x=0} = k\frac{i_0}{s_0^2} \tag{2.8}$$

In the setting described above, the nominal air gap s_0 is given by the geometry of the system. It is the air gap present on each side if the rotor is in the center position. The bias current i_0, however, can now be arbitrarily chosen.

As can be seen from Equation (2.7) and Equation (2.8), the *force–displacement factor* k_s and the *force–current factor* k_i in the above equation depend on the bias current i_0 as follows

$$k_i = k_1 i_0, \text{ and } k_s = k_2 i_0^2, \tag{2.9}$$

where k_1 and k_2 are constants depending on the bearing geometry (material, dimensions, air gap, and coil turns). This implies that the bearing stiffness can be adjusted by means of the bias current i_0.

In principle, the stiffness in each of each axis can be adjusted individually. However, in almost all practical applications, the two axes of a radial bearing are designed to be identical. Besides being intuitive, this also is favorable for the system's rotor dynamics. Identical bearing stiffness imply a symmetrical support, which entails that in operation the rotor's backward modes cannot be excited by unbalance, see Chapter 2.3.3. Throughout this work, the radial bearings are assumed to be symmetrical, allowing to characterize them by a single force–displacement factor k_s and a single force–current factor k_i.

One can show that magnetic bearings operated in differential driving mode have an almost linear current–force relation even for slightly eccentric rotor positions (up to 10% of the air gap) [Schweitzer94].

2.1.3   Other Components of the AMB Support

The AMB support does not only consist of the magnetic coils but also of amplifiers and sensors, see Figure 1.3. The modeling of these components will be addressed next.

Power Amplifiers

System Description

In the setting of this work, AMBs are operated with current control, i.e. at each sampling step the controller calculates the size of the control current that is to be applied to the coils. This current is then generated by the power amplifiers. To this end, the coil current i_{is} is measured and subtracted from the set current i_{set}. An internal controller in the amplifier then adjusts the amplifier's output voltage such that the desired coil current is achieved. The internal control loop often is of very simple structure, in many cases a simple proportional gain controller is used. The overall configuration consisting of amplifier and coil is depicted in Figure 2.1. The transfer function from set current to coil current for such an assembly is

$$\mathbf{T} = \frac{P}{sL + (R_c + P)}. \tag{2.10}$$

This first order transfer function has a corner frequency $\omega_{\mathbf{T}} = (P + R_c)/L$, which restricts the current output at high frequencies. The amplifier bandwidth (defined by $\omega_{\mathbf{T}}$) strongly depends on the size of the internal amplifier gain P.
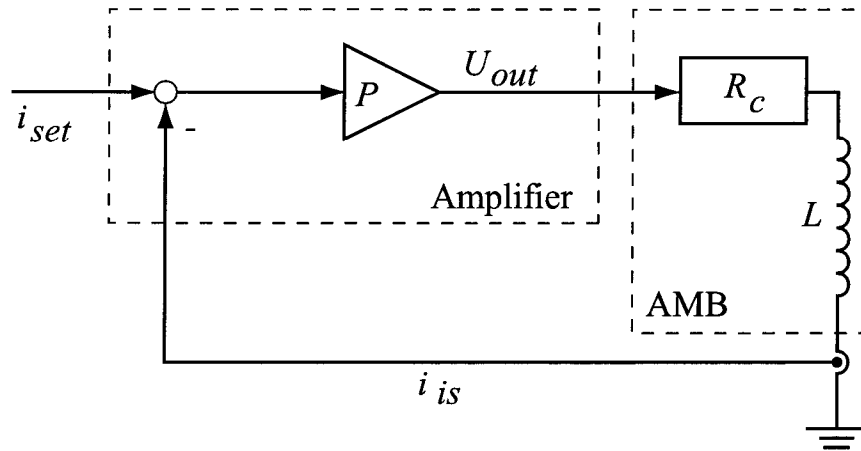
Figure 2.1: *Scheme of current amplifier with AMB*

Further restrictions result from the fact that switched or pulse width modulated amplifiers are typically employed. In these devices, the demanded set current is created by means of very quick switching among a positive or negative voltage that is applied to the coil. If the coil current is too small, the positive voltage U_p is applied. If it is too large, the negative voltage $-U_p$ is used. The switching takes place at a frequency far above the sampling rate and the band width of the AMB control, e.g. at 80kHz.

This procedure has two consequences. First, the set current value is not exactly achieved but the true current oscillates around this value. This causes remagnetization losses in the system. Then, due to the finite voltage used in the amplifier, the current cannot be made rise or fall arbitrarily fast.

The AMB coil can be interpreted as the series interconnection of a copper resistance R_c and an inductance L. The coil's transfer function from voltage to current is that of a first order lowpass filter with cutoff frequency $\omega_0 = R_c/L$. Inserting the maximum voltage U_p (valid for all frequencies) then yields for the maximum achievable bearing current the following upper limit:

$$i_{max,voltage} = \frac{U_p}{sL + R_c} \tag{2.11}$$

In the above, the achievable *constant* maximum current is solely determined by the resistance R_c and the maximum amplifier voltage U_p, i.e. $i_{UR} = U_p/R_c$. As this value is typically very large (e.g. 300A), it is only of theoretical nature. To protect the coils and the power amplifier from overheating, an artificial set current limit $i_{max,hw}$ is introduced (e.g. 8A). As a consequence, two limits are effectively restricting the current output:
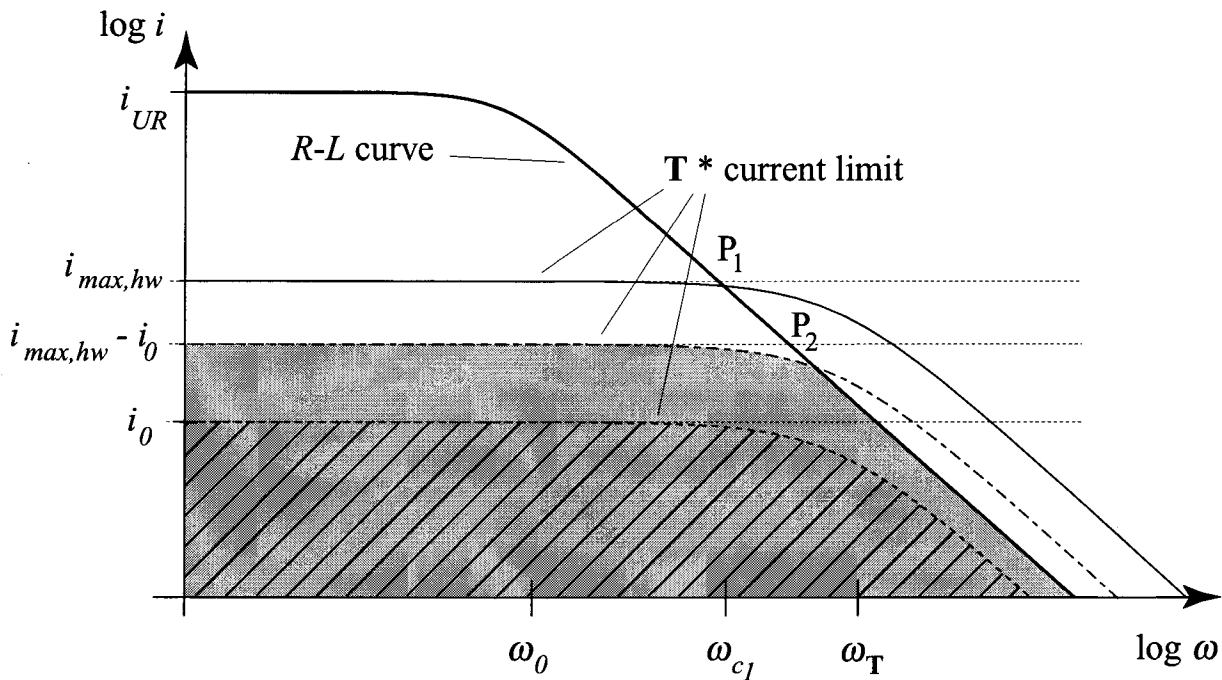
Figure 2.2: *Transfer behaviour of AMB amplifier for different bias currents*

In the low frequency range up to the intersection point P_c of the limit line with the *R-L* curve, the output is limited by the artificial limit $i_{max,hw}$. Beyond the crossover frequency ω_c, the current output is limited by the coil's lowpass characteristic, see Figure 2.2.

For analysis of the *control relevant* limitations, the bias currents must be considered in the above analysis. Being constant, the bias currents simply reduce the available control current from $i_{max,hw}$ to $i_{max} = i_{max,hw} - i_0$. Typically, the bias currents are chosen to be $i_{max,hw}/2$, yielding an equally large current amplitude available for control. It is worthwhile noting that with decreasing current amplitude available the limitations imposed by voltage saturation (intersection point with the *R-L* curve) are shifted to higher frequencies.

These current limitations are superimposed on the amplifier transfer function **T**, whose roll–off may further limit the amplifier output current. All control-relevant limitations can be shown in one diagram if the transfer function **T** is scaled by the control relevant current limit i_{max} and included in the picture, see Figure 2.2.

Model

A good model for the system described above should capture the men-

tioned restrictions without too much conservatism and at the same time be as simple as possible. Furthermore, it is of interest to find a *linear* model description that allows inclusion of the model in the standard (linear) framework of robust controller design presented in Chapter 3.

These requirements are best achieved with a model that is based on the transfer characteristics of the unsaturated amplifier (Equation (2.10)) and adequate limitations (weighting functions) that help keep the set currents in a range that *avoids* saturation during closed loop operation of the plant rather than explicitly modeling the complex behavior of the saturated actuator.

The model resulting from this approach is rather simple, linear, and of low order, as will be shown in the following.

How exactly the above behavior is adequately expressed in a model suitable for controller design depends on the system parameters like the corner frequency ω_T and the intersection frequency of the $\mathbf{T} \cdot i_{max}$ curve with the R-L curve:

- In cases where the function $\mathbf{T}$ shows no significant decrease (in both amplitude and phase) within the control relevant frequency range (e.g. up to 1200Hz), the amplifier dynamics can be neglected. If in this case the R-L curve does not intersect $\mathbf{T} \cdot i_{max}$ within the control relevant range, the model consists of a single constant weighting function $\mathbf{W_1}$ (see Figure 2.3a), and the model order is zero. In the case where there is an intersection of the curves at relevant frequencies, the model structure is the same, but $\mathbf{W_1}^{-1}$ must be chosen to approximate the limit i_{max} up to the intersection point, and then the R-L curve, yielding a first order weighting function and hence a model order of one state per control channel.

- If $\mathbf{T}$ decreases significantly within the control relevant frequency range and no intersection with the R-L curve occurs before the decrease is significant, the amplifier dynamics cannot be neglected. If in this case no intersection with the R-L curve occurs within the control relevant frequency range, the model consists of the transfer function $\mathbf{T}$ and a weighting function $\mathbf{W_1}$ limiting the set current to i_{max} (Figure 2.3b). In this case, the model order is again one state per channel.

  If however such an intersection does occur, the most general case is encountered and the amplifier should be modeled as indicated in Figure 2.3c, where the dynamics are taken care of by the transfer
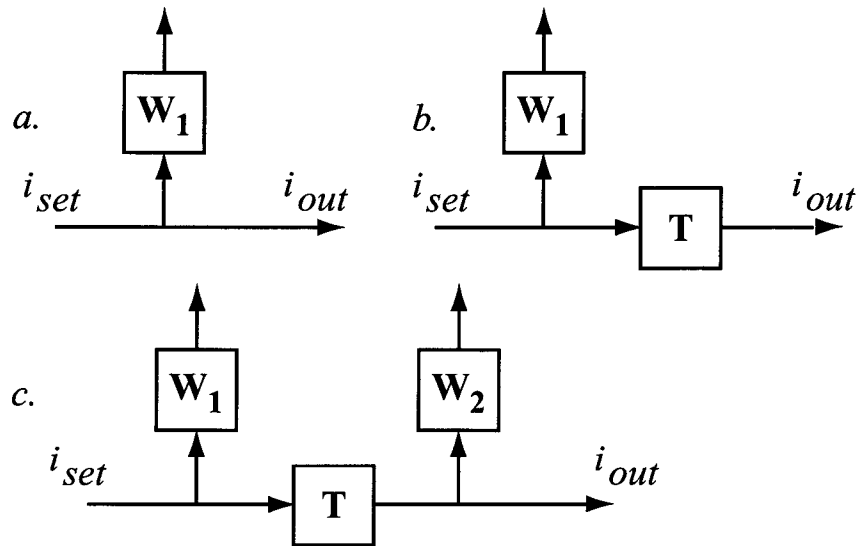
Figure 2.3: *Block diagrams of different amplifier models*

function **T** and the saturation effects are captured by two weighting functions, $\mathbf{W_1}$ limiting the set current to i_{max} and a second weighting function $\mathbf{W_2}$ equal to the inverse of the R-L curve accounting for voltage saturation effects. The cost of this model is 2 states per control channel, one from **T** (Equation (2.10)) and one from the output weighting function $\mathbf{W_2}$. Being constant, $\mathbf{W_1}$ does not increase the model order.

• In the special case where the function **T** decreases non-negligibly within the relevant frequency range but intersection with the R-L curve occurs before the decrease is significant, the adequate model consists again of that from Figure 2.3a with $\mathbf{W_1}^{-1}$ chosen to approximate i_{max} up to the intersection point, and then the R-L curve, and the model order is one state per channel.

The above modeling procedure yields a both simple and adequate representation of the actuators in the controller design process.

Operation with Reduced Bias Current

In most of the standard literature and the majority of applications operation of AMBs with a bias current half the size of the maximum amplifier output current is considered ($i_0 = i_{max,hw}/2$). Practical experience shows however that in numerous cases it is attractive to operate AMB systems with a lower bias current than $i_{max,hw}/2$. This yields both a reduced power consumption and an easier to control system due to less unstable poles,

see Chapter 2.2.

In the context of this work, additional interest in operating AMBs with reduced bias current arises from the requirement to levitate rotors with unknown high frequency dynamics, see Chapter 5.1, motivating the following detailed analysis of the subject.

In context of what has been said in the last section, reduction of the bias current forces the control system designer to choose among two operating modes emerging from the adaptation of bias current:

- The set current can be artificially restricted not to exceed the bias current. This guarantees linear operation. However, this approach is conservative as a considerable part of the actuator power is given away. This is reflected by the hatched region in Figure 2.2.

- Alternatively, the amplifiers can be exploited up to their hardware limit, i.e. a set current limit of $i_{max,hw} - i_0$ can be used. This entails loss of linearity due to nominally negative coil currents being approximated by zero currents for set current amplitudes larger than i_0. The corresponding amplifier limitations are indicated by the grey region in Figure 2.2.

For both of the above approaches, amplifier model descriptions can be directly derived based on the results from the last section and an adequate adaptation of the notion of i_{max}.

However, in order to choose among the two options it is necessary to obtain an understanding of the consequences entailed by the loss of linearity encountered in the second case presented above.

In order to obtain this understanding, the set current to force transfer behavior of an amplifier/bearing combination has been simulated in SIMULINK. The model included the full nonlinear dynamics of the switched amplifiers as well as bearing nonlinearities[1]. The bearing has been operated with a bias current of $i_0 = i_{max,hw}/4$. Sinusoidal set current signals of different amplitudes $\hat{i}$ and frequencies have been fed into the amplifier, and the resulting bearing forces have been analyzed.

The results of this investigation are shown in Figure 2.4. The figure shows

---

[1]The amplifier and bearing modeled are those from the test rig used in Chapter 7 for experimental validation of the algorithms derived in this thesis. The system parameters are given in detail in Chapter 7.1.
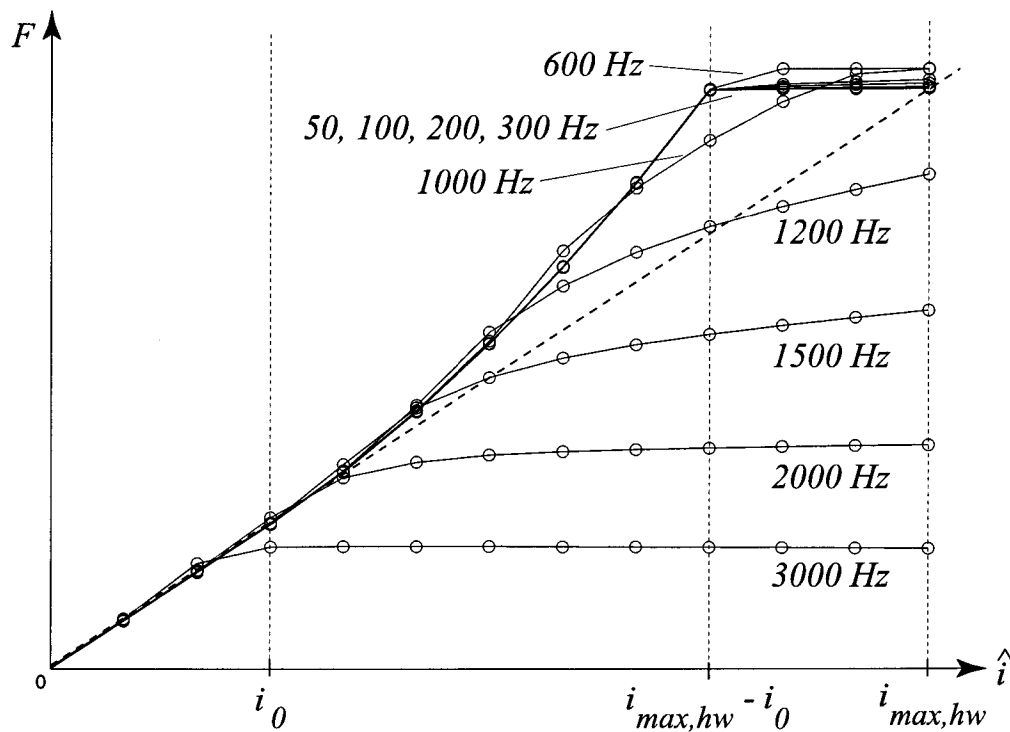
Figure 2.4: *Nonlinear transfer behavior of amplifier/bearing when operated with* $i_0 = i_{max,hw}/4$

that for set current frequencies up to 600Hz, the behaviour is qualitatively always the same:

- Perfect linearity as predicted by the model is achieved for excitation signals with $\hat{i} \leq i_0$.

- A *larger* output force than predicted by the linear model for excitation amplitudes between i_0 and $i_{max-hw} - i_0$. This is caused by the fact that zero current is applied to the coil counteracting the force due to saturation.

- For amplitudes $\hat{i}$ larger than $i_{max,hw} - i_0$, the amplitude difference decreases again and the force exerted on the rotor approaches the value predicted by the linear model (dashed line). This is due to the fact that saturation now occurs on *both* bearing coils.

For excitation frequencies of 1000Hz and more, it can be observed that the force amplitudes achieved decrease and converge to a limit value smaller than the maximum bearing force. This is due to the limitations imposed

by voltage saturation (*R-L* curve). This effect is covered by the linear model presented in the last section.

Summarizing the above observations, it can be stated that AMBs can be operated beyond their linear operating range without overly strong consequences. In the present example, the deviation of linear prediction and nonlinear simulation is in the order of 25% of force amplitude and only a few degrees of phase.

To what extent this is possible must however be judged from case to case — in the limit case when i_0 is selected to be very small, the dotted line representing the linear model's prediction of the force–current factor k_i will be almost horizontal, and the nonlinear curves will be parabolic, yielding an arbitrarily large error between model prediction and actual force output. How large deviations can be tolerated finally depends on the system's gain margin. In critical cases, problems can be avoided by increasing the bias current i_0 or by using a set current limit *between* i_0 and $i_{max,hw} - i_0$.

For high precision measurements, however, excitation amplitudes considerably larger than the bias current should be avoided.

Finally, it is important to realize that in spite of the fact that the nonlinear force amplitude coincides rather well with the linear prediction in the range $i_{max,hw} - i_0 < \hat{i} \leq i_{max,hw}$, these amplitudes must be avoided in practice due to a large phase error (about 30 degrees in this example) that results from the double-sided saturation and is not covered by the linear model.

Sensors

Different types of displacement sensors are used in today's AMB machinery, among them inductive sensors, eddy current sensors, capacitive sensors, magnetic sensors, and optical sensors [Schweitzer94]. Well-designed sensors have micrometer resolution and very good linearity properties with very small phase lag within a sufficiently large measuring range. Their measurement frequency range is many times larger than the sampling frequency of the system. As a consequence, no special model for the sensors is considered, merely the low-pass filters (if any) for noise reduction are included in the model. Inclusion of a reasonable (small) amount of sensor noise in the controller design algorithms used in this work is even favorable for a successful design, see Chapter 3.3.1.

2.1.4 Dynamic Model of the Bearing

Based on the bearing model from Equation (2.3) and the remarks made in the last section, the magnetic bearing can be modeled as a linear device. The equation of motion for a single mass m supported by a magnetic bearing can be expressed as follows:

$$m\ddot{x} = k_s x + k_i i_x \tag{2.12}$$

Based on this equation, the Laplace transform can be used to derive the following model for the 1-dof AMB:

$$X(s) = \frac{\frac{k_i}{m}}{s^2 - \frac{k_s}{m}} I_x(s) \tag{2.13}$$

This implies that a single mass supported by an AMB in one degree of freedom is a second order system with poles at

$$p = \pm\sqrt{\frac{k_s}{m}} \text{ and a static gain of } k_{plant} = -\frac{k_i}{k_s}. \tag{2.14}$$

From the existence of a pole on the positive real axis it can be directly concluded that the system is unstable.

2.2 Modeling of Rigid Rotor AMB Systems

In this section, a model description for rigid rotors in AMBs without control will be introduced. Figure 2.5 schematically shows the system under discussion. As is indicated in the diagram, the axial support is not considered here. This is justified by the negligible coupling of axial and radial dynamics and the fact that for the vast majority of cases the axial dynamics can be described by the single mass model derived in section 2.1.

Furthermore, the analysis is restricted to rigid rotors at standstill. This conforms with the requirements of this thesis, where the rigid rotor model will only be used for the non-rotating rotor. This restriction is convenient since at standstill there is no coupling between the radial motion in two perpendicular planes. As a consequence, it is sufficient to analyze the motion in one plane.

The radial rotor motion in one plane can be completely described by a rigid beam model, i.e. by the displacement x of the rotor's center of gravity S and the rotation of the rotor about an axis through S.
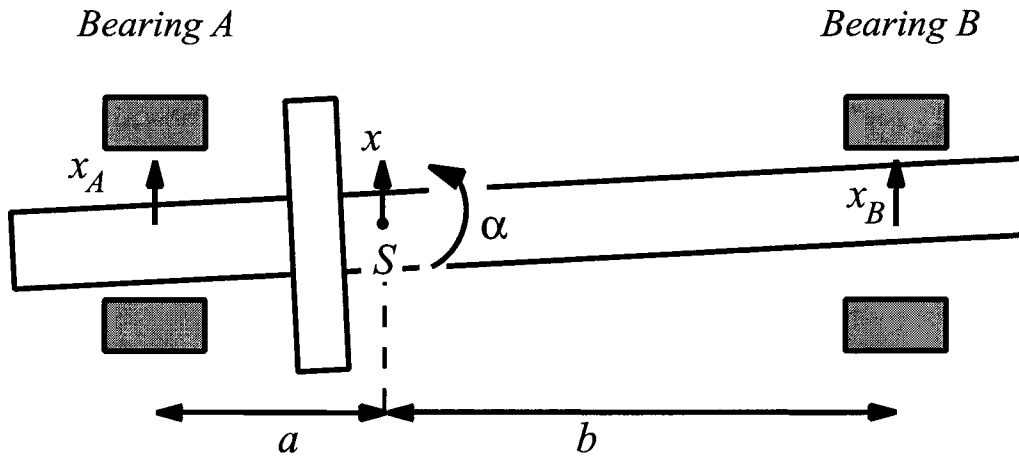
Figure 2.5: *Schematic view of AMB system (one plane, radial dynamics)*

Using the notation from Figure 2.5 and the expressions for the bearing force derived in the last chapter, Equation (2.3), the dynamics of the rigid, non-rotating rotor supported by AMBs can be described in one plane by the equation

$$
\begin{bmatrix} m & 0 \\ 0 & I_r \end{bmatrix} \begin{bmatrix} \ddot{x} \\ \ddot{\alpha} \end{bmatrix} = T_1 \begin{bmatrix} k_{s,A} & 0 \\ 0 & k_{s,B} \end{bmatrix} \begin{bmatrix} x_A \\ x_B \end{bmatrix} + T_1 \begin{bmatrix} k_{i,A} & 0 \\ 0 & k_{i,B} \end{bmatrix} \begin{bmatrix} i_A \\ i_B \end{bmatrix} - \begin{bmatrix} \tilde{m}g \\ 0 \end{bmatrix}
$$
(2.15)

In the above, m is the rotor's total mass, I_r is its radial moment of inertia, $k_{s,A}$ and $k_{s,B}$ are the force–displacement factors of bearing A and bearing B, and $k_{i,A}$ and $k_{i,B}$ represent the corresponding force–current factors. The matrix T_1 describes the transformation of the forces generated by the bearings to the center of gravity and is given by

$$
T_1 = \begin{bmatrix} 1 & 1 \\ -a & b \end{bmatrix}
$$
(2.16)

The rightmost expression from Equation (2.15) describes the influence of gravity on the system. The term $\tilde{m}g$ stands for the force of gravity radially acting on the rotor in the plane under consideration.

If the rotor is horizontal, for the vertical plane $\tilde{m}g = mg$, and for the horizontal plane $\tilde{m}g = 0$. If the two planes rotated by 45° with respect to the vertical/horizontal are considered (the typical case), $\tilde{m}g = 1/\sqrt{2} \cdot mg$ for both planes. For vertical rotors, $\tilde{m}g = 0$ for both planes since no component of gravity is acting in radial direction.

The above system can be entirely transformed to bearing coordinates using the transformation matrix T_2 defined by

$$\begin{bmatrix} x \\ \alpha \end{bmatrix} = T_2 \begin{bmatrix} x_A \\ x_B \end{bmatrix}, \text{ i.e. } T_2 = \frac{1}{a+b} \begin{bmatrix} b & a \\ -1 & 1 \end{bmatrix}. \quad (2.17)$$

The transformed system then is of the form

$$\begin{bmatrix} m_1 & m_3 \\ m_3 & m_2 \end{bmatrix} \begin{bmatrix} \ddot{x}_A \\ \ddot{x}_B \end{bmatrix} = \begin{bmatrix} k_{s,A} & 0 \\ 0 & k_{s,B} \end{bmatrix} \begin{bmatrix} x_A \\ x_B \end{bmatrix} + \begin{bmatrix} k_{i,A} & 0 \\ 0 & k_{i,B} \end{bmatrix} \begin{bmatrix} i_A \\ i_B \end{bmatrix} - T_2 \begin{bmatrix} \tilde{m}g \\ 0 \end{bmatrix}$$
$$(2.18)$$

with

$$m_1 = \frac{mb^2 + I_r}{(a+b)^2}, \ m_2 = \frac{ma^2 + I_r}{(a+b)^2}, \text{ and } m_3 = \frac{mab - I_r}{(a+b)^2}, \quad (2.19)$$

This representation exists for any rigid beam motion in the plane.

2.2.1 Poles of the Rigid Rotor System

For the above system, the poles can be directly calculated from the homogeneous system (without external forces from gravity or currents):

$$\begin{bmatrix} m_1 & m_3 \\ m_3 & m_2 \end{bmatrix} \begin{bmatrix} \ddot{x}_A \\ \ddot{x}_B \end{bmatrix} - \begin{bmatrix} k_{s,A} & 0 \\ 0 & k_{s,B} \end{bmatrix} \begin{bmatrix} x_A \\ x_B \end{bmatrix} = \begin{bmatrix} 0 \\ 0 \end{bmatrix} \quad (2.20)$$

Defining λ_1 and λ_2 as the eigenvalues of the matrix

$$-\begin{bmatrix} m_1 & m_3 \\ m_3 & m_2 \end{bmatrix}^{-1} \begin{bmatrix} k_{s,A} & 0 \\ 0 & k_{s,B} \end{bmatrix}, \quad (2.21)$$

the system poles are

$$p_{1,2} = \pm\sqrt{\lambda_1}j \text{ and } p_{3,4} = \pm\sqrt{\lambda_2}j. \quad (2.22)$$

A schematic plot of typical Laplace plane pole locations for one plane of a rigid rotor AMB system without control is shown in Figure 2.6. The uncontrolled AMBs move the four rigid body poles of the free rotor from the origin to symmetric positions on the real axis.

Like in the case of the lumped mass supported by an AMB investigated in Chapter 1.1.1, the one-plane rotor is an unstable system. The model of
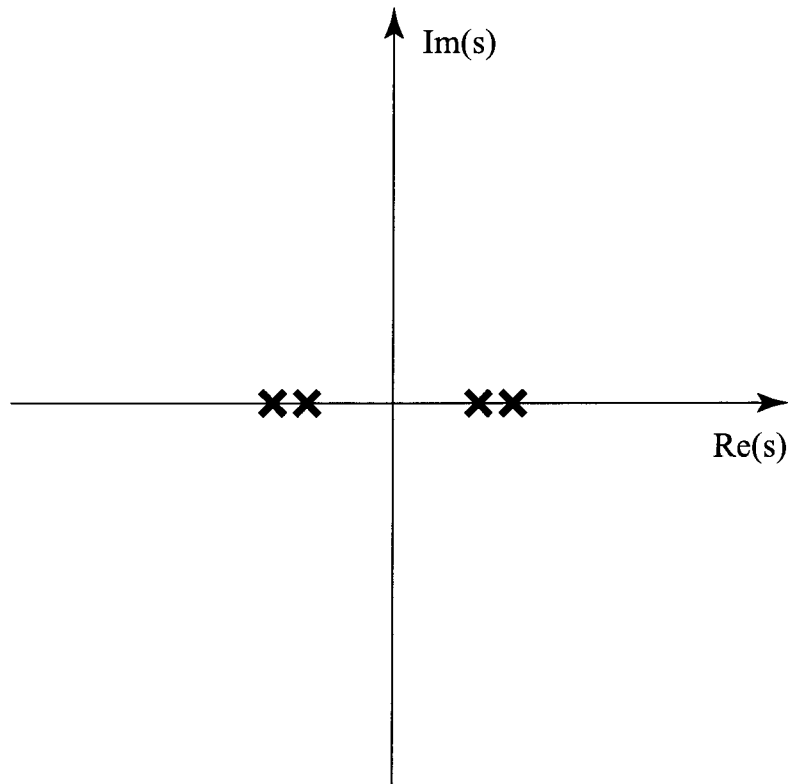
Figure 2.6: *Pole distribution of a rigid rotor AMB system (one plane)*

the full rotor at standstill consists of the two (in case of an axisymmetric rotor and symmetrical support identical) models for the two perpendicular planes. The pole distribution is identical to that from Figure 2.6, but each pole occurs twice. The model describing the radial motion of the rigid rotor in AMBs without control hence has eight poles, four of which are unstable.

2.2.2   State Space Description

The model derived above is easily transformed into a first order system of differential equations of the following form:

$$\dot{\underline{x}}(t) \;=\; A\underline{x}(t) + B\underline{w}(t) \quad \text{with } \underline{x}(0) = \underline{x}_0 \tag{2.23}$$
$$\underline{z}(t) \;=\; C\underline{x}(t) + D\underline{w}(t)$$

With the definitions

$$M_P = \begin{bmatrix} m_1 & m_3 \\ m_3 & m_2 \end{bmatrix}, \; K_P = -\begin{bmatrix} k_{s,A} & 0 \\ 0 & k_{s,B} \end{bmatrix}, \text{ and } T_P = \begin{bmatrix} k_{i,A} & 0 \\ 0 & k_{i,B} \end{bmatrix}$$
$$\tag{2.24}$$

and

$$M_F = \begin{bmatrix} M_P & 0 \\ 0 & M_P \end{bmatrix}, \; K_F = \begin{bmatrix} K_P & 0 \\ 0 & K_P \end{bmatrix}, \text{ and } T_F = \begin{bmatrix} T_P & 0 \\ 0 & T_P \end{bmatrix}, \quad (2.25)$$

the matrices A, B, C, and D in Equation (2.23) are

$$A = \begin{bmatrix} 0^{4 \times 4} & I^{4 \times 4} \\ -M_F^{-1} K_F & 0^{4 \times 4} \end{bmatrix} \in \mathbb{R}^{8 \times 8} \quad B = \begin{bmatrix} 0^{4 \times 4} \\ M_F^{-1} T_F \end{bmatrix} \in \mathbb{R}^{8 \times 4}$$

$$C = \begin{bmatrix} T_S & 0^{l \times 4} \end{bmatrix} \in \mathbb{R}^{l \times 8} \quad D = [0] \in \mathbb{R}^{l \times 4} \quad (2.26)$$

In the above, the matrix $T_S \in \mathbb{R}^{l \times 4}$ represents the transformation matrix from the rotor's displacement at the bearings to the displacement at the locations of the l sensors. In typical configurations, one sensor is used for each AMB axis, i.e. $l = 4$. In the case of pairwise coincidence of sensor and actuator locations (*collocation*), $T_S = I^{4 \times 4}$.

The state space model describing the radial motion of the rigid rotor has four inputs (the two current components on each bearing) and four outputs (the sensor outputs). The poles calculated above are identical to the eigenvalues of the matrix A.

2.3   Modeling of AMB Systems with Flexible Rotors

In this section, the model of a flexible rotor in uncontrolled AMBs is presented. Like in the rigid case, the axial dynamics are neglected. First, some general assumptions are formulated. Then, a model for the flexible free rotor (without bearings) at standstill is presented. In the next step, rotation is included into the model. Finally, the AMBs are added to the rotor model.

2.3.1   General Setup

The following is assumed for all rotors considered in this thesis

- The rotor is axisymmetric (up to small unbalances)

- All displacements of points from their reference positions are small with respect to the rotor dimensions.

- All system parameters are time-invariant.

- The rotational speed is changing slowly enough to be considered constant.

- Rotor torsion is negligible.

- The rotor's inner damping is weak and acts like a moderate structural damping (material damping) that can be modeled as proportional damping.

- Sensors and actuators can be associated with discrete points on the structure.

These boundary conditions are fulfilled in the majority of practical cases and ensure that the problem can be treated by the linear theory presented below. Besides admitting linear analysis of the problem, assuming small deviations permits us to regard the rotor's axial dynamics as independent from its radial dynamics.

2.3.2 Model Descriptions for a Free Flexible Rotor at Standstill

In the following, the model for the flexible rotor at standstill is derived and several model representations are presented. The derivation is based on the finite element method. However, this is only for the sake of convenience and formal completeness. The goal of the controller design technique presented in this thesis is to *avoid* finite element modeling (and in particular the time consuming model updating it entails). Instead, the rotor model is to be obtained by identification. In the identification, the Finite Element (FE) method will not play a role. Nevertheless, the FE method yields an adequate model structure for the systems to be identified.

Finite Element Modeling

Complex flexible structures subject to small deformations can be modeled by means of the so-called Finite Element (FE) method. The basic concept of this method is to partition a continuous structure into discrete elements
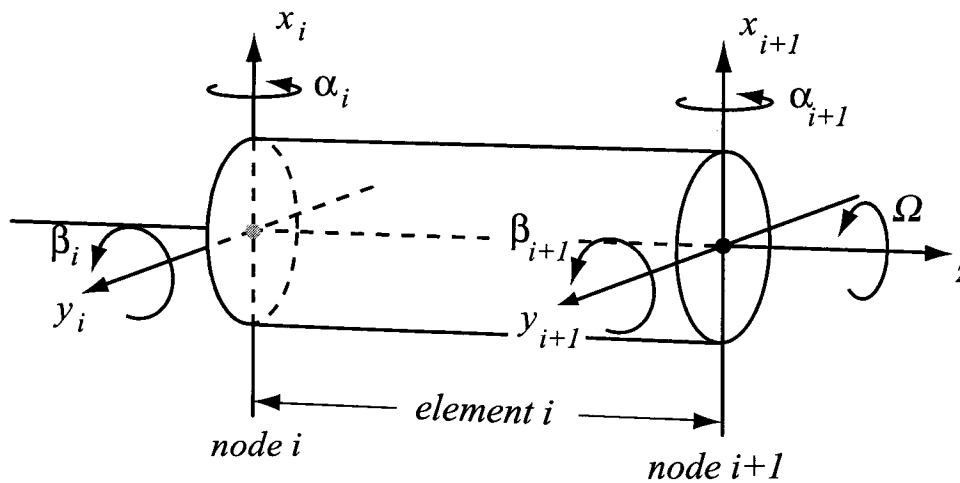
Figure 2.7: *Finite Element representation of rotor element*

of simple geometry. Between neighboring elements, connecting *nodes* are introduced. Each of these nodes has six degrees of freedom about which it can move. For each element a local description of its possible deformation is formulated, based on which a mass, damping, gyroscopic and stiffness matrix can be derived for the element. The deformation of each individual element can be described by the displacement of its nodes. The fact that nodes are shared by several elements enforces an interdependence of the deformation of the different elements of the structure. Using the information on the location and orientation of the individual elements with respect to the global coordinate system, the individual element matrices can be transformed and assembled to global matrices that form a model of the complete structure. A comprehensive introduction to the Finite Element method can be found in [Gasch89].

Rotors fulfilling the conditions from Chapter 2.3.1 can be modeled using cylindrical beam elements. For the individual elements, typically the Timoshenko beam model is used. The nodes are all located on the rotor's axis of symmetry. Since the axial motion is independent from the radial motion and since the rotor is expected to rotate, only four degrees of freedom per node are considered. These are the rotations α_i and β_i about the x and y axes as well as the displacements x_i and y_i in these directions, see Figure 2.7.

The local law of motion for each element is entirely described by the choice of the beam model, the geometry, and the constants describing the material properties of the element. Transformation of the individual elements to the global coordinate system and connecting the elements at the nodes yields

the following equation of motion for the free rotor (without external forces):

$$M\ddot{\underline{q}} + (D + \Omega G)\dot{\underline{q}} + (K + N)\underline{q} = 0 \qquad (2.27)$$

with

M the symmetrical, positive definite mass matrix,

D the symmetrical damping matrix,

G the skew-symmetric gyroscopic matrix,

K the symmetrical, positive semi–definite stiffness matrix,

N the skew-symmetric matrix of non conservative bearing forces,

$\underline{q}$ the displacement vector, and

Ω the rotational speed.

In the above, all matrices are square and the displacement vector $\underline{q}$ consists of the displacements and rotations of the individual nodes as follows:

$$\underline{q} = \left[\underline{q}_x, \underline{q}_y \right]^T \text{ with } \underline{q}_x = [\ldots, x_i, \alpha_i, \ldots] \text{ and } \underline{q}_y = [\ldots, y_i, \beta_i, \ldots].$$

The dimension of the system is $q = 4k$, where k is the number of nodes in the model. Furthermore, the matrices M, D, and K have the following structure:

$$T = \begin{bmatrix} T_x & 0 \\ 0 & T_y \end{bmatrix} \text{ with } T_y = T_x, \ T = M, D, K \qquad (2.28)$$

The identity of the matrices from the x and y planes results from the rotational symmetry of the rotor. The matrices G and N have the structure

$$T = \begin{bmatrix} 0 & T_x \\ -T_x & 0 \end{bmatrix} \text{ with } T = G, N \qquad (2.29)$$

Furthermore, due to the assumed weak internal damping, N, can be neglected ($N \approx 0$).

A comprehensive treatment of the FE modeling technique for rotors can be found in [Bathe82]. In the following, some special model representations of the system are presented for future reference. The derivation is not comprehensive. For details, the reader is referred to any rotor dynamics textbook, e.g. [Krämer93] or [Gasch75].

Assuming that external forces are acting on the rotor at n nodes in each the x and y direction, with the appropriate degrees of freedom selected

by matrix $F \in \mathbb{R}^{q \times 2n}$ and that the rotor position can be observed at l nodes by displacement sensors representable by a transformation matrix $S \in \mathbb{R}^{2l \times q}$, the model from Equation (2.26) can be rewritten as follows:

$$
\begin{aligned}
M\ddot{\underline{q}} + (D + \Omega G)\dot{\underline{q}} + K\underline{q} &= F\underline{w} \\
\underline{z} &= S\underline{q}
\end{aligned}
\qquad (2.30)
$$

where $\underline{w}$ stands for the force input and $\underline{z}$ is the sensor output of the free rotor. With appropriate input and output ordering F and S can be decomposed as follows:

$$
F = \begin{bmatrix} F_x & 0 \\ 0 & F_y \end{bmatrix} \text{ with } F_x, F_y \in \mathbb{R}^{q/2 \times n} \text{ and} \qquad (2.31)
$$

$$
S = \begin{bmatrix} S_x & 0 \\ 0 & S_y \end{bmatrix} \text{ with } S_x, S_y \in \mathbb{R}^{l \times q/2} \qquad (2.32)
$$

State Space Model

The model derived above is easily transformed into a first order system of differential equations of the following form:

$$
\begin{aligned}
\dot{\underline{x}}(t) &= A\underline{x}(t) + B\underline{w}(t) \quad \text{with } \underline{x}(0) = \underline{x}_0 \qquad (2.33) \\
\underline{z}(t) &= C\underline{x}(t) + D\underline{w}(t)
\end{aligned}
$$

In the above,

$$
A = \begin{bmatrix} 0^{q \times q} & I^{q \times q} \\ -M^{-1}K & -M^{-1}(\Omega G + D) \end{bmatrix} \in \mathbb{R}^{2q \times 2q} \quad B = \begin{bmatrix} 0^{q \times 2n} \\ M^{-1}F \end{bmatrix} \in \mathbb{R}^{2q \times 2n}
$$

$$
C = \begin{bmatrix} S & 0^{2l \times q} \end{bmatrix} \in \mathbb{R}^{2l \times 2q} \quad D = [0] \in \mathbb{R}^{2l \times 2n} \qquad (2.34)
$$

The state variable $\underline{x}$ is defined as $\underline{x} = \begin{bmatrix} \underline{q} , \dot{\underline{q}} \end{bmatrix}^T$.

Modal Decomposition

As has been shown above, the motion in the two planes in Equation (2.30) is only coupled by the matrix G. At standstill ($\Omega = 0$), G has no influence and the motion in each of the two planes does not depend on the motion in the other plane.

At standstill, Equation (2.30) simplifies to

$$
\begin{aligned}
M\ddot{\underline{q}} + D\dot{\underline{q}} + K\underline{q} &= F\underline{w} \\
\underline{z} &= S\underline{q}
\end{aligned}
\tag{2.35}
$$

Application of an *ansatz* of exponential form to the undamped system with no external forces ($D = 0$, $F = 0$) leads to the generalized eigenvalue problem

$$
(K - \omega_{0i}{}^2 M)\underline{\phi}_i = \underline{0}
\tag{2.36}
$$

whose q solutions $(\omega_{0i}{}^2, \underline{\phi}_i)$ give information about the system's free vibration which is a superposition of components of the form

$$
\underline{q}_i(t) = \underline{\phi}_i \cdot \cos(\omega_{0i}t + \alpha_i)
\tag{2.37}
$$

with arbitrary phase angles α_i. The numbering of the eigenfrequencies can be chosen in such a way that the they are of ascending frequency. Subsequent compilation of the corresponding eigenvectors in a matrix yields:

$$
\Phi =
\begin{bmatrix}
| & \cdots & | \\
\underline{\phi}_1 & \cdots & \underline{\phi}_q \\
| & \cdots & |
\end{bmatrix}
\in \mathbb{R}^{q \times q}
\tag{2.38}
$$

This matrix can be used to transform Equation (2.35) from physical coordinates q to modal coordinates $\tilde{q}$ by substituting

$$
\underline{q} = \Phi\underline{\tilde{q}}.
\tag{2.39}
$$

Subsequent multiplication of Equation (2.35) from the left by Φ^T then yields

$$
\begin{aligned}
\tilde{M}\ddot{\underline{\tilde{q}}} + \tilde{D}\dot{\underline{\tilde{q}}} + \tilde{K}\underline{\tilde{q}} &= \tilde{F}\underline{w} \\
\underline{z} &= \tilde{S}\underline{\tilde{q}}
\end{aligned}
\tag{2.40}
$$

with

$$
\tilde{F} = \Phi^T F \text{ and } \tilde{S} = S\Phi.
\tag{2.41}
$$

Due to the symmetry of M and K, the matrices $\tilde{M}$ and $\tilde{K}$ in Equation (2.40) are of diagonal structure. The above transformation becomes particularly effective when the columns of the transformation matrix Φ are scaled in such a way that the matrix $\tilde{M}$ becomes the identity matrix. In this case we obtain

$$\tilde{M} = \Phi^T M \Phi = I \qquad (2.42)$$

$$\tilde{K} = \Phi^T K \Phi = \mathrm{diag}(\omega_{0i}^2). \qquad (2.43)$$

In the case of proportional damping, i.e. when $D = \alpha M + \beta K$ for $\alpha, \beta \in \mathbb{R}$, the damping matrix is also diagonalized, i.e.

$$\tilde{D} = \Phi^T D \Phi = \mathrm{diag}(2\xi_i \omega_{0i}). \qquad (2.44)$$

In this case, Equation (2.40) is completely decoupled into q distinct one degree of freedom oscillators with poles

$$
\begin{aligned}
p_i &= -\xi_i \omega_{0i} + j\omega_{0i}\sqrt{1 - \xi_i^2} \text{ and} \\
\\
p_i^* &= -\xi_i \omega_{0i} - j\omega_{0i}\sqrt{1 - \xi_i^2}.
\end{aligned}
\qquad (2.45)
$$

Each oscillator is associated with one eigenmode with shape $\underline{\phi}_i$. The free vibration of the shape has frequency $\omega_i = \sqrt{1 - \xi_i^2}\,\omega_{0i}$ and decays with $e^{-\xi_i \omega_{0i} t}$.

Based on the poles from Equation (2.45), the state space description for the proportionally damped one-plane system at standstill can be written in the following very simple form:

$$
A = \begin{bmatrix}
& 0^{q \times q} & & I^{q \times q} & \\
-(p_1 \cdot p_1^*) & & 0 & (p_1 + p_1^*) & 0 \\
& -(p_2 \cdot p_2^*) & & & (p_2 + p_2^*) \\
& & \cdots & & \cdots \\
0 & & -(p_q \cdot p_q^*) & 0 & (p_q + p_q^*)
\end{bmatrix}
\qquad (2.46)
$$

$$B = \begin{bmatrix} 0 \\ \tilde{F} \end{bmatrix} \in \mathbb{R}^{2q \times 2n} \quad C = \begin{bmatrix} \tilde{S} & 0 \end{bmatrix} \in \mathbb{R}^{2l \times 2q} \quad D = [0] \in \mathbb{R}^{2l \times 2n}$$

Model Reduction by Modal Truncation

Up to here, the size of the model was determined by the number of nodes in the finite element model. Even simple models typically have 10 nodes, which leads to 40 degrees of freedom for the one plane model, entailing a state space model of order 80. The majority of the associated single mass oscillators have very high eigenfrequencies. For technical applications however, in particular for AMB control, one is only interested in the model behaviour up to a certain frequency limit. Furthermore, besides the fact that the FE method merely approximates the behaviour of the structure, no structure can be expected to behave linearly up to arbitrarily high frequencies.

For these reasons and in order to limit the computational burden in subsequent calculations, one is interested in adapting the model such that it describes the system in a frequency range where this is reasonable.

This can be simply achieved as follows. First, the columns $\underline{\phi}_i$ of Φ are ordered such that the corresponding eigenfrequencies are monotonously increasing. In the next step, the columns of Φ belonging to too large eigenfrequencies are truncated. If the first r eigenfrequencies are relevant, the new matrix Φ_r has q rows and r columns. Then the transformation to modal coordinates is carried out with Φ_r instead of Φ. The resulting system then has the same properties as before, but lower dimension:

$$
\begin{aligned}
\tilde{M}_r \ddot{\underline{\tilde{q}}}_r + \tilde{D}_r \dot{\underline{\tilde{q}}}_r + \tilde{K}_r \underline{\tilde{q}}_r &= \tilde{F}_r \underline{w} \\
\underline{z} &= \tilde{S}_r \underline{\tilde{q}}_r
\end{aligned}
\tag{2.47}
$$

$$
\text{with } \tilde{M}_r, \tilde{D}_r, \tilde{K}_r \in \mathbb{R}^{r \times r}, \tilde{F}_r \in \mathbb{R}^{r \times 2n}, \tilde{S}_r \in \mathbb{R}^{2l \times r}.
\tag{2.48}
$$

As a result of the reduction, in Equation (2.47) a low order model with a very similar input–output behavior to the model from Equation (2.8) is obtained.

Furthermore, the transformation

$$
\underline{q} = \Phi_r \underline{\tilde{q}}_r
\tag{2.49}
$$

allows to interpret general results obtained for the reduced system in the physical coordinates of the full system.

This reduction technique also yields a low order state space description for the system with the same structure as Equation (2.46).
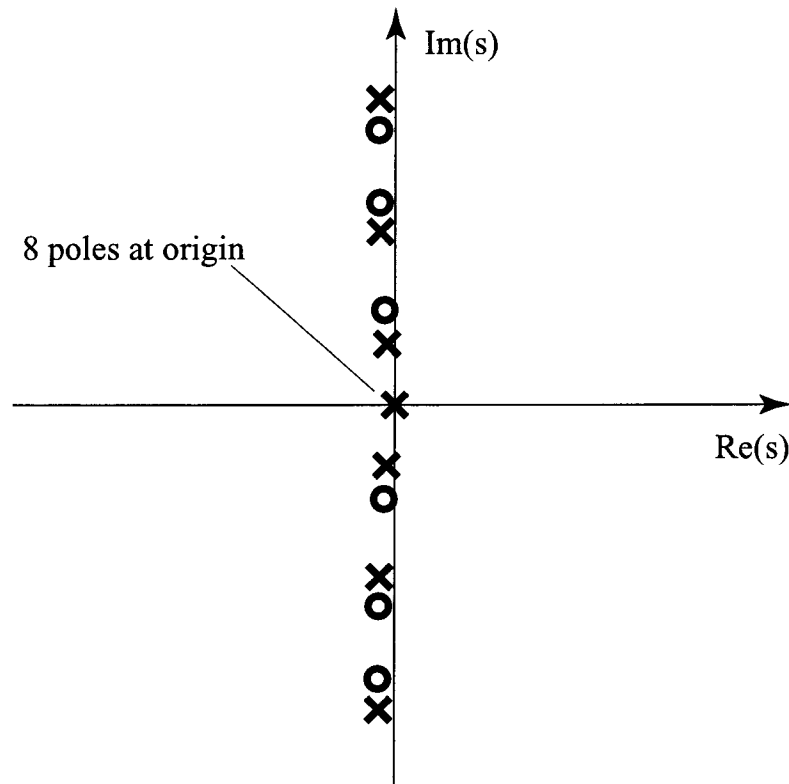
Figure 2.8: *Typical pole–zero distribution of a flexible rotor at standstill*

Poles of the Flexible Rotor System

A typical pole–zero distribution for a free flexible rotor at standstill is shown in Figure 2.8. Due to the symmetry of the system, each pole occurs twice, once for each plane. The eight rigid body poles are located at the origin. Additionally, the model exposes $q-4^2$ conjugate complex pole pairs slightly to the left of the imaginary axis. These poles are associated with the flexible eigenmodes of the rotor and usually are very weakly damped, in some cases the damping is as low as $\xi_i = 0.0005$. These poles are what makes control of flexible rotors so much more demanding than that of rigid rotors.

---

[2] For reduced systems: $r - 4$.

2.3.3 Model Description for a Free Flexible Rotor when Rotating

For the case of a rotating rotor ($\Omega \neq 0$), the motion in the two planes in Equation (2.30) are coupled by the gyroscopic term ΩG. A reduced state space model of the rotating rotor with modal damping is given by the following equation:

$$A = \begin{bmatrix} 0^{r \times r} & I^{r \times r} \\ -\tilde{K}_r & -(\tilde{D}_r + \Omega \tilde{G}_r) \end{bmatrix} \in \mathbb{R}^{2r \times 2r} \tag{2.50}$$

$$B = \begin{bmatrix} 0 \\ \tilde{F}_r \end{bmatrix} \in \mathbb{R}^{2r \times 2n} \quad C = \begin{bmatrix} \tilde{S}_r & 0 \end{bmatrix} \in \mathbb{R}^{2l \times 2r} \quad D = [0] \in \mathbb{R}^{2l \times 2n}$$

where all matrices are defined as above and $\tilde{G}_r = \Phi_r^T G \Phi_r$. $\tilde{G}_r$ remains skew-symmetric under this transformation and the structure of the A matrix is that from Equation (2.46) up to the lower right block which now is full and skew-symmetric. The coupling of the two planes causes the system's flexible poles to move with increasing Ω from the positions indicated in Figure 2.8 in opposite directions along the imaginary axis towards increasing and decreasing frequencies. Instead of independent vibrations in each of the two planes, the rotating system has eigenmodes affecting both planes. In the (typical) case of an axisymmetric foundation, all orbits are circular. The modes with increasing frequencies expose a rotation in the same direction as the rotor and are therefore called forward modes or *nutations*. The modes with decreasing frequencies rotate in the opposite direction and are called backward modes or *precessions*. The splitting of the flexible eigenfrequencies with increasing rotational speed is shown in the Campbell diagram in Figure 2.9. When sped up from standstill, successively several of the eigenfrequencies are passed (intersection points). The associated rotational speeds are the *critical speeds* of the rotor. At these speeds, the unbalance force may excite flexible modes of the rotor. If the rotor is free or supported by homogeneous bearings, unbalance forces can only excite nutation modes. If however the bearings are not symmetrical, also precession modes may be excited.
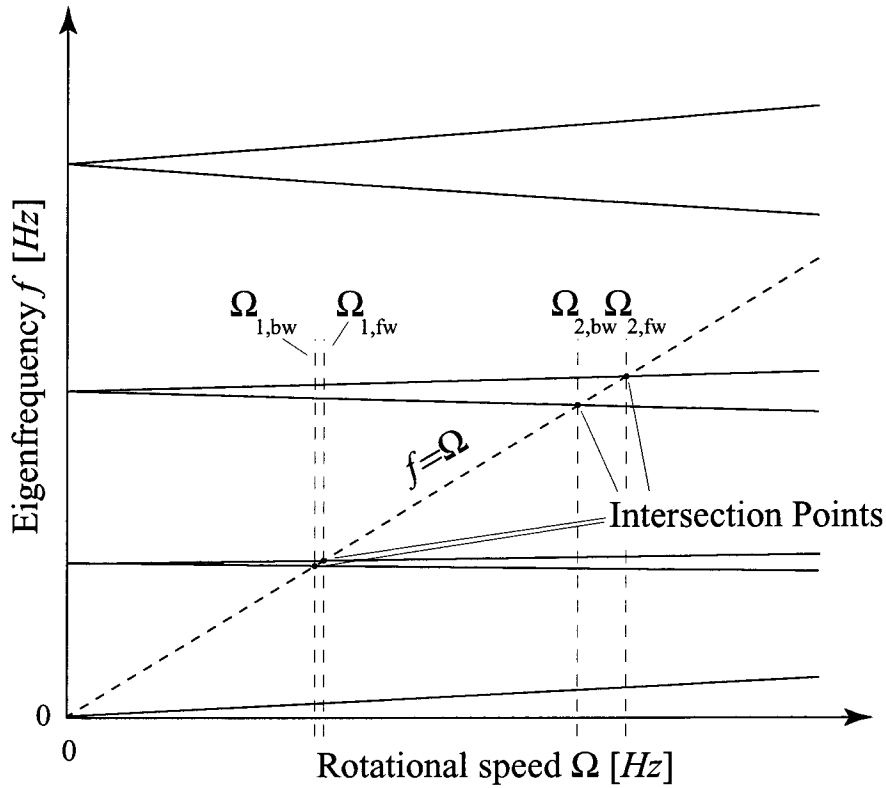
Figure 2.9: *Campbell diagram of a flexible rotor. The rotational speeds $\Omega_{1,bw}$, $\Omega_{1,fw}$, $\Omega_{2,bw}$, and $\Omega_{2,fw}$ are the critical speeds associated with the first and second backward and forward flexible modes.*

2.3.4 Model Description for AMB Systems with Flexible Rotors

Flexible rotor AMB systems can be modeled by combining the model of the flexible rotor derived above with the model of the AMBs. To this end, the AMBs are first introduced as external forces acting on the free rotor:

$$M\underline{\ddot{q}} + (D + \Omega G)\underline{\dot{q}} + K\underline{q} = K_s\underline{q} + K_i\underline{i}$$
$$\underline{z} = S\underline{q}$$
$$(2.51)$$

In the above, $K_s \in \mathbb{R}^{q \times q}$ is a matrix that is except for four force–displacement factors k_s ($k_{s,A}$ and $k_{s,B}$ each occurring twice) on the diagonal positions associated with those translational degrees of freedom to which the bearings are attached. Furthermore, $\underline{i}$ is a vector of length four representing the current inputs to the bearing. The matrix $K_i \in \mathbb{R}^{q \times 4}$ contains at the appropriate locations the force–current factors k_i of the four AMB axes.

As before, the eigenvector matrix Φ_r is calculated based on the matrices

M and K and the system is transformed to modal coordinates. This yields

$$\tilde{M}_r \ddot{\underline{\tilde{q}}}_r + (\tilde{D}_r + \Omega \tilde{G}_r)\dot{\underline{\tilde{q}}}_r + \tilde{K}_r \underline{\tilde{q}}_r = \tilde{K}_{sr}\underline{\tilde{q}}_r + \tilde{F}_r \underline{i}$$
$$\underline{z} = \tilde{S}_r \underline{\tilde{q}}_r \tag{2.52}$$

with

$$\tilde{K}_{sr} = \Phi_r^T K_s \Phi_r \text{ and } \tilde{F}_r = \Phi_r^T K_i. \tag{2.53}$$

Combining the stiffness terms one finally obtains

$$\tilde{M}_r \ddot{\underline{\tilde{q}}}_r + (\tilde{D}_r + \Omega \tilde{G}_r)\dot{\underline{\tilde{q}}}_r + (\tilde{K}_r - \tilde{K}_{sr})\underline{\tilde{q}}_r = \tilde{F}_r \underline{i}$$
$$\underline{z} = \tilde{S}_r \underline{\tilde{q}}_r \tag{2.54}$$

The resulting compound stiffness matrix $\tilde{K}_r - \tilde{K}_{sr}$ is not exactly diagonal, but the diagonal entries are significantly larger than the other elements. Therefore, the AMB stiffness mainly affects the rigid body modes (which had zero stiffness before) and the standard transformation of Equation (2.54) yields a state space description that is approximately of the form of Equation (2.51).

In fact, a state description that is exactly of this form exists for the system, but it cannot be derived by the modal decomposition approach since for the rotor supported by AMBs, the matrix K loses its definiteness properties due to the negative AMB stiffness. This leads to complex solutions of the generalized eigenvalue problem from Equation (2.36), prohibiting the subsequent transformation steps.

The pole–zero map of the flexible rotor in uncontrolled AMBs typically looks like that shown in Figure 2.10. As has been shown for the rigid rotor, the AMBs bring the poles associated to rigid body motion away from the origin to symmetrical positions on the real axis, yielding an unstable system. Just like in Figure 2.8, all poles occur twice.

Application of stabilizing controllers of the AMBs brings the unstable rigid body poles to the left half plane. With increasing controller gain, the poles first move to the left along the real axis. If the gain is further increased, they split and follow the positive and negative imaginary axis. By adding a damping behaviour to the controller, the poles can additionally be moved to the left of the imaginary axis, yielding a stable oscillating system.

Under rotation, the poles of the flexible rotor in controlled bearings behave similar to those from Figure 2.9. The rigid body modes now located in the left half plane show a splitting behaviour similar to that of the flexible modes.
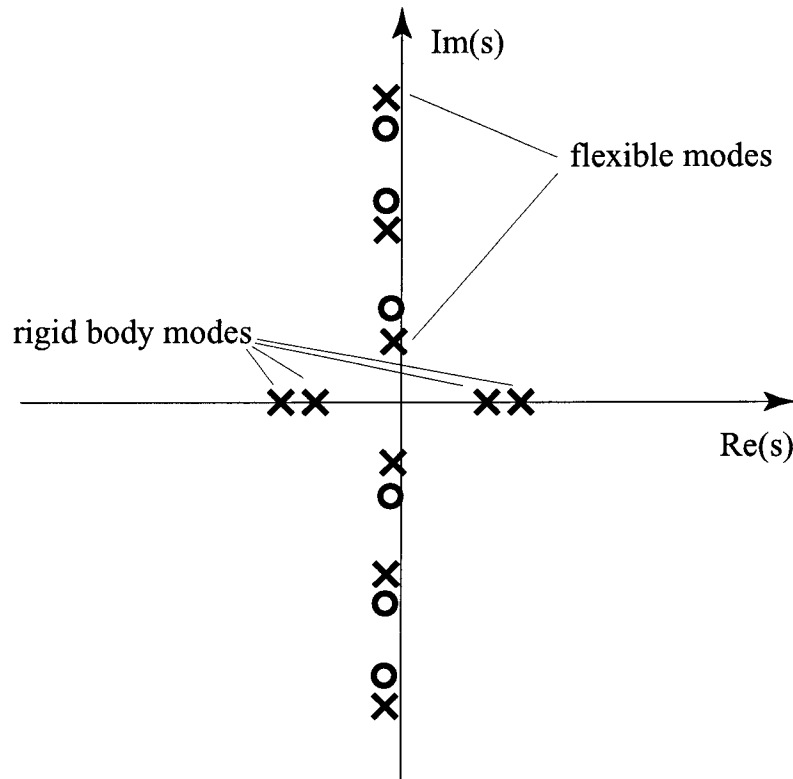
Figure 2.10: *Typical pole–zero distribution of a flexible rotor in AMBs at* $\Omega = 0$

In the above, stability may appear to be easily achievable. However, this conjecture is wrong. In fact, finding a controller that stabilizes the rigid body modes of the flexible rotor *without destabilizing* the weakly damped flexible modes is a very complex task and the central problem in AMB controller design. In particular, the fact that the eigenfrequencies change with speed requires special care and application of adequate controller design methods. The issue of controlling AMB systems is further pursued in the next chapter, where an introduction to robust controller design is given.

2.4 Summary

In this chapter, the modeling of AMB rotor systems has been addressed. In the first section of the chapter, models for different components of AMB systems have been presented. Based on the simple case of a single–sided bearing, a linear model for two–sided bearings has been introduced. Then, a new amplifier model suited to avoid actuator saturation has been pre-

sented. The model is based on weighting functions and has been designed for employment in the μ-synthesis and μ–analysis settings.

In the second section, the standard model for rigid rotors supported by AMBs has been presented. The third section deals with the modeling of flexible rotors. Methods for coordinate transformation and model reduction have been introduced. In view of their important role throughout the rest of this work, special attention has been paid to weakly damped flexible poles and gyroscopic effects.

Chapter 3

Robust Controller Design

In this chapter, the basics of robust control theory are outlined. The general assumption made is that the reader is fairly familiar with the basic terminology of general control theory. Furthermore, some knowledge of some elementary concepts of robust control, e.g. $\|\cdot\|_\infty$, are presupposed. For background information the reader is referred to Appendix B.

This chapter is organized as follows. First, the concept of uncertainty is introduced. After this, the most common controller design objectives are formulated. In this context, the concepts of nominal and robust stability and performance are presented, and the importance of the maximum singular value as a measure of tolerable unstructured uncertainty is elaborated. Then, the scope is extended to structured uncertainty and the structured singular value μ is introduced as the appropriate tool to analyze systems with structured uncertainty. In next chapter, controller synthesis is addressed. The $\mathcal{H}_\infty$ algorithm is presented and application issues as well as its limitations are discussed. Then μ-synthesis is introduced as a robust controller design method that overcomes some of these limitations. The chapter ends with an introduction to μ–analysis, the state of the art tool for analyzing controller performance. μ–synthesis and μ–analysis constitute the basis of the controller design method developed in Chapter 5.

3.1   Model Uncertainty

Whenever a controller is to be designed for a real system, a model G_n of this system is required. Unfortunately, no model of a physical system can be exact, hence if a controller C works well with G_n, no conclusions can be drawn concerning the behaviour of the real system when controlled by C. The solution to this problem lies in the extension of G_n by explicit models for the possible differences between G_n and the real system, which are interpreted as uncertainties in the model G_n.
This yields a set of models, that is expected to comprise the real system. The controller design is then performed for this set of models, i.e. in particular for the real system. This is the key concept of robust control. In the following, we first name some of the main sources of uncertainty. Then, techniques to include uncertainties into system models will be presented.

3.1.1   Sources of Uncertainty

Model uncertainty may result from one or several of the following points:

Model parameter uncertainty. , Since perfect system identification is impossible, uncertainties occur in all models of physical systems.

Neglected high frequency dynamics. The model behaviour at high frequencies cannot be identified, and therefore not modeled. This inevitably entails model uncertainty.

Non-linearities. These may have been neglected or approximated by linear models even in the range of low frequencies.

Changing operating conditions. For example temperature changes may lead to sensor drifts.

Neglected dynamics. Some of the system dynamics may have been deliberately neglected or simplified, e.g. the vibrations of rotor blades.

Parameter changes due to wear. For example in pumps the system dynamics may change considerably due to seal wear.

Setup variations. In some cases, the desired controller is to work with different system setups, for example a controller for an AMB milling spindle should function with tools of different mass.

Change of operating point. The system behaviour may change with the operating point, as is for example the case for gyroscopic rotors. Due to gyroscopic effects, the pole locations change with the rotational speed. This must be considered in the controller design to guarantee stability over the whole range of operating speeds.

In all cases, it is the responsibility of the control engineer to judge which of the above factors are relevant for the given problem, and how large the respective uncertainties are. In the following, the issue of quantification and formal introduction of uncertainty is addressed.

3.1.2   Linear Fractional Transformations

An equally efficient and general way of formulating uncertainty and introducing it into a system is by means of linear fractional transformations (LFTs). Given a complex matrix M that is partitioned into four blocks and relates the vectors u and v as follows,
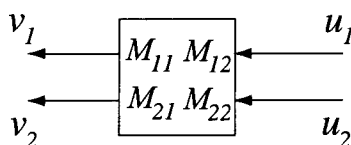
Assume existence of a second matrix Δ relating u_1 and v_1 by $u_1 = \Delta v_1$. Graphically, this relationship can be represented as:
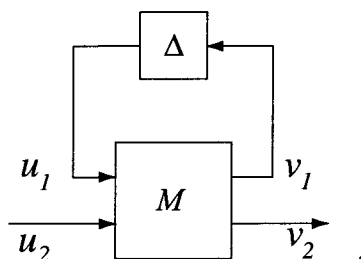
It is straightforward to show that the relation between v_2 and u_2 in this configuration is given by

$$v_2 = [M_{22} + M_{21}\Delta(I - M_{11}\Delta)^{-1}M_{12}]u_2. \tag{3.1}$$

This is abbreviated $v_2 = F_U(M, \Delta)u_2$.

In the above example, the upper loop has been closed with Δ. This config-
uration is *called upper fractional transformation*. If the lower loop is closed,
this is referred to as a *lower fractional transformation*. The corresponding
analytic relationship is then

$$v_1 = [M_{11} + M_{12}\Delta(I - M_{22}\Delta)^{-1}M_{21}]u_1 \qquad (3.2)$$

and is abbreviated by $v_1 = F_L(M, \Delta)u_1$.

This concept does not only hold for matrices and vectors but can be ex-
tended to dynamical systems and signals without any modification. In
literature, uncertainty is traditionally represented by upper linear trans-
formations. One of the key features of the LFT framework is that arbitrary
interconnections (series, parallel, cascades, etc.) of different LFTs always
can again be expressed by an LFT.

3.1.3   Structured and Unstructured Uncertainty

As stated above, expected differences between the nominal system model
and the real world are included in the controller design process by aug-
menting the system model with an adequate model of the uncertainty.
The only information assumed to be known is the maximum size of the
expected uncertainty for each frequency ω. This leads to norm bounded
perturbations $\Delta(s)$, that are added to the system, yielding a set with an
infinite number of possible systems to be considered in the subsequent
controller design. While different ways of linking the uncertainty to the
system exist, two classes of uncertainty can be distinguished:

Unstructured uncertainty is used whenever unknown or neglected system
dynamics are to be represented. Unstructured uncertainty is typically rep-
resented as additive or multiplicative uncertainty, see Figure 3.1. While
the norm $\|\Delta\|_\infty$ of the delta block is generally considered to be limited to
1, the blocks $\mathbf{W_a}$ and $\mathbf{W_m}$ represent weighting functions that express the
size of the uncertainty over frequency — typically, the uncertainty is small
at low frequencies and large at high frequencies. Often, the uncertainty's
size at high frequencies is several times larger than that of the nominal
system $\mathbf{G_n}$ itself. Note that for multiplicative uncertainty the uncertainty
block is always quadratic while in the MIMO case with additive uncer-
tainty the uncertainty block may have a different number of inputs than
outputs, depending on the number of input and output channels of $\mathbf{G_n}$.
Unstructured uncertainty often also is referred to as *lumped uncertainty*.
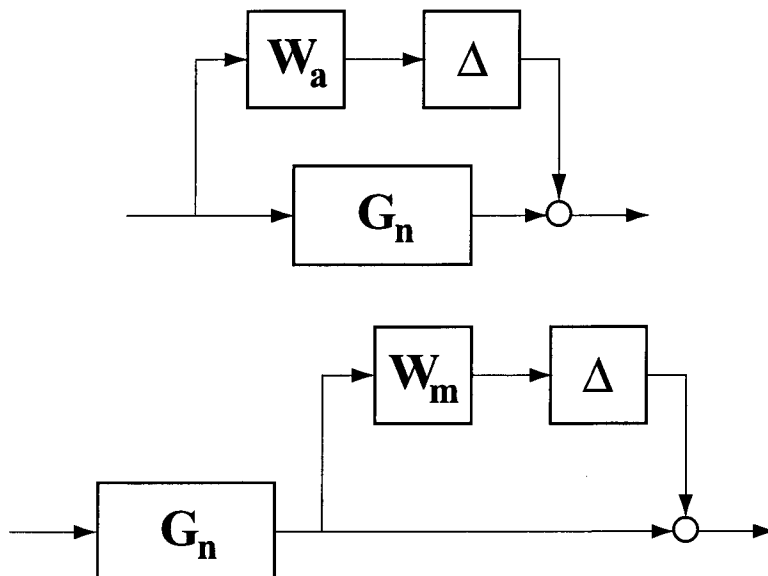
Figure 3.1: *Systems with unstructured uncertainty, top: additive uncertainty, bottom: multiplicative uncertainty*

Structured uncertainty occurs whenever more than a single uncertainty is encountered. A special example of structured uncertainty is that of a nominal model with two or more specific parameters being uncertain. An additional output path is then included into the model for each parameter, and the parameter change is represented by a delta block that is implicitly assumed to be norm-bounded by one and an appropriate scalar scaling factor reflecting the size of parameter variation to be expected. The individual delta blocks can be assembled to a single delta block similar to that in the unstructured case. The key difference however lies in the fact that the delta block encountered here has only entries on its diagonal, which makes this a structured uncertainty in contrast to the full delta block in the unstructured uncertainty case.

As an example a single mass oscillator can be considered. The systems motion can be described by the following differential equation:

$$m\ddot{y} + d\dot{y} + ky = f \tag{3.3}$$

This system can be represented by the transfer function $\mathbf{G_n}$ shown in Figure 3.2. Assume that the damping and stiffness parameters d and k are only approximately known, with 30% uncertainty on d and 10% uncertainty on k. This leads to the system with structured uncertainty depicted in Figure 3.2.

In practical systems, unstructured and parametric uncertainty are often
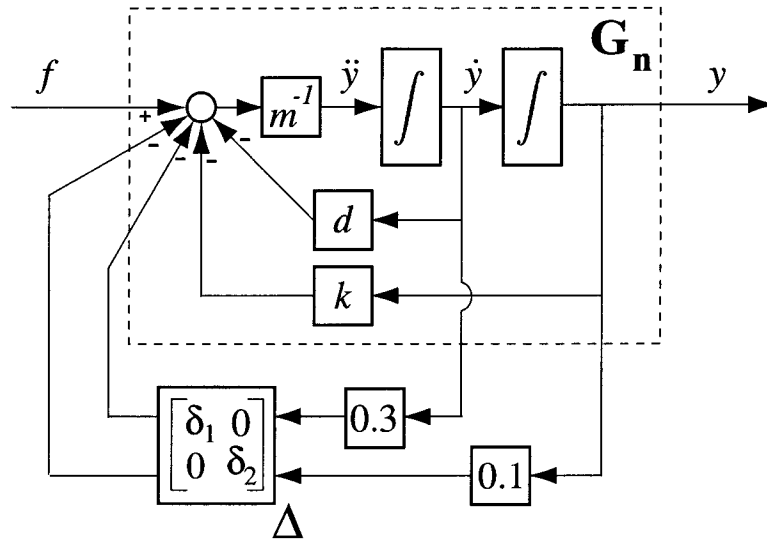
Figure 3.2:   *Single mass oscillator with uncertain stiffness and damping parameters*

combined, e.g. whenever a system has unmodeled high frequency dynamics and a varying spring stiffness. These blocks can then again be unified in one delta block which again is *structured* — the resulting delta block is then block-diagonal. Any combination of two or more blocks of unstructured uncertainty always yields a plant with *structured uncertainty*. Although multiple unstructured uncertainties are not often used in the uncertainty modeling of practical applications, it is of considerable importance in the synthesis of controllers with robust performance. This will be elaborated in Chapter 3.2.4. Figure 3.3 shows structured uncertainty blocks resulting from a combination of parametric and unstructured uncertainty (left) and repeated unstructured uncertainty (right).

By adequate algebraic manipulation, the uncertainties can always be pulled out of the system and the uncertainty model can be written as an (upper) linear fractional transformation with an uncertainty block of respective structure.

Figure 3.3: *Examples of structured uncertainty blocks*

3.1.4 Uncertainty in State Space Descriptions

A special case of uncertainty is given if the model uncertainty can be expressed as an uncertainty on the matrices of a state space description of the model. In a general form, for a state space system with n states, n_u inputs and n_y outputs this can be expressed as

$$\begin{bmatrix} \dot{\underline{x}}(t) \\ \underline{y}(t) \end{bmatrix} = \left(\begin{bmatrix} A_0 & B_0 \\ C_0 & D_0 \end{bmatrix} + \sum_{i=1}^{m} \delta_i \begin{bmatrix} A_i & B_i \\ C_i & D_i \end{bmatrix} \right) \begin{bmatrix} \underline{x}(t) \\ \underline{u}(t) \end{bmatrix}. \tag{3.4}$$

In the above, the nominal system is denoted by the state space system with suffix 0, and m independent uncertainties acting on the same or all of the state space parameters have been considered. Again, $|\delta_i| \leq 1$ is implicitly assumed.

For each of the uncertainty matrices holds

$$\begin{bmatrix} A_i & B_i \\ C_i & D_i \end{bmatrix} \in \mathbb{R}^{(n+n_y) \times (n+n_u)}. \tag{3.5}$$

By letting r_i denote the rank of uncertainty matrix i, this uncertainty can be expressed by means of a linear fractional transformation. To this end, the singular value decomposition of the matrices is used to factor them as follows:

$$\begin{bmatrix} A_i & B_i \\ C_i & D_i \end{bmatrix} = \begin{bmatrix} E_i \\ F_i \end{bmatrix} \begin{bmatrix} G_i & H_i \end{bmatrix} \tag{3.6}$$

where the row and column dimensions of the factors are equal to r_i:

$$\begin{bmatrix} E_i \\ F_i \end{bmatrix} \in \mathbb{R}^{(n+n_y) \times r_i}, \quad \begin{bmatrix} G_i & H_i \end{bmatrix} \in \mathbb{R}^{r_i \times (n+n_u)}. \tag{3.7}$$

Then a new, extended system is assembled:

$$\begin{bmatrix} \dot{\underline{x}} \\ \underline{z_1} \\ \vdots \\ \underline{z_m} \\ \underline{y} \end{bmatrix} = \begin{bmatrix} A_0 & E_1 & \dots & E_m & B_0 \\ G_1 & 0 & \dots & 0 & H_1 \\ \vdots & \vdots & \vdots & \ddots & \vdots \\ G_m & 0 & \dots & 0 & H_m \\ C_0 & F_1 & \dots & F_m & D_0 \end{bmatrix} \begin{bmatrix} \dot{\underline{x}} \\ \underline{w_1} \\ \vdots \\ \underline{w_m} \\ \underline{u} \end{bmatrix} \tag{3.8}$$

In block form, this system looks like this:

$$
\begin{array}{c}
w_1 \longrightarrow \\
w_2 \longrightarrow \\
\vdots \\
w_m \longrightarrow \\
u \longrightarrow
\end{array}
\boxed{\mathbf{G_{SS}}}
\begin{array}{c}
\longrightarrow z_1 \\
\longrightarrow z_2 \\
\vdots \\
\longrightarrow z_m \\
\longrightarrow y
\end{array}
$$
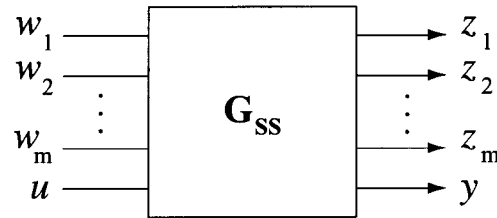
and the uncertainty from Equation (3.4) is represented as an upper LFT around it,

$$y = F_U(\mathbf{G_{SS}}, \Delta)u, \qquad (3.9)$$

where Δ maps $w \mapsto z$ and has the structure

$$\mathbf{\Delta} = \{\mathrm{diag}(\delta_1 I_{r_1}, \ldots, \delta_m I_{r_m}) : \delta_i \in \mathbb{R}\} \qquad (3.10)$$

It is straightforward but somewhat cumbersome to verify that this system is indeed equivalent to the one presented above.

This method of uncertainty modeling goes back to [Morton85] and can be used to incorporate gyroscopic effects into a rotor model. The nominal system is then modeled like in Equation (3.4), with a rotational speed Ω that is half of the maximum speed of operation. Only one uncertainty matrix is needed ($m = 1$), and it is chosen to be zero up to a matrix $-\Omega_{max}/2 \cdot G$ that adds to the lower right part of the matrix A_0 of the nominal system. The uncertainty matrix is then decomposed as above, and a new system is formed correspondingly.

The number of new inputs and outputs is equal to the rank of the gyroscopic matrix, and the uncertainty block is in this case a single identity matrix of appropriate dimension scaled by a scalar δ_1 . The resulting LFT then describes the system behaviour for rotational speeds from 0 to Ω_{max}.

3.1.5   Uncertainty in Eigenfrequencies

In some cases the technical understanding of the system yields an uncertainty that cannot be directly expressed in terms of system parameters but in terms of uncertainty of the system poles. This is for example the case for AMB systems, where the flexible eigenfrequencies are weakly damped

and the pole frequency may vary by several percent due to system changes or manufacturing tolerances.

Balas and Young have developed a method [Balas95b] to express this type of uncertainty in an LFT setting for systems with state matrices that are non-defective (diagonal Jordan form). The A matrix of such systems can be brought into diagonal form by applying a similarity transformation with the eigenvector matrix Φ of A. On the diagonal of the resulting matrix $\tilde{A} := \Phi^{-1}A\Phi$ the (generally complex) eigenfrequencies p_i of the system can be found. Since the matrix A is real, a complex eigenvalue implies that also its conjugate complex is an eigenvalue of A. By ordering the columns of Φ appropriately, the diagonal entries of $\tilde{A}$ can be forced to occur in pairs of two, with the eigenvalue with positive imaginary part first.

If this matrix $\tilde{A}$ is now subjected to a second similarity transformation with a block diagonal matrix with entries

$$T = \text{diag}(B_i), \quad B_i^{-1} = \begin{bmatrix} 1 & 1 \\ \rho_i + j\iota_i & \rho_i - j\iota_i \end{bmatrix}, \quad \text{where } p_i = \rho_i \pm \iota_i \quad (3.11)$$

the resulting matrix $\hat{A} = T^{-1}\tilde{A}T$ then is block diagonal with blocks $\hat{A}$. The individual block matrices now are the same as in the standard state space description of a one mass oscillator:

$$\hat{A}_i = \begin{bmatrix} 0 & 1 \\ -(\rho_i^2 + \iota_i^2) & 2\rho_i \end{bmatrix} = \begin{bmatrix} 0 & 1 \\ -\omega_{0i}^2 & -2\xi_i\omega_{0i} \end{bmatrix}. \quad (3.12)$$

A variation of the natural frequency of this 2×2 system can now be expressed as follows:

$$\hat{A}_{i,\delta_i} = \begin{bmatrix} 0 & 1 \\ -(\omega_{0i}(1+\delta_i))^2 & -2\xi_i\omega_{0i}(1+\delta_i) \end{bmatrix}. \quad (3.13)$$

In order to fit the uncertainty description to the linear framework, one must linearize with respect to δ_i, yielding

$$\hat{A}_{i,\delta_i} \approx \begin{bmatrix} 0 & 1 \\ -\omega_{0i}^2 & -2\xi_i\omega_{0i} \end{bmatrix} + \begin{bmatrix} 0 & 0 \\ -2\omega_{0i}^2\delta_i & -2\xi_i\omega_{0i}\delta_i \end{bmatrix} \quad (3.14)$$

$$= \begin{bmatrix} 0 & 1 \\ -\omega_{0i}^2 & -2\xi_i\omega_{0i} \end{bmatrix} + \begin{bmatrix} 0 \\ 1 \end{bmatrix} \delta_i \begin{bmatrix} -2\omega_{0i}^2 & -2\xi_i\omega_{0i} \end{bmatrix} \quad (3.15)$$
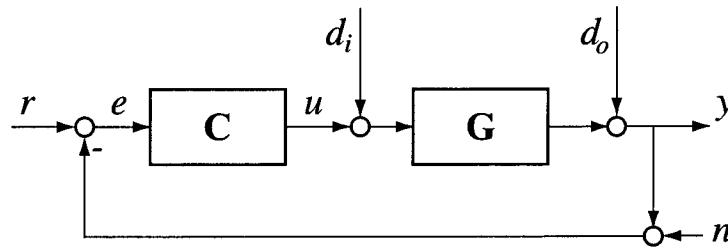
Figure 3.4: *Sample closed loop system with various disturbance inputs*

By these operations, the problem has been transformed to the case of linear state space uncertainty treated in the last chapter. Using Equation (3.15), the methodology described there can be directly applied. This method has been used in [Schönhoff00b].

3.2   Controller Design Objectives

The ultimate goal of every feedback controller design effort is to achieve a desired behaviour of the controlled plant (also referred to as the closed loop system) by means of appropriately processing measurements $\underline{y}$ from the physical plant **G** and feeding back the control signals $\underline{u}$ as indicated in Figure 3.4.

In this section different possible objectives of controller design are introduced and discussed. Unfortunately, not all goals can be achieved to the fullest extent at the same time. In practice, the various goals are conflicting and have to be traded off against each other. This point is elaborated in the section on performance limitations.

3.2.1   Nominal Stability

Any linear, time-invariant system is stable if and only if it is in $\mathcal{RH}_\infty$, i.e. if all its poles are contained in the open left half plane, see Appendix B.3. A MIMO system's stability is equivalent to the stability of all its constituent transfer functions.

The term nominal stability refers to the stability of the closed loop made up by the nominal system (without uncertainty) and the controller. This is achieved if and only if the closed loop is stable in the sense above and no unstable pole–zero cancellations occur in the forming of the product **CG** [Zhou96].

Historically, nominal stability was the most important goal of all controller design efforts. Nowadays however, this property is obtained for free. As will be pointed out later, the $\mathcal{H}_\infty$ algorithm searches an optimal controller from the set of all internally stabilizing controllers. This allows the control engineer to focus on the more advanced design goals addressed next.

3.2.2 Nominal Performance

In control design, the term performance refers to the closed loop system's behaviour. Performance requirements can be formulated either in the time domain or in the frequency domain. Typical *time domain requirements* are often defined in terms of the response behaviour to a step of size one. Typical examples of such requirements are

- limited overshoot (degree to which the step value is temporarily exceeded),

- small asymptotic tracking error (how precisely the set value is attained after all transient effects have decayed),

- short rise time (the time it takes the system to reach a certain percentage of the set value), and

- short settling time (time required until the trajectory remains within a certain band around the set value)

Frequency domain performance requirements often are expressed by demands on the sensitivity function, **S**, which is defined as

$$\mathbf{S} = (\mathbf{I} + \mathbf{GC})^{-1} \qquad (3.16)$$

and the complementary sensitivity function **T**, which is defined as

$$\mathbf{T} = (\mathbf{I} + \mathbf{GC})^{-1}\mathbf{GC} = \mathbf{SGC} \qquad (3.17)$$

In Figure 3.4 it can be seen that **S** is the closed loop transfer function from the reference input $\underline{r}$ to the system error $\underline{e}$ as well as the transfer function from the output disturbance $\underline{d}_o$ to the system output $\underline{y}$ and that from the sensor noise $\underline{n}$ to the reference error $\underline{e}$. **T**, on the other hand, is the transfer function from the reference input $\underline{r}$ to the system output $\underline{y}$

and, in the SISO case, that from the input disturbance $\underline{d}_i$ to the controller output $\underline{u}$[1].

Typical frequency domain performance requirements comprise

- a certain minimum bandwidth (i.e. $\mathbf{T}$ must be large up to a certain frequency to achieve a short rise time and good tracking),

- limits on the sensitivity function (i.e. $\mathbf{S}$ must be small up to a certain frequency for disturbance rejection),

- limits on certain transfer functions from some inputs to some outputs in Figure 3.4 (e.g. to avoid actuator saturation),

- minimum amplitudes for certain transfer functions (e.g. for $\mathbf{T}$ in order to achieve good tracking at certain frequencies), and

- a minimum damping of resonance poles (to ensure stability of the closed loop)

Weighting Functions

In robust controller design, performance requirements are typically formulated in the frequency domain. The basic setup for the nominal performance problem consists in a system $\mathbf{G}$ that is to be controlled by a controller $\mathbf{C}$ as shown in Figure 3.4. Additionally, some requirement on the frequency shape of one or more transfer functions of the closed loop is given. As an example consider the requirement on $\mathbf{S}$ to be smaller than a user–defined, stable, minimal phase SISO transfer function $\mathbf{w}^{-1}(j\omega)$ for all frequencies ω. In other words, $\mathbf{S}$ is to fulfill the condition

$$\bar{\sigma}(\mathbf{S}(j\omega)) \leq \bar{\sigma}(\mathbf{w}^{-1}(j\omega)) \quad \forall \omega \in \mathbb{R}. \tag{3.18}$$

Since $\mathbf{w}$ is SISO,

$$\bar{\sigma}(\mathbf{w}^{-1}(j\omega)) = \mathbf{w}^{-1}(j\omega). \tag{3.19}$$

Therefore, one can rewrite the above condition as

$$\bar{\sigma}(\mathbf{w}(j\omega)\mathbf{S}(j\omega)) \leq 1 \quad \forall \omega \in \mathbb{R}. \tag{3.20}$$

---

[1]In the MIMO case, the transfer function from $\underline{d}_i$ to $\underline{u}$ is $\mathbf{T}_i = (\mathbf{I} + \mathbf{CG})^{-1}\mathbf{CG}$, which is not exactly equal to $\mathbf{T}$, but usually of similar size.
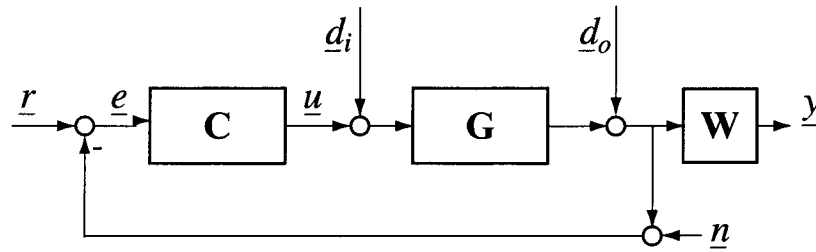
Figure 3.5: *Sample closed loop system with performance weighting function*

which by blowing up the weighting function **w** to a diagonal function with identical entries $\mathbf{W} = \mathbf{w}\mathbf{I_n}$ yields a restated requirement on **S**:

$$\|\mathbf{SW}\|_\infty \leq 1. \tag{3.21}$$

This requirement can now be introduced into the system from Figure 3.4 by inserting the weighting function **W** in the system as indicated in Figure 3.5.

For the system in Figure 3.5, a controller **C** fulfills the performance requirement (3.18) if and only if the $\|\cdot\|_\infty$-norm of the transfer function from the input $\underline{d}_o$ to the output $\underline{y}$ is less than 1, i.e.

$$\|\mathbf{T}_{\underline{y}\underline{d}_0}\|_\infty \leq 1. \tag{3.22}$$

Therefore, testing if a performance criterion is fulfilled by the closed loop amounts to a test on the $\|\cdot\|_\infty$-norm of an appropriate transfer function.

The above considerations become particularly important in the context of controller design by means of the $\mathcal{H}_\infty$ algorithm that will be presented in Chapter 3.3.1. If the design is successful, condition (3.21) is fulfilled, and with it the original condition (3.18). The allpass property of the optimal solution to the $\mathcal{H}_\infty$ problem[2] furthermore yields that if only one constraint is given, the shaping achieved by the function $\mathbf{w}^{-1}(j\omega)$ will be exact up to a constant factor.

Performance Limitations

In the last sections, a number of performance criteria has been stated. While in many cases the majority of these criteria seems attractive to

---

[2]The properties of the $\mathcal{H}_\infty$ algorithm are stated in Chapter 3.3.1. Allpass systems are defined in Appendix B.3.5.

achieve, there are unfortunately some mechanisms intrinsic to control theory that make some of the objectives contradictory to others. As a consequence, not all goals can be achieved to the fullest extent at the same time. Instead, the control engineer is forced to trade–off these goals against each other, aiming at a solution that is the best compromise. This decision is often complex and requires thorough understanding of the control problem to be solved. In the following, some of the classical conflicts and trade–offs in controller design are presented.

Tracking vs. Sensor Noise Rejection

Consider the system shown in Figure 3.4. A typical performance requirement is that the output y is to follow the reference input r. This implies that the complementary sensitivity function $\mathbf{T}$, which is the transfer function from r to y, should be one, i.e. large. On the other hand, the system output should not be affected by sensor noise, i.e. the transfer function from n to y should be as small as possible. It is evident from Figure 3.4 that this transfer function is $-\mathbf{T}$. Obviously, this constitutes a conflict that cannot be fully resolved. The designer must trade–off these two goals against each other over frequency.

S+T=I

This simple equality is easily verified by adding Equation (3.16) and Equation (3.17). The implications are far reaching: $\mathbf{S}$ and $\mathbf{T}$ can never both be small. This implies that good disturbance and sensor noise rejection ($\mathbf{S}$ small) are contradictory to good robustness to multiplicative uncertainty ($\mathbf{T}$ small), as will become clear in Chapter 3.2.3. Typical systems have a high level of uncertainty at high frequencies. This demands for $\mathbf{T}$ being small at high frequencies. $\mathbf{S}$ however must be small at low frequencies in order to have good tracking. In the mid frequency range, a cross over must take place, and robustness must be traded off against performance.

The Waterbed Effect

Trade–offs are not only to be made between transfer functions, but are already required when considering the sensitivity function $\mathbf{S}$ alone. For rational open loop systems $\mathbf{L}(s) = \mathbf{G}(s)\mathbf{C}(s)$ with a pole excess of at least two (denominator degree at least by two larger than the numera-

tor degree)[3], the following theorem states that prescriptions for **S** in one frequency range have effects on **S** at other frequencies.

BODE SENSITIVITY INTEGRAL FORMULA
Given a rational SISO open–loop system **L**(s) = **G**(s)**C**(s) *with denominator degree at least two larger than its numerator degree, with N unstable poles at locations* p_i, *for closed loop stability the following condition must be fulfilled:*

$$\int_0^\infty \ln|\mathbf{S}(j\omega)|d\omega = \pi \sum_{i=1}^N Re(p_i), \qquad (3.23)$$

where $Re(p_i)$ *denotes the real part of* p_i.

In the case of a stable system, the right hand side of the equation is 0, which implies that the area where **S** is smaller than one must be compensated by a region of equal (logarithmic) size where **S** is larger than one.

When the system is unstable, things get worse. Depending on the number and location of the unstable poles, the area where **S** must be larger than one increases, making good tracking harder to achieve for these systems.

The condition imposed by the bode sensitivity formula becomes difficult to fulfill due to the fact that the vast space of large frequencies cannot be used to compensate for low values of **S** in the low frequency range: Due to the roll–off of the plant, **T** is forced to rapidly approach zero for high frequencies, and since **S**+**T**=**I**, **S** must equally quickly approach one. This leaves only a limited frequency range to fulfill the conditions of the bode sensitivity integral, in which the areas with small **S** must be balanced by areas with large **S**. This gives rise to an analogy to a waterbed: Pushing down in one area reduces the water level there, but leads to a rise of water level in another area.

Limitations due to Unstable Zeroes and Poles

Performance limitations can also be imposed by the system itself. If for example the system has unstable zeros, this limits the permissible system gain, since for increasing gain the closed loop system poles move toward the open–loop system zeros. A limitation on the gain, however, directly translates into a limit on the frequency up to which the sensitivity function **S** can be made small. Unstable poles, on the other hand, require a minimum bandwidth — for stabilization of the poles a minimum amount of feedback is required at the pole frequency. This inevitably leads to a

---

[3]This condition is fulfilled for all practical cases where physical systems are involved.
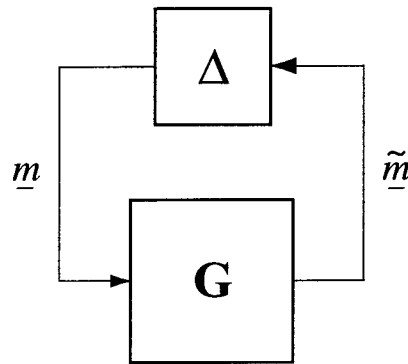
Figure 3.6: *Small gain theorem*

minimum value for the frequency at which the complementary sensitivity function **T** can start rolling off, which imposes restrictions on the amount of uncertainty the closed loop will be robust to.

3.2.3   Robust Stability

As has been argued in Chapter 3.1, no physical system can be described absolutely accurately by means of a model. As a consequence, a controller that achieves merely nominal stability cannot satisfy the control engineer, as no knowledge is available if also the similar but slightly different physical system will be stabilized. Therefore the nominal model is replaced by the concept of a set of models which is obtained by augmenting the nominal model with an appropriate uncertainty description.

Robust stability is achieved for such a set of models, if the controller stabilizes not only the nominal model, but *all* models in the uncertainty set (which is always comprises the nominal model). In contrast to pure nominal stability, the concept of robust stability is also meaningful for physical systems — if the uncertainty set is intelligently chosen and covers the dynamics of the physical system, this system will be stabilized by all controllers achieving robust stability.

The key question in robust stability analysis and design is the question how much uncertainty a nominally stable system can bear before it becomes unstable. For unstructured uncertainty as introduced above, this question is answered by the so-called small gain theorem:

SMALL GAIN THEOREM
Let $\mathbf{G} \in \mathcal{RH}_\infty$. *Then the system from Figure 3.6 is internally stable for all* $\Delta \in \mathcal{RH}_\infty$ *with* $\|\Delta\|_\infty \leq \gamma$ *if and only if* $\|\mathbf{G}\|_\infty < 1/\gamma$.

The small gain theorem states that the maximum allowable size for an unstructured uncertainty is determined by the size of the transfer function from its inputs to its outputs. The practical relevance of the theorem becomes evident, when $\mathbf{G}$ is interpreted as the closed loop system consisting of the nominal model $\mathbf{G_n}$ and the controller $\mathbf{C}$. The amount of unstructured uncertainty the closed loop system can handle can be directly obtained from the $\| \cdot \|_\infty$-norm of the closed loop transfer function from its uncertainty inputs to its uncertainty outputs.
For the case of additive uncertainty from Figure 3.1a this means that the closed loop's robustness against this type of uncertainty is defined by the $\| \cdot \|_\infty$-norm of the complementary sensitivity function $\mathbf{CS}$. For multiplicative uncertainty shown in Figure 3.1b, the robustness level is determined by the norm of $\mathbf{T}$.

For structured uncertainty, the above unstructured analysis is conservative. This is due to the fact that the structured uncertainty which is physically expected is merely a subset of the unstructured uncertainty discussed above. In order to capture the structured uncertainty's effects without conservatism, the following reflections are useful:

First the uncertainty is characterized. As has been seen in Chapter 3.1.3, structured uncertainty can consist of two types of blocks on the diagonal, full uncertainty blocks $\Delta \in \mathcal{RH}_\infty$ and scalar blocks $\delta \in \mathcal{RH}_\infty$ that also may be repeated $(\delta \cdot I \in \mathcal{RH}_\infty)$. Therefore, for fixed frequencies ω any structured uncertainty is a complex matrix of the form

$$\mathbf{\Delta} = \{\mathrm{diag}(\delta_1 I_{r_1}, ..., \delta_s I_{r_s}, \Delta_1, ..., \Delta_f) : \delta_i \in \mathbb{C}, \Delta_j \in \mathbb{C}^{m_j \times m_j}\}$$

and the set of all block diagonal, stable, rational transfer functions that have the same block structure as $\mathbf{\Delta}$ can be written as

$$\mathcal{M}(\mathbf{\Delta}) := \{\Delta(\cdot) \in \mathcal{RH}_\infty : \Delta(s) \in \mathbf{\Delta} \; \forall s \in \mathbb{C}\}.$$

Then the unstructured singular value is analyzed and extended to structured uncertainties:

For the system in Figure 3.6 one can show that the closed loop is stable if and only if

$$\det(I - \mathbf{G}(s)\Delta(s)) \neq 0 \; \forall s \in \bar{\mathbb{C}}_+.$$

Starting with a very small value $\alpha > 0$, for which the closed loop is stable for all $\Delta \in \mathcal{M}(\mathbf{\Delta})$ with $\|\Delta\|_\infty < \alpha$, it is interesting to investigate how far α can be increased until the above expression becomes 0 for any $s \in \bar{\mathbb{C}}_+$ for the first time. This value, α_{max}, is referred to as the robust stability

radius of the closed loop. For unstructured uncertainty, the small gain theorem yields:

$$\frac{1}{\alpha_{max}} = \|\mathbf{G}\|_\infty = \sup_{\omega \in \mathbb{R}} \bar{\sigma}(\mathbf{G}(j\omega)) \qquad (3.24)$$

For fixed values of ω and $\mathbf{G}(j\omega) \neq 0$, this can be used to rewrite the unstructured singular value of $\mathbf{G}(j\omega)$ as follows:

$$\bar{\sigma}(\mathbf{G}(j\omega)) = \frac{1}{\min\{\bar{\sigma}(\tilde{\Delta}) : \det(I - \mathbf{G}(j\omega)\tilde{\Delta}) = 0, \ \tilde{\Delta} \ \text{unstruc.}\}}$$

This implies that the maximum singular value of $\mathbf{G}(j\omega)$ is a measure for the smallest unstructured complex matrix $\tilde{\Delta}$ destabilizing the closed loop for fixed ω. If $\mathbf{G}(j\omega) = 0$, no destabilizing $\tilde{\Delta}$ exists, and as would be suggested by the formula, $\bar{\sigma}(\mathbf{G}(j\omega)) = 0$.

Then, the same system with *structured* uncertainty is considered, i.e. $\tilde{\Delta} \in \mathbf{\Delta}$, eliminating all undesired cross coupling in the uncertainty block. For this system, one can analogously to the above define the *structured singular value* as

$$\mu_{\mathbf{\Delta}}(\mathbf{G}(j\omega)) := \frac{1}{\min\{\bar{\sigma}(\tilde{\Delta}) : \det(I - \mathbf{G}(j\omega)\tilde{\Delta}) = 0, \tilde{\Delta} \in \mathbf{\Delta}\}}$$

For the exceptional case when $\mathbf{G}(j\omega) = 0$, we define $\mu_{\mathbf{\Delta}}(\mathbf{G}(j\omega)) = 0$.

Based on this, the stability radius for structured uncertainties, β_{max}, results from

$$\frac{1}{\beta_{max}} = \sup_{\omega \in \mathbb{R}} \mu_{\mathbf{\Delta}}(\mathbf{G}(j\omega)), \qquad (3.25)$$

and by defining

$$\|\mathbf{G}\|_{\mathbf{\Delta}} := \sup_{\omega \in \mathbb{R}} \mu_{\mathbf{\Delta}}(\mathbf{G}(j\omega)) \qquad (3.26)$$

a new measure for the size of systems is obtained, yielding information on how robust a system is to *structured* uncertainty.

The following theorem constitutes the basis for the importance of $\| \cdot \|_{\mathbf{\Delta}}$:

STRUCTURED UNCERTAINTY ROBUSTNESS THEOREM
Let $\mathbf{G} \in \mathcal{RH}_\infty$. Then the system from Figure 3.6 is internally stable for all $\Delta \in \mathcal{M}(\mathbf{\Delta})$ with $\|\Delta\|_\infty \leq \gamma$ if and only if $\|\mathbf{G}\|_{\mathbf{\Delta}} < 1/\gamma$.

Analogously to the small gain theorem, this theorem permits analysis of the maximum size of tolerable system uncertainty, now for *structured* uncertainty.

This extension avoids unnecessary conservatism in the analysis. A comparison of the above representation of $\bar{\sigma}$ with the definition of $\mu_{\mathbf{\Delta}}$ directly shows that $\|\mathbf{G}\|_{\mathbf{\Delta}} \leq \|\mathbf{G}\|_{\infty}$. This is due to the smaller uncertainty set considered in the case of structured uncertainty. As an implication of this, analysis based on the structured singular value μ (μ–analysis) will be less conservative than any analysis based on the unstructured singular value $\bar{\sigma}$, as soon as the uncertainty is structured. In the unstructured case, μ–analysis yields the same results as the standard ($\mathcal{H}_{\infty}$–) analysis based on the maximum singular value.

It must be noted that the expression $\| \cdot \|_{\mathbf{\Delta}}$ only makes sense in the context of a predefined uncertainty structure $\mathbf{\Delta}$. This is indicated by the suffix of the norm[4]. Furthermore, unstructured uncertainty can always be considered a special case of structured uncertainty (one single full, complex uncertainty block).

Concerning the evaluation of $\|\mathbf{G}\|_{\mathbf{\Delta}}$, no method for efficient estimation like in the case of $\|\mathbf{G}\|_{\infty}$ is available[5]. Evaluation is based on calculation of upper and lower bounds of $\|\mathbf{G}\|_{\mathbf{\Delta}}$ by evaluating $\mu_{\mathbf{\Delta}}(\mathbf{G}(j\omega))$ on a finite frequency grid.

Unfortunately, there is no way to directly calculate $\mu_{\mathbf{\Delta}}$. However, the following formulae for upper and lower bounds are available [Zhou96]:

$$\max_{U \in \mathcal{U}_{\mathbf{\Delta}}} \lambda_{max}(UM) \leq \mu_{\mathbf{\Delta}}(M) \leq \inf_{D \in \mathcal{D}_{\mathbf{\Delta}}} \bar{\sigma}(DMD^{-1}) \qquad (3.27)$$

where

$$\begin{aligned} \mathcal{U}_{\mathbf{\Delta}} &= \{U \in \mathbf{\Delta} : U^*U = I\} \text{ and} \\ \mathcal{D}_{\mathbf{\Delta}} &= \{\mathrm{diag}(D_1, \, ... \, , D_s, \delta_1 I_{m_1}, \, ... \, \delta_{f-1} I_{m_{f-1}}, I_{m_f}) : \\ & \qquad D_i \in \mathbb{C}^{r_i \times r_i}, D_i = D_i^*, d_j \in \mathbb{R}^+\} \end{aligned}$$

and the dimensions from the definition of $\mathcal{D}_{\mathbf{\Delta}}$ are matching those from the definition of $\mathbf{\Delta}$.

Doyle has shown [Doyle82] that the left inequality of Equation (3.27) always is an equality. Unfortunately, the maximization of the left expression is a non-convex problem with multiple local maxima. The upper bound, however, can be calculated by means of convex optimization. For block structures with $2s + f \leq 3$, $\mu_{\mathbf{\Delta}}$ is equal to the upper bound, which covers

---

[4]Strictly speaking, $\| \cdot \|_{\mathbf{\Delta}}$ is *not* a norm since it does not fulfill the triangle inequality (For a formal definition of norms, see Appendix B.1).

[5]An algorithm for computing $\| \cdot \|_{\infty}$ is presented in Appendix B.3.6

already a large number of application problems. For more complex uncertainties, the bound is not tight. However, Stein and Doyle [Stein91] have investigated this problem experimentally and state that despite extensive search no example has been found where the upper bound exceeded μ_Δ by more than 15%.

3.2.4   Robust Performance

In the last chapter, the concept of robust stability has been introduced as the extension of the stability concept from a single system (nominal stability) to a set of systems (i.e. a system with uncertainty).

Robust performance is the analogous extension of the concept of performance of a single system (nominal performance) to a system with added uncertainty. As is true for robust stability, this extension has important consequences. While nominal performance only is a statement referring to the model that has been used in the controller design (the nominal model), robust performance refers to the whole set of similar systems contained in the uncertainty set. If this set is chosen in such a way that it covers the physical system to be controlled, the control engineer can be sure that the performance requirements are met for the real system if robust performance is achieved in the controller design procedure.

The robust performance problem can be illustrated by the system from Figure 3.7a, where the system $\mathbf{G_n}$ subject to an additive uncertainty is to achieve the performance requirement $\|\mathbf{W_p S}\|_\infty \le 1$ not just for $\mathbf{G_n}$ but for all models covered by the uncertainty set. As has been pointed out in Chapter 3.2.2, this performance requirement can be interpreted as a requirement on the transfer function from $\underline{d}$ to $\underline{y}$.

This problem can be tackled formally by remembering the key statement of the structured robust stability theorem presented in the last section: For the system $\mathbf{G}$ and given $\gamma > 0$, $\|\mathbf{G}\|_\Delta < \gamma$ is equivalent to stability of $\mathbf{G}$ under feedback with all uncertainties Δ_p fulfilling the condition $\|\Delta_p\|_\infty \le 1/\gamma$.

For the setup above this implies that the transfer function from $\underline{d}$ to $\underline{y}$, $\mathbf{S}$, will be smaller than one for all systems covered by the uncertainty model, if the system is not destabilized by any additional fictitious uncertainty block Δ_p with $\|\Delta_p\|_\infty \le 1$ between the performance outputs and the performance inputs, see Figure 3.7b. This yields a reformulation of the robust performance problem as a robust stability problem with structured
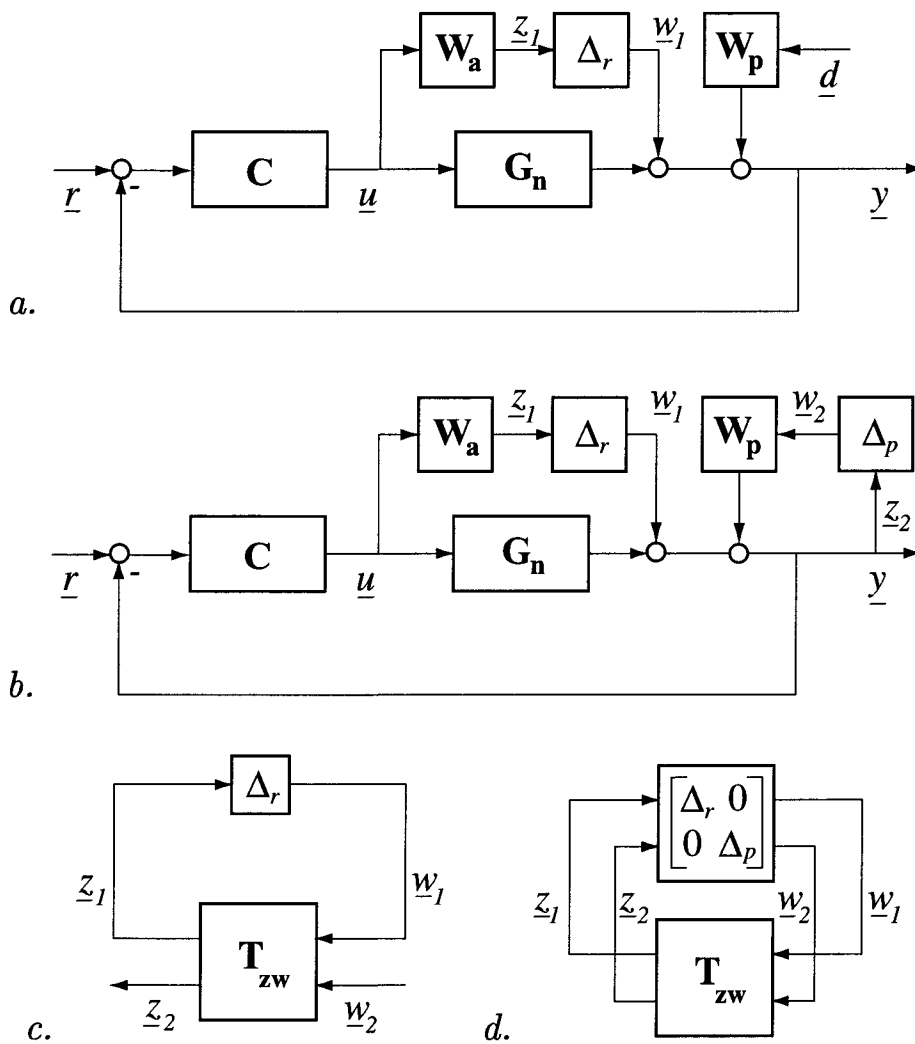
Figure 3.7: *Robust performance problem (a), interpretation as robust uncertainty problem (b), transformation from robust performance (c) to robust stability form (d)*

uncertainty. The general procedure is shown in the last row of Figure 3.7, where a general uncertain system with uncertainty $\Delta_r \in \mathbf{\Delta}_r$ which is subject to robust performance requirements (Figure 3.7c) is transformed into the corresponding robust uncertainty description with the augmented uncertainty structure $\mathbf{\Delta}_{rp}$ consisting of the diagonal augmentation of the block structure describing the uncertainty, $\mathbf{\Delta}_r$, and that describing the relation of the performance inputs and outputs, $\mathbf{\Delta}_p$ (Figure 3.7d).

The principle outlined above can be generalized to the following theorem relating the robust performance problem to a structured robust stability problem.

ROBUST PERFORMANCE THEOREM
Given a system with uncertainty structure $\mathbf{\Delta}_r$ and performance structure $\mathbf{\Delta}_p$, the following are equivalent for all $\beta > 0$:

(*i*) For all $\Delta(s) \in \mathcal{M}(\mathbf{\Delta}_r)$ with $\|\Delta\|_\infty < 1/\beta$, the system shown in Figure 3.7c is well-posed, internally stable and $\|F_U(\mathbf{T}_{\underline{zw}}, \Delta_r)\|_\infty \leq \beta$

(*ii*) $\|\mathbf{T}_{\underline{zw}}\|_{\mathbf{\Delta}_{rp}} \leq \beta$ with
$\mathbf{\Delta}_{rp} = \{\Delta : \Delta = \mathrm{diag}(\Delta_r, \Delta_p), \Delta_r \in \mathbf{\Delta}_r, \Delta_p \in \mathbf{\Delta}_p\}$

In other words, robust performance of any system is equivalent to it being robustly stable with respect to the uncertainty structure consisting of the augmentation of the robustness and the performance structure, see Figures 3.7c and 3.7d.

As a consequence, the analysis of robust performance can only be performed without conservatism by means of μ–analysis, i.e. by investigation of the closed loop's norm $\|\mathbf{T}_{\underline{zw}}\|_{\mathbf{\Delta}_{rp}}$.

As has been pointed out in the last chapter, this norm is a measure for the robust stability of the closed loop system from Figure 3.7d. The above theorem shows that analyzing the robust stability of the system from Figure 3.7d by means of $\|\mathbf{T}_{\underline{zw}}\|_{\mathbf{\Delta}_{rp}}$ is equivalent to analyzing the robust performance of the system from Figure 3.7c.

For the synthesis of controllers, the above theorem implies that a controller with minimal $\|\mathbf{T}_{\underline{zw}}\|_{\mathbf{\Delta}_{rp}}$ will have maximum stability radius on the system from Figure 3.7d and the best possible robust performance on that from Figure 3.7c. This is the motivation for controller design techniques minimizing the structured singular value of the closed loop transfer function as outlined in the next chapter.

3.3   Controller Design

In this chapter, the $\mathcal{H}_\infty$ controller design technique is outlined and the most relevant practical aspects are discussed. Towards the end of this chapter, the limitations of $\mathcal{H}_\infty$ design are addressed, and the more capable μ–synthesis design is presented.

3.3.1 The $\mathcal{H}_\infty$ Algorithm

The optimal $\mathcal{H}_\infty$ synthesis problem is defined as follows:

OPTIMAL $\mathcal{H}_\infty$ SYNTHESIS PROBLEM
For the system in standard control configuration[6] find from the set of all proper, real-rational controllers $\mathbf{C}(s)$ that achieve internal stability a controller for which the closed loop transfer function from all inputs to all outputs, $\mathbf{T}_{\underline{zw}}$, has minimal $\mathcal{H}_\infty$ norm.

This has the following practical implication. Since the norm $\|\cdot\|_\infty$ is the norm induced by the norm $\|\cdot\|_2$ on $\mathcal{L}_2$ (see Appendix B.3), i.e.

$$\|\mathbf{G}\|_\infty = \sup_{w\neq0} \frac{\|\mathbf{G}w\|_2}{\|w\|_2}, \qquad (3.28)$$

and due to the $\|\cdot\|_2$-norm's relation to signal energy, this implies that the optimal $\mathcal{H}_\infty$ controller will lead to a closed loop with minimum worst-case amplification of signals. For reasons of well–behavedness of the solution and computability, the problem stated above is slightly relaxed in practical applications and the following sub-optimal problem is solved instead:

SUBOPTIMAL $\mathcal{H}_\infty$ SYNTHESIS PROBLEM
Given the setup from the optimal case and a positive scalar γ, find a proper, real rational controller $\mathbf{C}(s)$ that achieves internal stability of the closed loop system and achieves $\|\mathbf{T}_{\underline{zw}}\|_\infty < \gamma$.

In practice, this problem is solved as follows. Starting out with conservative upper and lower bounds for γ, repeated synthesis attempts are made with the average of the bounds. Depending on whether or not a solution to the problem existed, the upper or the lower bound is adjusted. This process is iterated until the difference between the bounds falls below a predefined threshold value. This procedure is called γ–iteration. In this way, the minimum is usually not exactly reached but it can be approximated with great precision. In each attempt to solve the suboptimal $\mathcal{H}_\infty$ problem, two algebraic Riccati equations must be solved. Powerful software tools are available to perform this task [Balas95a]. However, the following three requirements apply as to the structure of the design system in standard control configuration:

A1 In the state space description of the system the pair (A, B_2) must be stabilizable and the pair (C_2, A) must be detectable.

---

[6]The formal definition of standard control configuration is recapitulated in Equation (B.28) in Appendix B.3.4.

A2 D_{12} must have full row rank, D_{21} must have full column rank.

A3 The following two matrices must have full column rank respectively row rank for all $\omega \in \mathbb{R}$: $\begin{bmatrix} A - j\omega I & B_2 \\ C_1 & D_{12} \end{bmatrix}$ and $\begin{bmatrix} A - j\omega I & B_1 \\ C_2 & D_{21} \end{bmatrix}$

The first requirement, **A1**, is indispensable for the existence of a stabilizing controller and can be checked by means of the so-called Hautus test [Ackermann88]. It is important to understand that any choice of unstable weighting functions will lead to a violation of this condition. Condition **A2** is required to avoid singular problems and non-realizable controllers. It can be enforced by penalizing the controller output $\underline{u}$ in the problem or by including a sensor noise input $\underline{n}$, see Figure 3.4. Relaxation of **A2** is possible where required [Stoorvogel92]. Condition **A3** is of technical nature and is required for solvability of the Riccati equations involved in the design.

The solution to the $\mathcal{H}_\infty$ problem has some important properties:

- The optimal controller yields an allpass[7] closed loop transfer function. This allows precise shifting of transfer functions by means of weighting functions as introduced in Chapter 3.2.2.

- Concerning the order of the controller, it can be said that for a plant of order n (including weighting functions), an optimal $\mathcal{H}_\infty$ controller of order $n-1$ exists. Suboptimal controllers are of order n [Glover91].

- The controller can be shown to be decomposable into two parts, an optimal state observer estimating the system states and a constant feedback of these states [Zhou96].

After the design has been performed, the result of the γ–iteration directly gives information on whether or not the objectives have been reached:
A γ value of exactly one means exact achievement of the robustness and performance goals. If γ is smaller than one, the robustness and performance radii are $1/\gamma$ times larger than demanded. If γ is greater than one, the design failed and the robust performance objectives have only been achieved up to $1/\gamma$ times the desired values. In the latter case, the designer has the option to accept the results as good enough, to modify

---

[7]A definition of allpass systems is given in Appendix B.3.5.

the problem formulation by selecting different transfer functions for the minimization or by adjusting the weighting functions, or to use the more advanced μ–synthesis techniques described at the end of this chapter.

A complete derivation of the $\mathcal{H}_\infty$ solution method is beyond the scope of this thesis. The above statements are sufficient to understand the concepts applied in the present work. The reader interested in the details of the theory is referred to [Zhou96].

3.3.2 The $\mathcal{H}_\infty$ Controller Design Procedure

After the explanation of the background of $\mathcal{H}_\infty$ controller design in the last chapter, this chapter deals with the practical issues of the design. In the following, a step by step procedure for the design of $\mathcal{H}_\infty$ controllers is given.

The first step in the $\mathcal{H}_\infty$ controller design procedure is the choice of an adequate system model. To this end, a suitable nominal model must be determined e.g. by means of identification. The model and the physical system must then be analyzed for possible deviations and other sources of uncertainty. This uncertainty is to be adequately quantified and added to the nominal system model in the form of a upper fractional transformation (see Chapter 3.1.2), yielding a set of systems that is large enough to cover the physical plant and small enough to avoid unnecessary conservatism in the design.

Once this has been achieved, performance issues are to be addressed. Based on physical considerations and the guidelines from Chapter 3.2.2, those transfer functions leading to a desired system behaviour when adequately shaped must be identified. Additional inputs and outputs may be added to the system and equipped with weighting functions to achieve a suitable shaping in the subsequent design. This step is further elaborated in the next chapter.

In the next step, the plant is to be transformed to standard form (standard control configuration, see Appendix B.3.4), and the feasibility requirements from the last chapter are to be checked. If they are fulfilled, the $\mathcal{H}_\infty$ algorithm can be used to derive an adequate controller, otherwise the choice of transfer functions to be included in the design must be altered.
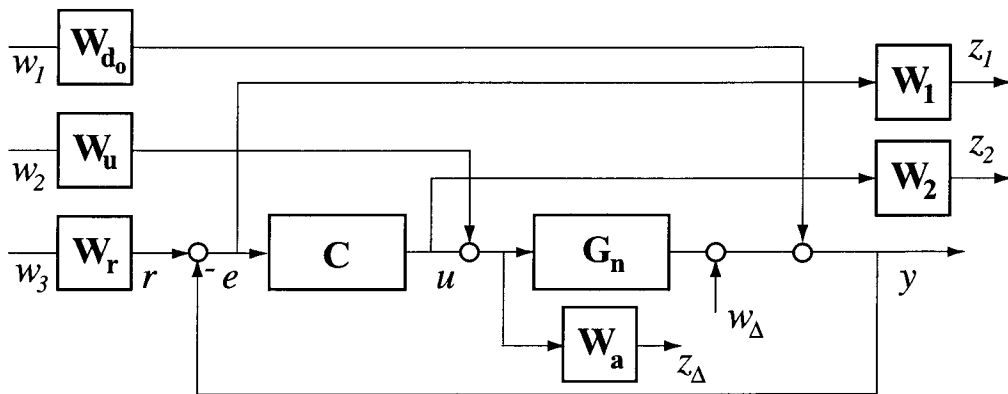
Figure 3.8: *Signal based design scheme*

3.3.3   Discussion of Controller Design Schemes

While the choice of transfer functions to be minimized is up to the control designer within the limits of the requirements imposed by the $\mathcal{H}_\infty$ algorithm, there are some schemes that correspond to classical design problems. These will receive special attention in this chapter. The multitude of design schemes can be split into two categories, that of *signal based schemes* and that of *loop-shaping based schemes*.

Signal Based Controller Design Schemes

Signal based schemes rely on information of the physical size of signals that are to be expected / can be accepted. From all possible transfer functions (many of which are indicated in Figure 3.8) those that seem the most important for the present design problem are selected, and the corresponding weighting functions are defined to reflect the size of the inputs and the inverse of the maximum acceptable size of the output signals. The advantage of this approach lies in the direct mapping of the physical reality to the design problem. However, this approach often leads to rather complex problems since typically a larger number of transfer function constraints is considered. Also, the approach may be conservative — in the design always the worst case of all signals is used as a reference. In reality, however, it may be unlikely that all signals attain their worst case values at the same time. An example of successful implementation of a signal-based scheme can be found in [Lösch98].

Loop Shaping Based Controller Design Schemes

Loop-shaping based schemes are somewhat more abstract than signal-based schemes. Here, the choice of the transfer functions to be considered and the size of the weighting functions is not mainly based on considerations concerning the size of the physical signals encountered. Instead the scheme is set up in such a way, that certain meaningful closed loop transfer functions show a desired behaviour in a more qualitative way. A well known example of this type of schemes consists in the weighted mixed sensitivity scheme introduced next.

Weighted Mixed Sensitivity Scheme

As an example of a loop-shaping based scheme, consider the so-called weighted mixed-sensitivity design approach. As the name suggests, this approach aims at minimizing the infinity norm of the sensitivity function $\mathbf{S}$ and the complementary sensitivity function $\mathbf{T}$ at the same time. In the section on nominal performance, Chapter 3.2.2, it has been pointed out that minimization of $\mathbf{S}$ leads to good tracking of reference signals and good disturbance rejection, while minimizing $\mathbf{T}$ leads to good robustness against multiplicative uncertainty. A look at Figure 3.4 shows that besides $\mathbf{S}$ and $\mathbf{T}$ there are two other transfer functions in the framework that might be interesting to minimize, $\mathbf{CS}$ and $\mathbf{SG}$. $\mathbf{CS}$ is the transfer function from the set signal $\underline{r}$ to the control signal $\underline{u}$, and as such its size determines how large the controller output will be in response to specific set commands. Hence, if avoidance of actuator saturation is critical, $\|\mathbf{CS}\|_\infty$ must be limited. Furthermore, $\mathbf{CS}$ is the transfer function from the output disturbance $\underline{d}_o$ to $\underline{u}$, which implies (via the small gain theorem) that $\|\mathbf{CS}\|_\infty$ determines the system's robustness to additive uncertainty. $\mathbf{SG}$ on the other hand is the transfer function from the input disturbance $\underline{d}_i$ to the output $\underline{y}$. As a consequence, $\|\mathbf{SG}\|_\infty$ determines the worst case effect of input disturbances on the system output. Since $\mathbf{CS}$ and $\mathbf{SG}$ are small whenever $\mathbf{S}$ is small, commonly only $\mathbf{S}$ and $\mathbf{T}$ are explicitly considered in the controller design. These considerations lead to the controller design scheme from Figure 3.9.

Unfortunately, the smallness requirements on $\mathbf{S}$ and $\mathbf{T}$ cannot be met at the same time. As has been pointed out in the section on performance limitations in Chapter 3.2.2, $\mathbf{S}$ and $\mathbf{T}$ are not unrelated and certain restrictions concerning their size apply, like for example $\mathbf{S}+\mathbf{T}=\mathbf{I}$. As a consequence, the smallness of $\mathbf{S}$ has to be traded off versus that of $\mathbf{T}$ and vice
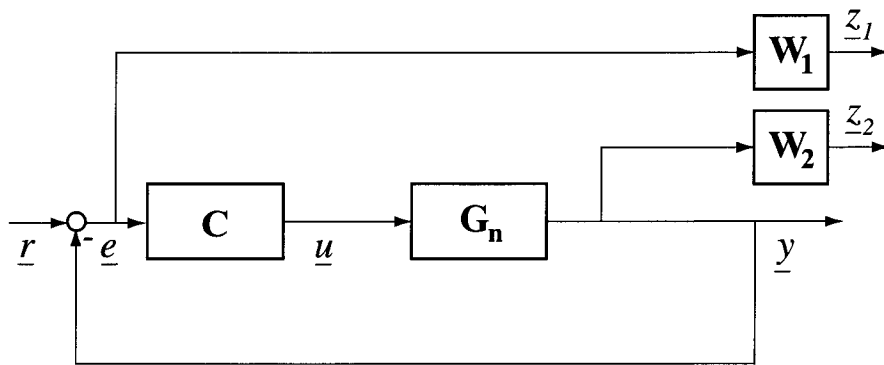
Figure 3.9: *Weighted mixed sensitivity problem setup*

versa. This trade–off typically is frequency dependent. In the range of low frequencies requirements on tracking and disturbance rejection are usually high and the system is comparably well known. This is in favor of **S** being small at the cost of a larger **T**. In the range of high frequencies, the situation is different. Here, the situation is dominated by the large system uncertainty, such that **T** should be small at the cost of poor performance (large **S**).

The desired shape of **S** and **T** is achieved by introducing weighting functions $\mathbf{W_1}$ and $\mathbf{W_2}$ to shape **S** and **T** over frequency as indicated in Figure 3.9.

Performance limitations and the use of weighting functions to shape transfer functions are discussed in Chapter 3.2.2. The typical setup for this problem is [Chiang92] that of Figure 3.9 and the suboptimal $\mathcal{H}_\infty$ problem from Chapter 3.3.1 is solved with

$$\underline{w} = \underline{r} \text{ and } \underline{z} = \begin{bmatrix} \underline{z}_1 \\ \underline{z}_2 \end{bmatrix}.$$

Minimization of $\|\mathbf{T}_{\underline{zw}}\|_\infty$ will include minimization of $\mathbf{W_1 S}$ and $\mathbf{W_2 T}$. Due to the allpass property of the solution to the $\mathcal{H}_\infty$ problem, the function **S** will be small at those frequencies where $\mathbf{W_1}$ is large, and analogously **T** will be small where $\mathbf{W_2}$ is large. Due to these considerations, $\mathbf{W_1}$ is to be chosen large in the low frequency range and small at high frequencies while $\mathbf{W_2}$ is to be chosen small for low frequencies and large for high frequencies. The freedom and responsibility of the control designer lies in deciding how large 'large' and 'small' are to be in each case, where the low frequency range ends and the high frequency range starts, and how steep the transition between these areas should be. There are no

generic answers to these questions, they depend on the physical system to be controlled and the external signals to be expected during operation. After application of the $\mathcal{H}_\infty$ algorithm, the γ value gives clear information about whether or not the goals have been reached or not (see last chapter). In case adjustments are necessary, these can be carried out on either one or both of the weighting functions $\mathbf{W_1}$ and $\mathbf{W_2}$. Often certain minimum robustness limits are intrinsic to the problem — relaxing the requirements on $\mathbf{T}$ too much would make the implicit uncertainty set too small, such that the true physical system can no longer be guaranteed to be covered. In this situation, the control engineer typically holds the weight $\mathbf{W_2}$ fixed and relaxes the restrictions on $\mathbf{S}$ by suitably adapting $\mathbf{W_1}$.

Problems with Mixed Sensitivity Scheme,
More Complex Schemes

As has been pointed out above, one of the aspects making the weighted mixed sensitivity scheme attractive is that it allows to cover almost all requirements on any of these closed loop transfer functions in a simple scheme. However, a closer analysis exposes that there are some drawbacks to this approach. These consist in pole–zero cancellations in the closed loop.

Since no explicit weight is used to limit the controller output $\underline{u}$, typically high-gain controllers result from the design. This leads to the closed loop poles moving towards the open–loop zeros of the plant.

Considering the SISO case and with the notation $\mathbf{G} = \frac{N_G}{D_G}$ and $\mathbf{C} = \frac{N_C}{D_C}$, the closed loop denominator is $D_{CL} = D_C D_G + N_C N_G$. If the open loop zeros are part of the closed loop poles this implies that the closed loop denominator can be rewritten with the open–loop zeros factored out: $D_{CL} = N_G(\bar{D}_C D_G + N_C)$. This again implies that N_G is a factor of D_C since $D_C = N_G \bar{D}_C$. This however shows that the controller poles cancel the open–loop plant zeroes.

In the mixed sensitivity design described above, the resulting $\mathbf{S}$ and $\mathbf{T}$ are smooth (following the shape prescribed by their respective weighting functions). The consequence of this together with the zero cancelling mentioned above is that $\mathbf{CS}$ has peaks at the zeros of the open–loop plant $\mathbf{G}$. This is undesired as this may cause actuator saturation and limit robustness.

Besides the above, no input disturbances have been assumed in the weighted sensitivity design. As a consequence, the poles of the observer contained in the $\mathcal{H}_\infty$ controller move towards the stable images of the system poles

[Skogestad96]. Since these poles are part of the closed loop one can with the same argument as used above show that the controller's numerator can be written as $N_C = D_G \bar{N}_C$, which implies that the controller zeros cancel the poles of the open–loop plant. This is particularly undesired for weakly damped flexible modes.

Furthermore, the relative smoothness of **S** resulting from the design implies that the function **SG** will expose large peaks at the poles of **G**, entailing large effects of input disturbances on the system output for these frequencies.

The undesired phenomena mentioned above can be avoided by modifying the **S/T** design scheme. As has been shown above a limit on **CS** will prevent plant zero cancellations by controller poles. Limiting **SG** on the other hand will avoid plant poles from being cancelled by controller zeros. These considerations suggest the application of more complex loop-shaping schemes than the classical weighted-sensitivity scheme, for example a **S/T/CS** or **S/CS/SG** scheme or even a **S/CS/SG/T** scheme, as proposed by [Braembussche98]. The latter has been successfully applied to magnetic bearing control by [Schönhoff00b]. A drawback of this scheme lies in the large number of transfer functions to be minimized simultaneously. This imposes restrictions on the choice of weighting functions, which constitutes an artificial obstacle in the design and limits the freedom of the control engineer. This causes problems particularly when both the robustness and performance requirements are demanding in a certain task.

3.3.4 μ–Synthesis Controller Design

In the above, the $\mathcal{H}_\infty$ algorithm has been introduced as a powerful tool for designing controllers with guaranteed properties for user-specified transfer functions. However, there is an important drawback to this method. In every $\mathcal{H}_\infty$ controller design, the $\| \cdot \|_\infty$-norm of the transfer function from all closed loop inputs to all closed loop outputs is minimized. This usually is conservative for several reasons: The maximum size of the combined transfer function matrix from all inputs to all outputs usually is a conservative estimate for the size the individual transfer matrices. Even worse, this approach may bring into play transfer functions that have no physical meaning. This may lead to the design minimization problem being dominated by transfer functions without physical relevance, which may produce very conservative solutions.

Consider for example the system from Chapter 3.2.4, where robust performance has been shown to be equivalent to a requirement on the structured singular value associated with a specific uncertainty structure, see Figure 3.7d. The $\mathcal{H}_\infty$ algorithm, however, does not minimize the *structured* singular value $\mu_{\mathbf{\Delta}_{rp}}$ as would be desired, but the *unstructured* singular value $\bar{\sigma}$ of the transfer function $\mathbf{T}_{\underline{zw}}$, which includes functions without physical meaning like that from $\underline{w}_1$ to $\underline{z}_2$ and that from $\underline{w}_2$ to $\underline{z}_1$.

Obviously, the situation would be significantly improved if the $\mathcal{H}_\infty$ algorithm could be modified to minimize the *structured* singular value of the closed loop transfer function, i.e. if it would solve the following optimization problem:

$$\min_{\substack{\mathbf{C} \\ \text{stabilizing}}} \sup_{\omega} \mu_{\mathbf{\Delta}_{rp}}(\mathbf{T}_{\underline{zw}}(\mathbf{C}, j\omega)) \tag{3.29}$$

This is referred to as μ–synthesis. Unfortunately, currently no algorithm is available that can achieve this goal directly and guarantee to find the global optimum of the above problem. However, a procedure called D–K iteration yields local optima and constitutes a significant improvement over the classical $\mathcal{H}_\infty$ approach for most practical control problems. In the following D-K iteration is briefly outlined.

Since μ cannot be calculated directly (see Chapter 3.2.3), the synthesis approach consists in minimizing the upper bound of μ instead of μ itself, i.e. the above optimization problem is relaxed to

$$\min_{\substack{\mathbf{C} \\ \text{stabilizing}}} \sup_{\omega} \inf_{D_\omega \in \mathcal{D}_{\mathbf{\Delta}_{rp}}} \bar{\sigma}(D_\omega \mathbf{T}_{\underline{zw}}(\mathbf{C}, j\omega) D_\omega^{-1}). \tag{3.30}$$

Then the matrices D_ω which in the above formulation are chosen individually for each ω, are restricted to be parts of functions from $\mathcal{RH}_\infty$ with the same structure. This simplifies the problem to

$$\min_{\substack{\mathbf{C} \\ \text{stabilizing}}} \inf_{\mathbf{D} \in \mathcal{M}(\mathcal{D}_{\mathbf{\Delta}_{rp}})} \|\mathbf{D}\mathbf{T}_{\underline{zw}}(\mathbf{C})\mathbf{D}^{-1}\|_\infty. \tag{3.31}$$

The D–K iteration now finds locally optimal solutions to this problem by the following two-step procedure:

K-Step: *Given scaling functions $\mathbf{D} \in \mathcal{RH}_\infty$ (initially identity) and holding these fixed, an optimal controller $\mathbf{C}$ for the problem (3.31) is calculated by means of the $\mathcal{H}_\infty$ algorithm.*

D-Step: *Given the controller* **C**, *matrices* D_ω *minimizing the expression*

$$\inf_{D_\omega \in \mathcal{D}_\Delta} \bar{\sigma}(D_\omega \mathbf{T}_{\underline{zw}}(\mathbf{C}, j\omega) D_\omega^{-1})$$

are computed for each frequency in the grid. Then the optimal matrices D_ω *are approximated by a stable, minimal phase transfer function* **D**(*s*).

This procedure is iterated until the performance requirements are reached or no further improvement of the minimum of Equation (3.31) in can be achieved.

Although fairly complex, well-developed software tools for performing D-K iteration are available [Balas95a]. The order of the controllers resulting from the procedure is that of the plant (including the weighting functions) plus that of all D-scales (twice that of **D**(*s*)). Since high order D-scales may be required for efficient minimization of the objective function, this implies a trade–off between closed loop performance and controller size.

Both the choice of maximum scaling function order and of the frequency grid are up to the user. While no guidelines for these issues are available in literature, practical experience shows that the frequency grid should comprise all weakly damped eigenfrequencies of the plant. Furthermore, with the development of powerful controller reduction algorithms [Wortelboer99], the trend can be expected to go towards increasing D-scale orders.

3.3.5 μ–Synthesis: Limitations of Available Algorithms

The μ-synthesis controller design framework described above is a versatile and effective method for designing robustly performant controllers. Commercially available implementations of the algorithms (e.g. the μ–Analysis and Synthesis Toolbox for MATLAB, [Balas95a]) have been successfully applied in numerous practical applications from a variety of fields. Nevertheless, the currently available algorithms are subject to some significant restrictions that will be discussed in the following.

A first restriction to be mentioned consists in the iterative nature of the procedure, where controllers and scalings are successively improved in separate steps. This entails relatively long controller design times (typically 3-5 iterations). Furthermore, the algorithm cannot be guaranteed to find a global minimum of the optimization problem which typically has many local minima.

Another significant restriction results from the fact that the μ values cannot be calculated directly, but can only be assessed via bounds that are tight only for simple block structures, see Chapter 3.2.3. This results in (moderate) conservatism of the estimates.

Finally, it must be stated that the currently available algorithms have considerable problems in dealing with real valued uncertainty. This constitutes a severe drawback since this type of uncertainty is often encountered in practical applications. For example uncertain mass values or uncertain rotational speeds will always be real valued. While unstructured real uncertainty cannot be dealt with at all, parametric real uncertainties can be nominally treated. However, the computation of the μ bounds for real-valued uncertainty is not very reliable. As a consequence, convergence problems are often encountered.

However, replacing real uncertainty by complex uncertainty often is not a viable alternative since this introduces considerable amounts of conservatism (in the complex plane, the parameter then lies in a circular disc rather than on a line). This makes the problem not tractable in some cases as the physically meaningless complex parameter values may lead to awkward, equally meaningless systems being considered in the uncertainty model. It is then possible that these systems are particularly difficult to stabilize and/or control. This results in controllers that have poor performance on the physically relevant systems.

A workaround for this difficulty has been presented in [Balas95a]. It consists in duplicating the inputs and outputs associated with the real uncertainties, and adding a small, complex uncertainty to these new channels. This 'mixed' (real *and* complex) setup results in a less conservative uncertainty model (the parameter now lies in a narrow, oval–shaped area around the line) and yields much better convergence of the μ computation. Unfortunately, additional input and output channels also imply a higher plant order and more scaling matrices to be computed in the D–K iteration, resulting in higher order controllers, as well as longer controller design times. Therefore, the benefits of this approach for controller design may be restricted, depending on the number of real uncertain parameters. For analysis purposes however, this constitutes a considerable improvement over analyzing systems with complex uncertainty.

3.3.6 μ–Synthesis: Advanced Algorithms

Besides the standard D–K iteration described above, there are some refined algorithms that aim at obtaining controllers with μ values closer to the global optimum. Among these is the D–G–K iteration which, based on an alternative characterization of μ, tries to perform a mixed real/complex synthesis with an additional set of scalings (G scalings) [Zhou98].

Unfortunately, these algorithms require considerably more time to design controllers, which limits their benefits. Furthermore, numerical problems are very often encountered in their application [Schönhoff00b], [Schönhoff00a]. Overall, these methods must be considered experimental methods at their current stage of development.

3.4 μ–Analysis

After a controller has been designed for a system, it is natural to ask how 'good' this controller is. This question is answered by μ–analysis.

3.4.1   Interpretation of the μ Value from μ-Synthesis

A first analysis result already comes for free with the controller design: as has been mentioned before the achieved μ value conveys information as to if all design specifications (robust performance) has been fulfilled. A μ value below or equal to one indicates a successful design, while a value above one indicates that this is not the case.

This statement can be further refined. In fact, if a final μ value of γ is achieved, this implies that for uncertainties up to $1/\gamma$ times the size of those used in the design framework, the performance transfer functions will be at most γ times larger than desired. For $\gamma = 2$ this implies that with the given controller, there is an uncertainty of norm $1/2$ for which the closed loop transfer function from the performance inputs to the performance outputs of the design setup has norm 2. (This coupled statement on performance and robustness led to development of an iterative design procedure in which the performance channels are successively weighted by scalars in order to trade–off performance vs. stability in problems where such a trade–off is possible and desired [Balas95a].)

It is important to realize that no statement beyond the above is made. In particular, this statement cannot be scaled. For the example of $\gamma = 2$, no

statement can be made on the size of the performance transfer functions for disturbances of norm 1, in particular it is wrong to conclude that these be 4 (double uncertainty does not mean half as good performance, performance may in some cases be twenty times worse, in others be hardly affected).

3.4.2 Advanced Analysis

From the above, it becomes obvious that the μ value resulting from controller design only gives rather limited information on closed loop performance. In many cases, this information is not detailed enough. Fortunately, additional information on arbitrary performance criteria can be easily obtained.

A standard step in advanced analysis of closed loop performance consists in eliminating the conservatism entailed by the often 'lumped' design problem (e.g. in case of mixed sensitivity or other design schemes). This can be easily done by considering only a subset of the closed loop's performance inputs and outputs, which allows analysis of individual closed loop transfer functions.

Additional insight can be gained from a special feature offered by MATLAB's μ–Analysis and Synthesis Toolbox, which allows explicit computation of a disturbance of norm $1/\gamma$ for which the transfer function from the performance inputs to the performance outputs has norm γ. This worst case disturbance can be used to identify critical uncertainty parameters [Balas95a].

3.5 Summary

In this chapter, an overview over the key concepts and methods in robust controller design has been given. Although a considerable effort has been made to roll out the basic theory required to understand the methods used and decisions taken in the chapter on controller design for AMB systems, Chapter 5, the extent of the subject does not permit a comprehensive treatment within this thesis. For more detailed information on general control theory, the reader is therefore referred to [Franklin94] and [Geering90]. For theoretical aspects of robust control [Green95] and [Zhou96] are recommended. Furthermore, [Zhou98] and [Skogestad96] are textbooks that cover the basic theory and contain valuable information concerning application aspects.

Chapter 4

Identification of AMB Rotor Systems

In this chapter, the identification of AMB rotor systems is addressed. In the first part, a new identification procedure for rigid rotors is presented. The method is designed to identify rigid rotors with unknown properties (mass, moment of inertia, dimensions) that are part of an AMB system of which the bearing properties are known.

The second part of this chapter deals with identification of flexible rotors. The method presented has been developed in [Gähler97] and is based on measurements of the multiple–input multiple–output (MIMO) open–loop frequency response function of the levitated rotor.

In the last part of this chapter, a new method for identification of the rotation dependent part of the model, the gyroscopic matrix G, is presented.

4.1 Identification of Rigid Rotors in AMBs

This chapter is concerned with the identification of unknown rigid rotors that are part of an AMB system with known bearing characteristics. No knowledge about the rotor's size, mass, moment of inertia or location of center of gravity is assumed. The bearings are assumed to operate in differential driving mode and are considered linear[1]. Their character-

---

[1]This is a strong assumption since the experiments performed are not restricted to rotor positions near the bearing center. The justification for this procedure will be given

istics for one specific operating point must be known, i.e. one triplet $(i_{0,ref}, k_{s,ref}, k_{i,ref})$ must be given.

The identification procedure presented here is based on step experiments that are performed on the two radial bearings and the axial bearing.

This chapter is organized as follows: First, the identification problem is formulated in its general form. Then, the core of the method, identification by step experiments, is described. To this end, the identification problem is formulated for a single, one–dimensional bearing, and the analytical solution is presented. In the next two sections, this approach is extended to the case of complete rotors with five degrees of freedom that are to be controlled. With gravity playing an important role in the method, the orientation of the rotor determines how exactly the algorithm is to be applied. Therefore, configurations with horizontal and vertical rotors are addressed separately.

4.1.1   The Identification Problem

The model to be identified in this context is the rigid body model introduced in Chapter 2.2. As has been shown there, any rigid rotor supported by AMBs has the one plane model description (assuming standstill)

$$\begin{bmatrix} m_1 & m_3 \\ m_3 & m_2 \end{bmatrix} \begin{bmatrix} \ddot{x}_A \\ \ddot{x}_B \end{bmatrix} = \begin{bmatrix} k_{s,A} & 0 \\ 0 & k_{s,B} \end{bmatrix} \begin{bmatrix} x_A \\ x_B \end{bmatrix} + \begin{bmatrix} k_{i,A} & 0 \\ 0 & k_{i,B} \end{bmatrix} \begin{bmatrix} i_A \\ i_B \end{bmatrix} - T_2 \begin{bmatrix} \tilde{m}g \\ 0 \end{bmatrix}$$

(4.1)

with

$$m_1 = \frac{mb^2 + I_r}{(a+b)^2}, \ m_2 = \frac{ma^2 + I_r}{(a+b)^2}, \ m_3 = \frac{mab - I_r}{(a+b)^2},$$

(4.2)

and

$$T_2 = \frac{1}{a+b} \begin{bmatrix} b & a \\ -1 & 1 \end{bmatrix}.$$

(4.3)

As has been mentioned above all bearing parameters (and therefore $k_{s,A}$, $k_{s,B}$, $k_{i,A}$ and $k_{i,B}$) are assumed to be known. The identification problem consists in determining the unknown mass coefficients m_1, m_2 and m_3.

---

by experimental investigations in Chapter 7.

4.1.2   1–D Identification by Means of Step Experiments

Identification

In this section, the identification problem is solved for a single mass that is to be levitated in one degree of freedom. This analysis goes back to [Fritsche95].

Consider a one–dimensional bearing as schematically depicted in Figure 4.1, where the rotor is a ball, x_s denotes the radial distance between the rotor and the retainer bearing when the rotor is in the center position, and x represents the displacement of the rotor from the center position. Let further m denote the mass of the rotor, and $k_{s,ref}$ and $k_{i,ref}$ the force–displacement and force–current factors of the bearing for a given bias current $i_{0,ref}$, respectively.

With the above notation and i being the bearing current's deviation from the bias current, the linearized equation describing the rotor's motion around the bearing center can be written as follows:

$$m\ddot{x} = k_s x + k_i i - m \cdot g. \tag{4.4}$$

In the above setting, full identification of the system is equivalent to identification of the unknown mass m of the rotor. To this end, the following experiment is performed. First, the current is switched off such that the rotor rests at the position $x = -x_s$. Then, a current step of size I_s is applied to the upper magnet and the rotor is accelerated upwards until it hits the upper part of the retainer bearing at $x = x_s$.

By applying the Laplace transform considering the initial condition $x = -x_s$, the rotor's response to the current step can be expressed in the frequency domain as:

$$m(s^2 X(s) + s x_s) = k_s X(s) + k_i \frac{I_s}{s} - \frac{mg}{s}. \tag{4.5}$$

Rearranging terms yields

$$X(s) = \frac{-x_s \cdot s}{s^2 - \frac{k_s}{m}} + \frac{\frac{k_i}{m}}{s^2 - \frac{k_s}{m}} \cdot \frac{I_s}{s} - \frac{\frac{g}{s}}{s^2 - \frac{k_s}{m}}, \tag{4.6}$$

where the first factor of the second term describes the plant's transfer function from current to displacement and the first and third terms stem from the initial conditions and the influence of gravity, respectively.
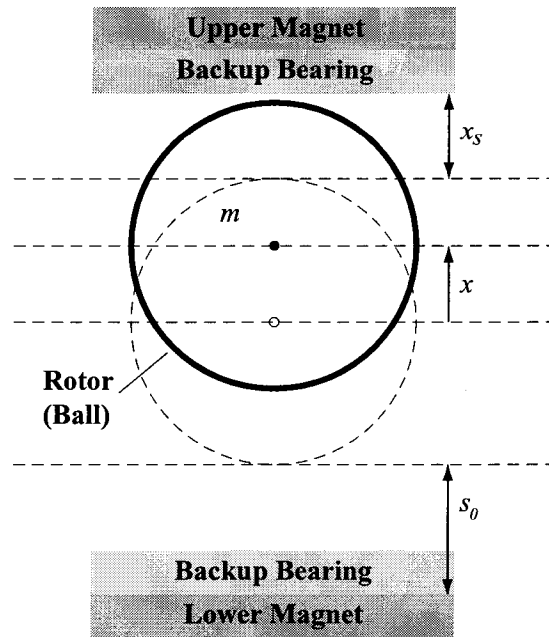
Figure 4.1: *1–dof Active Magnetic Bearing*

Investigation of the second term reveals the dynamical system known from Chapter 2.1.4, Equation (2.13). This system is of second order with poles at

$$p = \pm\sqrt{\frac{k_s}{m}} \text{ and a static gain of } k_{plant} = -\frac{k_i}{k_s}. \tag{4.7}$$

Transformation of Equation (4.6) to the time domain and scaling by $1/x_s$ then yields for the step response of the rotor:

$$x(t) = \left(-1 + \frac{I_s \, s_0}{x_s \, i_0} - \frac{g \, m}{x_s \, k_s}\right) \cosh\left(\sqrt{\frac{k_s}{m}} \, t\right) - \left(\frac{I_s \, s_0}{x_s \, i_0} - \frac{g \, m}{x_s \, k_s}\right). \tag{4.8}$$

As can be seen from Equation (4.8), the function describing the rotor's path contains the unknown system pole p as an argument to the hyperbolic cosine term. This parameter can be identified by means of the following procedure.

1. Perform a step experiment as described above with on–line measurement of the rotor's position.

2. From the time data obtained, extract the moments of take–off and contact with the upper part of the retainer bearing.

3. Fit a function of type $x(t) = a \cdot \cosh(p_i \cdot t) - c$ to the position measurements made during the flight–phase of the rotor.

The parameter p_i resulting from this procedure then directly yields an estimate for the system's poles at $\pm p$.

It is important to understand that in the experiment described above the size of the current step implicitly defines the operating point of the (linear) bearing. A current step of size I_s implies that a linear bearing with bias current $i_0 = I_s/2$ is subjected to a current step from $i = -I_s/2$ to $i = I_s/2$. As mentioned in Chapter 2.1.2, the force–displacement factor k_s and the force–current factor k_i both depend on the bearing's bias current i_0, i.e.

$$k_s \propto i_0^2 \text{ and } k_i \propto i_0. \tag{4.9}$$

Based on this relationship and the known operating point ($i_{0,ref}$, $k_{s,ref}$, $k_{i,ref}$), the force–displacement factor and the force–current factor that have been valid during the experiment can be calculated as follows:

$$k_{s,eff} = k_{s,ref} \cdot \left(\frac{i_{0,eff}}{i_{0,ref}} \right)^2, \text{ and } k_{i,eff} = k_{i,ref} \cdot \frac{i_{0,eff}}{i_{0,ref}}, \tag{4.10}$$

with $i_{0,eff} = I_s/2$.

Based on the effective value of k_s from the above formula and the estimated pole p_i the rotor mass m can be determined using Equation (4.7). Once this has been done the system is fully identified. Its transfer function is

$$\mathbf{G}(s) = \frac{\frac{k_i}{m}}{s^2 - \frac{k_s}{m}}. \tag{4.11}$$

This equation is valid not only for the nominal operating point ($i_{0,ref}$, $k_{s,ref}$, $k_{i,ref}$) but also for arbitrary other values of i_0. For any choice of i_0 the corresponding values for the force–displacement factor k_s and the force–current factor k_i can be determined using Equation (4.10).

It is important to appreciate the significance of Equation (4.10). This equation can be used to transform the identified model (4.11) from the operating point at which the experiment has been carried out to any other operating point. In particular, it allows formulation of low–bias current models that could not have been identified with the above method since the required current step would have been too small to lift the rotor.

Controller Design

A controller for this system can be derived as follows. Since this system has a constant phase of -180 degrees, the controller must provide positive phase and sufficient gain in order to stabilize the unstable system pole. A straightforward solution to achieve stabilization for this type of plant is by means of a lead compensator [Muntwyler00]. The structure of this element is as follows:

$$\mathbf{R}(s) = k_{ld}\frac{Ts + 1}{\alpha Ts + 1} \text{ with } T = \frac{1}{c_f\sqrt{\alpha p}}, 0 < \alpha < 1. \qquad (4.12)$$

The parameters k_{ld}, c_f, and α must be chosen such that the system is robustly stabilized.

One can show that k_{ld} corresponds directly to the gain margin of the closed loop system. To achieve stabilization, the product of k_{ld} and the static plant gain k_{plant} must be less than -1. A value of -1.5 for this product yields a gain margin of 3dB, which can be considered a minimum requirement.

An additional requirement on the controller is that its gain must be large enough to actually lift the rotor (sufficient disturbance rejection at $s = 0$). This condition is not fulfilled by all stabilizing controllers.

From the equation

$$k_s \cdot x + k_i \cdot i = m \cdot g \qquad (4.13)$$

which describes the balance of forces if the rotor is at rest at position x in the air gap and from the static force current relation defined by the controller $i = -k_{ld} \cdot x$ (negative feedback), it follows that the gain required to hold the rotor statically at a position $x = -x_{stat}$ in the air gap a controller gain k_{ld} of

$$k_{ld} = \frac{k_s}{k_i} + \frac{m \cdot g}{k_i \cdot x_{stat}} \qquad (4.14)$$

is required. When no integrator is employed, a reasonable minimum choice for the static position error is one quarter of the air gap from the bearing center, yielding

$$k_{ld} = \frac{k_s}{k_i} + 4\frac{m \cdot g}{k_i \cdot x_s}. \qquad (4.15)$$

The controller gain can then be chosen as the maximum of this gain and the minimum stabilizing gain described above.
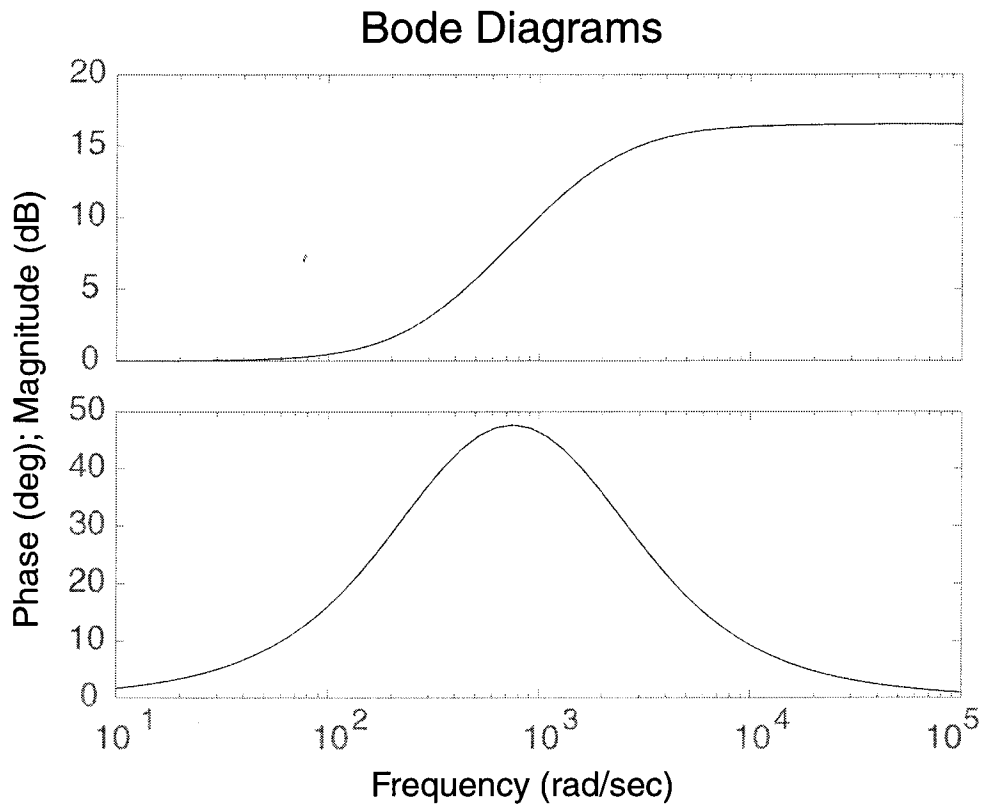
Figure 4.2: *Bode plot of lead compensator*

When an integrator is added to the controller, the stiffness can be set to a lower value. It is then only to be chosen large enough for stabilizing the rotor while levitation is achieved by the (very slow) integrator. In this situation, it is enough to set the gain k_{ld} to several (e.g. 5) times the the inverse of the plant gain. This low gain approach is favorable when excitation of unmodeled high frequency modes is to be avoided as is the case in application of the method to AMB systems with flexible rotors.

The parameter α determines the maximum phase lift φ_{max} of the compensator [Franklin94], i.e.

$$\sin(\varphi_{max}) = \frac{1 - \alpha}{1 + \alpha}. \tag{4.16}$$

Small values of α result in a large phase lift. This is good for stabilization, but entails a large high frequency gain k_{ld}/α of the controller. A good compromise is $\alpha = 0.15$. This yields a phase lift of nearly 50 degrees at frequency $c_f \cdot p$ and an increase in high frequency gain of 15dB.

Finally, the coefficient c_f can be used to select the frequency ω_{max} for which the maximum phase lift is achieved. The relationship between T

and ω_{max} is

$$\omega_{max} = \frac{1}{T \cdot \sqrt{\alpha}} = c_f \cdot p. \tag{4.17}$$

Experiments have shown that the choice $\omega_{max}=1.5 \cdot p$ yields good results, [Muntwyler00], suggesting a choice of $c_f = 1.5$. Figure 4.2 shows a bode plot of the controller for $\alpha = 0.15$, $k_{ld} = 1$, $p = 500$, and $c_f = 1.5$.

4.1.3   Identification Procedure for Vertical Rotors

The procedure described above can be applied directly to the controller design for axial bearings of AMB systems with vertical rotor. Once this has been done, the identification of the radial dynamics can be addressed.

Determination of m_1 and m_2. The diagonal entries of the mass matrix can be determined as follows: First, the rotor is pulled to the retainer bearings in both bearings by means of constant currents. While the current is held constant in one AMB, a step experiment as described in the previous section is applied to the other bearing. In terms of Equation (4.1) (without the gravity term), this means for the case that the step experiment is performed on bearing A

$$m\ddot{x}_A = k_{s,A} x_A + k_{i,A} i_A \tag{4.18}$$

This equation is identical to the one derived in the section describing the one dimensional case. Therefore, the identification approach developed in the last section can be directly applied, yielding the mass coefficient m_1. The coefficient m_2 can be identified from application of the same procedure to bearing B.

Determination of m_3. In order to determine the remaining coefficient, m_3, it is important to notice that the sum of the entries of the mass matrix is equal to the total rotor mass m:

$$m_1 + m_2 + 2m_3 = m \tag{4.19}$$

The total mass can be calculated from the force of gravity acting on the rotor, which in turn can be determined from the position and currents in the axial bearing and the known characteristics of this bearing. Together with the known values of m_1 and m_2, Equation (4.19) can be used to determine the remaining coefficient m_3. The system is then fully identified.

4.1.4 Identification Procedure for Horizontal Rotors

For the axial movement of horizontal rotors, the equations of motion are similar to those given in Chapter 4.1.2. Merely the gravity disturbance force is now replaced by a term describing the friction of the rotor in the retainer bearings. However, this constitutes merely a disturbance force and has no influence on the system's transfer function. Therefore, the procedure described above can be applied 'as is' for the design of axial controllers for horizontal rotors. Due to the horizontal orientation of the system, a current must be applied to one side of the axial bearing before the experiment to bring the rotor into contact with the retainer bearing.

Once an axial controller has been designed, the issue of radial control can be addressed. In typical AMB systems the radial bearings are rotated by 45 degrees with respect to the vertical axis, see Figure 4.3. Therefore it is necessary to extend the 1–D procedure described above to two dimensions.

2–D Case: Identification

Compared to the one–dimensional case described above, the main difference in the system model is the existence of two independent axes. In order to achieve the desired vertical upward acceleration of the rotor, a current step must be applied to both axes at the same time. The movement along each of two axes can then be analyzed separately. The model description is analogous to that of the one–dimensional case, with the difference that both the air gap relevant during the vertical lift experiment, x_s, and the gravitation constant g are reduced by a factor of $\sqrt{2}$. As a result, the equation of motion becomes

$$m\left(s^2 X(s) + s\frac{x_s}{\sqrt{2}}\right) = k_s X(s) + k_i I(s) - \frac{mg}{s\sqrt{2}} \qquad (4.20)$$

The Laplace transform yields for a step current input

$$X(s) = \frac{-\frac{x_s}{\sqrt{2}} \cdot s}{s^2 - \frac{k_s}{m}} + \frac{\frac{k_i}{m}}{s^2 - \frac{k_s}{m}} \cdot \frac{I_s}{s} - \frac{\frac{g}{s\sqrt{2}}}{s^2 - \frac{k_s}{m}} \qquad (4.21)$$

which in time domain is

$$x(t) = \left(-1 + \frac{\sqrt{2}\, I_s\, s_0}{x_s\, i_0} - \frac{g\, m}{x_s\, k_s}\right)\cosh\left(\sqrt{\frac{k_s}{m}}t\right) - \left(\frac{\sqrt{2}I_s\, s_0}{x_s\, i_0} - \frac{g\, m}{x_s\, k_s}\right).$$
$$(4.22)$$
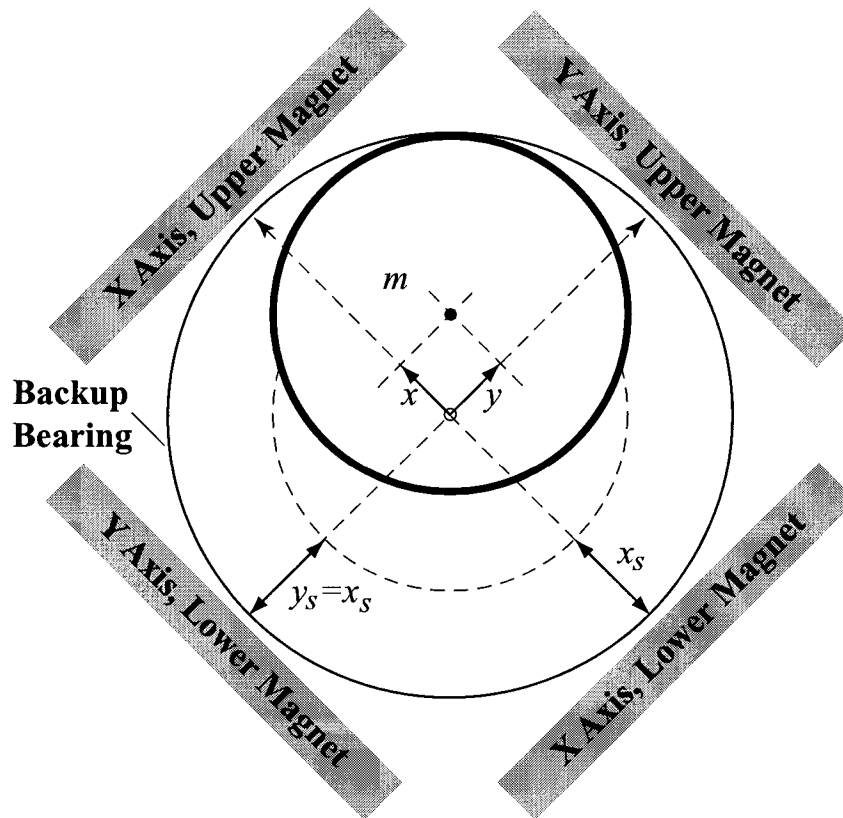
Figure 4.3: *2–dof radial Active Magnetic Bearing*

As a consequence, the pole for each of the system's axes can again be estimated from a fit of a function of type $x(t) = a \cdot \cosh(p_i \cdot t) - c$ and the transfer function from current to displacement for each of the two axes again is that given in Equation (4.11) with the same comments valid concerning the adaptation of the bearing's operating point.

2–D Case: Controller Design

The two dimensional system can be controlled by designing an individual controller for each of the two axes. Since the transfer function from current to displacement along each of the axes is identical to the one dimensional case and the factor $\sqrt{2}$ cancels out in the calculation of the minimum gain required for lifting the rotor to a certain position, the design procedure remains identical.

Horizontal Rotor: Identification

As has been shown in Chapter 4.1.1, the identification problem consists in determining he three unknown masses m_1, m_2 and m_3 . How this can be achieved will be described in the following:

Determination of m_1 and m_2. The diagonal entries of the mass matrix can be determined as follows: While one bearing remains switched off, the step experiment described in the previous section is applied to the other bearing. During the experiment, the rotor is held at rest by gravity on one side, while at the other side it is moved upward. In terms of Equation (4.1), this means for the case that the step experiment is performed on bearing A,

$$m_1 \ddot{x}_A = k_{s,A} x_A + k_{i,A} i_A - \frac{b}{a+b} \cdot m \cdot g \qquad (4.23)$$

Up to the gravity term, this equation is identical to the one derived in the section describing the two dimensional case. The difference in the last term merely is a difference in the disturbing gravity force. It has no influence on the transfer function to be identified, see Equation (4.22). Therefore, the identification approach developed in the last section can be directly applied, yielding the mass coefficient m_1. The coefficient m_2 can be identified from application of the same procedure to bearing B. Based on this information and the controller design method described in the last section, controllers capable of lifting each side of the rotor individually (with the other bearing switched off) can be designed. It must be understood, however, that these controllers in general do not stabilize the rotor when *both* bearings are active. While the two individual systems each have two real axis poles per plane, the completely levitated rotor has four such poles poles per plane, see Chapter 2.6. These poles are associated to the rigid body motions of the rotor (tilt mode and translational mode) and cannot be derived from the poles observed with one of the bearings switched off.

Determination of m_3. In order to determine the remaining parameter, m_3, it is important to notice that the gravity term in Equation (4.23) can easily be expressed in terms of the mass coefficients to be identified:

$$\frac{b}{a+b} \cdot m = m_1 + m_3 \qquad (4.24)$$

This can be seen from the following thought experiment: let the rotor fall freely, with both bearings switched off. Then $k_{s,A}$ and $k_{s,B}$ are zero, and

the first line of Equation (4.1) becomes

$$m_1 \cdot g + m_3 \cdot g = \frac{b}{a+b} \cdot m \cdot g \qquad (4.25)$$

from which the above statement follows immediately.

After having determined stabilizing controllers for each of the individual bearings with the other bearing switched off, we are able to bring the rotor to the bearing center by means of a (very slow) integrator. Then the gravity term in Equation (4.23) can be determined from measurements of the control currents. Based on this measurement and the known mass m_1, the remaining parameter m_3 can be determined from Equation (4.24), which concludes the identification of the system.

4.2   Identification of Flexible Rotor AMB Systems

This chapter deals with the problem of obtaining an analytical model of a given AMB rotor system with flexible shaft. The implicit assumption is that the rotor has been levitated by some primitive controller that allows execution of the required experiments. Such a controller can be obtained based on the identification procedure for the rotor's rigid body dynamics described in Chapter 4.1 and a subsequent controller design for the system with unknown high frequency dynamics as described in Chapter 5.1. Integration of the identification algorithm in the overall controller design procedure will be discussed in Chapter 6.

The analysis in this chapter is based on the model description from Chapter 2.3. First, the issue of measuring open–loop frequency response functions is addressed. Then, an algorithm that allows the identification of the open–loop MIMO system model from the measured transfer functions is presented.

4.2.1   Closed Loop Measurement of open–loop Transfer Functions

In the context of this work, we are interested in obtaining models for controller design, i.e. open–loop models of the system. To identify such models, open loop measurement data of the system's frequency response
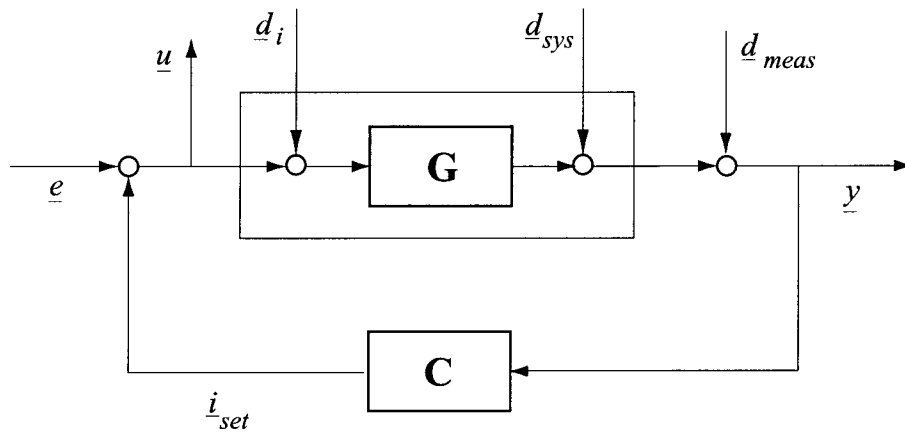
Figure 4.4: *MIMO Transfer Function Measurement*

function from the current inputs to the sensor outputs is indispensable. At first sight, this data appears to be difficult to obtain since employment of the stabilizing controller for levitation of the rotor always makes the system a closed loop system. However, this does not pose any substantial problems. By exciting and measuring adequate system variables, the system's open–loop frequency response function can be measured while the system is operated in closed loop [Gähler98].

To clarify this statement, consider the system setup in Figure 4.4. The MIMO frequency response function to be measured is that from the system's input $\underline{u}$ to its output $\underline{y}$. Several sources of disturbance are present, $\underline{d}_i$ represents disturbances in the amplifiers and actuators, $\underline{d}_{sys}$ indicates disturbance forces acting on the system, and $\underline{d}_{meas}$ accounts for measurement and sensor noise. No additional noise needs to be taken into account for the input $\underline{u}$ (the sum of the controller set current and the excitation signal fed to the system) since the values are not measured but directly obtained from the processor board, [Gähler98].

The system is excited from variable $\underline{e}$. From the above diagram the following closed loop frequency response functions can be derived (for simplicity, the complex argument is omitted):

$$\underline{y} = (I - \mathbf{CG})^{-1}\mathbf{G}(\underline{e} + \underline{d}_i) + (I - \mathbf{CG})^{-1}(\underline{d}_{sys} + \underline{d}_{meas}) \tag{4.26}$$

$$\underline{u} = (I - \mathbf{CG})^{-1}\underline{e} + (I - \mathbf{CG})^{-1}\mathbf{C}(\underline{d}_{meas} + \underline{d}_{sys}) + (I - \mathbf{CG})^{-1}\mathbf{CG}\underline{d}_i \tag{4.27}$$

For the case of negligible noise (adequate signal to noise ratio) it follows that

$$\frac{\underline{y}}{\underline{u}} = \frac{(I - \mathbf{CG})^{-1}\mathbf{G}\underline{e}}{(I - \mathbf{CG})^{-1}\underline{e}} = \mathbf{G} \qquad (4.28)$$

i.e. the open–loop frequency response function $\mathbf{G}$ of the system can be obtained from closed loop measurements of $\underline{y}$ and $\underline{u}$ with excitation at $\underline{e}$.

In practice, the symbolic division in the above formula is a matrix division. Given a system with n inputs and l outputs, for each frequency point ω_i, n measurements are made. During each measurement, all input and output signals are recorded. This yields complex measurement matrices

$$\mathbf{U}(j\omega) = \begin{bmatrix} | & \cdots & | \\ \underline{u}_1 & \cdots & \underline{u}_n \\ | & \cdots & | \end{bmatrix} \in \mathbb{R}^{n \times n} \qquad (4.29)$$

$$\mathbf{Y}(j\omega) = \begin{bmatrix} | & \cdots & | \\ \underline{y}_1 & \cdots & \underline{y}_n \\ | & \cdots & | \end{bmatrix} \in \mathbb{R}^{l \times n} \qquad (4.30)$$

To actually compute the frequency response function value $\mathbf{G}(j\omega)$, the matrix $\mathbf{U}(j\omega)$ must be invertible. Therefore, the excitation patterns must be chosen in such a way that the n columns of $\mathbf{U}(j\omega)$ are linearly independent. The frequency response function value is then calculated for each frequency point as

$$\mathbf{G}_m(j\omega) = \mathbf{Y}(j\omega)\mathbf{U}(j\omega)^{-1} \qquad (4.31)$$

Successive application of this procedure allows to measure the system's MIMO open–loop frequency response function on an arbitrary frequency grid.

4.2.2   The Identification Problem

As has been shown in Chapter 2.3, proportionally damped flexible rotors in uncontrolled AMBs can be represented for $\Omega = 0$ by a dynamical system $\mathbf{G}$ defined by a system of second order differential equations

$$M\underline{\ddot{q}} + D\underline{\dot{q}} + K\underline{q} = F\underline{w} \qquad (4.32)$$
$$\underline{z} = S\underline{q}$$

Transformation of this system to the Laplace domain and application of the modal decomposition from Chapter 2.3.2 yields the following decomposition of the system:

$$
\begin{aligned}
\mathbf{G}(s) &= S(s^2 M + sD + K)^{-1} F \\[2mm]
&= S[V^{-T}(s^2 \tilde{M} + s\tilde{D} + \tilde{K})V^{-1}]^{-1} F \\[2mm]
&= SV(s^2 \tilde{M} + s\tilde{D} + \tilde{K})^{-1} V^T F \\[2mm]
&= \tilde{\Phi}[(s^2 \tilde{M} + s\tilde{D} + \tilde{K})]^{-1} \tilde{\Psi}^T \\[2mm]
&= \sum_{i=1}^{q} \frac{\underline{\tilde{\phi}}_i \underline{\tilde{\psi}}_i^T}{s^2 + 2\delta_i \omega_{0i} s + \omega_{oi}^2} \\[2mm]
&= \sum_{i=1}^{q} \frac{R_i}{s^2 + 2\delta_i \omega_{0i} s + \omega_{oi}^2}
\end{aligned}
\tag{4.33}
$$

where the matrices $R_i = \underline{\tilde{\phi}}_i \underline{\tilde{\psi}}_i^T$ are dyadic vector products of rank one.

The order q of the system is to be chosen based on the measured FRF of the open–loop system. Due to the weak damping of the hovering rotor, all flexible poles are clearly visible in the open–loop FRF. As a consequence, the issue of determining an adequate order for the model, often a critical point in system identification, does not pose a problem here. The identification problem consists in determining the numerator and denominator entries of the addends in the last row of Equation (4.33).

4.2.3 Identification Algorithm for Flexible Rotors at Standstill

Several algorithms are available to derive state space models from measured frequency response functions (FRFs). However, the special characteristics of AMB systems, in particular the real–axis poles (see Figure 2.6), require application of a special procedure to achieve robust identification. An algorithm to perform this task based on the closed loop measurement of open loop transfer functions presented in Chapter 4.2.1 has been presented in [Gähler97]. In the following, this algorithm is briefly described.

Based on measured FRF data $\mathbf{G}_m(j\omega)$ obtained from the rig by applying the measurement procedure from the last chapter, the following steps are performed:

1. **Introduction of Feedback Term.** A constant proportional feedback term F_K is numerically introduced into the open–loop measurement data:

$$\tilde{\mathbf{G}}_m(j\omega_i) = (I + \mathbf{G}_m(j\omega_i)F_K)^{-1}\mathbf{G}_m(j\omega_i) \qquad (4.34)$$

This is equivalent to introduction of a proportional feedback controller on the open loop system, which moves the real-axis poles towards the origin and then further up and down the imaginary axis, making them clearly visible in the transfer functions of the system $\tilde{\mathbf{G}}_m(j\omega_i)$.

2. **Determination of Denominator Polynomial.** From the modified FRF, the determinant $\det(\tilde{\mathbf{G}}_m(j\omega_i))$ is calculated for each frequency point $j\omega_i$. A least squares procedure is used to estimate the polynomial describing the determinant $\det(\tilde{\mathbf{G}}_m(j\omega))$. The denominator polynomials of all SISO transfer functions contained in $\tilde{\mathbf{G}}(j\omega)$ are identical to the identified polynomial [Gähler97]. The system poles can therefore be extracted by determining the roots of this polynomial.

3. **Determination of Residual Matrices.** The residual matrices R_i from Equation (4.33) are estimated by means of another least squares problem. In the next step, the rank one condition is enforced by calculating optimal rank 1 approximations to the estimated matrices based on their singular value decomposition.

4. **Assembly of Model.** Based on the identified parameters, a minimal state space description of the model is constructed.

5. **Elimination of Feedback Term.** Finally, the proportional feedback term is again removed from the identified model by introduction of an identical feedback term with opposite sign analogous to step 1. This yields, using Equation (4.34)

$$
\begin{aligned}
\left[I + \tilde{\mathbf{G}}(s)(-F_K)\right]^{-1}\tilde{\mathbf{G}}(s) &= \\
\left[I + (I + \mathbf{G}(s)F_K)^{-1}\mathbf{G}(s)(-F_K)\right]^{-1}(I + \mathbf{G}(s)F_K)^{-1}\mathbf{G}(s) &= \\
\left[(I + \mathbf{G}(s)F_K)(I + (I + \mathbf{G}(s)F_K)^{-1}\mathbf{G}(s)(-F_K))\right]\mathbf{G}(s) &= \mathbf{G}(s)
\end{aligned}
$$

$$(4.35)$$

The result of the procedure consists in a MIMO state space model of the open–loop AMB system of a form similar to that from Equation (2.46):

$$
A = \begin{bmatrix}
0^{q \times q} & I^{q \times q} \\
\begin{matrix}
-(p_1 \cdot p_1^*) & 0 & (p_1 + p_1^*) & 0 \\
& -(p_2 \cdot p_2^*) & & (p_2 + p_2^*) \\
& \cdots & & \cdots \\
0 & -(p_q \cdot p_q^*) & 0 & (p_q + p_q^*)
\end{matrix}
\end{bmatrix}
\tag{4.36}
$$

$$
B = \begin{bmatrix} 0 \\ \tilde{\Phi} \end{bmatrix} \in \mathbb{R}^{2q \times 2n} \quad C = \begin{bmatrix} \tilde{\Psi}^T & 0 \end{bmatrix} \in \mathbb{R}^{2l \times 2q} \quad D = [0] \in \mathbb{R}^{2l \times 2n}
$$

where n and l denote the number of AMBs and sensors in the system, respectively.

The method has been shown to work efficiently and robustly. From the identified single–plane model, a two plane model can be derived by simple duplication of this model, yielding a system with twice as many states, inputs, and outputs. By simply reordering of the states in the state vector such that they are

- planewise alternating, with the modes from the x–plane first,

- with identical modes of different planes next to each other,

- beginning with the rigid body modes, and

- with increasing frequencies,

i.e. in the form

$$
\tilde{\underline{q}}_{id,2p} = \left(\nu_{r_1,p_x}, \nu_{r_1,p_y}, \nu_{r_2,p_x}, \nu_{r_2,p_y}, \nu_{f_1,p_x}, \nu_{f_1,p_y}, ..., \nu_{f_{q-2},p_x}, \nu_{f_{q-2},p_y} \right)^T,
\tag{4.37}
$$

with ν_{r_i,p_j} denotes the state associated with the i-th rigid body mode of plane j and ν_{f_i,p_j} denotes the state associated with the i-th flexible mode of plane j ($j \in \{x, y\}$).

The resulting two–plane model can be brought into a form very similar to that from the above equation with the sub–matrices in the lower right

and left of the matrix A having $2q$ diagonal entries. A two plane model
of this structure will be used in the following for the identification of the
gyroscopic matrix G.

4.3   Identification of the Gyroscopic Matrix

The above identification of the rotor system is not yet complete. It only
covers the rotor at standstill. The gyroscopic matrix G describing the
dynamical changes to the system due to rotation cannot be determined
from the system at rest.

In the past, several attempts have been made to identify the matrix G
[Mohler96], [Senn97]. To this end, frequency response functions have been
measured on a rotating AMB system. Based on these measurements, it
has been attempted to find a skew–symmetric matrix G expressing the
gyroscopic effects by means of different least squares approaches. However,
these attempts were not successful. The optimization problem turned out
to have many local minima and too many variables. As a consequence,
the algorithms yielded solutions that were by no means similar to the
reference solution obtained from Finite Element programs. Even in the
case of strongly relaxed demands, where the attempt was made to find G
starting with an only slightly disturbed $\tilde{G}$, no convergence was achieved
[Senn97].

4.3.1   Problem Definition

Due to the experiences made in the prior research, the above concept of
identifying G by brute force methods has not been pursued any further
in this work. Instead, it has been decided to step back and address the
following issues in order to arrive at a problem solution:

Simplification: The maximum amount of structural information on the
gyroscopic matrix should be gathered and used to reduce the number
of unknowns in order to simplify the problem.

Approximation: Instead of searching for 'the true' gyroscopic matrix,
could the problem be simplified by finding a matrix that affects the
system's transfer function in a very similar way but has much simpler
structure?

Modularity: If possible, the new identification procedure should consist of several smaller problems that can be solved more reliably than a single large problem with many variables.

In order to achieve any of the above, a deeper understanding of the nature of gyroscopic effects and how they affect the system was required. To this end, following analysis has been carried out.

4.3.2 Problem Analysis

In Chapter 2.3.2 the matrix G has been introduced as a skew–symmetric matrix that has the same size as the other system matrices. This information alone yields a number of $r(r - 1)/2$ coefficients to be determined by identification, with r denoting the size of the square matrix G.

However, by performing a state transformation to modal form with the states ordered with increasing frequency and alternating planewise as defined in Equation (4.37) G can be forced to have a special structure. It then consists of skew–symmetric 2 by 2 blocks with zero diagonal, see Figure 4.5. This structure results from the fact that G only contains coupling terms between modes of different planes and the rotational symmetry of the rotor.

This reduces the number of unknown coefficients to $r(r + 2)/8$, which amounts to a reduction of about 50–70% for typical systems (with $r = 4$ to $r = 16$ modes in the control relevant frequency range). Therefore it is favorable to base both the analysis and identification of the gyroscopic matrix on the system description in modal coordinates.

When analyzing the entries of the G matrix it shows that unfortunately, all entries of the different 2 by 2 blocks typically are approximately of the same size with irregular variation of about two orders of magnitude. No specific structure (like for example dominance of the diagonal blocks) can be made out. This observation suggests that all blocks contained in the matrix are equally significant and that hence all coefficients must be identified in order to arrive at a useful description of the gyroscopic effects. This conjecture however is not correct as will be shown in the following.

At standstill, the two planes of the system are decoupled. In the modal description, this is obvious in the structure of the A matrix of the system, see Equation (2.46), which shows the structure of the one plane system and also of the two plane system if the state ordering of Equation (4.37) is applied. Additionally, in this description the modes of each individual

Figure 4.5: *Structure of gyroscopic matrix with state ordering from Equation (4.37). The matrix is skew symmetric and composed of two–by–two blocks G that themselves are also skew–symmetric and have zeros as diagonal values. Only a few block entries of the (full) matrix are explicitly shown for better readability.*

plane are completely decoupled, i.e. no vibration of any mode of any plane has any influence on any other mode of the system.

This situation is changed as soon as the rotor starts rotating. A scalar multiple of the matrix G is then added to the lower right part of the state space matrix A. Due to the structure of G, this will introduce a cross coupling between the modes of different planes. This effect can be analyzed on the example of a simplified system featuring only one flexible, undamped mode per plane. In this situation, the gyroscopic coupling consists in a single coefficient g.

For a given undamped flexible mode pair from the x and y–planes with eigenfrequencies f and $c \cdot f$ (c being a constant factor) that is coupled by a gyroscopic matrix entry g the following equation for the two coupled modes is obtained:

$$\begin{bmatrix} \ddot{\nu}_{f_i,p_x} \\ \ddot{\nu}_{f_j,p_y} \end{bmatrix} = - \begin{bmatrix} f^2 & 0 \\ 0 & c^2 f^2 \end{bmatrix} \begin{bmatrix} \nu_{f_i,p_x} \\ \nu_{f_j,p_y} \end{bmatrix} - \begin{bmatrix} 0 & -\Omega g \\ \Omega g & 0 \end{bmatrix} \begin{bmatrix} \dot{\nu}_{f_i,p_x} \\ \dot{\nu}_{f_j,p_y} \end{bmatrix} \qquad (4.38)$$

In order to investigate the relevance of the different blocks in more general systems (see Figure 4.5), it is instructive to investigate the effect of the gyroscopic coupling term g as the eigenfrequency ratio c is altered.

In Figure 4.6 the change in eigenfrequencies of the coupled system with respect to the eigenfrequencies of the uncoupled system is depicted for a variety of eigenfrequency ratios c for a fixed value of $g = 0.1$.
As can be seen from the figure, the effect the gyroscopic coupling Ωg has on the eigenfrequencies of the coupled modes is the larger the closer the two uncoupled eigenfrequencies are. For all rotational speeds, by far the maximum eigenfrequency shift resulting from the gyroscopic matrix coefficient g is obtained for $c = 1.$[2]

An important implication of this observation is that the seemingly similar entries of the typical gyroscopic matrix are similar in *size*, but not similar in *effect*. While already small coefficients coupling two modes with identical frequency have a considerable impact on the dynamics of the system, significantly larger entries linking modes with very different frequencies have virtually no effect.

This constitutes a *de facto* block diagonal dominance of the gyroscopic matrix G, attributing special relevance to the $(r - 4)/2$ coefficients describing the mutual coupling between identical modes of the two planes. Figure 4.7 shows that these few coefficients alone yield a good description of the gyroscopic effects acting on the system for small rotational speeds. It shows a transfer function of a system obtained from a Finite Element model at a rotational speed of 7'500rpm. The first graph (dotted) is made with the full G matrix with 50 nonzero entries. For the second graph, a matrix $\tilde{G}$ with only the 6 nonzero entries describing the coupling of the three flexible modes of identical frequency has been employed.

Figure 4.8 shows the same systems at a higher rotational speed (60'000rpm). Close inspection of the plots shows that the eigenfrequencies match fairly well, but exposes large differences in the amplitudes of the flexible modes, in particular for the critical forward modes. Furthermore, for the second mode an interesting effect can be observed: While the forward mode is underestimated by about 10dB, the backward mode is overestimated by

---

[2]Concerning the asymmetry of the plots, it must be noted that due to the normalization of the rotational speed with the mode eigenfrequency f, the right half of the plot is more relevant to practical application than the left half – at the very left of the plot the dashed line for $\Omega=3.4f$ represents a rotational speed 34 times higher than the lower one of the flexible modes under consideration. Even for highly flexible rotors with a first flexible mode at 100Hz this amounts to a rotational speed of more than 200000rpm.
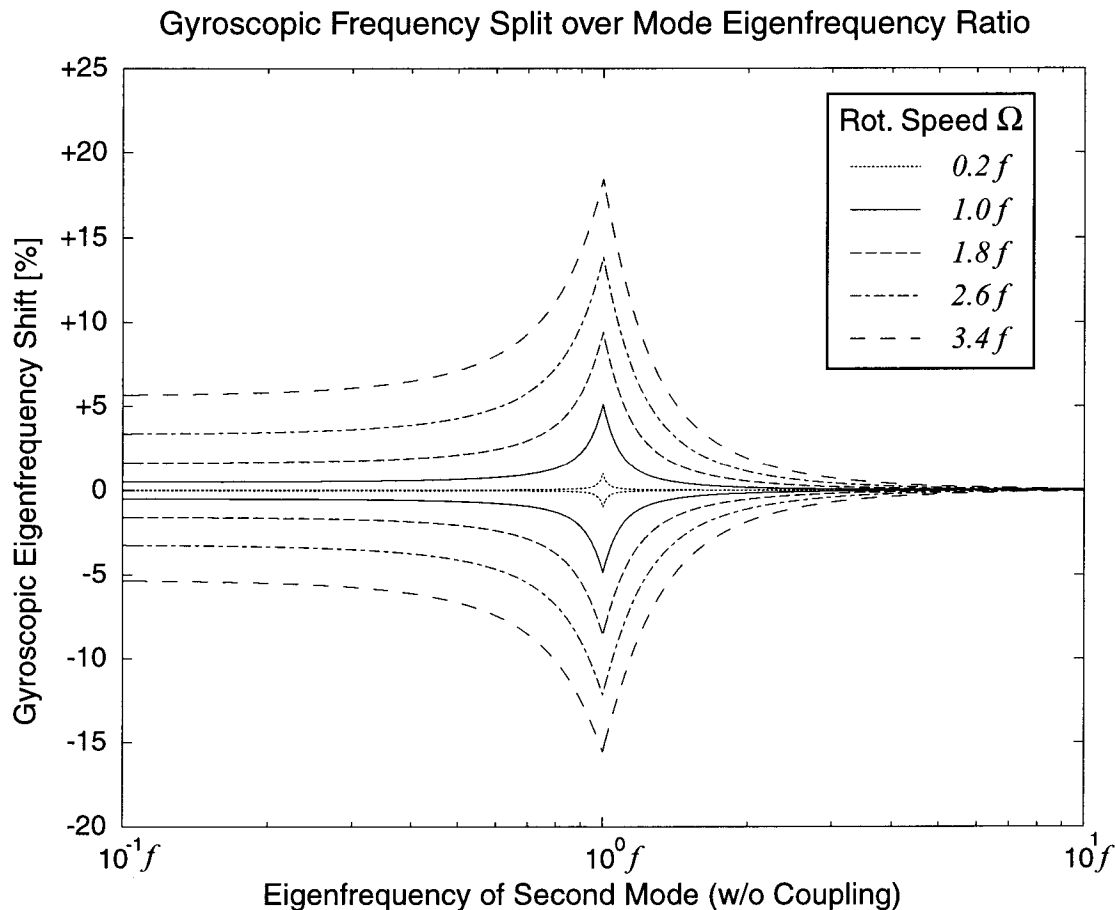
Figure 4.6: *Eigenfrequency shift due to a gyroscopic term $\Omega \cdot g$ coupling two otherwise decoupled, undamped flexible modes of the x-plane and the y-plane. One of the modes has eigenfrequency f, the other one an eigenfrequency from $0.1f$ to $10f$. The slower mode is always decelerated by the gyroscopic coupling (lower half of plot), the faster one is accelerated (upper half). For all rotational speeds Ω, the coupling effect is strongest when – before introduction of the coupling term – the two modes have equal eigenfrequencies. This plot is valid for all f. The situation for a typical value of $g=0.1$ is shown here. The situation for different g can be directly assessed from the plot as scaling of g is equivalent to scaling of Ω, see Equation (4.38).*

about the same order of magnitude. Physically this can be explained by changing mode shapes that the coarse 6–entry–G model does not reproduce properly.

Following the argument from above, one of the reasons for these errors is that due to the shift in eigenfrequencies, the difference of eigenfrequencies of *adjacent* modes becomes so small that their cross coupling can no longer be neglected. The third (dotted) plot in Figure 4.8 shows that the

Figure 4.7: *System with full gyroscopic matrix (solid) and model with reduced gyroscopic matrix (6 entries coupling identical modes, dash–dotted) at medium speed (7'500rpm). Hardly any difference can be made out between the systems.*

discrepancies can be significantly reduced when these coupling terms are introduced in the matrix $\tilde{G}$ (the enlargements have only been scaled in horizontal direction, no vertical scaling has been applied). This improvement can be achieved by determining only $k = (r - 4)/2$ (in the example $r = 10$, i.e. $k = 3$) additional coefficients.

The above analysis is based on a transfer function *within one single plane* of the two–plane model. While the system as assembled up to now matches the reference system well for these transfer functions, the situation is different for transfer functions *between planes*. In Figure 4.9 it can be seen that the match of these transfer functions is still very bad. In particular the 180 degree phase error in the low frequency range is not tolerable. This discrepancy is due to the fact that up to now only gyroscopic effects of flexible modes have been considered while nothing has been said about the gyroscopic coefficients associated to the rigid body modes.

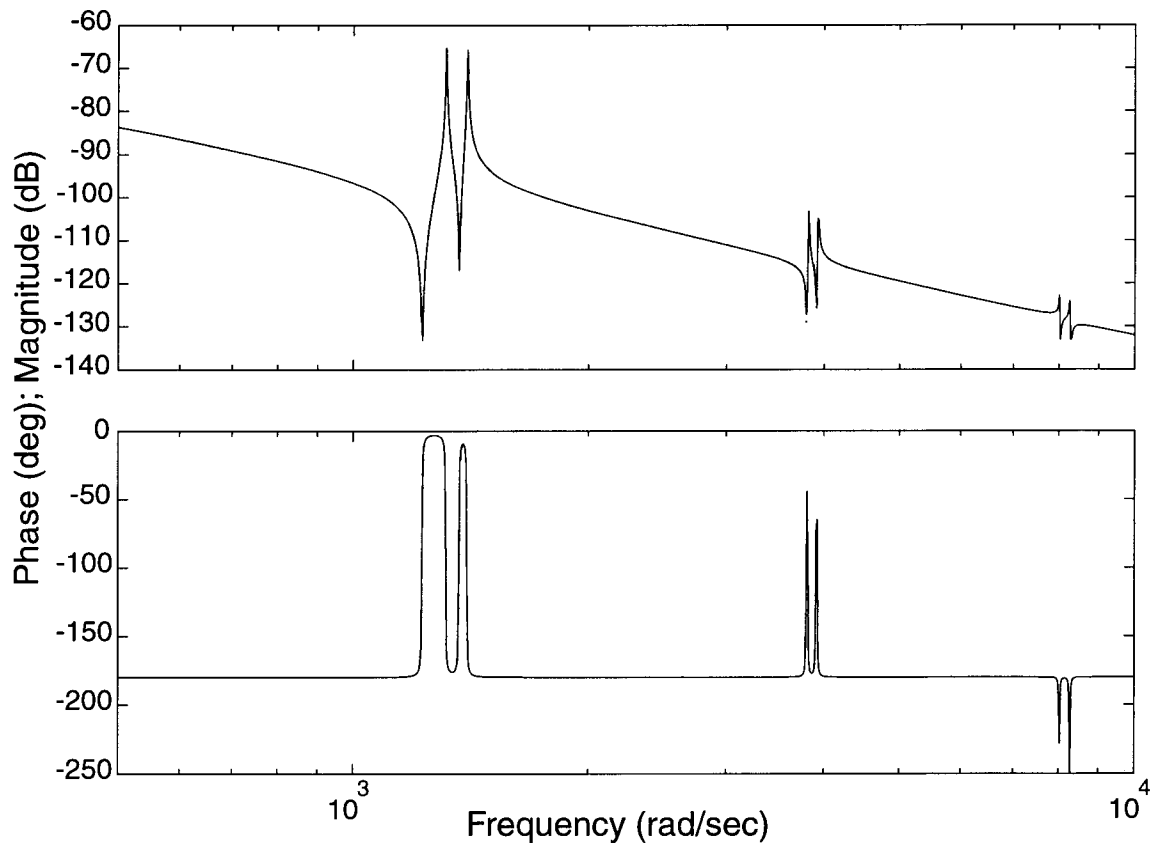In the modal problem formulation, the rigid body coupling of the two
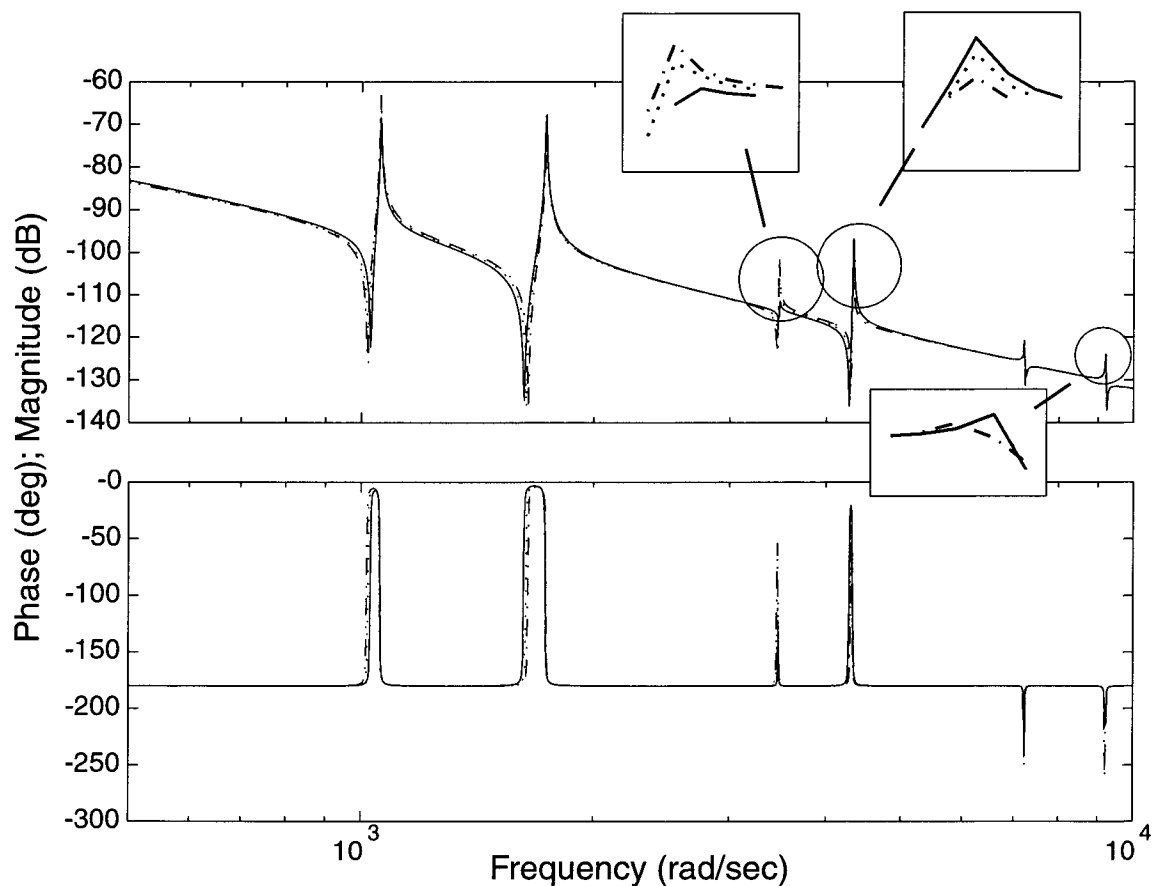
Figure 4.8: *System with full gyroscopic matrix (solid) and model with reduced gyroscopic matrix (6 entries coupling identical modes, dash-dotted) at high speed (60'000rpm). Additionally, the model with coupling between adjacent modes is shown (dotted).*

planes for each mode and the coupling of the two modes among each other are described by totally 3 coefficients of the gyroscopic matrix G. Introduction of these three coefficients mentioned in $\tilde{G}$ above fixes this problem and yields a good match also of the transfer functions between planes, see Figure 4.9. It turns out that the introduction of the rigid body elements has virtually no effect on the flexible modes of the system.

4.3.3   Identification Algorithm

Based on the above observations, the following identification algorithm can be formulated. Figure 4.10 shows the coefficients to be identified for the case $r=12$, i.e. for a system with four pairs of two flexible modes in addition to the rigid body modes.
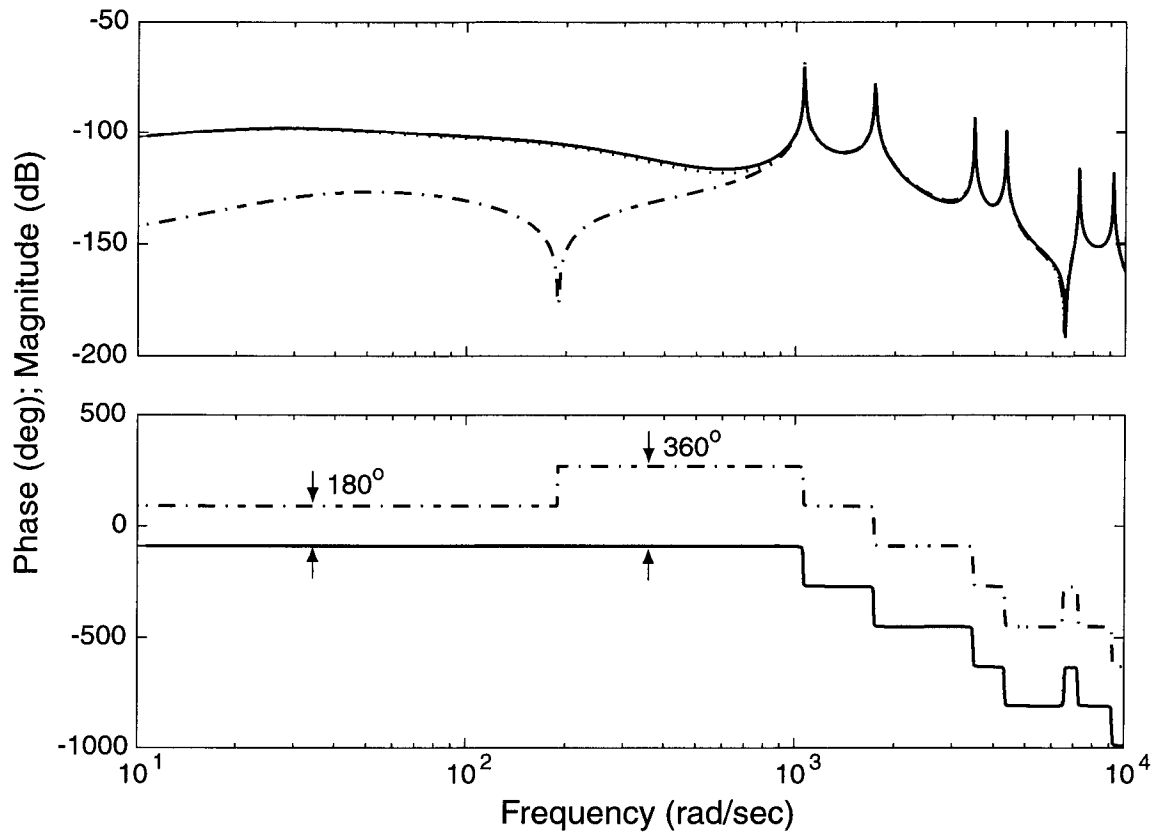
Figure 4.9: *Cross-plane transfer function at high speed (60'000rpm). Model with full gyroscopic matrix (solid), model with terms for flexible modes (same as in the last Figure, dash-dotted), and system with additional rigid body gyroscopic terms (dotted).*

Input:

- Model of AMB system at standstill in modal form, e.g. from the identification procedure for flexible rotor AMB systems presented in Chapter 4.2.

- Measured flexible poles (peak frequencies) of the rotating system, measured at one particular rotational speed.

- Vibration amplitudes at the peak frequencies in one plane.

- Rotational speed of the system during the measurements.

- Amplitude of the cross coupling transfer functions (i.e. from the x-plane to the y-plane) at a few frequencies below the first flexible mode.

Figure 4.10: *Coefficients being identified by the identification algorithm. The different shades of grey indicate represent different steps of the algorihm. Dark grey/f_i: coefficients directly related to flexible mode pairs (one per pair). Medium grey/r_i: the three coefficients related to the rigid body modes. Light grey/c_i: off–diagonal block entries coupling (mainly the forward and backward) modes of adjacent mode pairs. The other matrix entries have no significant effect on the transfer functions of the rotating rotor and are set to zero. (The case $r=12$ is shown here.)*

Procedure:

1. Based on the measured pole locations, adjust the coefficients associated with the $(r\text{-}4)/2$ flexible mode pairs such that the pole locations of the model match the measured ones as well as possible. Because there is no cross coupling at this stage, this can be done sequentially, yielding $(r\text{-}4)/2$ optimization problems in one single variable.

2. Using the amplitude information of the flexible poles, determine the $(r\text{-}4)/2$ coupling terms c_i between adjacent modes such that the model amplitudes of each pair of adjacent backward and forward modes match the measured ones as well as possible. This yields another $(r\text{-}4)/2$ one dimensional optimization problems.

3. Based on the transfer function measurements of the cross coupling transfer function, determine the 3 matrix coefficients r_1, r_2 and r_3

associated to the rigid body modes that achieve an optimal fit of the measurements and the model for the cross coupling functions. This is done at once (one single optimization problem with 3 unknowns).

4.3.4 Simulation Results

To test its feasibility, the above procedure has been applied to a system obtained from an FE model. In a first step, input data for the algorithm has been obtained from simulations based on this model at a rotational speed of 5'000rpm. Then, the algorithm has been applied to the FE model with a zero gyroscopic matrix, generating an estimated gyroscopic matrix. The transfer functions of the systems based on the true and estimated gyroscopic matrices are depicted in Figure 4.11. The comparison shows that the two curves can hardly be distinguished.

For the purposes pursued in this work, it is not enough to obtain a gyroscopic matrix that describes the system behaviour at the measurement speed. In order to design controllers for higher rotational speeds, it is of great importance that the identified gyroscopic matrix can be used for *prediction* of the system behaviour at different (typically higher) rotational speeds. To verify this, the rotational speed has been set to 60'000rpm on the above two models. The resulting transfer functions are again depicted in Figure 4.11. As can be seen, the match of the transfer functions is still very good although the rotational speed has been increased by a factor of 12. The peak locations are accurate within 1.5% and the amplitudes at the peaks within 0.5dB – merely the second backward mode has an amplitude error of 2dB.

These results are even *considerably better* than those from the analysis based on the system with a gyroscopic matrix that contained elements from the full gyroscopic matrix. This can be explained by the optimization actually compensating for the missing matrix elements and finding a better gyroscopic matrix than given by the original matrix with some elements deleted.

Based on these excellent results, the new identification procedure can be stated to capture the relevant aspects of the system's gyroscopic behaviour. The identified model can be used for precise analysis and prediction of the model behaviour at higher rotational speeds.

The above results have been based on noise–free data. To assess the algorithm's potential for application to real problems, the analysis has been repeated with noisy data on the system rotating with 5'000rpm and
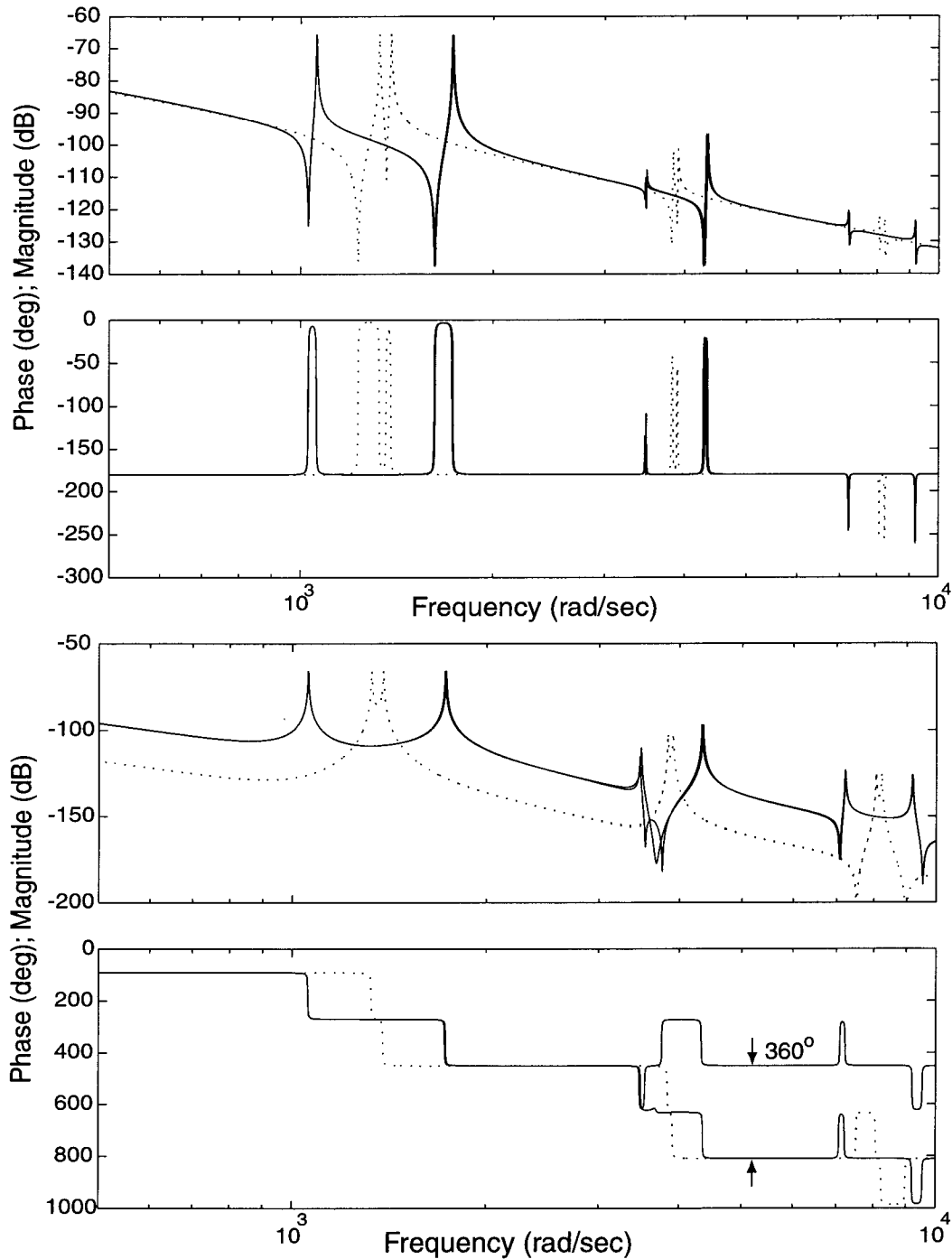
Figure 4.11: *In-plane (top) and cross-plane (bottom) transfer functions of one bearing. True system and identified system at 5'000rpm (dotted) and — based on this — predicted behaviour at 60'000rpm (solid). The dotted systems coincide almost perfectly, the solid ones have slight differences (less than one percent in pole location, less than 2dB in amplitude at the flexible poles) up to a clearly visible deviation in the cross-plane function at the zeros of the second mode.*

30'000rpm. To assume realistic conditions, the peak frequencies have been disturbed by 0.5%. For the amplitude at the peaks that is difficult to measure accurately [Gähler98], an error of 20% has been introduced. For the amplitudes in the low frequency range, an error of 10% has been considered.

The cross–plane frequency response function of the system identified based on this data is shown in the top part of Figure 4.12 (The in–plane transfer function is not shown because for this function the results have been found to be considerably better than those displayed here). As was to be expected, the results no longer match the true system accurately. However, the fit is still good, with the peak frequencies accurate to 1% and the amplitudes accurate to 1dB.

In the next step, the rotational speed was again increased on the models, this time by a factor of two (to 10'000rpm, and 60'000rpm, respectively) in order to analyze the suitability of the identified model for prediction of the system behaviour at higher speeds. The results are shown in the lower part of Figure 4.12. Again, the deviations became larger. Nevertheless the accuracy achieved is in the range of 2% / 2dB for the critical flexible modes.

As deviations of this size can easily be covered with the uncertainty modeling techniques that have been presented in Chapter 3.1, these results justify an optimistic prognosis for applicability of the algorithm to real world problems.

Finally, it is worth noting that recursive application of the algorithm does virtually not at all change the resulting gyroscopic matrix. This legitimates the identification being carried out in three isolated steps and further increases the confidence in the results.

4.3.5 Practical Aspects of Identification

The model obtained from identification is a state space representation of the physical open–loop AMB system. This representation is not unique. In fact, for a given state space system $\mathbf{S}_1 = (A, B, C, D)$ all state space systems of the form $\mathbf{S}_T = (T^{-1}AT, T^{-1}B, CT, D)$ with an invertible real matrix T have the same input–output behavior as the original system. This implies that any physical system that has a state space representation $\mathbf{S}_1$ can be equivalently described by means of any other state space system $\mathbf{S}_T$ given above. Due to this input–output equivalence, identification, being based on measurements of the system's input–output behavior, can not be
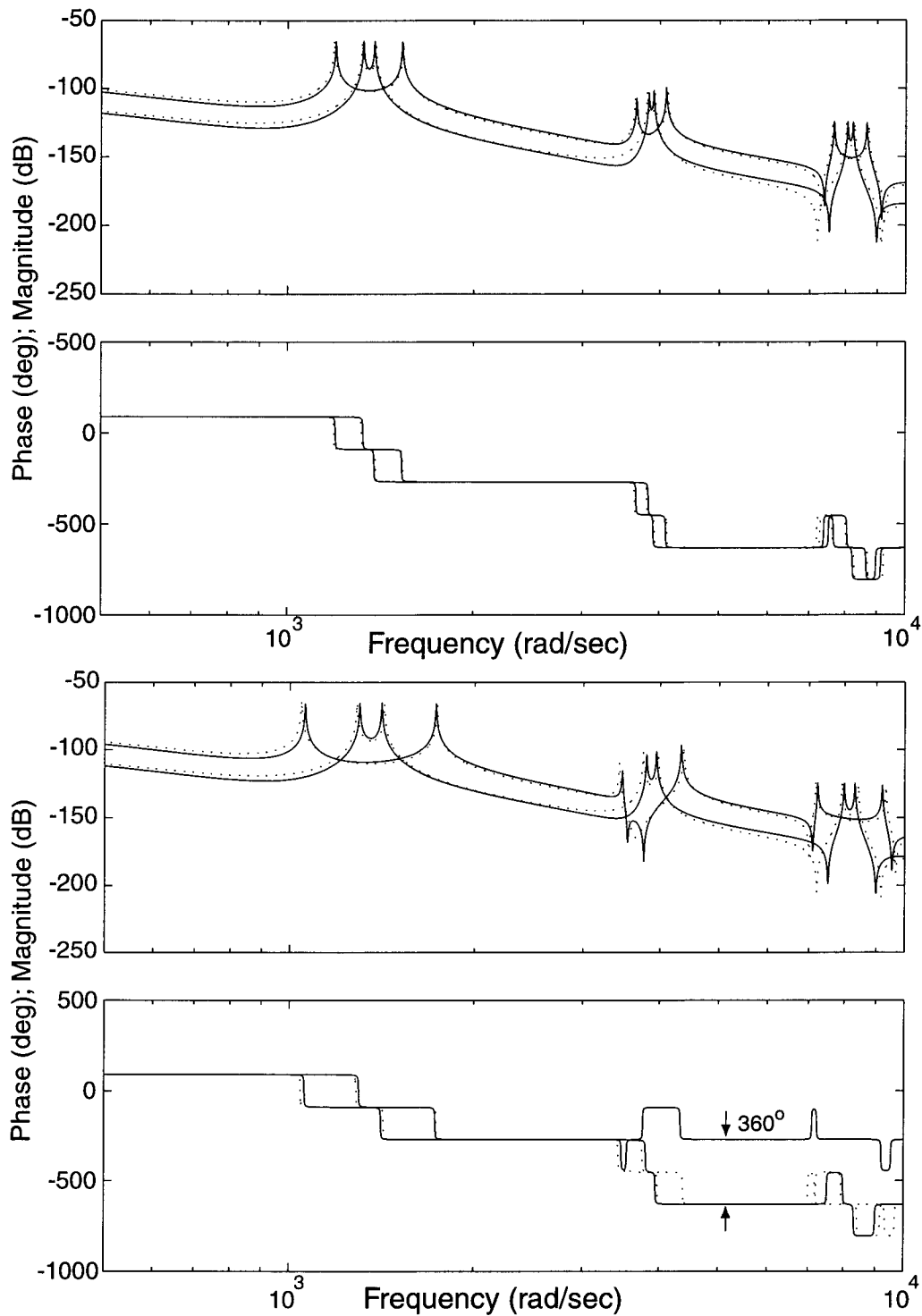
Figure 4.12: *Cross–plane transfer function of one bearing, with noisy data. Top: identified systems (dotted) and models (solid) at 5'000 and 30'000rpm. Bottom: The same models with doubled rotational speed. The poles for the prediction are accurate within 2% and the peaks match within 2dB.*

expected to yield 'the' state space description, but merely one description out of many, unless a priori information on the matrices' structure is used in the identification procedure.

In the algorithm used for identification of the flexible rotor, such information *is* used, ensuring that the resulting state space system's A matrix is of the form from Equation (4.36). This condition on the matrix structure reduces the number of state space systems that can result from identification. However, the identification result is still not rendered unique:

For any state space system (A,B,C,D) with an A matrix as given in Equation (4.36), the transformed system $(T^{-1}AT, T^{-1}B, CT, D)$ is of identical form if the matrix T fulfills the following condition:

$$T = diag(T_1, T_1) \quad \text{with} \quad T_1 = diag(t_1, t_2, ..t_q), t_i \in \mathbb{R}\backslash 0. \qquad (4.39)$$

This statement can be slightly refined. If one considers that the full system has two identical planes and that its states are ordered in pairs of two such that identical states from different planes are adjacent to each other (see Equation (4.37)), the set of possible similarity transformations for the two plane system is restricted to matrices $\tilde{T}$ of the form

$$\tilde{T} = diag(\tilde{T}_1, \tilde{T}_1) \quad \text{with} \quad \tilde{T}_1 = diag(t_1, t_1, t_3, t_3, .., t_{2q-1}, t_{2q-1}), t_i \in \mathbb{R}\backslash 0.$$
$$(4.40)$$

However, this still does not yield a unique model description[3]. This has important consequences for the adaptation of model stiffness and identification of the gyroscopic matrix G, as will be described in the following.

Consequences for Identification of G

In Equation (4.40) transformation matrices $\tilde{T}$ have been characterized for which the A matrix of the state space representation of the identified two–plane flexible rotor model (without gyroscopic effects) remains invariant. However, the system *with* gyroscopic effects (the gyroscopic matrix $-G \cdot \Omega$ being added to the lower right block of the A matrix), *is* affected by

---

[3]In a simpler form, this problem is already encountered when considering the 1-dof system $\ddot{x} + \frac{k}{m}x = 0$. Identification yields the fraction $\frac{k}{m}$, but neither k nor m. Although this makes no difference in terms of finding solutions to the equation, identification does not allow to fully restore the original technical problem – the physical system parameters may be 1N/m and 1g or 1000N/m and 1kg.

similarity transformation with $\tilde{T}$ – its columns are multiplied by t_i and its rows by $1/t_i$.

This implies that for almost all state space descriptions of the system, the gyroscopic matrix G to be identified is *not skew-symmetric* but of the more general structure

$$\tilde{T}_1^{-1} G \tilde{T}_1 = \begin{bmatrix} G_{1,1} & \frac{t_3}{t_1} G_{1,2} & & \\ \frac{t_1}{t_3} G_{2,1} & G_{2,2} & \frac{t_5}{t_3} G_{2,3} & \\ & \frac{t_3}{t_5} G_{3,2} & \ddots & \ddots \\ & & \ddots & G_{q,q} \end{bmatrix} \tag{4.41}$$

where the $G_{i,j}$ are 2×2 blocks with $G_{j,i} = -G_{i,j}^T$ as shown in Figure 4.5 and the t_i are the scalar diagonal entries of the matrix $\tilde{T}_1$ given in Equation (4.40).

Unlike in the case of system transformation discussed above, there is no simple workaround for this situation. The only remedy lies in introducing an additional optimization parameter for each pair of two columns that tries to identify the scalar values t_i.

It should be noted however, that the problem described above only occurs in connection with *identified* flexible rotor models. Models computed by a Finite Element software package are not subject to unknown similarity transformations. As a consequence, the identification algorithm can be applied in its original form in case such a model is provided.

The problem also disappears for identified systems with collocation. For these systems, it is known that the B and C matrices are equal in the physical representation, which allows to extract the scaling parameters t_i from the identified model.

4.4   Summary

In this chapter, identification of AMB systems with known bearing properties and unknown rotors has been discussed.

In the first section identification of the rotor's rigid body dynamics in the absence of any stabilizing controller has been addressed. The identification problem has been formalized as a problem to identify three unknown mass coefficients.

A method for successively determining these coefficients has been developed. The approach chosen is based on current step experiments during which the rotor's motion is measured. Assuming linear model behavior, two of the mass coefficients are determined from pole values obtained from fitting a hyperbolic cosine function to the step response. The remaining coefficient is computed based on the first two coefficients and a measurement of the rotor mass. For vertical rotor configurations the mass is obtained from current measurements performed on the axial bearing. For horizontal rotors current measurements obtained during single–sided static levitation of the rotor in the two radial bearings are used.

The second section of the chapter deals with identification of flexible rotor models at standstill. An existing method fulfilling this task based on open–loop frequency response measurements has been presented.

In the third section, a new algorithm for identification of the gyroscopic matrix G has been developed. Based on an analysis of the interaction of the modes of the two perpendicular planes, the matrix elements near the diagonal have been identified as those that are mainly responsible for the system changes associated to gyroscopic effects. The influence of the individual coefficients on the system's transfer function has been elaborated. A modular, optimization based procedure for extraction of a matrix having virtually the same effect on the model as the gyroscopic matrix G has been presented. Simulations have been carried out to prove the effectiveness of the algorithm. In particular, the identified gyroscopic model has been shown to be suited for predicting the rotor's gyroscopic behavior at significantly higher speeds than the identification speed. Finally, some practical aspects relevant when applying the algorithm in conjunction with identified rotor models have been discussed.

Chapter 5

Controller Design for AMB Rotor Systems

In the context of this work, controller design for AMB systems consists of two steps. First, a controller to stabilize the 'rigid' rotor (in fact a flexible rotor with unknown flexible modes) must be found based on the identified rigid body model. The only requirement on this controller is to stabilize the rotor at standstill robustly enough to perform the identification of the full model as described in Chapter 4.2. After identification of the flexible model, the second controller design step considering the flexible modes is performed. It is this second controller that is to meet all requirements from practical application of the system.

The present chapter is organized along the lines of this procedure. First, the controller design for rotors with unknown high frequency dynamics is discussed. Like in the chapter on identification of rigid rotor systems, the vertical and horizontal cases will be addressed separately, and again the vertical case will turn out to be easier to handle than that of horizontal rotors.

In the second section, the flexible case is addressed. Based on the robust control concepts from Chapter 3, the uncertainty model and the design setup used are described. An automated procedure being the goal of this thesis, special attention is paid to automation of the controller design algorithms developed in both sections.

5.1   Rotors with Unknown High Frequency Dynamics

The problem addressed in this section is that of lifting a flexible rotor of which only the rigid body dynamics are known. In the following, we will first state requirements that controllers must meet in order to stabilize such systems.

Then, we will develop a robust design framework that is suited for the design of controllers robustly achieving the performance requirements. Special attention is paid to sensible uncertainty modeling and the avoidance of operating the system outside of its linear range of operation. Based on this framework, the characteristics of the resulting closed loop systems are analyzed, and an algorithm automating the design procedure is presented. Finally, practical issues are addressed. While no special adaptations are necessary for vertical rotors, it is shown that due to effects caused by gravity, for horizontal rotors the bearings cannot be made arbitrarily soft. The consequences of this phenomenon are discussed.

The last section of this chapter deals with the issue of how low frequency flexible modes that cannot be stabilized a priori can be handled.

5.1.1   Requirements on Stabilizing Controllers

In this section, conditions for the stability of the plant are formulated. In the context of MIMO systems, the standard tool for stability analysis is the MIMO Nyquist stability criterion. It is based on the determinant of the MIMO open–loop system. However, the determinant makes the argument clumsy and little intuitive. Thus, for sake of clarity, the concept will be explained in a SISO setting. This is justified by the fact that in the vast majority of control applications the AMB system is - due to relatively weak cross coupling of the channels - interpreted as a parallel interconnection of several SISO plants ([Gähler98], [Bleuler84], and many others).

In order to reach the objective of stabilizing the rotor, the controller must not destabilize any of the weakly damped high frequency poles (see Figure 2.8).

To avoid this, the controller must satisfy one of two criteria [Franklin94]. The first one is to actively damp the eigenfrequencies. In the SISO setting, this can be directly translated in requirements on the controller's phase - in the collocated case, positive phase is required in the vicinity of the eigenfrequencies to achieve a damping behaviour of the controller. This

approach is referred to as phase stabilization.

Unfortunately, positive controller phase results in increasing controller gain, and holding the controller phase positive over a wide range of frequencies leads to controllers that fail to comply with actuator limitations and exhibit poor stability and noise rejection behaviours. As the location and number of the flexible eigenfrequencies is unknown, it is not possible to design a controller that can be guaranteed to have adequate phase to damp all flexible modes. Therefore this approach is not suited to solve the stabilization problem encountered here.

The second approach to avoid destabilization is called amplitude stabilization. Here, the idea is to have the controller amplitude decrease early and steeply enough to bring the open–loop gain below one even at the flexible eigenfrequencies and hence to avoid destabilization. This approach is generally feasible for AMB systems, with the only restriction that the controller gain must be large enough near the rigid body poles to stabilize the system. Furthermore, the decrease of amplitude (roll–off) can not be made arbitrarily steep. However, the rigid body poles can be shifted towards low frequencies by decreasing the bearing stiffness, increasing the gap between the rigid body modes and the area where flexible modes can be expected to occur.

Besides the issue of dealing with the unknown high frequency dynamics, it is also of interest that the controller be robust with respect to variations in the rigid body dynamics. Like any experiment based procedure, the identification algorithm for the rigid body model described in Chapter 4.1 is prone to yield approximations of the mass coefficients rather than their exact values, and the controller should be robust with respect to reasonable differences between the nominal system obtained from the identification procedure and the true plant.

In the following, we will describe an approach to the design of controllers with steep roll–off and robustness to variations in rigid body dynamics.

5.1.2 Algorithm for Automated Robust Controller Design

This chapter deals with the design of stabilizing controllers for magnetic bearing systems with unknown high frequency dynamics and uncertainty in the rigid body modes. The objective is to obtain controllers that stabilize the rotor at standstill robustly enough to perform the identification of the

flexible system as described in Chapter 4.2.

As has been already mentioned, a soft support of the rotor is favorable for the intended amplitude stabilization of the plant. Equation (2.9) shows that the key parameter for adjusting the bearing stiffness is the bias current i_0. For the design of a soft controller, the bias current is set to a low value that still allows linear operation of the bearings, e.g. 5 percent of the maximum amplifier current i_{max}. The system with modified force displacement and force–current factors is then transformed to a state space description.

In the next step, the system is normalized by means of scalar scaling factors such that an input amplitude of one represents the maximum amplifier current and an output amplitude of one corresponds to a rotor displacement of the system's air gap (rotor touching the retainer bearings).

Uncertainty Structure

For each plane, the system to be stabilized is that identified in Chapter 4.1, namely

$$
\begin{bmatrix} m_1 & m_3 \\ m_3 & m_2 \end{bmatrix} \begin{bmatrix} \ddot{x}_A \\ \ddot{x}_B \end{bmatrix} = \begin{bmatrix} k_{s,A} & 0 \\ 0 & k_{s,B} \end{bmatrix} \begin{bmatrix} x_A \\ x_B \end{bmatrix} + \begin{bmatrix} k_{i,A} & 0 \\ 0 & k_{i,B} \end{bmatrix} \begin{bmatrix} i_A \\ i_B \end{bmatrix} \tag{5.1}
$$

Due to possible errors in the identification, the mass coefficients m_1, m_2, and m_3 may be imprecise. Typically, the step experiments yield mass estimates for m_1 and m_2 that lie within 20% of the true values. The measurement of the rotor weight, however, can be performed more accurately and it is reasonable to assume a precision of 5% for the weight measurements. Considering that the symmetric structure of the mass matrix should be preserved, this can be appropriately formulated by means of an uncertain mass matrix of the following form:

$$
\tilde{M} = \begin{bmatrix} m_1 & m_3 \\ m_3 & m_2 \end{bmatrix} + \delta_1 \begin{bmatrix} -1 & 1 \\ 1 & -1 \end{bmatrix} + \delta_2 \begin{bmatrix} 1 & 0 \\ 0 & 0 \end{bmatrix} + \delta_3 \begin{bmatrix} 0 & 0 \\ 0 & 1 \end{bmatrix} \tag{5.2}
$$

with $|\delta_1| \leq 0.2 \max(m_1, m_2)$, $|\delta_2| \leq 0.05(m_1 + m_2)$ $|\delta_3| \leq 0.05(m_2 + m_3)$.

In order to simplify the controller design it is sensible to choose an uncertainty model that keeps the number of uncertain parameters to a minimum without making the uncertainty model too coarse.

In the above situation, the model behaviour is dominated by the first part of the uncertainty. The uncertainties associated with δ_2 and δ_3 have only a relatively small effect, but require two additional uncertainty channels. Furthermore, the restrictions on the complementary sensitivity function **T** and the function **CS** imposed in the design will guarantee robustness to additional multiplicative uncertainties. Therefore it has been decided to omit these terms. This simplification reduces controller size and increases the design speed without considerably altering the problem. The resulting simplified uncertainty structure is

$$\tilde{M} = \begin{bmatrix} m_1 & m_3 \\ m_3 & m_2 \end{bmatrix} + \delta_1 \begin{bmatrix} -1 & 1 \\ 1 & -1 \end{bmatrix} \tag{5.3}$$

with $|\delta_1| \leq 0.2 \max(m_1, m_2)$.

Preservation of Model Structure

Furthermore, it must be ensured that the structure of model is not inadvertently changed by the uncertainty. This may happen if several parameters vary at the same time. Concerning the structure of the uncertain mass matrix of Equation (5.1), it is important to preserve its symmetry. However, this is not enough. An analysis of the explicit parameter values furthermore shows that the parameters m_1 and m_2 must always be positive and that the parameter m_3 never can be larger than both m_1 and m_2, see Equation (2.19). These boundary conditions must also be considered in the uncertainty formulation. Otherwise models with very different behaviour (unstable with sharp peaks in the transfer function) and no physical relevance are included in the set of plants the controller has to stabilize. This strongly impairs the performance of the resulting controllers, if stabilizing controllers can be found at all.

This additional restriction imposes a limit on the size of the scalar uncertainty δ_1. Whether or not this limit actually reduces the size of the permissible uncertainty set from Equation (5.3) depends on the parameters m_1, m_2, and m_3. Preservation of structure can easily be checked by analyzing the matrix M for $\delta_1 = 1$, which constitutes the worst case disturbance with respect to the above structural constraint.

If the structure condition imposed by Equation (2.19) is violated, this can easily be compensated for by restricting $|\delta_1|$ to a lower maximum permissible value. However, this clipping procedure may strongly restrict the uncertainty set in *both* directions of positive and negative δ_1 while the

structure constraint always only restricts δ_1 from becoming too positive. This holds the risk of eliminating a large and important part of the uncertainty set that may include the real system. To avoid this, the following procedure is proposed for cases where the uncertainty set from Equation (5.3) contains undesired models:

Let the original bound on δ_1, $0.2 \cdot \max(m_1, m_2)$, be represented by b and assume that the structure problem occurs for the first time at $\delta_1 = w$ ($w < b$). Assume for simplicity of notation that it is m_1 which causes the problem. One can then calculate new mass coefficients $\tilde{m}_1$, $\tilde{m}_2$, and $\tilde{m}_3$ and a new uncertainty limit $\tilde{b}$ such that the uncertainty is unrestricted in direction of negative δ_1 and the structure problem mentioned above is avoided.

The condition that the same uncertainty is to be covered in direction of negative δ can be expressed by the equation

$$\tilde{m}_1 + \tilde{b} = m_1 + b. \tag{5.4}$$

The fact that the limit of structural defectiveness is just barely to be touched is expressed by

$$\tilde{m1} - \tilde{b} = m_1 - b_1 = m_3 + b = \frac{m_1 + m_3}{2}. \tag{5.5}$$

From these two equations and the additional constraint that the row sum of the mass matrix (i.e. the weight distribution on the bearings) is to remain constant, a new nominal mass matrix with coefficients

$$
\begin{aligned}
\tilde{m}_1 &= \frac{3}{4}m_1 + \frac{1}{2}b + \frac{1}{4}m_3, \\
\tilde{m}_2 &= m_2 - \frac{1}{4}m_1 + \frac{1}{2}b + \frac{1}{4}m_3 \\
\tilde{m}_3 &= \frac{1}{4}m_1 - \frac{1}{2}b + \frac{3}{4}m_3
\end{aligned}
\tag{5.6}
$$

can be derived. This mass matrix then has the same row sum (i.e. weight distribution on the bearings) as the original one. With the new uncertainty limit

$$\tilde{b} = \tilde{m}_1 - \frac{m_1 + m_3}{2} \tag{5.7}$$

on δ_1, a new model for the uncertain mass matrix

$$\tilde{M} = \begin{bmatrix} \tilde{m}_1 & \tilde{m}_3 \\ \tilde{m}_3 & \tilde{m}_2 \end{bmatrix} + \delta_1 \begin{bmatrix} -1 & 1 \\ 1 & -1 \end{bmatrix} \tag{5.8}$$

with $|\delta_1| \leq \tilde{b}$ is obtained. The left matrix replaces the mass matrix from Equation (5.1).

This new uncertainty set fully covers the original uncertainty in the feasible direction while ending just at the barrier where the structure constraints are violated.

Model with Uncertainty

In this section, the uncertainty defined above is added to the nominal system as follows. With $\tilde{M}$ from above and K_s, and K_i denoting the stiffness matrices of Equation (5.1) from left to right, the system from Equation (5.1) without uncertainty has the following state space description:

$$\left[\begin{array}{c|c} A & B \\ \hline C & D \end{array}\right] = \left[\begin{array}{c|c} \begin{bmatrix} 0 & I \\ -\tilde{M}^{-1}K_s & 0 \end{bmatrix} & \begin{bmatrix} 0 \\ \tilde{M}^{-1}K_i \end{bmatrix} \\ \hline \begin{bmatrix} I & 0 \end{bmatrix} & [0] \end{array}\right] =: \mathbf{G}. \tag{5.9}$$

Additive uncertainty on the nominal mass matrix M can be added to the model by adding inputs and outputs to the system as follows

$$\left[\begin{array}{c|c} A & B \\ \hline C & D \end{array}\right] = \left[\begin{array}{c|c} \begin{bmatrix} 0 & I \\ -\tilde{M}^{-1}K_s & 0 \\ -\tilde{M}^{-1}K_s & 0 \\ I & 0 \end{bmatrix} & \begin{bmatrix} 0 & 0 \\ -\tilde{M}^{-1} & \tilde{M}^{-1}K_i \\ -\tilde{M}^{-1} & \tilde{M}^{-1}K_i \\ 0 & 0 \end{bmatrix} \end{array}\right] =: \tilde{\mathbf{G}}, \tag{5.10}$$

and by closing the loop with the uncertainty between the first input and output as follows:
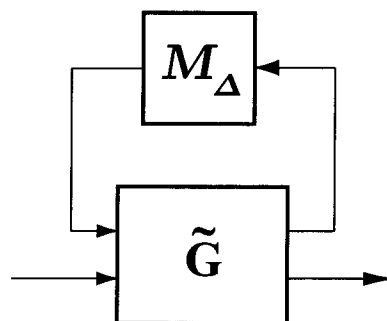
This system has the same inputs and outputs as the nominal system from Equation (5.9), but a modified mass matrix $M + M_\Delta$ (the uncertainty is

parametric here since M_Δ is a matrix, not a dynamical system).
In our example, M_Δ is equal to the uncertainty model derived above, i.e.

$$M_\Delta = \delta_1 \begin{bmatrix} 1 & -1 \\ -1 & 1 \end{bmatrix}. \qquad (5.11)$$

By means of singular value decomposition, the above uncertainty can be decomposed into

$$M_\Delta = \begin{bmatrix} 1 \\ -1 \end{bmatrix} \delta_1 \begin{bmatrix} 1 & -1 \end{bmatrix}. \qquad (5.12)$$

By pulling the outer matrices from the uncertainty into the matrices B and C of the system from Equation (5.10), the size of the uncertainty can be reduced to one, yielding an uncertain system
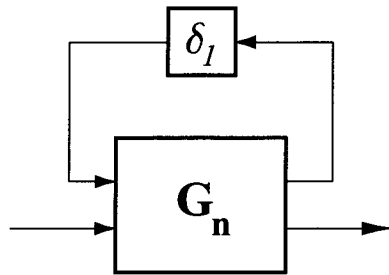
with $\delta_1 \in \mathbb{R}$. This system is the basis for all following considerations.

Design Framework

The next step after having defined the uncertainty model consists in defining an appropriate design framework that forces the controller to achieve the desired performance goals. In the present case, the performance goals are the following:

- The most important goal is to achieve a steep roll–off of the controller. This is enforced by adding a suitable additive uncertainty to the system, yielding minimization of **CS**.

- Since the objective of levitating the rotor is to identify its flexible dynamics by the method described in Chapter 4.2, it is important to ensure that a reasonable signal/displacement ratio is maintained during the measurement of the frequency response functions. As has
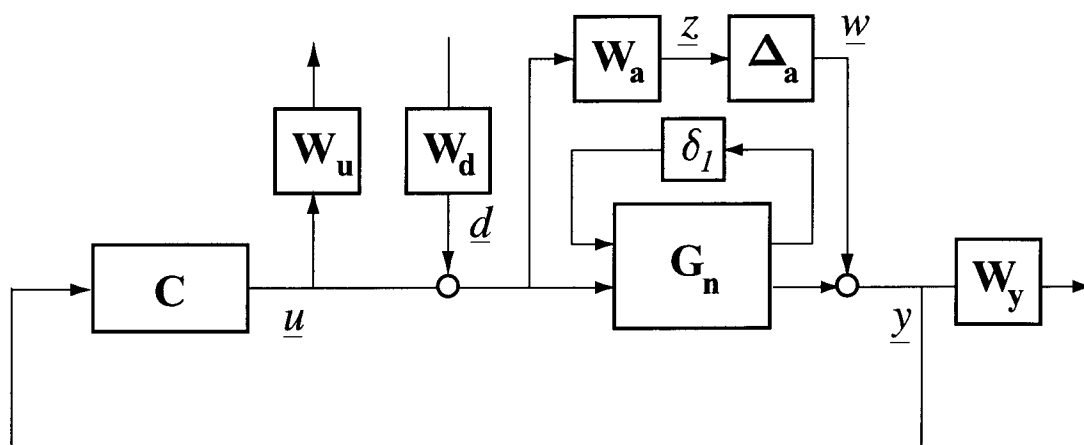
Figure 5.1: *Framework for 'rigid' rotor controller design*

been shown in Chapter 4.2, the AMB system's open–loop FRF will be determined by excitation at the system input and displacement measurement at the system output.

During the experiment, the displacements occurring at the system output must remain limited. Theoretically, this could be simply achieved by making the excitation signals arbitrarily small. However, this is technically not feasible. For the amplifiers to produce accurate excitation signals, the excitation must have a certain minimum amplitude. Furthermore the signal amplitude must be sufficiently much larger than the noise level. Therefore it is necessary to limit the transfer function from the disturbance input $\underline{d}$ to the system output $\underline{y}$, **SG**.

- A third restriction is imposed by the fact that we are intending to identify a linear rotor model without explicit consideration of the nonlinear actuator characteristics, see Chapter 2.1.3. Therefore it is indispensable to avoid critically large set currents that would drive the amplifiers into saturation. To this end, the transfer function $\mathbf{T}_i$ from the disturbance input $\underline{d}$ to the control signal $\underline{u}$ must be limited.

The design framework resulting from these considerations is shown in Figure 5.1.

Overall, this is a **CS/SG/T** design framework. From the figure, the corresponding standard control configuration can be directly shown to be

$$
\begin{bmatrix} 1 & & & \\ & \mathbf{W_a} & 0 & \\ & & \mathbf{W_y} & \\ & 0 & \mathbf{W_u} & \\ & & & I \end{bmatrix}
\begin{bmatrix} 1 & 0 & 0 & 0 \\ 0 & 0 & I & 0 \\ 0 & I & 0 & 0 \\ 0 & 0 & 0 & 1 \\ 0 & I & 0 & 0 \end{bmatrix}
\begin{bmatrix} \mathbf{G}_n & 0 & 0 \\ & I & 0 \\ 0 & I & 0 & 0 \\ 0 & 0 & 0 & I \end{bmatrix}
\begin{bmatrix} 1 & 0 & 0 & 0 \\ 0 & 0 & I & I \\ 0 & I & 0 & 0 \\ 0 & 0 & 0 & I \end{bmatrix}
\begin{bmatrix} 1 & & 0 \\ & I & \\ & \mathbf{W_d} & \\ 0 & & I \end{bmatrix}
$$

$$(5.13)$$

and the corresponding delta structure for the design is

$$
\begin{bmatrix} \delta_1 & \mathbf{0} & \mathbf{0} \\ \mathbf{0} & \mathbf{\Delta_1} & \mathbf{0} \\ \mathbf{0} & \mathbf{0} & \mathbf{\Delta_2} \end{bmatrix}
$$

with uncertainty related delta blocks $\delta_1 \in \mathbb{R}$ and $\Delta_1 \in \mathbb{C}^{2\times 2}$, and a performance block $\Delta_2 \in \mathbb{C}^{2\times 4}$.

Weighting Function Selection

The weighting functions in the above framework are chosen as follows:

1. The input disturbance is to represent the excitation of the system for FRF measurement. Typical excitation amplitudes are about 2% of the maximum current. Therefore, the input weight $\mathbf{W_d}$ is chosen as a constant 0.02.

2. To remain within the linear operating range of the sensors and actuators, the rotor displacement should not exceed 10% of the air gap. This yields a constant value of 10 for the output weight $\mathbf{W_y}$.

3. For the additive uncertainty, the weight $\mathbf{W_a}$ is chosen such that the uncertainty is small up to a corner frequency ω_c and then rises sharply up to a second corner frequency, ω_a, from which on it is constant and covers any flexible modes, see Figure 5.2.
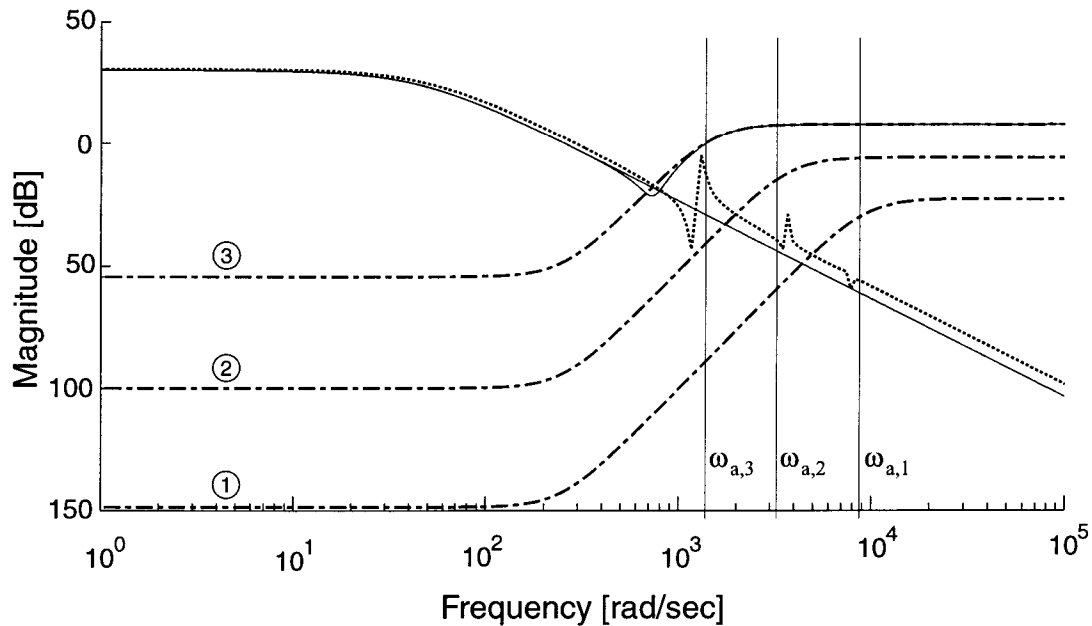
Figure 5.2: *Additive uncertainties of different sizes yielding stabilization of one, two, and three flexible modes of the true system (dotted). Weighting functions are drawn dash-dotted, the rigid system model without uncertainty solid.*

4. The output weighting function $\mathbf{W_u}$ is selected depending on the bias currents along the guidelines that have been developed in Chapter 2.1.3. The case when the amplifier transfer function is to be included requires only minor adaptations of the scheme. In cases when the amplifier model consists of two weighting functions, these are stacked and then treated as one weighting function in the design. For the sake of simple notation, the (typical) case where the amplifier behavior can be described by a single weighting function is described throughout this chapter. Figure 5.3 shows the case where the bandwidth of the amplifier's internal transfer function is large and only the limitations imposed by the R-L curve must be considered.

Being parametric, the uncertainty on the rigid body model does not require any weighting functions.

Control System Analysis

The above framework has two free parameters. These are the bias current i_0 and the exact choice of the weighting function $\mathbf{W_a}$. Independent
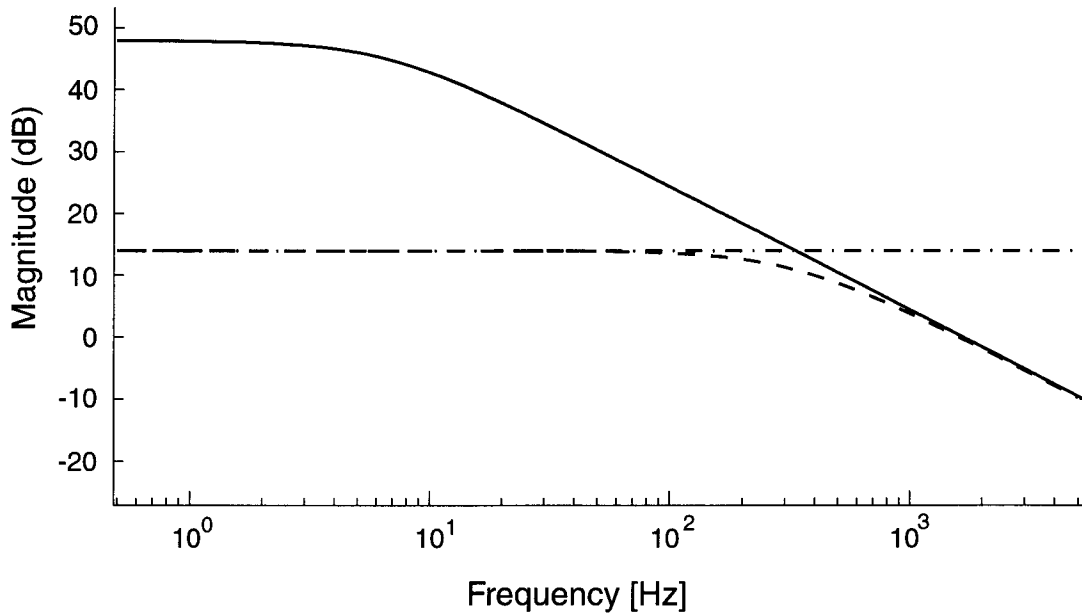
Figure 5.3: *R-L curve of amplifier (solid), set current limit i_0 (dash-dotted), and (dashed) first order approximation $\mathbf{W_u}^{-1}$ (schematically, for one channel)*

from how these parameters are chosen, application of D–K iteration to the system above always yields closed loop systems with a sensitivity function that qualitatively looks like the one shown in Figure 5.4. This function is characterized by three frequency ranges, that result from the design framework chosen above:

At low frequencies (up to ω_1), the sensitivity function is small. This is due to the output weight $\mathbf{W_y}$ which imposes a limit on the transfer function $\mathbf{SG}$. Since $\mathbf{G}$ is fixed and particularly large at low frequencies (due to the small pole values caused by the low bias current), the objective is achieved by adequate adaptation of $\mathbf{S}$.

At high frequencies (above ω_2), the sensitivity function is one. This is generally the case, but is enforced to happen early in the above framework due to the additive uncertainty which imposes a limit on the transfer function $\mathbf{CS}$ in the area of high frequencies.

Between these two areas, a transition area in which the relevant restriction changes from $\mathbf{SG}$ to $\mathbf{CS}$ can be found. In this area, the sensitivity function must be larger than one due to the waterbed effect described by the bode sensitivity integral presented in Chapter 3.2.2
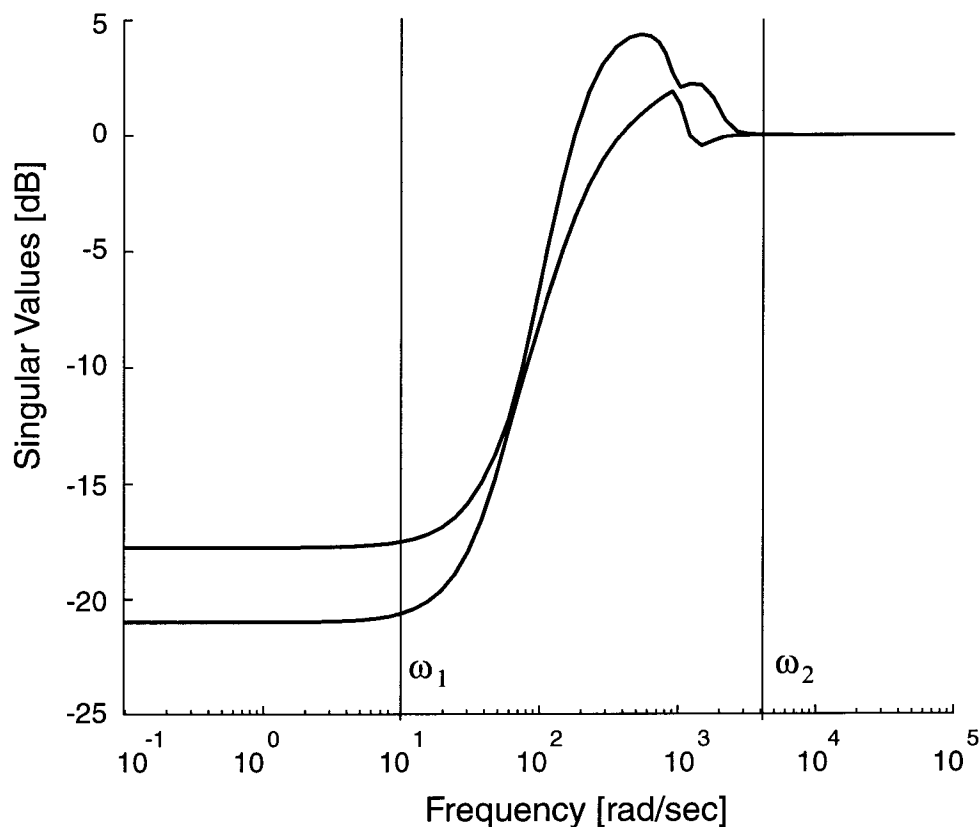
Figure 5.4: *Typical sensitivity function of rigid rotor closed loop system*

In this situation, adaptation of the two free parameters, i_0 and $\mathbf{W_a}$ now has the following effects.

- Large corner frequencies of $\mathbf{W_a}$ imply a restriction to high frequency additive uncertainties. This leads to large values of ω_2 and a wide transition area with a wide, low peak (e.g. 3dB) of the sensitivity function. With increasing corner frequency ω_c of $\mathbf{W_a}$, smaller μ values can be achieved.

- Small values of the corner frequency will bring down ω_2 and lead to a narrow transition area with a rather high peak of the sensitivity function. As the corner frequency is lowered, the μ value successively increases. This complies with engineering intuition — no system can handle arbitrary amounts of uncertainty.

- Large values of i_0 will bring large unstable pole values, which due to the waterbed effect increases the height and/or width of the sensitivity function's peak. Furthermore, the starting frequency of the transition area will be increased, since the controller gain must re-

main large up to higher frequencies in order to stabilize the system. As a result, large μ values are obtained when i_0 is increased too far.

- Very small values of i_0 will bring two types of restrictions: The small pole values lead to a very large steady-state gain of the plant, which due to the limit on **SG** imposes hard restrictions on the allowable size of the sensitivity function **S** at low frequencies. Furthermore, with decreasing i_0, the set currents up to which the system can be considered linear is decreased, see Chapter 2.1.3. In the limit case where $i_0 = 0$, the rigid body poles of the system are at the origin, yielding a limit stable system with infinite static gain and 0 set current available to stabilize it. This shows that if i_0 is made too small, the system becomes more and more difficult to control, which finds its expression in increasing μ values.

In short, the above results can be summarized as follows. While the μ values resulting from the design increase with increasing uncertainty (decreasing ω_c), the curve describing the dependence of μ on the bias current i_0 looks like a bathtub: large values are attained for both small and large bias currents, and a minimum can be found somewhere in the middle. The above discussion strongly suggests that this function is convex. Convexity implies uniqueness of the minimum.

Automated Controller Design Procedure

Based on the above, the following algorithm can be formulated for solving the rigid rotor controller design problem:

1. Starting with a low value for i_0 and a large value for the corner frequency ω_a of $\mathbf{W_a}$, calculate the achievable μ. Increase i_0 until a reasonable value for μ (e.g. 0.9) is achieved.

2. Decrease ω_a until μ reaches 1.

3. Find the bias current i_0 that minimizes the μ value. If the minimum is sufficiently low, go to step 2, otherwise end the iteration

The condition in step 1 can be fulfilled for any reasonable rotor-bearing configuration for sufficiently large i_0.

The above algorithm has been implemented in MATLAB. Each of the steps involves iterative application of D–K iteration (see Chapter 3.3.4). Due to

the restrictions of this method, it makes no sense to directly compare μ values. Therefore, a threshold up to which similar μ values are considered equal has been introduced. Furthermore, a minimum current step has been defined. The uncertainty weight $\mathbf{W_a}$ is scaled such that it exceeds the rigid body model by about 25dB at the corner frequency ω_a, allowing for flexible modes from about this frequency on (see Figure 5.2). Whenever the value of i_0 is changed, a new weighting function $\mathbf{W_u}$ reflecting the new actuator limitations is automatically computed. The algorithm typically finds a solution to the above problem close to the optimal one within one to three iterations, taking about 5 to 10 minutes of computation time on a PIII-500 PC.

5.1.3 Controller Design for AMB Systems with Vertical Rotor

In the case of vertical suspension of the rotor, the weight of the rotor is fully supported by the axial bearing. The radial bearings are in this case solely required to avoid contact between rotor and stator during the subsequent identification of the flexible system. This can be obtained from application of the above algorithm. The achievable low rigid body modes allow to create a wide gap between the (low) frequency area where large gain is required for stabilization and those frequencies where the flexible modes are expected and low gain is required to achieve amplitude stabilization. This situation is optimal for amplitude stabilization of flexible modes.

5.1.4 Controller Design for AMB Systems with Horizontal Rotor

In the case of a horizontal rotor, the radial bearings do not only have to achieve stable support of the rotor, but in particular must compensate for the rotor weight. This has important consequences that will be elaborated in the following.

Dynamics of the Horizontally Supported Rotor

In the literature on AMB systems, usually no difference is made between horizontal and vertical rotor systems. In the following we will point out that such differences generally exist and that they are significant for soft rotor supports, i.e. in case of low bias current i_0.

In the literature, the standard linear description for all AMB supports, regardless of rotor orientation is that from Chapter 2.1, where the nonlinear equation

$$f = \frac{1}{4}k\left(\frac{(i_0 + i_x)^2}{(s_0 - x)^2} - \frac{(i_0 - i_x)^2}{(s_0 + x)^2}\right) \tag{5.14}$$

with $k = \mu_0 n_c^2 A_c \cos(\alpha_p)$ is linearized to

$$f = k_s x + k_i i_x. \tag{5.15}$$

In the last equation

$$k_i = \left.\frac{\partial}{\partial i_x} f\right|_{x,i_x=0} = k\frac{i_0}{s_0{}^2} \tag{5.16}$$

and

$$k_s = \left.\frac{\partial}{\partial x} f\right|_{x,i_x=0} = k\frac{i_0{}^2}{s_0{}^3}. \tag{5.17}$$

In the horizontal case, any static displacement of the controlled rotor is then compensated by means of an integrator which brings the rotor to the bearing center. This integrator is typically designed to be slow, which is used as a justification to neglect its effects on the dynamics of the support [Gähler98].

However, the integrator causes a constant control current in order to lift the rotor to the bearing center. The size of this current can be calculated from the nonlinear bearing force relation, Equation (5.14), for $x = 0$ and the bearing force F_g required to lift the rotor to the bearing center. This yields

$$F_g = k \cdot \frac{i_0 i_x}{s_0{}^2} \tag{5.18}$$

and as a direct consequence one obtains for the constant control current

$$i_\Delta = i_x = \frac{F_g \cdot s_0{}^2}{k \cdot i_0}. \tag{5.19}$$

It is now instructive to consider this constant bias current explicitly in the linearization of Equation (5.14). This yields:

$$f = \frac{1}{4}k\left(\frac{(i_0 + i_\Delta + \tilde{i}_x)^2}{(s_0 - x)^2} - \frac{(i_0 - i_\Delta - \tilde{i}_x)^2}{(s_0 + x)^2}\right) \tag{5.20}$$

where $\tilde{i}_x = i_x - i_\Delta$. Linearizing again as above we obtain for the force–current factor as before

$$\tilde{k}_i = \left. \frac{\partial}{\partial \tilde{i}_x} f \right|_{x, \tilde{i}_x = 0} = k \cdot \frac{i_0}{s_0^2} \tag{5.21}$$

but for the force–displacement factor surprisingly,

$$\tilde{k}_s = \left. \frac{\partial}{\partial x} f \right|_{x, \tilde{i}_x = 0} = k \frac{(i_0^2 + i_\Delta^2)}{s_0^3} = k_s + k \cdot \frac{i_\Delta^2}{s_0^3}. \tag{5.22}$$

is obtained. The above equation shows that the constant current that is required to lift the rotor to the bearing center has an influence on the stiffness of the bearing. By substituting Equation (5.19) in Equation (5.22) one can express $\tilde{k}_s$ exclusively by bearing parameters. This yields

$$\tilde{k}_s = k_s + \frac{F_g^2 \cdot s_0}{k \cdot i_0^2} \tag{5.23}$$

In addition to the above, the integrator imposes a minimum value on the current passed through the upper bearing half - even if the bias current is set to be very small, a minimum current i_{min} is needed to bring the rotor to the center position. Obviously the current required to support the rotor is minimal if no downward force is exerted by the coils on the lower part of the bearing. As a consequence, the value of i_{min} can be explicitly calculated for a given mass supported by the bearing based on the nonlinear equation for the single sided bearing, see Chapter 2.1.1. Inserting the gravitational force $f = F_g$ for the external force, one obtains

$$i_{min} = 2\sqrt{F_g \frac{s_0^2}{k}} \tag{5.24}$$

Furthermore, linearization of the current force relationship of the single sided bearing, Equation (2.2), directly yields

$$k_{i,S} = \left. \frac{\partial}{\partial \tilde{i}_x} f \right|_{\substack{x = 0 \\ i_x = i_{min} - i_0}} = \frac{k}{2} \cdot \frac{i_{min}}{s_0^2} = \frac{\sqrt{k \cdot F_g}}{s_0}, \tag{5.25}$$

$$k_{s,S} = \left. \frac{\partial}{\partial \tilde{i}_x} f \right|_{\substack{x = 0 \\ i_x = i_{min} - i_0}} = \frac{k}{2} \cdot \frac{i_{min}^2}{s_0^3} = \frac{2F_g}{s_0}. \tag{5.26}$$

Whenever the rotor is held in the bearing center, at least the minimum current i_{min} is constantly applied to the upper half of the bearing.

Figure 5.5: *Force–displacement factor over bias current with (solid) and without (dashed) consideration of integrator effects*

Switching between single sided and double sided operation occurs at $i_0 = i_{min}/2$. For bias currents lower than this value, the control current i_x will be larger than $i_{min}/2$, since the total current through the upper coil must compensate exactly for the rotor weight, $i_x = i_{min} - i_0$. In this case however, the lower coil current is zero, since $i_0 - i_x$ is negative. This amounts to single sided operation of the bearing with $k_i = k_{i,S}$ and $k_s = k_{s,S}$.

If however the bias current i_0 is larger than $i_{min}/2$, the lower coil current will be positive in this static analysis, yielding two sided operation of the bearing with $k_i = \tilde{k}_i$ and $k_s = \tilde{k}_s$. At the corner point itself, i.e. for $i_0 = i_{min}/2$, both the double sided and single sided equations yield

$$k_{s,cp} = \frac{2 \cdot mg}{s_0} \text{ and } k_{i,cp} = \frac{\sqrt{k \cdot mg}}{s_0}. \tag{5.27}$$

The above considerations can be summarized as follows:

- For bearing axes affected by gravity, the magnetic bearing cannot be made arbitrarily soft. Due to gravity compensation, the constant current that is passed through the upper coil cannot fall below a certain limit value, i_{min}. If the bias current i_0 is selected to be smaller

than half of this value, the bearing is operated in single sided mode (with the upper coil active only). Any attempt to decrease the bias current below $i_{min}/2$ is ineffective since the integrators will compensate for this reduction.

As a result, the force–current factor k_i and force displacement factor k_s are choices of bias currents with $i_0 < i_{min}/2$ equal to the values attained for $i_0 = i_{min}/2$. These values,given by Equation (5.27), constitute the achievable minimum values for both k_i and k_s.

The size of these minimum values depends on the rotor mass to be supported by the bearing, the orientation of the system with respect to gravity, the bearing geometry (air gap s_0), and the bearing constant k, i.e. the number of windings n_c, the manet cross section A_c and the angle α (half the pole angle of the electromagnets).

- There exists a corner value for the bias current from which on the bearing stiffness exceeds the minimal single sided stiffness. This corner value, $i_{min}/2$, also depends on the rotor mass m, the air gap s_0, and the bearing constant k. At the switching point, the force–current factor and the force–displacement factor are given by Equation (5.27).

- For values of i_0 larger than $i_{min}/2$, the relation between the bias current and the force–current factor k_i and the force displacement factor k_s are expressed by Equation (5.21) and Equation (5.22), respectively.

  While the value of k_i for this selection of bias current is identical to the values predicted by the classical AMB model, the force–displacement factor k_s *never* is the same as in the gravity free case (see Equation (5.22)) due to the integrator compensating for gravity. However, for large bias current values the relative difference becomes small. This is indicated by Equation (5.23). Nevertheless, this effect may explain difficulties encountered in the stabilization of horizontal rotors when this effect is not considered in the underlying models.

  At the corner point($i_0 = i_{min}/2$), this effect exactly doubles the force–displacement factor k_s with respect to the conventional analysis that does not take into account the effect of gravity compensating integrators. This can be seen from Equation (5.22), when $i_\Delta = i_0 = i_{min}/2$.

Figures 5.5 and 5.6 show the situation in dimensionless variables. Based on the above, new formulae for determining *control relevant* k_i and k_s values
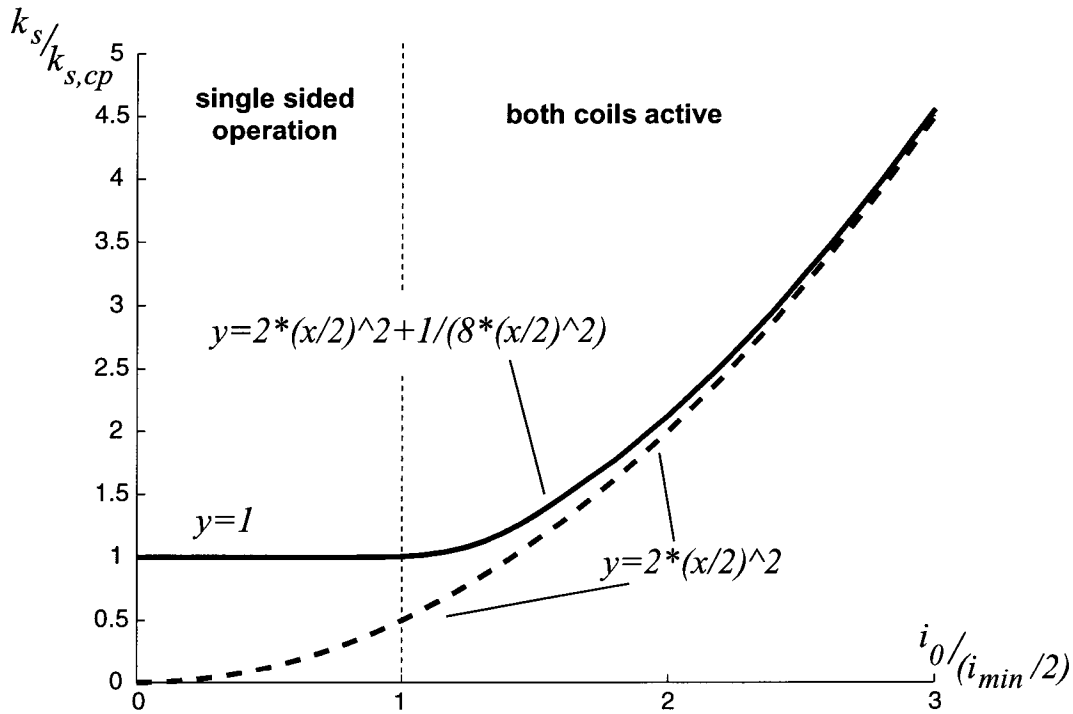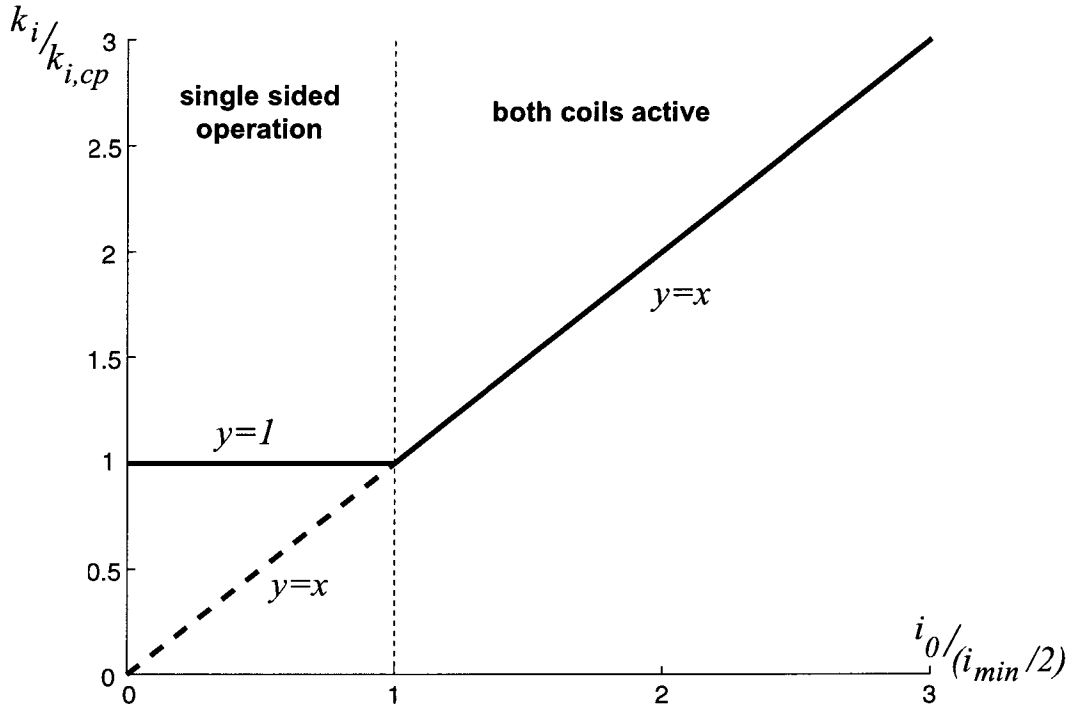
Figure 5.6: *Force–current factor over bias current with (solid) and without (dashed) consideration of integrator effects*

can be given as follows.

$$k_s = \begin{cases} \frac{2 \cdot F_g}{s_0} & : \quad i_0 \leq i_{min}/2 \\ k \frac{i_0{}^2 + i_\Delta{}^2}{s_0{}^3} & : \quad i_0 > i_{min}/2 \end{cases} \qquad (5.28)$$

and

$$k_i = \begin{cases} \frac{\sqrt{k \cdot F_g}}{s_0} & : \quad i_0 \leq i_{min}/2 \\ k \cdot \frac{i_0}{s_0{}^2} & : \quad i_0 > i_{min}/2 \end{cases} \qquad (5.29)$$

The insights gained above can be used to formulate an improved modeling technique for AMB rotor systems affected by gravity. This is presented in Appendix C.

Controller Design for Horizontal Rotors

As the reflections from the last section imply, the bearings cannot be made arbitrarily soft in the case of horizontal rotors. Instead, lower stiffness limits determined by the bearing characteristics and the rotor mass apply.
As a consequence, instead of performing a controller design with extremely

soft bearings, the minimum values $k_{s,S}$ and $k_{i,S}$ imposed by the rotor support must be considered. The design procedure is then analogous to the vertical case.

However, the minimum bearing stiffness directly translates into minimum values for the unstable rigid body poles. This again implies a minimum bandwidth of the controller. As a consequence, the controller's roll–off is forced to start at higher frequencies, increasing the frequency from which on amplitude stabilization occurs. This may lead to problems when trying to stabilize rotors with low frequency flexible modes. This issue is addressed next.

5.1.5 Dealing with Highly Flexible Rotors

In the last sections a method for controller design for flexible rotors with unknown high frequency dynamics has been presented. Therein, stability is achieved by a sufficiently steep roll–off. However, it has been shown that this roll–off cannot start at arbitrarily low frequencies. Although flexible modes not explicitly covered by the uncertainty model are not necessarily destabilized, this bears the risk of instability.

While in vertical setups this problem occurs only for highly flexible rotors, it is likely to be encountered in horizontal machines due to restrictions resulting from gravity compensation. In the following, methods to deal with this problem will be discussed.

Damping and Controlled Instability

The following truly 'hands on' method has proven to be equally pragmatic and effective: The idea of the approach is to avoid destabilization of any flexible modes not comprised in the additive uncertainty model from the design. This can be effectively achieved by touching the rotor when taking the system into operation, thus adding some manual damping. Since the rigid body modes are stabilized by the controller, the rotor can be lifted to the bearing center by means of a slow integrator. Once this has been achieved, data acquisition is started, and the rotor is released. Should the system become unstable, this leads to an oscillation of increasing amplitude and finally to rotor–stator contact which causes the system to be automatically switched off.

Typically, the period of time during which the vibration builds up is rather long (often several seconds). From the sensor signals recorded during this

process, the frequency of the unstable pole can be detected very precisely. In the next step, a narrow banded notch filter can be added to the controller, eliminating the unstable vibration from the closed loop.

This method also has proven effective for many systems when applied in conjunction with adequately designed lead–controllers [Lösch00]. These are quick to derive based on a given rigid body model, and although robustness issues are not explicitly addressed in their design, they often achieve robust stabilization of the rotor even in face of modeling errors. This is due to their phase, which is positive for all frequencies and hence has a stabilizing effect on all modes that do not have nodes between sensor and actuator (up to dead–time effects).

Alternative Approaches

In the introduction of this chapter, it has been pointed out that besides the amplitude stabilization approach described here, the rotor can also be stabilized by phase stabilization. With the possibilities offered by amplitude stabilization fully exploited, it is of some interest to investigate the potential of phase based stabilization approaches.

Two concepts are conceivable:

- Based on the rigid body model, iterative (phase) shaping of a controller transfer function that stabilizes the flexible modes occurring during the sequence of tests.

- Based on a sufficiently large set of precomputed controllers with known frequency characteristics, find a stabilizing controller by narrowing down the feasible set of controllers based on the information gained from the successively emerging flexible modes.

The first of these methods has been carefully investigated in [Haugstetter00] by means of different interpolation techniques. The result of these efforts was rather humbling. Problems were encountered with high controller gains, low damping, and unpleasantly steep phase transitions (although derivatives were also considered in the interpolation) that even led to instability.

The second approach avoids these problems by resorting to precomputed controllers. This appears to be feasible, particularly when assuming that by appropriately adjusting the bias current the rigid body modes can always be brought into the same frequency range. However, precomputing

the controllers and deriving an adequate selection rule may be a cumbersome task.

Furthermore, the fact that instability is not only likely but even expected to occur makes this concept appear inelegant and little suited for automated stabilization of rotors with unknown flexible modes.

In summary, it must be stated that instability is a risk that cannot be entirely eliminated *a priori*, necessitating in some cases pragmatic solutions as outlined in the last section.

5.2   Flexible Rotors

In this section, the topic of controller design for flexible rotors supported by AMBs is addressed. The goal of this section is to derive algorithms for automatically designing controllers suitable for operation of the system under real–world conditions. Availability of a sufficiently precise model describing the open–loop dynamics of the AMB system is assumed — such models can be obtained by applying the design algorithm presented in Chapter 5.1 in conjunction with the identification algorithm presented in Chapter 4.2.

This chapter begins with a discussion of the state of the art methods for controller design for flexible rotors and an analysis of their potential for automation. Then, the best suited method is presented in greater detail, followed by an analysis with respect to points that show potential for improvement. Finally, ways to work around these weak points are elaborated, and a procedure for automated controller design for flexible rotors is presented.

5.2.1   State of the Art

The requirements on controllers for flexible rotors have been broadly addressed in the introduction, Chapter 1.1.2. As has already been argued there, out of the large number of controller design methods, only two appear to be well suited for systematic controller design for flexible rotors. These are:

The phase shaping method systematically introduced by C. Gähler [Gähler98]. Based merely on information on the location of the plant's flexible and rigid body eigenfrequencies and the information

whether or not the individual modes have nodes between sensor and actuator, this method consists in the design of SISO controllers by adequate placement of poles and zeros in the complex plane. The goal of the procedure is to obtain controllers with sufficient gain for stabilization of the rigid body modes and with adequate phase to avoid destabilization of any flexible modes. The tuning knobs are besides the location of the poles and zeroes to be placed also the controller gain and the number of poles and zeros in the controller. A drawback of the method is that robustness and performance criteria cannot be explicitly considered in the design process, but must be included implicitly by adequately choosing the above parameters. In all cases, these controllers are subject to thorough testing. When successful, this method delivers low order controllers that can be directly implemented. Furthermore, the robustness properties of these controllers tend to be rather good since due to the low controller order phase transitions are relatively slow.

μ–**Synthesis based methods,** with the most advanced representative presented by U. Schönhoff in [Schönhoff00b]. These methods rely on a precise model of the plant and adequate choice of a design scheme as well as suitable weighting functions that sensibly represent robustness and performance criteria to be achieved in the design. These parameters also serve as tuning knobs in the method. The design process itself is encapsulated in the D–K iteration, guaranteeing closed loop stability as well as achievement of the desired performance objectives in case of successful design, see Chapter 3.2.4. Disadvantages are the method's high level of complexity, entailing comparably long computation times (several minutes on a modern PC), and the high controller order resulting from the design.

Both of the above methods have been shown suitable for designing controllers for flexible rotor AMB systems. However, all reported designs are *manual* designs, i.e. they have been performed by engineers who brought considerable amounts of knowledge, experience, and also patience into the design process.

The goal of this thesis however is to develop methods for *automated* controller design. Therefore, the above mentioned methods have been investigated with respect to possibilities to automate them.

For the phase shaping approach, this has been studied in [Haugstetter00]. In this work, based on papers focusing on the design
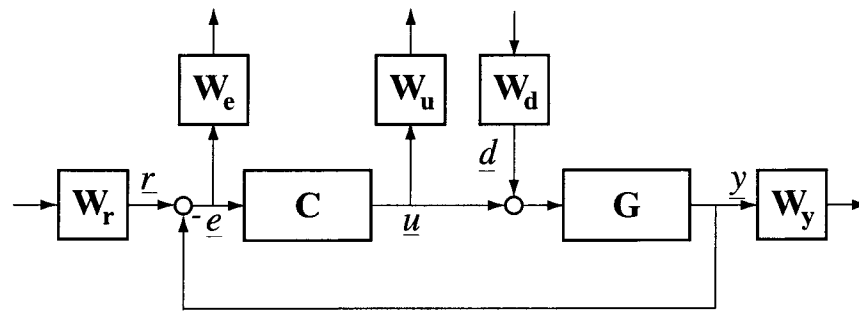
Figure 5.7: **S/CS/SG/T** *design scheme*

of electronic filters, [Henk81],[Fahmy79], and [Jarry83], it has been attempted to design transfer functions that fulfill certain predefined conditions concerning their phase. Although some fundamental difficulties not addressed in the literature have been overcome, even with great effort it was not possible to derive a generally applicable design procedure. Problems encountered comprise poor robustness properties due to very steep phase transitions, high controller orders, overly large gains, and problems in predicting stability of the closed loop due to controller poles crossing the imaginary axis even for small gains. The size and number of problems encountered finally led to the conclusion that the phase shaping method, although of considerable use when applied by an experienced engineer, is not suited for automation.

For the μ-synthesis approach, things are different. Already in its standard form, the design procedure is clearly structured into different modules and several steps. Furthermore, the majority of difficulties encountered during automation of the phase shaping approach is ruled out by the procedure itself, as closed loop stability is guaranteed and overly large gains as well as robustness issues can be addressed with adequately chosen weighting functions. Although computationally far more complex than the phase shaping procedure, this approach shows to be much better suited for automation.

5.2.2 μ–Synthesis: State of the Art Procedure

In [Schönhoff00b], U. Schönhoff extended a μ-synthesis based controller design method developed by Braembussche [Braembussche98] and adapted it to the specific needs of active magnetic bearing systems.

The method is based on rig models obtained from carefully (hand–) tuned finite element models. Two types of uncertainty are considered: A small uncertainty on the location of the flexible eigenfrequencies is taken into

account by means of the method described in Chapter 3.1.5. Furthermore, gyroscopic effects are treated as an uncertainty to the state space description of the nominal model that rotates at half the maximum speed. This is covered by uncertainty modeling techniques described in Chapter 3.1.4.

For the design, the **S/CS/SG/T** scheme depicted in Figure 5.7 has been used, with weighting functions chosen based on a loop shaping philosophy, i.e. with the aim to achieve specific shapes for the transfer function under consideration rather than directly relating to the size of the physical signals occurring in the closed loop plant, see Chapter 3.3.3.

In the above, the structure of the plant **G** is as follows:
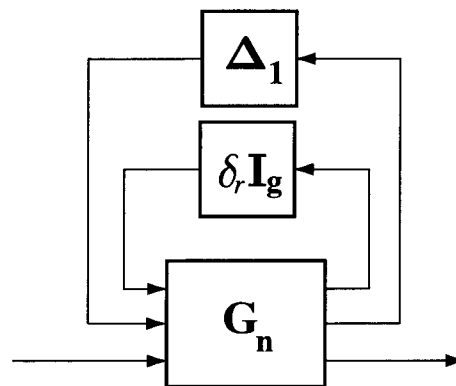
The resulting standard control configuration is of the form

$$
\begin{bmatrix} I & & & \\ & I & & 0 \\ & \mathbf{W_y} & & \\ & & \mathbf{W_e} & \\ 0 & & \mathbf{W_u} & \\ & & & I \end{bmatrix} \cdot T_1 \cdot \begin{bmatrix} & & 0 & 0 \\ \mathbf{G}_n & & 0 & 0 \\ & & 0 & 0 \\ 0 & 0 & 0 & I & 0 \\ 0 & 0 & 0 & 0 & I \end{bmatrix} \cdot T_2 \cdot \begin{bmatrix} I & & \\ & I & 0 \\ & \mathbf{W_r} & \\ 0 & \mathbf{W_d} & \\ & & I \end{bmatrix} \tag{5.30}
$$

with

$$
T_1 = \begin{bmatrix} I & 0 & 0 & 0 & 0 \\ 0 & I & 0 & 0 & 0 \\ 0 & 0 & I & 0 & 0 \\ 0 & 0 & -I & I & 0 \\ 0 & 0 & 0 & 0 & I \\ 0 & 0 & -I & I & 0 \end{bmatrix} \quad \text{and} \quad T_2 = \begin{bmatrix} I & 0 & 0 & 0 & 0 \\ 0 & I & 0 & 0 & 0 \\ 0 & 0 & 0 & I & I \\ 0 & 0 & I & 0 & 0 \\ 0 & 0 & 0 & 0 & I \end{bmatrix}. \tag{5.31}
$$

The corresponding uncertainty block structure for the design is

$$
\begin{bmatrix}
\delta_r \mathbf{I_g} & 0 & 0 \\
0 & \mathbf{\Delta_1} & 0 \\
0 & 0 & \mathbf{\Delta_2}
\end{bmatrix},
$$

where $\mathbf{\Delta_1}$ is a matrix consisting of real diagonal entries (one entry for each uncertain pole) and δ_r is a real parameter reflecting the change in rotational speed. The matrix $\mathbf{\Delta_2}$ referring to the performance block is a 12 by 8 complex matrix. With $\mathbf{P}$ denoting the open–loop system with weighting functions in standard configuration, the performance requirement minimized in the design is

$$
F_U(\mathbf{P}, \mathbf{C}) =
\begin{bmatrix}
\mathbf{W_y TW_r} & \mathbf{W_y SGW_d} \\
\mathbf{W_e SW_r} & -\mathbf{W_e SGW_d} \\
\mathbf{W_u CSW_r} & -\mathbf{W_u T_i W_d}
\end{bmatrix}. \tag{5.32}
$$

In the following, this approach is analyzed more closely, and suitable adaptations are made where this seems advisable. This has been significantly simplified by Ulrich Schönhoff, who made the algorithms he used in [Schönhoff00b] available for this purpose.

5.2.3 Drawbacks of the Method

With the approach described above, Schönhoff managed to design a controller suitable to speed up the moderately gyroscopic system under consideration in [Schönhoff00b] to a speed of 12000rpm, showing the feasibility of the approach.

In spite of this success, there are several points calling for improvement:

- The lumped design scheme makes tuning of individual transfer functions difficult, each time a weighting function is modified, this affects at least two transfer functions.

- The entirely loop shaping oriented design prohibits inclusion of hard limits on signals, like for example actuator limitations.

- Due to numerical problems encountered, the design must be based on complex uncertainties rather than the real uncertainties encountered in practice. For the weakly damped flexible poles, this means that uncertainty in frequency entails uncertainty in damping of identical size (the uncertainty region being a disc rather than a line parallel to the imaginary axis). This has been handled in [Schönhoff00b] by means of creating an enlarged uncertainty circle and moving the poles to the left in such a way that the line on which the poles are expected to be located in reality is covered by the uncertainty circle, but the uncertainty circle does not intersect the imaginary axis.
  The same problem, however, is encountered for the gyroscopic effects. They, too, are modeled by means of real uncertainties, and in a complex design, the gyroscopic effects also become disc-shaped uncertainty regions rather than lines reflecting the linear movements parallel to the imaginary axis. This effect went unnoticed in the prior studies. However, with pole movements due to gyroscopic effects typically exceeding by far pole movements caused by simple pole uncertainty, this effect plays a larger role in the design than the one mentioned above. Failure to consider this effect renders designs for gyroscopic rotors and/or high speeds ineffective due to very large controller gains stemming from the attempt to stabilize the poles mistaken to be potentially unstable.

- Using the overall μ value achieved as a criterion to assess the success or failure of the design typically is conservative in the present setup. Due to its lumped fashion, it can be observed in many cases when the compound μ value is considerably larger than one, that the size of all individual transfer functions to be minimized is smaller than one. This point is worth while investigating as good controllers may be wrongly rejected.

5.2.4   Adaptation of the Procedure

Investigation of Alternative Design Schemes

Any sensible weighting scheme for the presented controller design problem should explicitly limit **S**, **SG**, and **CS**, as limiting one of these functions indirectly via the other two leaves room for weakly damped poles or zeros

of the controller or plant deteriorating robustness and performance, see the last section of Chapter 3.3.3. In addition to the above, minimization of **T** also is attractive for increased robustness with respect to multiplicative uncertainty and sensor noise.

These considerations show that the scheme used by Schönhoff cannot be significantly simplified. Therefore, the same scheme as in [Schönhoff00b] has been used.

Weighting Function Selection

Choosing weighting functions based only on loop shaping aspects only makes consideration of hardware constraints like actuator limitations difficult. This approach can only be recommended for systems having sufficiently (i.e. over–) dimensioned actuators. In order to incorporate more information of the true system's behaviour in the design process, it has been decided to use a mainly signal based approach, choosing weighting functions based on the the physical quantities of the signals occurring in the system (see first section of Chapter 3.3.3).

The advantage of this procedure is that the nature of the system (hardware setup and constraints) is explicitly considered in the design. As a result, the controllers are tailored for the actual hardware rather than for a general system, and it can be noticed already in the design phase when physical constraints become relevant.

The smoothness criteria behind the loop shaping philosophy may of course not be neglected (see last section of Chapter 3.3.3), however, the range in which these rather loose criteria are fulfilled is considerable, such that for reasonably designed systems the closed loop does usually not strongly violate these constraints even if the weighting functions are based on a signal based philosophy.

The choice of weighting functions is done as follows:

1. The plant is scaled such that an input of size one is equivalent to the maximum current output of the amplifiers. The outputs are scaled such that contact to the stator (retainer bearings) yields an output of one.

2. The weighting function $\mathbf{W_u}$ (control current limit) directly follows from the knowledge of the amplifier behaviour. Depending on the type of amplifier chosen, $\mathbf{W_u}$ either is a first order weight, constant or an augmentation of two weights, see Chapter 2.1.3.

3. The weight $\mathbf{W_d}$ is to represent the size of the disturbances to be expected. A sensible choice of this weight reflects the balancing quality of the rotor, the corresponding speed, and the approximate rotor mass, based on which the maximum unbalance forces can be calculated for a frequency larger than the rigid body critical speeds, e.g. 100Hz. Division by the force–current factor k_i then yields the current amplitude generating forces at least as large as those expected from unbalance up to the considered speed (this estimate is conservative since the unbalance usually is shared among two bearings). Choosing $\mathbf{W_d}$ to be equal to the above value (constant), will then reflect large enough disturbance forces to pass the rigid body critical speeds.

4. The output weight $\mathbf{W_y}$ limiting the rotor's deviation from the center position is to be set to a sensible value reflecting tolerable and expected rotor deviations in operation. For short rotors a value around 10 (limiting deviations to 10% of the air gap under the considered loads) is sensible here, in cases of particularly small air gap, long rotors, or large loads, values may range down to 3 or 2.

5. Limiting the sensitivity function $\mathbf{S}$ to a reasonable value is of great importance in AMB controller design. Experience shows that in the SISO case peak values of about 2.5 are reasonable, while 4 is already critically large. (For comments on the size of $\mathbf{S}$, see Chapter 3.2.2). In the MIMO setting encountered here, these limits can be directly adopted and even slightly relaxed, since the MIMO transfer function's size is a conservative estimate of the size of the individual SISO functions.
   Furthermore, it is sensible to limit the complementary sensitivity function $\mathbf{T}$ by a value similar to the limit on $\mathbf{S}$. Since both functions are related to the same input ($\underline{r}$), it is therefore reasonable to choose the output weight $\mathbf{W_e}$ equal to $\mathbf{W_y}$.

6. A reasonable size for the input weight $\mathbf{W_r}$ is obtained, when considering that it is to ensure sensible sizes for $\mathbf{S}$ and $\mathbf{T}$. Based on the sizes of $\mathbf{W_e}$ and $\mathbf{W_y}$, $\mathbf{W_r}$ can then be directly calculated. The resulting disturbance size usually exceeds the size of the expected set position variations (usually none) and the other possible interpretations of $\underline{r}$, sensor noise and plant output disturbance.

In the present setting, all weighting functions (except for maybe $\mathbf{W_u}$) are chosen to be *constant*, yielding low order plants and reduced controller design times. Compensation for gravity is done by means of separate integrators that are not part of the controller designed here. These integrators are slow and do not affect the system dynamics beyond a low frequency of a few hertz. (However, the effect on bearing stiffness pointed out in Chapter 5.1.4 is considered by using the corrected force displacement factors from Equation (5.29) throughout the entire design.)

Dealing with Gyroscopic Effects

The problems arising from combining the model of gyroscopic effects with the required complex uncertainty model in an appropriate way has been addressed as follows. In the design procedure, the flexible poles are moved to the left by a certain distance. The design is then performed based on complex uncertainties.

The subsequent analysis of the resulting controller however is then performed based on the original system (with all poles at their nominal position) under the influence of *real* worst case disturbances, see Chapter 3.4.2. The analysis is performed in a 'mixed' setup, see Chapter 3.3.5. This procedure considerably reduces the controller gain at high frequencies and yields controllers with guaranteed performance in conjunction with the following analysis approach.

Controller Design Based on Closed Loop Analysis of Individual Transfer Functions and Pole Shifting

Due to the block structure of the present μ-synthesis design problem, the γ value resulting from the design merely is an upper bound of the γ value of the individual transfer functions to be minimized in the design.
Practical experience shows that in virtually all cases it pays off to analyze the size of the individual transfer functions rather than the compound γ. In contrast to the lumped analysis, performing this analysis on a system with real, full size, worst case uncertainty yields detailed information on the controller's robustness and performance properties. Overly large transfer functions and critical frequency ranges can be easily identified (by comparison of all transfer function sizes to the value one).

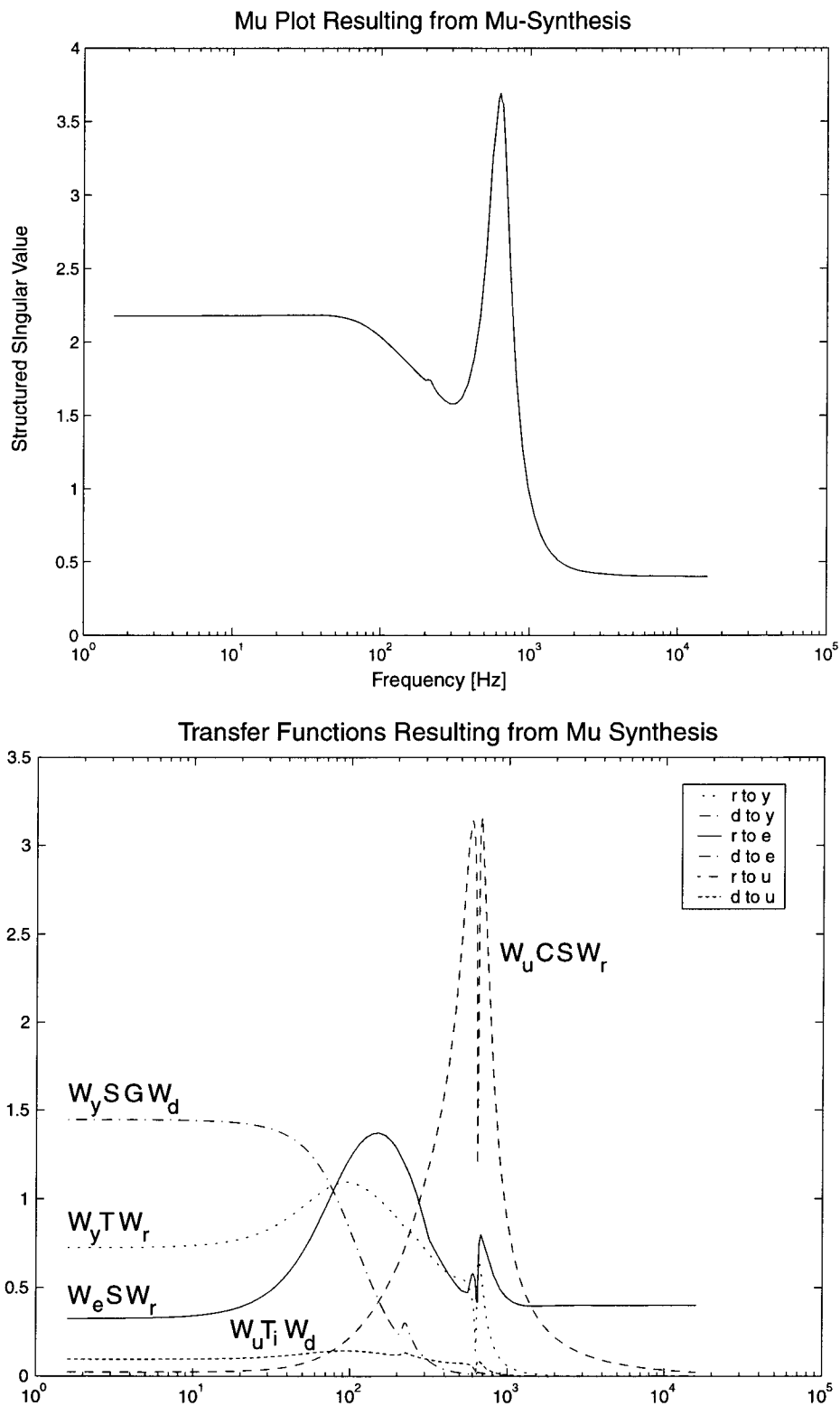This analysis typically shows the following results, see also the bottom part of Figure 5.8:

Figure 5.8: *Design result on model with original (weakly) damped pole locations. Top: μ-plot from design, Bottom: Individual weighted transfer functions*

At low frequencies (up to the rigid body poles of the rotor), the weighted sensitivity function **S** is small. Like in the rigid rotor case, this is due to the limit on the function **SG**, which, due to **G** being fixed and large in this area, leads to a minimization of **S**.
The weighted function **CS** is also small compared to the weighted **SG**, which dominates this frequency range.

At high frequencies, the sensitivity function **S** gradually approaches one, with more or less significant peaks at the rotor's flexible poles. The weighted function **CS** is large in this area, exposing sharp dents near the flexible poles. The other functions are small with insignificant peaks near the rotors's flexible poles.

Between these areas, there is a range of transition where the weighted **S** dominates the scenery due to the waterbed effect, see Chapter 3.2.2. The weighted function **SG** decreases sharply in in this range, caused by the decrease of **G**. The weighted **T**, relatively small in the low frequency range and small at high frequencies due to **S+T=I**, also reaches its maximum here.

In all cases investigated, the method has arrived at large μ values when applied without modifications, and the individual transfer functions often significantly exceeded the limit one. A typical plot of closed loop μ values is shown in the top part of Figure 5.8. The corresponding individual transfer functions can be seen in the bottom part of the same figure.

The observed behavior can be explained by the weakly damped rotor poles that dominate the μ–plot and cause the D–K iteration to focus particularly on the peaks caused by them while neglecting other frequency areas. In particular, the large values of **SG** in the range of low frequencies are not a necessity, but result from a lack of relevant limitation of this transfer function due to the large effort made to minimize **CS** at high frequencies, as will be shown in the following.

This behavior can be significantly improved if the weakly damped poles are manually shifted in direction of the stable half plane before the design. The resulting system transfer functions have lower peak values for the poles. As a consequence, the μ-synthesis algorithm focuses more on the overall optimization. In the top part of Figure 5.9, the μ–plot resulting from D–K iteration is shown for the same system as before, but with the dominant flexible pole moved to the left half plane by about 200. The
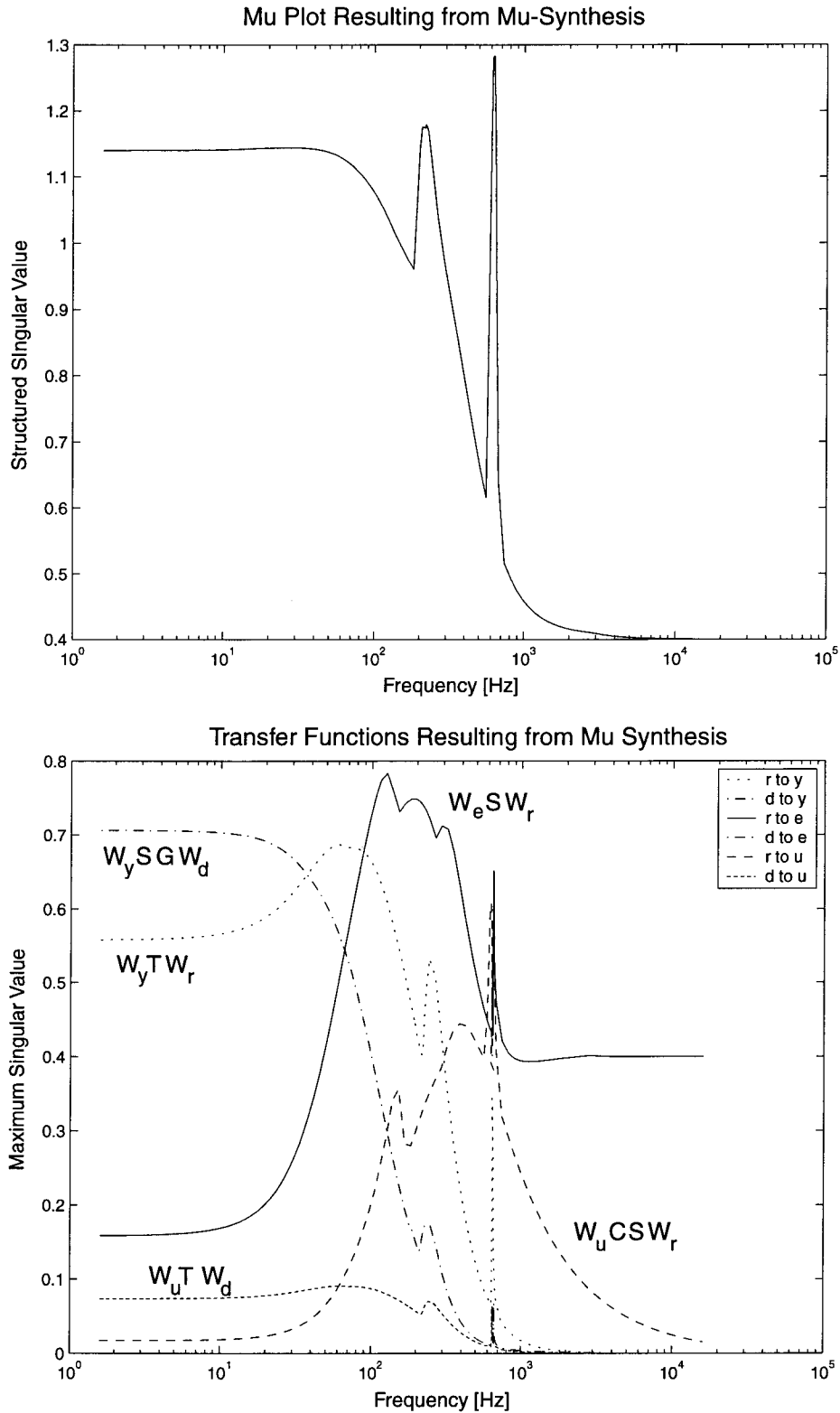
Figure 5.9: *Design result on model with shifted poles. Top: μ–plot from design, Bottom: Individual weighted transfer functions for closed loop of controller with model with original poles.*

lower μ values are not very surprising.

However, as remarkable side effect this modification has considerable impact on the individual transfer functions investigated before. This is due to the fact that in absence of the dominating peak in the μ–plot the D–K iteration makes a greater effort to achieve the objectives on minimizing the μ value in other frequency regions.

The bottom half of Figure 5.9 shows the new controller tested on *exactly the same system* as has been used for the test in Figure 5.8, bottom. While the figures look similar at first sight, closer inspection of the scaling reveals that the controller performance improved by a factor of about four, and that robust performance is achieved by this controller. The changed behavior of the D–K iteration becomes obvious when inspecting the size of the weighted transfer function **SG** for low frequencies — although no changes have been made in this frequency range, **SG** has been reduced by a factor of two.

This phenomenon can be generally observed, and it occurs gradually as the flexible poles are shifted further and further to the left. The limit of this procedure can be seen in in the bottom half of Figure 5.9; as the controller gain decreases, the sensitivity function around the pole under discussion increases. This is due to the increasing mismatch between the models used for design (with relocated poles) and for analysis (with original pole locations). The optimal amount of pole shifting is achieved at the point when the peaks of the weighted function **CS** and that of the weighted function **SG** are *equal*.

Due to its local impact, this procedure can for systems with multiple flexible modes be carried out in parallel and independently for the individual poles.

This gives rise to an iterative design procedure in which the system's flexible poles are individually shifted to the left until both the weighted sensitivity function and the weighted function **CS** have a maximum singular value below one, yielding a controller with robust performance.

In cases where this cannot be achieved (this can be stated as soon as the two peaks for one pole are both larger than one), the design has failed.

This approach constitutes the basis of the automated robust controller design algorithm formulated in the following.

5.2.5   Algorithm for Automated Robust Controller Design

Based on the above considerations, the following algorithm for automated controller design can be formulated. Required inputs to the algorithm are a system model in form of Equation (2.46), the various bearing parameters, and the amplifier characteristics. The system model could stem from modeling or identification, bearings and amplifiers are assumed to be known throughout this thesis. Furthermore, a gyroscopic matrix (obtained from FE programs or identification) can be supplied if available together with a desired maximum operating speed.

Algorithm

1. Weighting function selection as described in the last section.

2. Creation of two systems in standard control configuration based on the design setup from Figure 5.7, one with complex uncertainty and poles manually moved further into the stable half plane for controller design, the other one without modification and with mixed real/complex uncertainty for controller analysis (see Chapter 3.3.5).

3. Controller Design by D–K iteration using a frequency grid containing the flexible poles' frequencies and a densely spaced grid covering the adjacent frequency range affected by gyroscopic effects.

4. Computation of the worst case uncertainty (see Chapter 3.4.2). Individual analysis of all closed loop transfer functions with respect to the limit one using the system with mixed uncertainty in its nominal form as well as with worst case uncertainty scaled to full size (±1). If all functions are smaller than one, the design has been successful and the iteration is aborted.

5. For all flexible modes the following steps are performed:
   Verification if the transfer function from $\underline{r}$ to $\underline{u}$ is larger than one in the vicinity of the mode's eigenfrequency. If this is the case and the transfer function from $\underline{r}$ to $\underline{e}$ (related to the sensitivity function limit) is smaller than one in the corresponding frequency range, modify the design model in such a way that the pole under consideration is moved further to the left in the complex plane. This merely requires adjustment of two values in Equation (2.46).
   Verification if the inverse case of the above occurred (transfer function from $\underline{r}$ to $\underline{e}$ larger than one and transfer function from $\underline{r}$ to $\underline{u}$ smaller than one) — this indicates that the pole has been moved too far to the left. In this case, the pole is to be moved back to the right by a reasonable distance.
   If both transfer functions are larger than one, the amount of uncertainty (i.e. the demanded rotational speed) is too large and no adequate controller can be found, and the procedure is aborted.

6. Go to Step 3.

The above algorithm has been used to design controllers for several test rig configurations, and good controllers have been found within few iterations.

In fact, practical experience shows that even for systems with three or more flexible modes in the control relevant frequency range, typically only one or two poles in the mid-frequency range require several iteration steps since at low frequencies weakly damped poles typically entail comparably small controller action while at high frequencies the weighted sensitivity function is small (near one) due to plant roll–off (see Chapter 3.2.2), and remains small even when the pole is moved to decrease the control effort. Example results from application of the algorithm will be shown in Chapter 7.

5.3 Summary

In the first part of this chapter, the problem of controller design for rigid rotors with unknown high frequency dynamics has been addressed. The bias current i_0 and the uncertainty weight $\mathbf{W_a}$ have been determined as the most relevant design factors, and limitations concerning the size of these parameters have been identified. Based on this analysis, an automated iterative, μ-synthesis based controller design algorithm has been developed for levitation of flexible rotors of which only the rigid body model is known. It has been shown that as a direct consequence of the above, the flexible modes must exceed a certain minimum frequency depending on the rotor mass, the system's orientation with respect to gravity, the bearing characteristics, as well as the modes' damping, observability, and controllability in order for the controller to achieve guaranteed stability.

In this process, the standard linear model of current controlled active magnetic bearings had to be revised in oder to account for effects caused by the constant currents imposed by gravity compensating integrators. It has been shown that under the influence of gravity the bearing stiffness cannot be made arbitrarily small, hence limiting the size of the bias current from below.

As a result of the observations made in Chapter 5.1, it must be stated that the controller design for rotors with unknown flexible dynamics is considerably more difficult in the case of horizontal rotors than in the case of vertical rotors. This is due to the fact that in the horizontal case the bearings cannot be made as soft, limiting plant roll–off and hence increasing the risk of destabilization of flexible modes in the medium frequency range. To deal with this situation, a pragmatic workaround for stability problems possibly occurring in the horizontal case has been presented.

In the second part of this chapter, robust controller design for flexible rotors has been addressed. Based on an analysis of the state of the art,

the approach used in [Schönhoff00b] has been extended to be compatible with the restrictions imposed by non-negligible gyroscopic effects and the requirements of complex uncertainty modeling. The selection of weighting functions has been discussed in detail.

Particular attention has been paid to the issue of effective assessment of controller performance. Individual analysis of the weighted closed loop transfer functions involved in the design has been introduced as a tool to perform this task both efficiently and intuitively.

Based on this analysis tool, a deeper understanding of the minimization performed by D–K iteration has been obtained. The insights gained have been developed to a new controller design approach that involves adaptation of the model the controller design is performed on in order to achieve better optimization results in the D–K iteration. This procedure is justified by an a posteriori robust performance analysis that is based on the original model without modification. The superiority of the new method over the conventional approach has been shown on an example.

Furthermore, rules for systematic adaptation of the design system have been derived, including a condition that clearly states when the design method is unable to fulfill the performance requirements.

Based on these components, a new method for automated controller design for flexible rotor AMB systems has been formulated.

Chapter 6

Identification and Automated Controller Design

In this chapter, the results from the preceding chapters are recapitulated, collected, and assembled to form the procedure for identification and automated controller design for flexible rotor AMB systems. In the first part of the chapter, the overall procedure is presented and the individual modules are described. The second part of this chapter deals with newly invented tools, i.e. methods, procedures, and algorithms that have been developed to enable efficient execution of the design procedure. Also, a few auxiliary modules that are part of the procedure and have not been introduced in any of the other chapters are presented in this chapter.

6.1   Synthesis of Preceding Chapters

In this chapter, the developed automated controller design procedure for flexible rotor AMB systems is presented. The overall procedure is outlined graphically in Figure 6.1. The procedure is organized in three parts (phases) each of which comprises different modules. In the first subchapter of this section, the phases and the overall operation of the procedure are described. In the second one, the individual modules are explained.
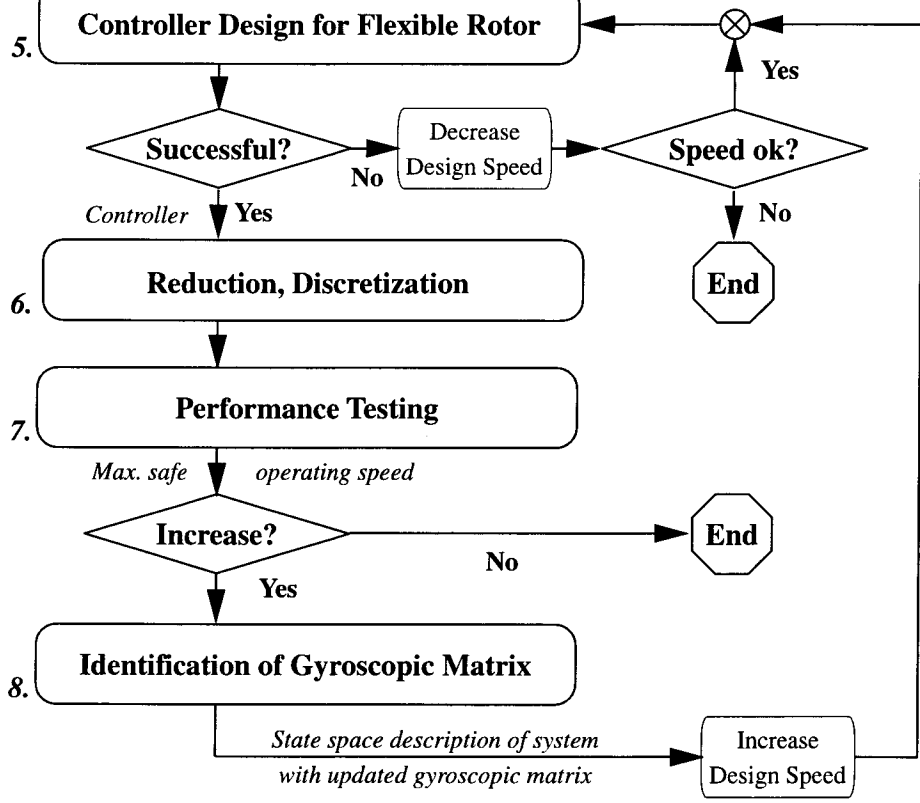
Figure 6.1: *Overview of Procedure for Identification and Automated Controller Design*

6.1.1 Procedure Description

The automated controller design procedure consists of three phases. In the first phase, a model of the rigid rotor is obtained. The second phase is concerned with arriving at a model of the flexible rotor open–loop system. The third phase finally is dedicated to designing a controller for operating the plant. These phases, also indicated in Figure 6.1, are described in the following.

Phase I: Identification of Rigid Body Model

The identification of a rigid body model of the rotor can be performed by the corresponding module, *Identification of Rigid Body Model.* Alternatively, the mass matrix can be directly taken from values obtained during the design phase of the rotor (CAD or Finite Element (FE) program).

Phase II: Identification of Flexible Rotor Model

Based on the rigid rotor model, a controller for levitating the rotor with unknown high frequency dynamics is designed (*Design of Controller for Low Stiffness Bearings* module). Then, this controller is used to identify the open loop model of the plant with low stiffness bearings (*Identification of Flexible Rotor* module). This model is then transformed to describe the rotor with stiff bearing settings. This is done by the *Model Transformation* module. Finally, uncertainties in the flexible poles are set to about 5 percent, and the gyroscopic matrix as well as the design speed are initialized to be zero.

This phase can be skipped if a sufficiently accurate finite element model of the rotor is provided. In this case, this model is used in the place of the transformed identified model.

Phase III: Controller Design

In this phase the final controller is designed. To this end, the following iterative procedure is executed:

1. Based on the current model, the available gyroscopic information, and the uncertainty limits on the poles, a controller is designed for

the current design speed (*Controller Design for Flexible Rotor* module). If the design has been successful, the procedure is continued, otherwise the attempt is repeated with a smaller design speed. If this speed gets too close to the prior controller's design speed, the iteration is aborted, and the prior controller is the best achievable controller.

2. The controller is reduced and discretized by the corresponding module.

3. The *Performance Testing* module is used to verify the controller's feasibility and to determine the maximum speed the plant can be safely operated at. If this speed is larger than the maximum speed achieved with the prior controller, the procedure is continued. Otherwise, the prior controller emerges from the procedure as the best achievable controller.

4. The gyroscopic matrix is identified at the maximum safe speed, and the model is updated with this matrix. The design speed is set to several times the maximum safe speed, the pole uncertainty is set to 3 percent, and the iteration is then continued at step 1.

The output of this last phase is the best achievable controller for the system. 'Achievable' in this context is a relative term — since already D–K iteration does not necessarily yield optimal controllers, this can of course also not be guaranteed by the above algorithm which is based on this technique.

It should be noted that in case of a design based on a Finite Element model, an identification of the flexible rotor model is performed as soon as the first controller is available. This is done since FE models usually do not match the true rig accurately enough to design reliable controllers. After the identification, the iteration process is restarted. The gyroscopic matrix from the FE model is preserved, and the design speed is now set to the desired maximum speed, i.e. it is attempted to directly design a controller for the maximum speed.

6.1.2 Modules

In this chapter, the constituent modules of the automated controller design procedure shown in Figure 6.1 are described with their corresponding inputs, the task performed, and the output.

Identification of Rigid Body Model (1.)

This module contains the identification routine for the rigid body information of the rotor. Basic information on the bearings being the only input, it performs step- and lift experiments to identify the rotor's mass matrix, which is the output of the module. The algorithms used are presented in Chapter 4.1.

Design of Controller for Low Stiffness Bearings (2.)

This module takes as input a rigid body model (4–element mass matrix and bearing information) of the rotor. Based on this information, a robust controller to stabilize the rotor with unknown high frequency dynamics is designed. To this end, the bias current is adjusted to a low value, yielding low stiffness bearings. The design procedure is presented in Chapter 5.1.

Identification of Flexible Rotor (3.)

This identification module requires a controller that is capable of stabilizing the rotor robustly enough to perform transfer function measurements. The procedure determines the most relevant frequency ranges and measures the MIMO transfer function on an optimized frequency grid. In the next step, the identification algorithm described in Chapter 4.2 is used to arrive at a model of the open–loop rotor.

Model Transformation (4.)

This module adapts bearing stiffness (bias currents) of a specific model. Given the old and the desired bias currents as well as the system model, it is used to compute a rotor model with bearing settings equal to those to be used during normal operation of the system. Details of the procedure are described in Chapter 6.2.1.

Controller Design for Flexible Rotor (5.)

Based on a model of the flexible open–loop rotor system with or without gyroscopic matrix, uncertainty limits on the flexible poles, and – in case a gyroscopic matrix is present – a maximum speed the controller is to be able to operate at, this module designs a controller to robustly stabilize

the rotor in normal operation from throughout the specified speed range (from standstill to the given maximum design speed). The algorithm is described in Chapter 5.2.

Controller Reduction and Discretization (6.)

The controllers resulting from the design procedure are in continuous time state space form. In order to be implemented on a digital signal processor, they must be discretized. Furthermore, the controllers are typically too large for direct implementation. Therefore, adequate controller reduction techniques must be applied. The algorithms used are briefly described in Chapter 6.2.2.

Performance Testing (7.)

Even with high quality models and careful uncertainty modeling, closed loop behaviour can only be accurately assessed from measurements on the plant. Different experiments are carried out and repeated as the speed is slowly increased until the maximum design speed is reached or indications are found that the limit of the range of safe operating speeds has been reached.
Output of this module is the maximum safe operating speed of the system with the given controller. The test algorithms used are presented in Chapter 6.2.3.

Identification of Gyroscopic Matrix (8.)

This module performs measurements to identify the gyroscopic matrix from the system operating at a given speed. Given a rotor model, this model is updated with a new gyroscopic matrix based on measurements from the system. The module is based on the algorithm presented in Chapter 4.3.

6.2 Tools

In this chapter, some newly developed tools supporting the efficiency and reliability of the above procedure are presented. Furthermore, those (few) modules of the procedure that did not fit into the context of any of the other chapters are described.

6.2.1 Model Transformation

In the procedure described above, the open–loop flexible rotor model is identified from a configuration with particularly soft bearing settings (low bias currents). The plant however is typically to be operated with significantly stiffer bearings.

A prerequisite for designing useful controllers is adaptation of the identified model such that it reflects the behaviour of the open–loop system with stiff bearings. How this can be done is presented in the following.

Model Transformation Based for Physical Models

The identified system model is of the form (2.46), which can be interpreted as a state space representation of a finite element model that has been transformed to modal coordinates with the mass matrix M being equal to the identity matrix.

$$
\begin{aligned}
\ddot{\tilde{q}} + \tilde{D}\dot{\tilde{q}} + \tilde{K}\tilde{q} &= \tilde{F}\underline{w} \\
\underline{z} &= \tilde{S}\tilde{q}
\end{aligned}
\tag{6.1}
$$

with

$$
\tilde{K} = \Phi^T K \Phi = \mathrm{diag}(\omega_{0i}^2)
\tag{6.2}
$$

and

$$
\tilde{D} = \Phi^T D \Phi = \mathrm{diag}(2\xi_i \omega_{0i})
\tag{6.3}
$$

To understand which adaptations are necessary to adjust the bias current i_0 it is instructive to go one step further back and to look at the underlying Finite Element model in physical coordinates (see Chapter 2.3.2):

$$
M\ddot{\underline{q}} + D\dot{\underline{q}} + (K - FK_sF^T)\underline{q} = FK_i\underline{i}.
\tag{6.4}
$$

In the above, the notation is that from Chapter 2.3.4, with F representing the matrix distributing the external forces to the correct nodes of the structure. Since the analysis performed in this chapter is rotation independent, the rotational speed Ω has been set to zero for the sake of simplicity. The 4 by 4 matrix K_i contains on its diagonal the force current factors of the bearings, and $\underline{i}$ represents the vector of input currents.

K_s at the same time is the diagonal 4 by 4 matrix of force displacement factors. This matrix is embraced by the matrices F and F^T, blowing it up to match the physical coordinates.

Adjusting the bias currents of this model amounts to calculating the new force–displacement and force–current factors from equations (5.28) and (5.29), respectively and adding the difference of the old and new values to the diagonal entries of the matrices K_i and K_s. For reasons of convenience, it is advantageous to interpret the operation performed on the matrix K_i as a multiplication by a suitable diagonal matrix $K_{i\Delta}$ from the right rather than an addition.

The adapted model with physical coordinates looks as follows:

$$M\underline{\ddot{q}} + D\underline{\dot{q}} + (K - F(K_s + K_{s\Delta})F^T)\underline{q} = FK_iK_{i\Delta}\underline{i}. \qquad (6.5)$$

Re–applying the modal transformation from above and adopting the notation from Equation (6.1) yields:

$$\underline{\tilde{\ddot{q}}} + \Phi^T D\Phi\underline{\tilde{\dot{q}}} + \Phi^T(K - F(K_s + K_{s\Delta})F^T)\Phi\underline{\tilde{q}} = \Phi^T FK_iK_{i\Delta}i \qquad (6.6)$$

$$\underline{\tilde{\ddot{q}}} + \tilde{D}\underline{\tilde{\dot{q}}} + (\tilde{K} - \Phi^T FK_{s\Delta}F^T\Phi)\underline{\tilde{q}} = \Phi^T FK_iK_{i\Delta}\underline{i} \qquad (6.7)$$

With the definition $K_\Delta = \Phi^T FK_{s\Delta}F^T\Phi$, the first row of the corresponding state space representation looks as follows:

$$
\begin{bmatrix} \underline{\dot{\tilde{q}}} \\ \underline{\dot{\tilde{q}}} \end{bmatrix}
=
\begin{bmatrix} 0^{q\times q} & I^{q\times q} \\ -(\tilde{K} - K_\Delta) & -\tilde{D} \end{bmatrix}
\begin{bmatrix} \underline{\tilde{q}} \\ \underline{\dot{\tilde{q}}} \end{bmatrix}
+
\begin{bmatrix} 0^{q\times 2n} \\ \Phi^T FK_iK_{i\Delta} \end{bmatrix}
\underline{i} \qquad (6.8)
$$

In the above, it becomes obvious what adjustments must be done to the state space representation of the original model in order to adapt it to a change in bias current on the system:

- The matrix $K_\Delta = \Phi^T FK_{s\Delta}F^T\Phi$ must be added to the lower left block of the matrix A. This can be easily done when realizing that

this matrix is simply equal to $ZK_{s\Delta}Z^T$, where $Z = \Phi^T F$ can be extracted from the lower half of the matrix B from the original system's state space description.

- In a second step, the matrix B is multiplied by the matrix $K_{i\Delta}$ from the right, which can be done without any further computation.

Practical Aspects of Model Transformation

The algorithm presented above has been shown to work well for models based on a Finite Element description of the rotor. These models have the nice property that they explicitly contain the system's physical quantities. In the context of identification of the gyroscopic matrix G it has been shown that this is not the case for general rotor models in state space form like those obtained from identification.

As has been elaborated in Chapter 4.3.5, the state space models obtained from input–output identification of physical systems are only known up to a transformation matrix T defined in Equation (4.39). This has the following implication.

In the algorithm for adaptation of k_s presented in the last section, similarity transformation of the system with a matrix $T = diag(T_1, T_1)$ as defined in Equation (4.39) affects the computation of the correction matrix K_Δ defined directly after Equation (6.8) as follows:

$$K_\Delta = \tilde{T_1}^T \Phi^T F K_{s\Delta} F^T \Phi \tilde{T_1}^{-T} \tag{6.9}$$

For stiffness adaptation, this matrix is added to the lower left part of the system's A matrix. It is obvious from Equation (6.9) that K_Δ depends on the choice of T_1 while, by definition of T_1, A does not. Since dependence of the stiffness adaptation matrix on an arbitrary parameter clearly is unacceptable[1], the algorithm for stiffness adaptation developed in Chapter 6.2.1 is not applicable to identified models.

Fortunately, there is a simple and effective workaround for this problem. Based on the matrix of stiffnesses to be added to the system, $K_{s\Delta}$, the

---

[1] Only the special matrix $T_{1,phys}$ transforming the identified state space system back to the 'natural' description resulting from FE modeling would yield the correct matrix K_Δ for the presented procedure. Due to the input–output equivalence of the systems under similarity transformations, $T_{1,phys}$ can unfortunately not be determined by experiments.

known input and output scaling factors $c_{in} = i_{max}$ and $c_{out} = 1/x_s$, and the diagonal matrix of force–current factors K_i, the constant matrix

$$K_{s\Delta,FB} = \frac{1}{c_{out} \cdot c_{in}} K_i^{-1} K_{s\Delta} \tag{6.10}$$

is computed and fed back from the system's outputs to its inputs.

This approach is equivalent to adding a proportional feedback with stiffness $K_{s\Delta}$ to the system between sensor and actuator locations.

Instead of using the (in the above sense uncertain) system matrices, it relies on modification on the (known) input–output behavior of the identified system for stiffness adaptation.

In contrast to the procedure that was originally proposed, this method is accurate only in the case of sensor–actuator collocation. However, for systems where sensors and actuators are close together, the deviations were found to be very small in numerical simulations.

6.2.2   Controller Reduction and Discretization

Reduction of Controller Order

Many different techniques for controller order reduction have been developed over the last decades, the best known of which may well be the balanced truncation approach (e.g. [Green95]). This classical technique aims at replacing the original high order linear controller $\mathbf{C}$ by a transfer function of lower order $\hat{\mathbf{C}}$ and minimal maximum deviation $\|\mathbf{C} - \hat{\mathbf{C}}\|_\infty$ of the frequency responses of the two systems.

The considerable degree of controller reduction achieved with this approach can even be increased if attention is focused on what the goal of controller reduction *really* is: A reduced controller with as similar as possible *closed loop robust performance*.

This problem is very different from the classical controller reduction problem since open-loop irrelevant dynamics of the controller may play an important role in the closed loop and vice versa [Wortelboer99].

This amounts to solving the problem

$$\min_{\hat{\mathbf{C}}} \sup_\omega (\mu_\Delta(F_L(\mathbf{P}, \mathbf{C})) - \mu_\Delta(F_L(\mathbf{P}, \hat{\mathbf{C}}))) \tag{6.11}$$

As is the case in K step of D–K iteration, μ is approximated by its upper bound, and rational D-scalings $\mathbf{D_l}$ and $\mathbf{D_r}$ (those obtained from the D–K iteration) are used for approximation. This yields a rational problem formulation

$$\min_{\hat{\mathbf{C}}} \|\mathbf{D_l} F_L(\mathbf{P}, \mathbf{C})\mathbf{D_r}^{-1} - \mathbf{D_l} F_L(\mathbf{P}, \hat{\mathbf{C}})\mathbf{D_r}^{-1}\|_\infty \qquad (6.12)$$

that is solved by means of the algorithm for frequency weighted balanced reduction in closed loop configuration developed and implemented by P. Wortelboer in the WOR-Toolbox [Wortelboer94]. This toolbox used to be publicly available via ftp and has been made available by U. Schönhoff, who also used this algorithm in [Schönhoff00b] and [Schönhoff00b].

Like the standard balanced truncation, this reduction technique aims at transforming the system to be reduced to a state space representation that has equal controllability and observability gramians (which makes it 'balanced') and then eliminating the least observable (and hence controllable) modes from it.

The difference however is, that instead of the controller gramians, the gramians of the entire closed loop configuration are used as a basis for reduction: First the gramians of the closed loop system are calculated. By adequate state ordering, portions of the gramians belonging to the controller can be separated from the portion belonging to the plant and extracted. In the next step the similarity transformation to balance the extracted gramians can be computed. Using this similarity transformation to transform the controller yields a description of the controller from which the least observable and controllable (with respect to the extracted closed loop controller gramians) can be truncated, yielding the desired reduced controller $\hat{\mathbf{C}}$.

This reduction technique has been shown to be superior to the classical techniques in a number of practical applications ([Wortelboer99], [Schönhoff00a], and [Schönhoff00b]), and has proven very effective in all test cases encountered in the context of this thesis.

Controller Discretization

Controller Discretization is a prerequisite for implementation of continuous time controllers as obtained from D–K iteration on DSP systems. Different discretization techniques are available, descriptions can be found in almost any book on control theory, like for example [Franklin94].

In the context of this work, the MATLAB function c2d has been used to perform the discretization task. Since only standard techniques have been applied and since the match of time discrete and time continuous controllers has been very good in all cases, this topic is not treated in any further detail here.

6.2.3   Performance Testing

In order to verify the validity of the designed controllers, systematic tests are carried out. Starting at standstill and at different constant speeds, the following are analyzed:

- Sensitivity function: The sensitivity function is measured over frequency, peaks are extracted and their size is compared to allowable threshold values.

- The system's flexible open–loop poles are extracted, their dislocation due to gyroscopic effects is analyzed and compared to the dislocation predicted by the model at the current rotational speed as well as the maximum dislocation permitted by the uncertainty considered in the design.

The above measurements are used for extrapolation of the measured quantities. Based on this extrapolation it is decided if the speed can be safely increased to the next higher test speed. This procedure is iterated until the maximum design speed is reached or the tests indicate that the iteration should be aborted.

During this iteration, the speeds at which the open–loop transfer function and the closed loop performance are tested and at which the gyroscopic matrix is identified are selected by the automated speed scheduler. This function defines the next design speed based on the following:

- Predictions of the systems' critical speeds (see Figure 2.9) are computed based on the current model. These critical speeds are always avoided by at least 2000rpm.

- Before a critical speed is passed, the system behavior is analyzed at the highest safe operating speed below this speed.

- At each test frequency, the pole's displacement due to gyroscopic effects is analyzed by measuring the system's open–loop transfer function. This displacement is compared to the displacement predicted by the model. In case the measured displacement exceeds that from the prediction, the maximum operating speed is decreased such that based on a linear extrapolation the poles' dislocation will not exceed the allowable maximum considered in the controller design for speeds up to the new speed limit.

- At each test frequency, the system's sensitivity function is measured based on the methods described in Chapter 6.2.4. The peak values are compared to predefined threshold values that indicate safe, noncritical, critical, and dangerous situations. Indication of a dangerous situation leads to direct abortion of the test with the last (lower) testing frequency being the maximum speed achieved. If the analysis indicates a critically large sensitivity function, the iteration is also aborted, but the *current* speed is accepted as the maximum speed achieved. In the noncritical (but not safe) case, the maximum allowable speed step is temporarily decreased. The iteration is then continued at a only slightly increased speed, which can be expected to expose an improved (safe) or worse (critical) situation.

- Generally, the maximum speed the controller has been designed for is considered an upper limit for the test speeds.

Furthermore, it is attempted to increase the speed by a certain minimum step size in each iteration. On the other hand, a maximum step size helps to avoid unexpected instability when the poles' movement due to gyroscopic effects is not linear with respect to the rotational speed as implicitly assumed.

In cases where a larger step size is required (e.g. whenever several critical modes must be passed in one step because no safe operating speed can be found in the (narrow) gap between them), the operator is prompted and can choose to proceed or abort the procedure.

6.2.4 Extraction of Transfer Function Peaks

Both the *Identification of Flexible Rotor Model* and the *Performance Testing* modules critically depend on reliable and time-efficient extraction of peaks from measured transfer functions.

In the present setting, this task is particularly challenging since nothing is assumed to be known a priori concerning the number or location of frequencies of interest (weakly damped eigenfrequencies, potential sensitivity peaks).

The classical approach to this problem is to define a 'sufficiently dense' frequency grid and to measure the corresponding transfer functions at the discrete frequencies. However, this approach is very time consuming, and once the peaks are determined only a small portion of the obtained data is actually required for model identification or assessing the plant's sensitivity function.

This lack of efficiency, the difficulties in defining what is 'sufficiently dense', and the knowledge that missing a peak may be fatal motivated the invention of a quicker and more reliable transfer function peak extraction procedure based on concepts known as *sweep sine excitation*.

The key feature of the new procedure is the abolition of the concept of discrete frequencies. While in the classical procedure the closed loop system is briefly excited in each of the four excitation channels with a sinusoidal signal of fixed frequency, the new measurement technique relies on four longer measurements during which the excitation frequency is swept through the frequency range of interest. Based on these measurements, the frequency response can be evaluated at *arbitrary* frequencies within the measurement range. The MIMO transfer function for a specific frequency point is calculated by cutting out the small piece of the measurements made when the excitation frequency was passing the evaluation frequency and subsequent application of the methods introduced in Chapter 4.2.1.

This procedure is efficient in two ways:

- When applied to a large range of frequencies (e.g. 100 to 1500Hz), the measurement data can be post processed with a relatively wide frequency grid (5 or 10Hz). Due to the fact that *all* frequencies are excited during the measurement and due to the quick variation of frequencies, a 'smearing' effect can be observed, making peaks visible even if they are not exactly at one of the grid points. Together with adequate normalization and extraction techniques the peaks of a transfer function can be reliably detected within little more than one minute.

- When applying the procedure to a small range of frequencies as identified by the above rough detection (e.g. 40Hz wide), results of remarkable precision are achieved in pinpointing the exact peak loca-

tions. Within about 30 seconds, a pole pair can be extracted with a precision of about 0.5% of the frequency window considered. The phase is typically accurate to 5 degrees even at the pole locations, where large jumps occur. This precision is enough to use the acquired data directly for system identification. Merely exactly at the extracted peak frequencies and at a few points in the low frequency range, the conventional method is used to extract the peak height as precisely as possible (see last chapter) respectively to avoid overly long measurement times.

6.2.5 Improvements to Flexible Rotor Identification

The identification algorithm for flexible rotors presented in Chapter 4.2 fulfills it task very well. The only weak point is that the height of the transfer function peaks caused by weakly damped flexible poles in many cases does not match the measurements very well.

However, avoiding underestimation of transfer function peaks in the identification procedure is a prerequisite for guaranteed stabilization of the respective mode by the designed controller.

Therefore, the identification algorithm has been extended with a model post processing module. This module is based on numerical optimization and fine–tunes the frequency and damping of the identified poles such that the measurements are perfectly matched.

6.2.6 Summary

In this chapter, the various identification and controller design methods presented in the previous chapters have been assembled to a procedure for identification and automated controller design for flexible rotor AMB systems. The procedure is organized in a modular way. Its constituent modules have been presented, and their interaction in the overall three phase procedure has been described.

Furthermore, new software tools for quick transfer function extraction and evaluation have been introduced. The software is documented in [Lösch01]. For further automated features, the reader is referred to Appendix A.

Chapter 7

Experimental
Investigations

This thesis would be incomplete, had the algorithms designed not been implemented and tested in practice. Such tests have been carried out, and in this chapter the test rig and the experiments performed are presented, followed by the experimental results and a discussion.

7.1 Test Rig

For testing of control, identification, and fault detection related algorithms, an AMB test rig has been designed and built. The main requirements on this rig were the following:

Flexibility. The test rig was to allow implementation and testing of as wide a range of AMB related algorithms as possible.

Versatility. Testing of algorithms was to be possible in a general setting, allowing to draw conclusions concerning the quality of the algorithms. Restriction to special cases was to be avoided, ruling out lucky guesses and similar effects in algorithm design.

Short implementation cycles. Implementation and adaptation of algorithms were to be as easy as possible. Debugging was to be facilitated by adequate tools and short compilation times.

Availability. Since the focus of work was on the design of algorithms for
   AMBs rather than on design of a test rig, the building of the rig was
   to consume as little resources (in particular: time) as possible.

Based on the last of the above criteria, it has been decided to modify an
existing system rather than developing a new AMB test rig from scratch.
The system of choice was a commercially available system, a MECOS Mini
VS, that had been used in an earlier project. In its original form, this sys-
tem consisted of two radial bearings, an axial bearing, and an asynchronous
drive with a maximum speed of 30000rpm. Available in different configu-
rations, the present version was equipped with a flexible rotor with a mass
of 2.10kg and a length of 310mm. Its first and second bending frequencies
were located at 233 and 722Hz, and the radial and polar moments of iner-
tia amounted to 1.87×10^{-2} kgm^2 and 6.43×10^{-4} kgm^2, respectively.
The five control axes were driven by ten power amplifiers with a maxi-
mum voltage of 50V and a current limited to 6A. The system was con-
trolled by decentralized SISO controllers encoded in MECOS proprietary
software running on a Texas Instruments TMS320C25 processor. The con-
trol unit and the power amplifiers were built into a cabinet with buttons
for performing basic operations such as lifting and dropping the rotor and
a potentiometer for adjusting the drive speed. The system was designed
to be self–contained, however interaction with the system was possible by
means of a link to a PC and a MATLAB interface that provided extended
functionality such as uploading and downloading controllers, monitoring
of signals, and measuring of transfer functions. The test rig in its original
form is shown in Figure 7.1.

The above system has been modified in various ways:

- The position measurement signals and the set current signals have
  been made available to the outside via BNC connectors, allowing for
  external control of the system.

- The radial controllers of the system have been disabled, and a new,
  powerful controller board (a DSPACE 1103 with a 300MHz Power
  PC processor) has been connected to the system. With its high com-
  puting power and the possibility to use SIMULINK as a graphical
  programming interface, it permits short development and test cy-
  cles for algorithms as well as implementation of centralized (MIMO)
  controllers.
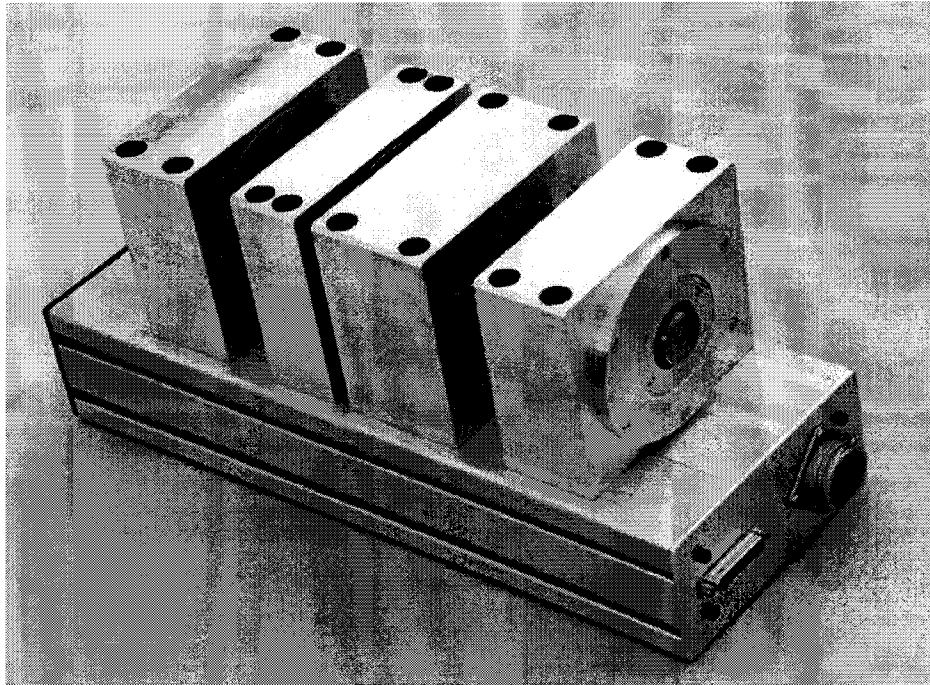
Figure 7.1: *Rig before modification. From left to right: Radial bearing A, axial bearing, asynchronous motor, radial bearing B. The components are mounted on a hollow aluminum profile through which the cables are passed to the connectors of the power amplifiers and the sensors in the lower right.*

- A new rotor has been designed for the system. Being equipped with conical ends and a movable clamping element, this rotor can be configured in many different ways by attaching discs of different sizes and diameters. These adaptations allow variation of the rotordynamic properties of the test rig in a wide range.

- Four additional position sensors have been added to the system for investigation and compensation of sensor faults and for implementation of other 'smart machinery' algorithms [IMP01].

- An extra input has been added to the system for controlling the drive's speed from the new controller board. This enables automated investigation of the rig's behavior at different test speeds without operator interaction.

Although the chosen solution based on an existing rig was considerably quicker than designing a complete new system, the redesign of the MECOS test rig required a considerable amount of time. In particular the entire control and system analysis software had to be rewritten from scratch,

including interrupt handling routines for measuring the rotor's speed (required for unbalance compensation and drive control).

The result, however, was rewarding; the new system met the expectations of providing a flexible, efficiently programmable basis for testing control algorithms not only on a specific system but, by reconfiguring the rotor, on a whole class of systems with very different rotordynamic properties.

The test rig is depicted in Figure 7.2, and its basic technical data is given in the following table:

Rotor

length:	491mm
mass:	3.38 - 6.91kg
moment of inertia, polar:	1.13×10^{-3} - $5.2 \times 10^{-3} \mathrm{kgm}^2$
moment of inertia, radial:	5.31×10^{-2} - $1.88 \times 10^{-1} \mathrm{kgm}^2$
first flexible mode:	101 - 216Hz
second flexible mode:	364 - 616Hz
third flexible mode:	705 - 1296Hz
higher modes:	from 1017Hz

Active Radial Magnetic Bearings

maximum bearing force:	104N
k_i at i_0 =2/3/4 A:	27/40/54 N/A
k_s at i_0=2/3/4 A	123/279/497 N/mm
nominal air gap (s_0):	0.4mm
air gap to retainer bearings (x_s):	0.25mm
maximum voltage (U_p):	50V
maximum coil current (i_{max}):	6A
nominal coil inductivity (L):	3.0mH
coil resistance (R_c):	0.2Ω
coil windings (n_c):	48×2
cross section (A_c):	$9 \times 20 \mathrm{mm}^2$
Sensor Filters:	3kHz second order lowpass
dead time:	0.18×10^{-3}s

Control System

Controller Board:	dSPACE 1103 board
Host Computer:	700MHz Intel P-III PC
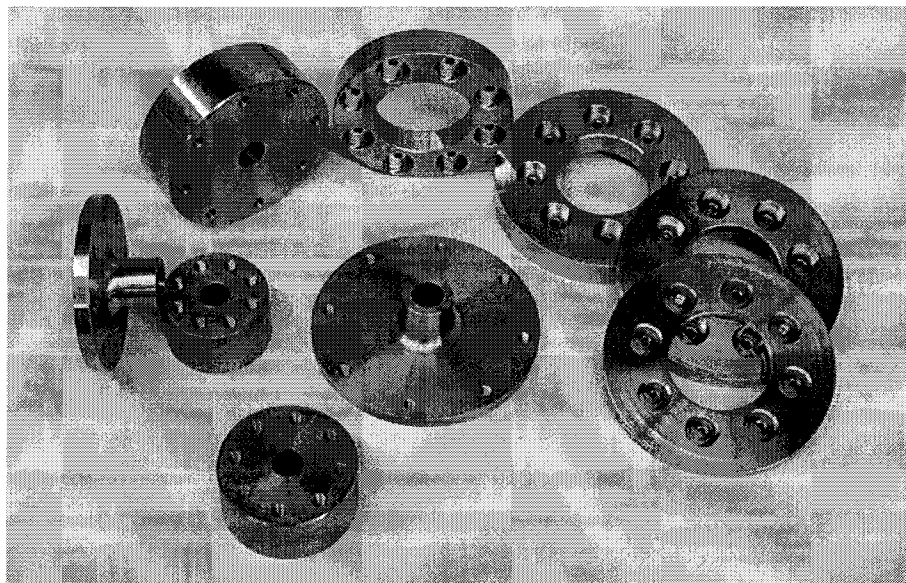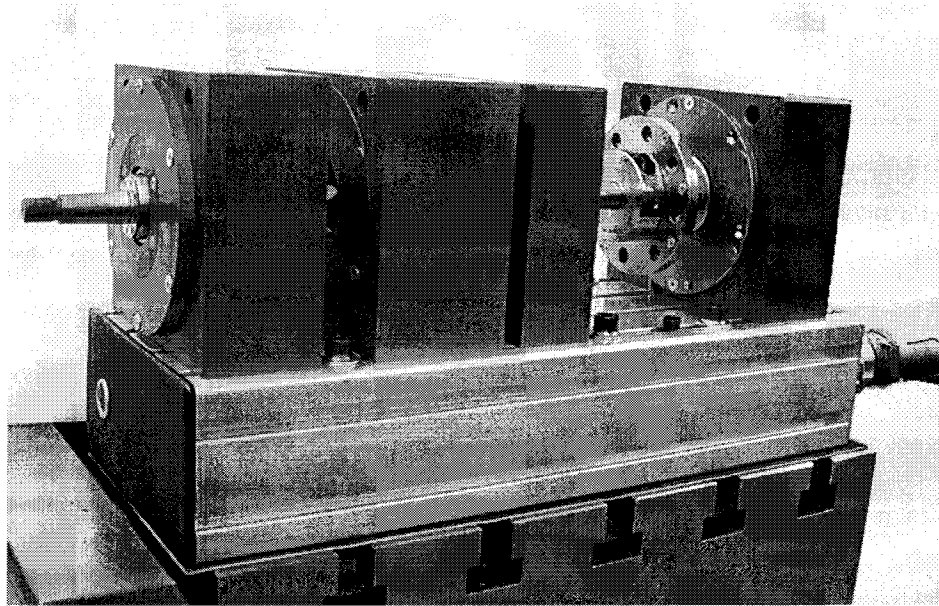
Figure 7.2: *Top: Rig after redesign. From left to right: Radial bearing A, asynchronous motor, axial bearing, radial bearing B. To the right of the axial bearing, the movable clamping element can be seen. At the left end of the rotor, one of its conical ends is visible. Attached to bearing B, the circular ring containing the new secondary sensors can be seen. Bottom: Selected add–on devices of different diameter and mass to modify the rig's rotordynamic properties. The four rings at the right can be attached to the clamping element at the rotor's midspan. The steel discs fit on the rotor's conical ends and are held in place by tightening nuts attached to the threads at the very end of the rotor (top picture).*

7.2   Experiments Performed

The algorithm for identification and automated controller design has been tested on three different configurations of the rig described above. These setups are depicted in Figure 7.3. For transferability of the results, all tests were carried out at a sampling frequency of 5kHz, which is a typical sampling frequency in industrial applications. The bias currents used in the cases presented here were 1.7A, 2.0A, and 2.3A for the three rig configurations, respectively. These values are slightly above the minimum values required for linear operation under the influence of gravity. In experiments performed with a bias current of $i_0 = i_{max}/2 = 3A$, very similar results were obtained.

7.3   Results

7.3.1   Identification of Rigid Body Model

The rotor's rigid body model was identified using the procedure in Chapter 4.1. The steps of this procedure are the following:

1. A current step of size i_{max} is applied to the radial bearing A. Position data from the bearing's two sensors is recorded during the experiment.

2. From the sensor data, the flight phase is extracted and a function of cosh–type (see Equation (4.8)) is fit to the data, yielding an estimate for the pole of the system under consideration. This is done for each of the two bearing axes. The estimate for the pole is obtained by averaging the two values.

3. Based on the estimated pole and the known bearing stiffness, the mass coefficient m_1 is computed using Equation (4.7).

4. A simple controller for levitating the rotor on one side is designed following the guidelines presented in Chapter 4.1.2.

5. With the rotor levitated in one bearing, the force required to hold the rotor in the bearing center is computed based on measurements of the control currents. The force for each of the axes is calculated based on Equation (2.1). The total gravitational force $F_{g,A}$ is then obtained from $F_{g,A} = \frac{1}{\sqrt{2}}(F_{g,A,x} + F_{g,A,y})$.
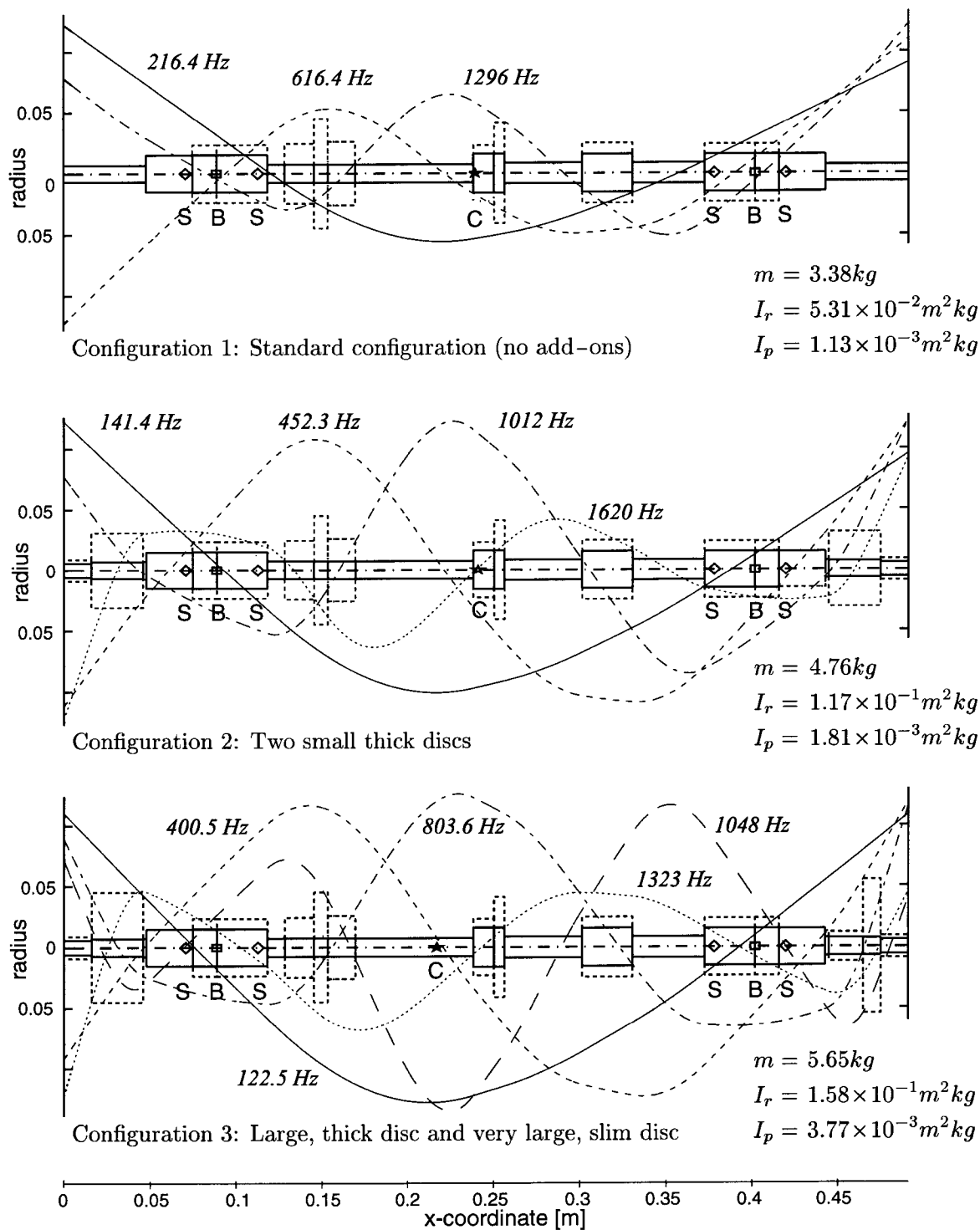
Figure 7.3: *Rig configurations used for testing the algorithms. The flexible mode shapes and frequencies as well as the masses and moments of inertia stem from an untuned Finite Element model. Bearing locations are indicated by a 'B', sensor locations by an 'S'. Only the main sensors (closer to the ends of the rotor) have been used for control in this work.*
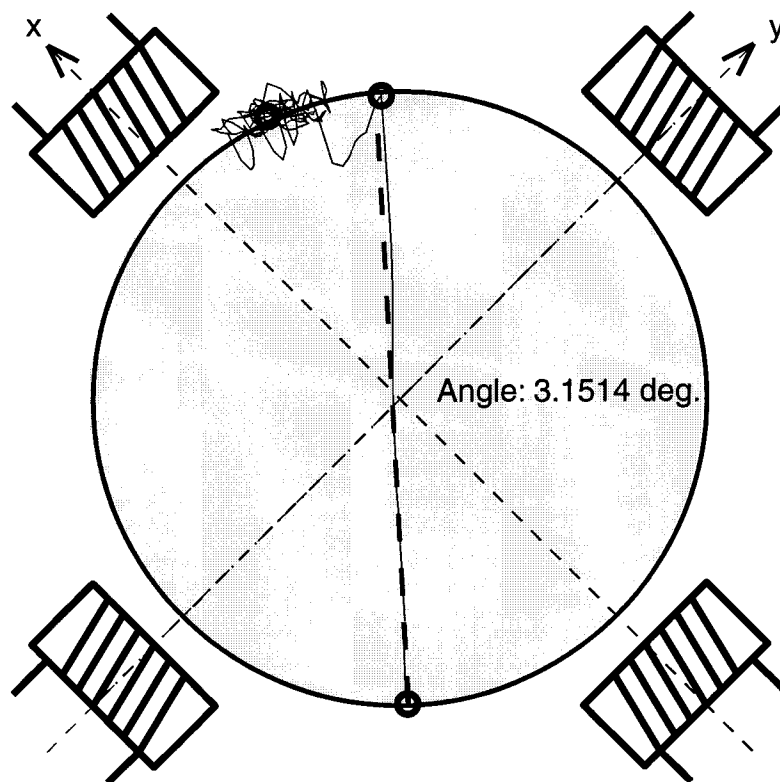
Figure 7.4: *Rotor's motion in the bearing during step experiment. The lift-off point, the location of impact, and the final position are indicated by circles. The angle of flight has been determined based on the lift-off and impact locations.*

6. Equation (4.23) is used to calculate an estimate of the mass coefficient m_3.

These steps are repeated for bearing B, yielding an estimate of the mass coefficient m_2 and a second estimate of m_3. The final estimate of m_3 is computed from the average of the two individual estimates.

Typical intermediate results from this procedure are shown in Figures 7.4 and 7.5. In the first of these figures, the rotor's flight path in the bearing is shown. The flight path is not always vertical, the angle of flight varies in a range of about $\pm 7°$.

In the top half of the second figure, the currents and sensor signals measured during the experiment are depicted, and in the bottom half, the extracted flight path with the fitted cosh–function can be seen.

The above identification procedure makes relatively strong assumptions on the linearity of the bearing. It implicitly assumes that the linear current–force relation derived in Chapter 2.1 holds not only when the rotor is
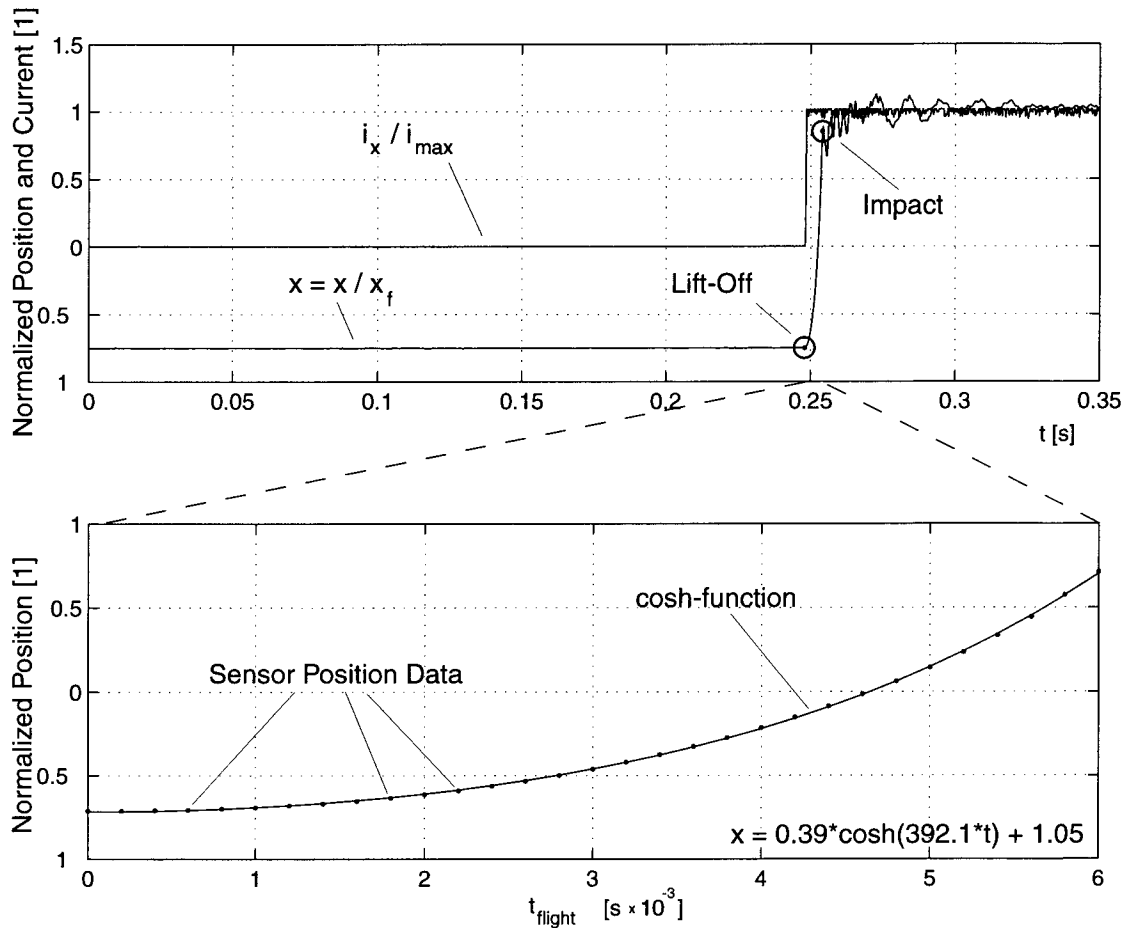
Figure 7.5: *Top: Time data acquired from position and current measurement during the step experiment (in direction of the x-axis). The moments of lift–off and impact are indicated by circles. Bottom: Enlarged view of the flight phase. The sampled position data is indicated by points. Furthermore, the cosh-function whose argument yields the estimate for the pole is shown.*

located at the bearing center but during the entire step experiment, i.e. everywhere in the air gap. Furthermore, all nonlinear effects like the varying stray fluxes affecting the force on the rotor during the different phases of flight are neglected. In view of these approximations, it is of interest to analyze how precisely the procedure works, and how large the systematic error is, i.e. what pole values the method tries to extract when statistical noise is removed.

To this end, the rotors were modeled in a Finite Element program from which their rigid body data was extracted, see Figure 7.3. By application of the transformation from Equation (2.17), this model was transformed to bearing coordinates, yielding reference values for m_1, m_2, and m_3. Based

on the these and the known bearing stiffnesses, reference values for the locations of the poles to be extracted, p_A and p_B (in the following denoted $p_{(A,B)}$), were computed.

If one assumes that

- for each rotor configuration the procedure measures certain pole values $p_{A,meth}$ and $p_{B,meth}$ (not necessarily identical to the respective reference values p_A and p_B due to systematic errors not accounted for in the model), and that

- the disturbances on the procedure are of stochastic nature such that the resulting pole values can be regarded to be of Gaussian distribution with standard deviations $\sigma_{p_{(A,B),meth}}$ and expected values $p_{(A,B),meth,exp}$,

one can compute estimates for the parameters $p_{(A,B),meth}$ the procedure tries to estimate. This can be done based on the fact that for any Gaussian distribution every sample lies within a certain interval about the expected value with a probability P. The size of the interval and the probability P are coupled, for example for a probability of 95% the interval is $\pm 1.96 \cdot \sigma$ about the expected value.

In addition to the above, it is known that given a random variable V with Gaussian distribution with an expected value v_{exp} and standard deviation σ, the average of n values of this random variable , V_{mean}, also is a random variable with Gaussian distribution and the same expected value but with a reduced standard deviation of $\sigma_n = \sigma/\sqrt{n}$ [Bronstein96].

In the present case, this means the following. Being Gauss distributed, the pole measurements $p_{(A,B),meth,i}$ lie within the interval $p_{(A,B),meth,exp} \pm a \cdot \sigma, a > 0$ with probability P. Assuming that n is large enough to replace σ by s, the standard deviation of the samples[1], the average of n samples of this parameter then lies with the same probability P within the interval $p_{(A,B),meth,exp} \pm (a \cdot s)/\sqrt{n}$.

This argument can be reversed to determine the parameter $p_{(A,B),meth,exp}$ the method is trying to identify. By computing the mean values $p_{(A,B),meth,mean} = \frac{1}{n}\sum_{i=1}^{n} p_{(A,B),meth,i}$ and the standard deviation s from $s^2 = \frac{1}{n-1}\sum_{i=1}^{n}(p_{(A,B),meth,i} - p_{(A,B),meth,mean})^2$ for the n samples, the standard deviation of the mean value of the samples can be computed

---

[1]As the number of samples n goes to infinity, s approaches σ asymptotically. For $n \geq 10$, the error is less than 5%.

from $s_n = s/\sqrt{n}$.

Due to the above, one can then state with a certainty level of 95% that the expected value $p_{(A,B),meth,exp}$ (i.e. the parameter the identification procedure tries to estimate) lies in the interval $p_{(A,B),meth,mean} \pm 1.96 \cdot \sigma_n$.

The results of this procedure for the three different rig configurations are presented in Table 7.1. In addition to the information on the poles, the reference and mean values for the mass coefficients m_1 and m_2 are also given. Furthermore, the interval bounds resulting for these parameters from the 95% intervals of the poles have been computed[2]. Finally, the total rotor mass as determined from the Finite Element program is given and contrasted with the average of the values obtained from the $n = 25$ experiments. While the values for m_1 and m_2 show a certain scatter over several experiments due to their dependence on the identified poles, the (static) measurement of the rotor's mass proved to be very repeatable with deviations in the order of one or two percent.

When comparing the pole values yielded by the experiments to a reference model, a good accordance is found. In the case of the first rotor configuration, the deviation is likely to be below 10%. For the second configuration the corresponding value is 15%, and for the third configuration with the two large discs it is below 20%.

This indicates that for the configurations under consideration, identification of the rigid body dynamics based on a linear bearing model is acceptable, as these values correspond to mass uncertainty in the range of 20%, which can be covered by uncertainty modeling (see Chapter 5.1.2).

The increase of the model error with the rotor mass can be explained by the resulting increase in the disturbing force of gravity. In the extreme case where the rotor's mass is so large that it can no longer be lifted by the bearing at all, the linear model clearly is no longer applicable to the pole identification problem. As this situation is gradually reached, heavier rotors can be expected to entail identification results of lower quality. In particular for the third rig configuration this effect is likely to play a role. Here, gravity amounts to about of 63% of the maximum load the bearing can lift from the bottom position, indicating that the border case described above is not very far away[3].

---

[2]The mass values depend in a deterministic way on the pole values. Since this relation is quadratic, the mass values are, given Gauss distributed pole values, themselves not Gauss distributed. This renders the averaging procedure applied for the pole values infeasible for the mass values.

[3]With a maximum load bearing capability of 104N per axis, the maximum load that can be held at the bearing center is $104\sqrt{2}$=147.1N. At the bottom of the bearing, the

Configuration 1					
Parameter	FE-Model	Mean	s	$s/\sqrt{n}$	95% interval
$p_A[1/s]$	467.5	465.5	11.01	2.204	[461.3,469.9]
$p_B[1/s]$	444.5	424.8	43.76	8.753	[407.6,442.0]
$m_1[kg]$	1.331	1.344			[1.318,1.368]
$m_2[kg]$	1.473	1.665			[1.490,1.752]
$M_{rot}[kg]$	3.410	3.359			

Configuration 2					
Parameter	FE-Model	Mean	s	$s/\sqrt{n}$	95% interval
$p_A[1/s]$	353.8	367.9	24.41	4.883	[363.1,372.9]
$p_B[1/s]$	344.3	305.9	39.48	7.896	[298.0,313.8]
$m_1[kg]$	2.324	2.185			[2.093,2.207]
$m_2[kg]$	2.455	3.248			[2.955,3.277]
$M_{rot}[kg]$	4.760	4.588			

Configuration 3					
Parameter	FE-Model	Mean	s	$s/\sqrt{n}$	95% interval
$p_A[1/s]$	337.2	376.9	20.47	4.095	[372.8,381.0]
$p_B[1/s]$	284.8	280.6	14.17	2.835	[242.7,248.4]
$m_1[kg]$	2.560	2.073			[2.005,2.094]
$m_2[kg]$	3.589	4.875			[4.716,4.940]
$M_{rot}[kg]$	5.650	5.267			

Table 7.1: *Results from $n = 25$ repeated rigid body model identification runs for the three rig configurations. The mean values of the pole measurements indicate the pole values the method is trying to estimate. Confidence intervals containing the 'true' parameter with a probability of 95% are given. The mass values result directly from the measured pole values. Their confidence interval has been computed from those of the pole values.*

---

air gap is increased by a factor of 13/8 (from 0.4mm to 0.65mm). This yields a force decrease by a factor of 64/169 for the (in this situation single sided) bearing, which results in a maximum load of 55.7N or 5.7kg that can be lifted by one bearing. The mass effective in bearing B is 3.589kg for the third rig configuration, amounting to 63%

7.3.2 Controller Design for Rigid Rotor Model

The new automated procedure for designing robust controllers for AMB systems with unknown high frequency dynamics has been applied to all three rotor configurations, and convergence has been achieved in all cases. However, due to the horizontal orientation of the test rig rotor, the corner frequency ω_c of the additive uncertainty weight was in all cases larger than 400Hz, which is well beyond the first flexible mode of the systems. Therefore, the algorithm had to be applied in conjunction with the pragmatic 'controlled instability' approach presented in Chapter 5.1.5.

Very good results were achieved with the lead compensator approach mentioned in that chapter. With this approach, stabilization of all test rotors was possible without user interaction. Instability of modes developed very slowly and could be identified and eliminated by an automated procedure that analyzes the sensor signals and introduces notch filters at noisy frequencies.

Taking into consideration the considerably shorter controller design time (five seconds versus five minutes), this second approach clearly outperformed the first one for the horizontal rotors under consideration. With this design method, the entire identification and controller design for the rigid rotor took in the order of 30 seconds for all rotors, automatic removal of noisy modes included.

7.3.3 Identification of Flexible Rotor Model

After levitation had been achieved, the full (flexible) models were identified by means of the procedure presented in Chapter 4.2 in conjunction with the algorithm for peak extraction presented in Chapter 6.2.4. Although the amount of measurements had been reduced to a minimum, flexible models matching the measured transfer functions with good accuracy have been extracted without difficulty. A sample of a transfer function and the corresponding model match for one channel of rotor configuration one is shown in Figure 7.6.

7.3.4 Model Transformation

Since identification of the the flexible rotor model is performed on the system with soft bearing settings (low bias current), the identified model
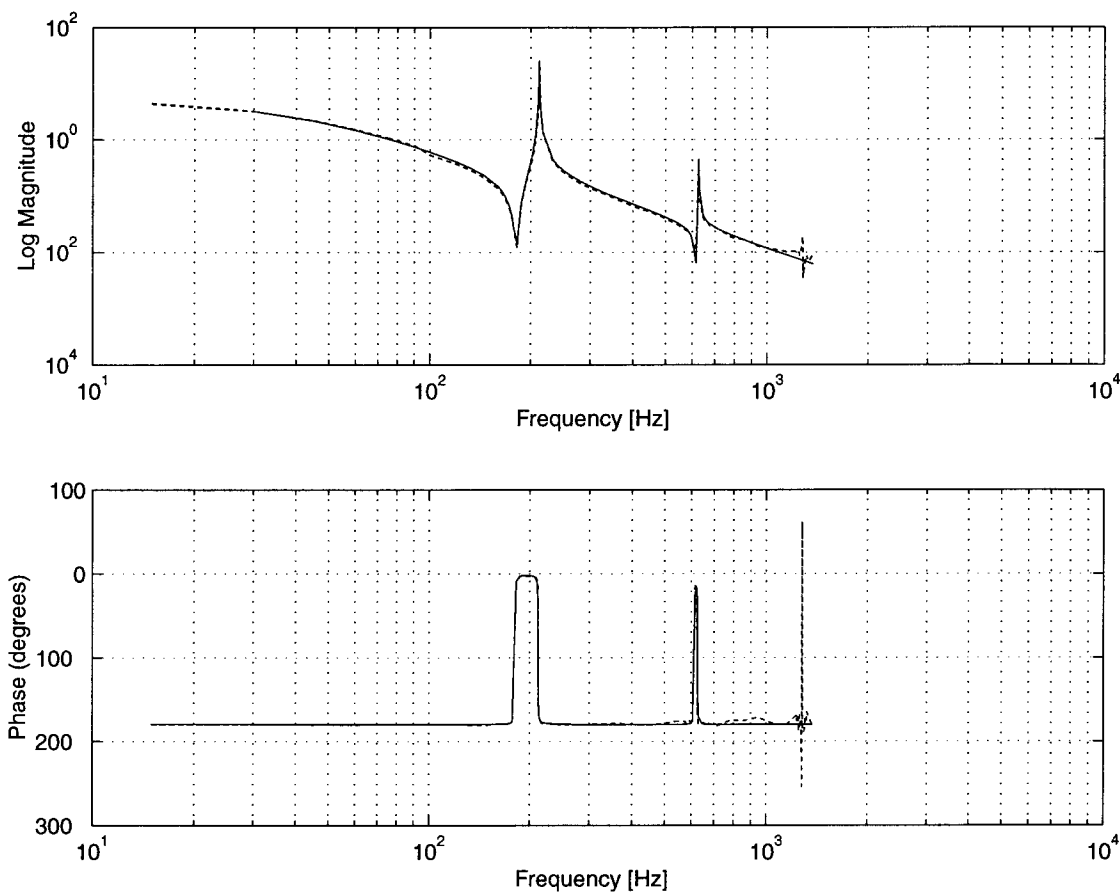
Figure 7.6: *Result from flexible rotor identification. Dashed: Measurement data. Solid: Identified model with 8 states per plane. Only modes up to 800Hz have been considered in the identification. The third mode at about 1300Hz has been ignored and is stabilized by amplitude stabilization.*

must be transformed to reflect the open–loop system with the bearings settings to be used during operation.

An algorithm to perform this task analytically for a state space system systems obtained from modeling of physical systems has been presented in the first part of Chapter 6.2.1. In the second part, application aspects have been discussed, and a procedure for adapting the bearing stiffness of models obtained from identification has been derived.

This method has been applied to increase the bearing stiffness for the models identified from the three configurations. For all systems, no significant difference could be made out between Finite Element models with stiff bearings and the identified models with soft bearings to which the above procedure had been applied. In particular for the critical flexible modes the error was below one percent in all cases.

7.3.5 Initial Controller Design for Flexible Rotor Model

Design of the initial controller is based on the same method as developed in Chapter 5.2. However, since at this point nothing is known about the gyroscopic matrix G, the gyroscopic effects can not be explicitly considered in the design. Therefore, the initial controller design for the flexible rotor model was carried out for the rotor at standstill with an increased (5%) uncertainty on the location of the flexible poles, which aimed at allowing for slow rotation in order to perform a first identification of the gyroscopic matrix G.

The design system was automatically assembled and augmented with second order time delays, the second order sensor filters and with weighting functions designed based on the system parameters and the guidelines from Chapter 5.2.4. The original system order was 16 and the order of the augmented system was 44.

For none of the three configurations were any problems encountered in the design of the initial controllers. Subsequent stability checks and performance analysis on the rig showed the sensitivity function to closely resemble the function predicted by the closed loop analysis based on simulations.

All three rig configurations have been successfully stabilized and accelerated to a low speed of 3000rpm when controlled by their initial controllers. Detailed information on the controllers' order and performance is given in the $K_{initial}$ rows in Tables 7.2-7.4.

7.3.6 Iterative Identification and Controller Design

With the preliminary steps mentioned above completed, the procedure enters its final stage, in which identification of the gyroscopic matrix G, controller design, and controller testing are iterated at increasing rotational speeds until the top speed of the rig is reached or no controller stabilizing the system up to the desired design speed can be found.

Controller Testing

The testing of the controllers is carried out by the module described in Chapter 6.1.2. This module automatically performs measurements and analysis of the system's open loop and closed loop (sensitivity) transfer

functions and identifies critical situations. The test speeds are chosen by an automated speed scheduler that uses model based predictions of the system's gyroscopic pole movements in order to avoid critical speeds, see Chapter 6.2.3. Both the speed scheduler and the analysis routines behaved robustly during the tests.

Identification of Gyroscopic Matrix

Identification of the gyroscopic matrix is performed by the module described in Chapter 6.1.2 based on the algorithm presented in Chapter 4.3 which showed very good performance in simulations. In Chapter 4.3.5 it has been argued that for identified systems with non–collocated actuators and sensors the identification algorithm must be extended with one parameter t_i per pole pair in order to account for the parametric flexibility in state space models obtained from identification.

In the three test rig configurations investigated, identification of these parameters was successful in some cases, however there were always parameters for which the optimization did not converge. This is due to the large range the values t_i may lie in, trading off observability versus controllability for each mode pair.

This however did not significantly hamper the successful operation of the procedure. As has been shown in the simulations in Chapter 4.3.4 , the influence of the off–diagonal parameters on the gyroscopic behavior of the system is rather small. The main part of the effect is covered by the elements in the 2×2 blocks on the diagonal that are unaffected by the scaling parameters t_i. In combination with the uncertainty assumed on the poles in addition to the gyroscopic effects, robust operation of the controllers based on the identified gyroscopic matrix was achieved in all test cases.

Controller Design

Like the design of the initial controller, the controller design method for the gyroscopic rotor model is based on the algorithm developed in Chapter 5.2.

The nominal model is defined to have half of the (maximum) design speed such that the uncertainty in the gyroscopic terms covers the whole operating range from standstill to the anticipated maximum speed. The model

in standard configuration and the weighting functions are automatically computed and assembled to form the design system. The design is automatically initiated. After its completion, the analysis tool described in Chapter 5.2.5 is started and the user is prompted to inspect the result and decide if he agrees that the controller be downloaded and tested on the rig in the next iteration cycle.

At this point, the user has full access to the system which allows him to perform further tests or to repeat the design with different parameters, if necessary.

The rules for weighting function selection from Chapter 5.2.4 were extended in two ways:

A second order high pass filter with a corner frequency of 600Hz was multiplied to the output weighting function $\mathbf{W_u}$, enforcing a roll–off of the controller at high frequencies. This led to a more quiet operation of the system. The price however, was an increase of the controller orders by $4\times2=8$ states.

Additional improvements have been achieved by adding a first order weight to each channel, penalizing the rotor displacement $\underline{y}$ at very low frequencies (below 1Hz) via the weighting function $\mathbf{W_y}$. Rather unspectacularly, this causes the controller to contain an integrator to compensate for static disturbance forces. However, as a side effect, this modification causes the resulting controllers to have a significantly reduced gain around the flexible modes that are located in the *medium* and *high* frequency ranges already before the relocation of poles described in Chapter 5.2.4 is started. This is in contradiction to the paradigm in robust control that local changes to weighting functions only have local effect on the closed loop behavior. A possible explanation for this behavior which was consistently observed is that the changes in the low frequency range affect the algorithms computing the D-scalings in the D–K iteration, which then directs the optimization towards a different local minimum.

The gain reduction achieved with this approach considerably accelerated the search for controllers that fulfill the performance requirements. With this modification, the number of iterations required in the design procedure has been significantly reduced — in the majority of cases investigated, robustly performant controllers were obtained in the first step, see Tables 7.2-7.4 in the next section.

Iteration Results

This section contains the results from application of the iterative identification and controller design algorithm to the three test rig configurations shown in Figure 7.3.

For each of the configurations, the information on the individual controllers and their performance has been summarized in a table. Besides the maximum design speed, the number of iteration runs that were required to arrive at the controller and the controller size (before and after reduction), the most important results from the testing of the controllers are presented. These comprise the speeds at which tests were carried out as well as a comparison of the measured pole locations with those predicted by the model based on which the controllers had been designed. Furthermore, the height of the highest sensitivity function peak is given for each rotor at its maximum test speed.

Table 7.2 contains the results for the first rig configuration. Besides the initial controller, three controllers were required to accelerate the rotor to its final speed. All of the controllers were designed in one step, i.e. without iteration. After reduction, the controller order was 24 in all cases. The test speeds for the initial controller were 0 and 3000rpm (the latter being predefined).

Based on the gyroscopic matrix identified at 3000rpm, a controller K_1 with maximum speed 9000rpm was designed. This controller was tested at 7312rpm, which indicates that a weakly damped closed loop pole was found at 9312rpm (2000rpm being the predefined security distance from potentially hazardous speeds[4]). No tests at higher speeds were made by the algorithm due to the controller's maximum design speed being (9000rpm) being less than 2000rpm away from the last test speed.

The gyroscopic matrix was again identified at 7312rpm, and based on the resulting model the controller K_2 with a maximum design speed of $3\times7312=21936$rpm was designed. This controller was tested at 10062rpm (2000rpm below the predicted critical speed at which the first flexible backward was going to be passed), at 15327rpm (The smallest acceptable speed beyond the first backward mode which in fact is 2000rpm after passing the

---

[4]It is important to understand that it is in general not sufficient to consider the flexible eigenfrequencies of the open–loop rotor as critical speeds. During operation, all *closed loop* poles must be taken into account. Since the location of the open–loop flexible poles is only marginally affected by the controller, these will always be among the weakly damped closed loop poles. However, they may be joined by weakly damped controller poles that also may not be destabilized, constituting addition critical frequencies.

Configuration 1							
					at Maximum Test Speed		
Ctrlr.	Design Speed [rpm]	# Des. Iter.	Order	Test Speeds [rpm]	Predicted Poles [Hz]	Measured Poles [Hz]	Sens. Peak
K_{inital}	0	1	44/24	0 3000^0	212.2^1 625.0^1	209.2/214.0 621.8/628.0	2.45
K_1	9000	1	54/24	7312^2	205.1/217.8 616.9/633.4	206.0/217.4 616.0/634.0	3.15
K_2	21936	1	62/24	10062^4 15237^4 20478^3	196.5/229.2 600.1/651.2	196.4/227.8 599.0/650.5	<2
K_3	30000	1	66/24	10062^4 15237^4 21237^5 26698^6	193.8/233.9 593.2/658.6	191.8/232.6 591.0/657.0	2.1

0: Predefined low set speed

1: No explicit prediction, but ±5% uncertainty margin on frequencies

2: Limited by critical speeds leaving no room for higher test speeds

3: Limited by stronger than predicted pole displacement found in prior test

4: Enforced by adjacent critical speeds

5: Limited by predefined max. speed step size of 6000rpm

6: Tests were aborted at this speed due to drive limitations

Table 7.2: *Experimental results for the first rig configuration.*

first forward mode), and at 20478rpm. This final speed resulted from a comparison the peak locations measured at 15327rpm with those predicted by the model underlying the controller design, which indicated that beyond 20478rpm the modes would leave the region considered in the design (not considering the 3 percent uncertainty margin, which justifies experiments being carried out at this speed).

Again, the gyroscopic matrix was extracted, and the controller K_3 aiming at stabilizing the rig up to its maximum speed (30000rpm) was designed.

The test speeds for this controller were the same as for the last one up to 15237rpm. The test performed at this speed indicated no nearby limitation, which allowed the automated speed scheduler to apply the maximum speed step size of 6000rpm, yielding the next set speed at 21237rpm. There, the acceptable maximum speed was identified to be 26698rpm. This speed was only barely reached due to limited drive power[5]. The tests performed at this speed indicated that no further speed increase should be made due to larger than predicted pole displacement.

The test rig being at its limit, the tests have been aborted at this point. The pole displacement controller K_3 successfully dealt with was 9.6% (for the first flexible mode, 5.4% for the second mode.)

The experimental results for the second rig configuration are shown in Table 7.3. Like in the case of the first rig configuration, three controllers were designed after the initial controller. Except for controller K_2, all controllers were obtained in one step. K_2 was derived after adjusting the pole damping as described in Chapter 5.2.5 in the third attempt. The order of the reduced controllers was between 18 and 22. The initial controller was again tested at 0 and 3000rpm. The gyroscopic matrix identified at 3000rpm was used to design controller K_1 that was tested at 5812rpm (limited by the first backward mode and the maximum design speed of 9000rpm).

At this speed, the gyroscopic matrix was again identified, and controller K_2 was designed with a maximum speed of 3×5812=17436rpm. In the first design attempts, the closed loop analysis indicated problems with the sensitivity function in the vicinity of the flexible modes. This was corrected by 'pulling back' the flexible poles into the stable half–plane as described in Chapter 5.2.5. In spite of an analysis result inferior to those typically achieved, the controller from the third iteration proved to levitate the rotor. It was used to accelerate the system up to 15709rpm, well beyond the first flexible mode. Intermediate stops were made at 5787rpm and 10812rpm, below and above critical frequencies caused by the first flexible mode pair. At the latter speed, the measured pole dislocation was found to be larger than expected, which led to the test at 15709rpm. This test indicated that the speed could be increased to 16176rpm. However, this was not done by the automated speed scheduler since the speed step would have been

---

[5]Due to the rotor's larger moment of inertia and increased air friction caused by the clamping element, the set speed could only be increased very slowly for speeds beyond 23000rpm. The speed of 26698rpm was reached after several unsuccessful attempts in which the drive's inverter shut down. Towards the end, the set speed steps employed were as small as 50rpm.

Configuration 2							
					at Maximum Test Speed		
Ctrlr.	Design Speed [rpm]	# Des. Iter.	Order	Test Speeds [rpm]	Predicted Poles [Hz]	Measured Poles [Hz]	Sens. Peak
K_{inital}	0	1	44/18	0 3000^0	142.1^1 457.6^1	139.8/143.8 453.4/462.0	2.84
K_1	9000	1	60/18	5812^2	137.9/146 449.4/467.2	138.0/145.8 450.2/466.6	3.48
K_2	17436	3^7	64/22	5787^4 10812^4 15709^3	132.5/154.2 436.9/482.3	133.0/152.6 435.5/479.0	3.81
K_3	30000	1	70/22	5787^4 10895^4 16895^5 22895^6	133.0/154.7 435.0/483.1	131.8/153.8 433.5/481.5	3.35

0: Predefined low set speed

1: No explicit prediction, but ±5% uncertainty margin on frequencies

2: Limited by critical speeds leaving no room for higher test speeds

3: Limited by stronger than predicted pole displacement found in prior test

4: Enforced by adjacent critical speeds

5: Limited by predefined max. speed step size of 6000rpm

6: Speed not reached. Drive failed to pass 21350rpm. Results are from 16895rpm

7: In the analysis, this controller still appeared to be a borderline candidate

Table 7.3: *Experimental results for the second rig configuration.*

smaller than the predefined minimum speed step size of 2000rpm.
As a consequence, the gyroscopic matrix was identified at 15709rpm, and a new controller, K_3, with a nominal maximum speed of 30000rpm was designed. This design was successful in the first step with the settings used in designing K_2, and the closed loop analysis for the resulting controller indicated slightly better closed loop characteristics than in case of K_2. This

controller brought the rotor via test speeds at 5787rpm and 10895rpm to 16895rpm. In the last step, the maximum speed step size of 6000rpm was applied. The test at 16895rpm again indicated that application of the maximum step size should be possible, defining the next test speed to be at 22895rpm. This speed, however, could not be reached since the drive failed to pass the limit of 21350rpm due to the increased axial moment of inertia.

Extrapolation of the values gathered at 16895rpm indicates that at this speed the pole displacement successfully handled by the controller was in the order of 10.4% percent (for the first mode, for the second mode the pole displacement was in the range of 6.6%).

For the third rig configuration, the experiments yielded the results from Table 7.4. Like in the two other cases, four controllers stabilizing the system over increasing speed ranges were successively designed. All controllers except K_1 were found in only one iteration step. For K_1, two such steps were required. After reduction, the controller orders were in the range from 22 to 24.

The gyroscopic matrix identified at the initial controller's maximum speed, 3000rpm, was used to design controller K_1, with which the rotor was accelerated to 5012rpm, limited by the first flexible mode pair and the maximum design speed of 9000rpm. At this speed, a new gyroscopic matrix was extracted, based on which controller K_2 was designed. Its maximum design speed was 15036rpm, and after critical speed related stops scheduled at 4962rpm and 10112rpm, a speed of 12766rpm was reached. At this speed, the test module indicated that no further speed increase should be made, and the gyroscopic matrix was again identified. In the next step, it was attempted to design a controller with a nominal maximum speed of 30000rpm. This however was not possible after 5 attempts. Therefore the maximum design speed was reduced to 20000rpm, at which the controller K_3 could be obtained. Using this controller, the rotor was spun up to the final speed of 16062rpm. The pole displacements at this speed were as large as 16.7% for the first mode and 18.7% for the second mode. Test results at this speed showed that with controller K_3, the speed should not be further increased. No attempts to design a new controller were made since speeding up the rotor to 16062rpm was already difficult with the underdimensioned drive. Furthermore, the test module indicated the second backward critical speed to be located near 20000rpm, which might have been difficult to pass at such low speed increments. In addition to this, the unsuccessful attempt to design a controller for 30000rpm indicated that the method would have difficulties to determine a controller

Configuration 3							
					at Maximum Test Speed		
Ctrlr.	Design Speed [rpm]	# Des. Iter.	Order	Test Speeds [rpm]	Predicted Poles [Hz]	Measured Poles [Hz]	Sens. Peak
K_{inital}	0	1	44/22	0 3000[0]	125.2[1] 402.0[1]	121.6/129.0 390.4/413.6	3.16
K_1	9000	2	62/22	5012[2]	119.4/131.6 383.3/421.6	118.6/132.0 382.5/421.5	3.02
K_2	15036	1	62/24	4962[4] 10112[4] 12766[3]	110.1/143.5 365.5/453.6	108.6/142.2 343.6/445.5	3.01
K_3	20000	1	54/22	4787[4] 10062[4] 16062[5]	107.5/147.3 340.7/459.6	104.5/146.0 327.0/453.0	3.60

0: Predefined low set speed

1: No explicit prediction, but ±5% uncertainty margin on frequencies

2: Limited by critical speeds leaving no room for higher test speeds

3: Limited by stronger than predicted pole displacement found in prior test

4: Enforced by adjacent critical speeds

5: Limited by predefined max. speed step size of 6000rpm

Table 7.4: *Experimental results for the third rig configuration.*

capable of reaching speeds beyond the second critical speed.

With increasing design speed being the second goal of the algorithm besides automation, it is important to report the time required for performing each of the steps taken in the algorithm. This is done in Table 7.5. The total time from the starting point of the procedure with no information on the rotor (beginning of algorithm phase one) to the end of the test of the final controller was in all cases below two hours (up to rig–specific problems with the drive that required manual acceleration of the rotor by very small set speed steps).

Task	Time required
Controller design, one iteration:	3–5 minutes
Controller testing, one test speed:	4–5 minutes
Identification of gyroscopic matrix:	2–3 minutes

Table 7.5: *Time requirements of individual steps of the design procedure.*

Run–Up Experiments

In order to further assess the controllers' performance on the different rig configurations, the vibration amplitudes occurring during run–up have been recorded. The results of this investigation are shown in Figures 7.7 and 7.8.

For rig configurations 2 and 3, the vibration amplitudes measured were found to be surprisingly large, in the order of 25% of the air gap instead of the anticipated 10%. This is due to convergence problems in identifying the off–diagonal blocks of the gyroscopic matrix G. As has been fully elaborated in Chapter 4.3.5, identification of G is particularly difficult in the context of identified rotor models. This is due to unknown scaling parameters that do not affect the model of the system at standstill (which makes them impossible to determine a priori). These parameters do however have significant impact on the off–diagonal blocks of the matrix G. In the algorithm for identification of the gyroscopic matrix G, it is attempted to determine these parameters. However, convergence is not always achieved due to the large search range.

Failure to correctly determine the off–diagonal block entries of G entails amplitude errors at the locations of the shifted poles for the rotating model, see Chapter 4.3.2. This effect caused the large vibration amplitudes encountered for rig the second configuration with controllers K_2 and K_3 as well as for the third rig configuration with controller K_2. For the last controller of this configuration, K_3, the identification converged, resulting in the considerably lower vibration amplitude during run–up, see Figure 7.8.

To confirm this statement controller design has been repeated for the most critical case, the second rig configuration, with a gyroscopic matrix obtained from a Finite Element model. The design has been performed with the identical settings as before. The model was (up to the gyroscopic matrix) the same as in the case analyzed above.

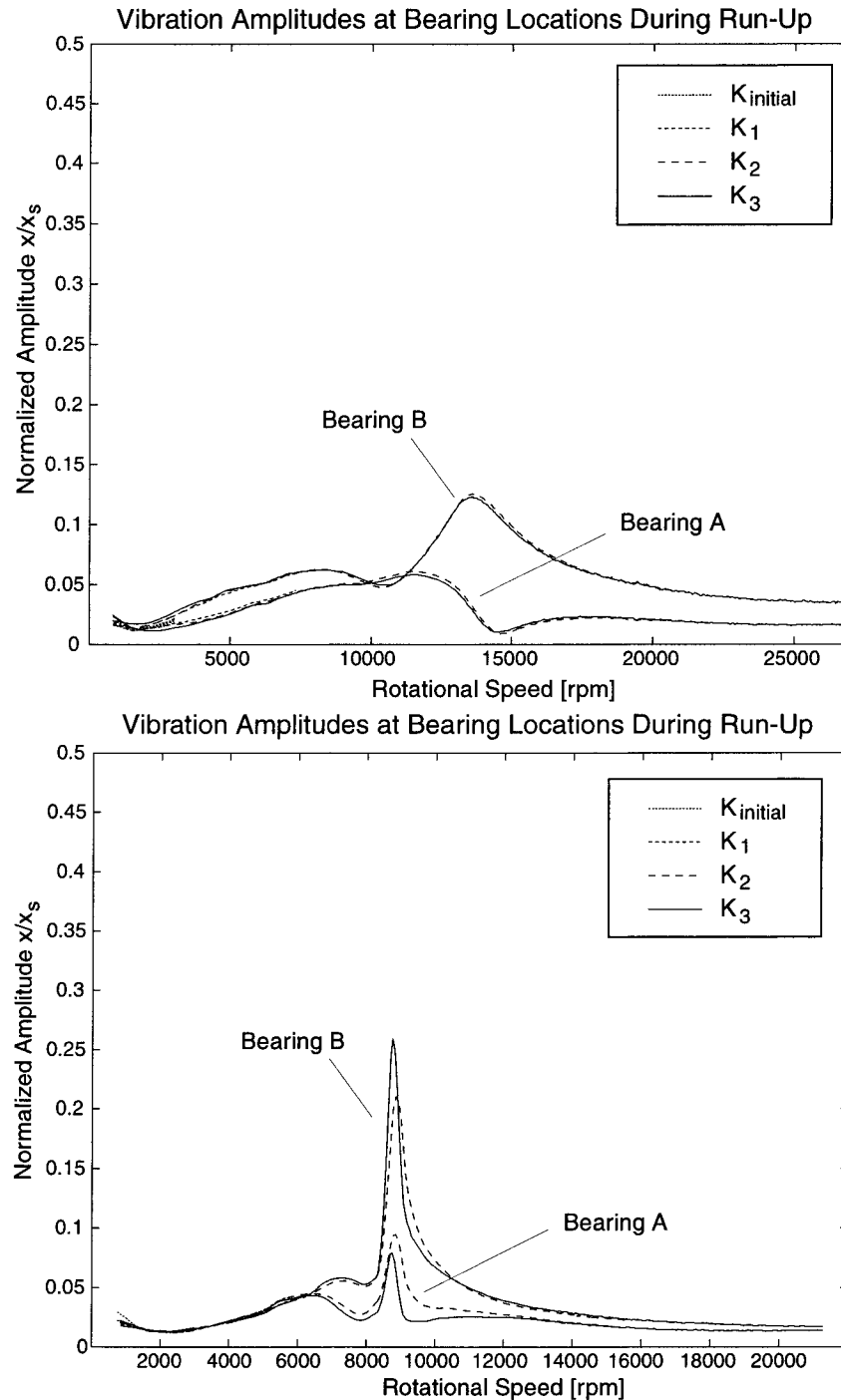Figure 7.7: *Vibration amplitudes caused by unbalance forces during run-up with different controllers. The deviations have been measured at the sensor locations. Top: Rig configuration 1. Bottom: Rig configuration 2. The unexpectedly large amplitude when passing the first forward mode of the second rig configuration results from problems in identifying the off-diagonal block entries of the gyroscopic matrix G.*
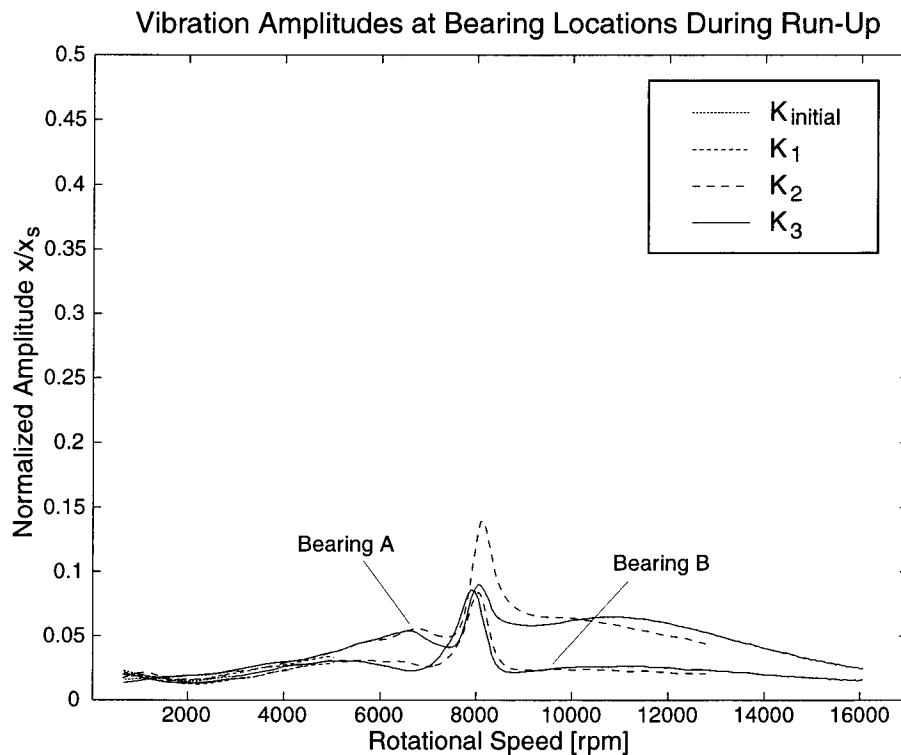
Figure 7.8: *Vibration amplitudes caused by unbalance forces during run-up with rig configuration 3. Controller K_2 exhibits increased amplitudes due to problems in identification of the gyroscopic matrix G. Controller K_3 shows good performance due to successful identification of G. The deviations have been measured at the sensor locations.*

Only one controller was designed (directly for the maximum speed). The vibration amplitudes resulting from operation of the rig with this controller are depicted in Figure 7.9. A much lower level of vibration has been reached (below the desired 10%).

As can be seen from the plots, the rigid body modes could in all cases considered virtually not be noticed when the corresponding critical speeds were passed. This shows that good damping was achieved which is confirmed by the fact that typically no stops are made by the speed scheduler due to rigid body modes.

Vibration Amplitudes at Bearing Locations During Run-Up
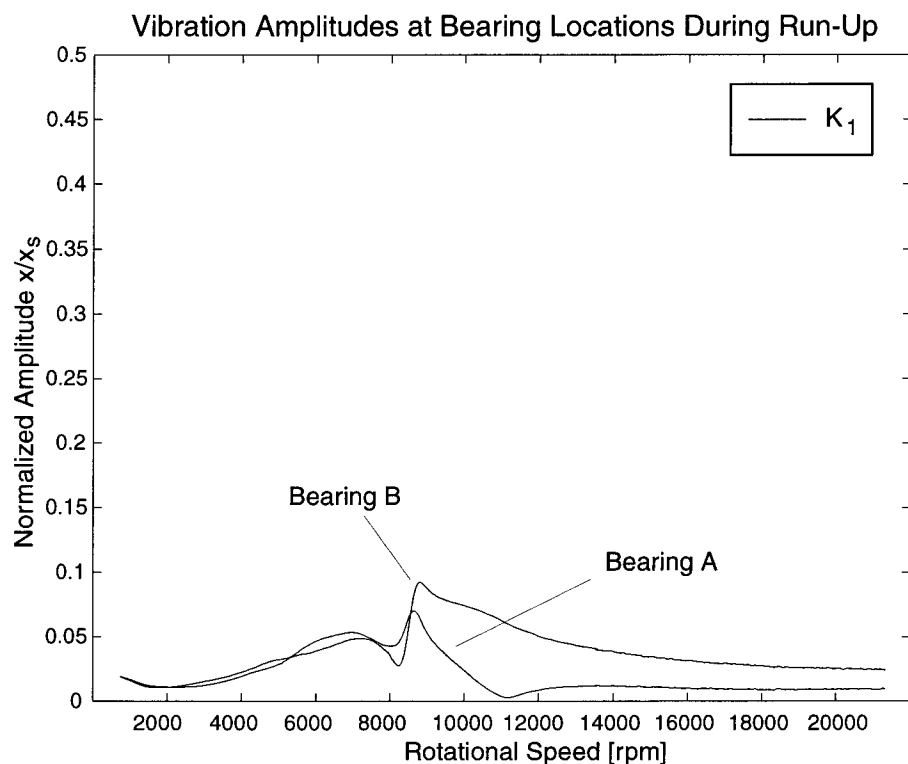
Figure 7.9: *Vibration amplitudes caused by unbalance forces during run–up of rig configuration 2 with controller designed using the gyroscopic matrix from the Finite Element model. All other design settings are identical to the case shown in Figure 7.8, bottom. Since no identification of G was required, the controller has been designed in one single step.*

7.4 Discussion

The experimental results presented above show the working of the identification and controller design algorithm developed in this thesis. The fact that three rig configurations with very different rotor dynamics were successfully identified and stabilized up to speeds well beyond the first flexible backward and forward modes justifies confidence in the general applicability of the method.

On the example of the third rig configuration which was equipped with a very heavy and highly gyroscopic rotor, the algorithm has been shown to be applicable also for demanding control tasks[6].

Although difficulties in identifying some entries of the gyroscopic matrix

---

[6]The rotor used in this configuration had a mass 2.7 times higher than the rotor originally commissioned with the system by the manufacturer, with gravity amounting to 30% of the maximum bearing force.

caused in some cases an increase in vibration amplitudes during run–up, the strong gyroscopic effects successfully dealt with in the experiments prove the effectiveness of the identification algorithms.

However, in cases where strongly gyroscopic flexible modes are to be passed at higher speeds than encountered in the above examples, it seems advisable to resort to a gyroscopic matrix or a rotor model (without gyroscopic matrix) from a Finite Element program in order to circumvent these problems.

The goal of accelerating the design process has been achieved. With controller design times of about 30 seconds for a first levitation and less than two hours for the final controller, the presented method sets new standards in controller design speed.

Furthermore, it was possible to reduce the user interaction and in particular the expertise required to a minimum. In contrast to the conventional methods, controllers can be designed by persons with only basic knowledge. Furthermore, the system runs independently during most of the design time, which leaves it up to the operator to use this time for other tasks.

In the traditional controller design methods, *each* of the steps modeling, model updating, controller design, and controller testing would have typically taken significantly longer and required substantially more know–how than the new procedure in its entirety.

It is tempting to move the judgement whether or not a controller is good away from the numerical analysis (based on comparison of the individual transfer functions' size to the limit one as described in Chapter 5.2.5) to the tests performed on the rig.

This approach is supported by the reliable test algorithm that automatically schedules the test speeds such that no critical speeds are passed without analyzing the system behavior at a speed closely below the critical speeds. Furthermore, the fact that the controllers are designed at a nominal speed of half the maximum speed implies that the system at standstill actually is a system with maximum disturbance, lying at the very border of the uncertainty set considered in the design, just opposite of the system with maximum speed. Therefore, levitation of the rotor at 0rpm in fact is a difficult test for a controller to pass. If this is accomplished, this gives confidence — but no guarantee — that the controller should be able to stabilize the system well beyond the nominal speed[7].

---

[7]No statement is made about performance here, instability may well occur due to actuator saturation or too large orbits entailed by unbalance forces!

In the cases where this strategy has been applied, it was always successful — a large portion of the controllers that did not pass the formal μ analysis test after the controller design failed to stabilize the system at standstill. *All* of those controllers, however, that passed this test were indeed suited to accelerate the rotor to speeds near the their maximum design speeds. In none of the cases were any problems observed. However, this cannot be formulated as a general rule. For different systems, things may look different. Generally, safe ground is left when a critical analysis result is ignored, and any further steps are at the user's risk.

As becomes apparent in the case of test rig configuration three, where no controller could be designed for 30000rpm, controller design for gyroscopic rotors becomes more and more difficult with increasing design speed. This results from the gyroscopic pole displacements that increase with the rotational speed, requiring the controller to be robust with respect to greater and greater uncertainty sets.

This is a general problem that holds independent of the design method chosen. With more than 18% the level of gyroscopic pole displacement that could be handled for flexible poles was not far below the value of 22.3% dealt with in [Gähler98] for the rotor with rigid disk, which could only be stabilized with large efforts by means of the phase shaping controller design method.
This is a significant increase compared to the 3% achieved in [Schönhoff00b] which has been the state of the art in μ-synthesis based AMB controller design to date.

Nevertheless, for sufficiently high design speeds it will always be possible to arrive at a system that cannot be stabilized directly by the method presented. For such systems, it is recommended to apply a controller scheduling technique. With minimal adaptations, the presented method can be modified such that when no controller has been found for operation of the plant from 0rpm to a certain maximum design speed, controllers for a limited range of high speeds are designed.
One of the existing controllers is then used in the range of low speeds up to its maximum operating speed determined in earlier tests, where the system switches to the new controller designed for the range of high speeds. This concept can be fully embedded in the presented iterative test, identification and design loop. Furthermore, switching is not limited to two controllers since the first controller can be replaced by a third one after having been relieved of its duty by the second controller. This technique allows to operate systems with strong gyroscopic effects at high speeds.

Furthermore, smooth switching between controllers is possible [Li01].
While testing of high speed controllers in any scheduling framework must
be considered a risky activity when conventional design methods are ap-
plied[8], the analysis tools available in the presented method are suited to
give *a priori* a maximum of reassurance that a given high speed controller
will actually stabilize the system.

---

[8]In case of instability, the rotating rotor will touch the retainer bearings. At
high speeds, rotor–stator contact in rotating machinery may have disastrous effects
[Bartha00]. This even holds in the presence of backup bearings [Larsonneur90].

Chapter 8

Conclusions and Outlook

8.1   Summary and Conclusions

Starting point of the present thesis was an analysis of the state of the art in AMB controller design for flexible rotors which revealed a situation governed by a number of difficulties and no adequate solution at hand.
Among the biggest problems that have been identified was the need for large amounts of both expertise and time in order to arrive at a suitable controller. Further difficulties arose from the interdisciplinary nature of the sub–problems encountered in controller design, among them model updating for rotor structures which falls into the domain of mechanical engineering and transfer function shaping by placement of poles and zeros, a field of expertise of control engineers.

This thesis aimed at improving this situation by eliminating the above weak points: A new controller design procedure was to be developed, with special focus on ease of use and reduced design time. In particular, the amount of special know–how required by the control engineer was to be reduced as far as possible.

One of the main challenges on the way to reaching these goals was to find a way to overcome the initial deadlock situation, in which neither a model nor a controller are present, and a controller is required to identify a model that in turn is a prerequisite for controller design in the first place.
This has been achieved by application of a step–wise procedure involving several identification and controller design steps.

First, a coarse rotor model containing only the rigid body information is identified by means of experiments that do not require levitation of the rotor. In a second step, this preliminary model is used for designing a controller that merely achieves levitation of the rotor in AMBs with low stiffness, allowing for identification of the entire rotor model including the flexible modes. After making adjustments for stiffer bearings, the resulting flexible rotor model is used to design a controller stabilizing the flexible rotor in AMBs with nominal settings.

For the identification of the rigid body model, a new method based on current step experiments and single sided levitation has been developed. The initial controller design is based on a μ-synthesis design with a framework focusing on robustness against uncertain high frequency dynamics. Model uncertainties from identification errors are also explicitly considered. For the identification of the flexible rotor, the algorithm from [Gähler97] has been employed with minor adaptations to improve model precision at the critical flexible peaks' amplitudes.

The subsequent flexible controller design is again performed by an algorithm based on μ–synthesis. The basic approach is that from [Schönhoff00b], however fundamental modifications in the uncertainty modeling, design system setup, and analysis have been made in order to better exploit the potential of the method.

When levitated by the new controller, the rotor is accelerated to a low speed at which the gyroscopic matrix is identified by means of a new identification algorithm. The resulting improved model is then used to design a controller that achieves robust performance up to a higher rotational speed. Identification of gyroscopic terms, controller design, and controller performance tests are iterated, and the rotational speed is successively increased until the desired maximum speed is reached or no further improvements can be made.

Both the controller design and the identification steps involved in the above procedure have been largely automated and integrated in a closed procedure that does not require any modeling. Nevertheless, when external models are supplied, the procedure can be started at any intermediate point, giving considerable flexibility to the advanced user.

The effectiveness of the designed algorithms has been proven in experiments on a test rig with reconfigurable rotor. The rotor configurations considered in the tests differed considerably with respect to their mass, eigenfrequencies, and gyroscopic behavior, proving the applicability of the algorithm to a wide range of AMB systems.

In the cases investigated, the model order of the AMB systems was 16, two flexible modes per plane have been considered while modes with a frequency higher than 800Hz have been cut off by means of a lowpass filter. The order of the augmented plant including weighting functions, time delays, and sensor filters was 44. The resulting controllers had orders up to 70, but were in all cases without difficulty reduced to 24 states or less. After the reduction, the controllers have been discretized and implemented on the rig with a sampling rate of 5kHz. In the subsequent experiments, the system was accelerated to speeds up to more than 26000rpm, limited by low drive power. In the analysis of the algorithm's performance, the limited speed was made up for by considering systems with particularly gyroscopic flexible modes.

The experimental results show that the goals defined at the outset of the work have been achieved. The new method is considerably faster than any existing controller design and identification approach. Less than two hours were required to design controllers even for highly gyroscopic rotors (18.7% mode displacement), and no initial rotor model was required for controller design. The majority of this time was actually spent on the testing of the controllers, which also has been automated and is an integral part of the design procedure.
Furthermore, the expertise required to perform controller design has been reduced to a minimum, the algorithm runs automatically and requires only minimal user interaction.

Due to its open structure, it is not necessary to run the algorithm from the very beginning. Available rigid body data of the rotor can be imported into the algorithm, skipping the rigid body identification phase.
In case a levitating controller exists already (for example from prior design attempts with different controller design methods or from studies carried out in the design phase of the rotor), this controller can serve as a starting point for the algorithm.
When the user–supplied controller only barely achieves levitation, the facilities for noise elimination (automated addition of notch filters) can be used, and the algorithm starts with the identification of the flexible rotor model, skipping the controller design based on rigid body rotor models.
If the controller supplied by the user is more advanced and has been shown to work on the hardware up to a certain speed, this speed can be handed to the algorithm together with the controller. After performing an identification of the system, the algorithm will then start with the user–supplied controller and the corresponding speed as a first test speed, which can fur-

ther reduce the amount of time required for arriving at a final controller. In this context, the algorithm developed in this thesis can be considered a tool for improving of existing controllers.

On the way towards the algorithm, several side-topics have been touched. The need for a sufficiently accurate and not too complex amplifier model has been met by a new amplifier modeling technique. In the context of investigations related to soft AMB supports, some interesting aspects of AMB behavior when operated with low bias current have been revealed. The results lead to a new, improved model for AMBs operated in differential driving mode and subject to constant disturbance forces. These results, as well as the identification algorithm for the gyroscopic matrix, may be of general interest to the research community.

8.2   Outlook

In the following, some areas for possible future research based on this work are outlined.

Although the presented algorithm for identification and automated controller design has been shown to work well in practice, its performance could still be further improved.

A point for improvement is the algorithm for identification of the gyroscopic matrix G. Although the algorithm shows very good performance on models based on Finite-Element or other physical modeling, convergence problems occur when *identified* rotor models are used due to additional parameters that must be determined in this case. Currently, this is not achieved in all cases, leading to model errors that may entail unexpectedly large transient amplitudes when critical speeds are passed. At present, this can be avoided by using parts of Finite Element models in the procedure in critical cases. Resolution of the parameter identification problem would eliminate the last remains of dependence on manual modeling from the procedure.

Furthermore, the experimental results showed that for very heavy horizontal rotors the identification of the rigid body poles by means of step experiments is impaired by the large disturbing forces. To improve this situation, the nonlinear effects occurring in the bearing during the step experiments could be analyzed more closely. This analysis could for example be based on a magnetic resistor network model as has been presented in [Gähler98]. It should be possible to derive an improved model of the ro-

tor's behavior during the step experiment and/or easy to apply correction factors that depend only on the bearing and yield improved pole estimates in the step experiments.

The automated controller design algorithm presented in this thesis has been developed based on μ-synthesis theory that marks the current state of the art. Although the algorithm has been shown to work well in practice, it is currently limited by some restrictions imposed by the state of development of this theory.

Today's μ-synthesis algorithms are not capable of handling systems of the given complexity in a setting with real uncertainties. This problem is currently circumvented by approximating real uncertainties by complex ones, incurring a considerable amount of conservatism. Being a field of ongoing research, new, improved μ-synthesis–based controller design algorithms are under development. Furthermore, with increasing computing power becoming available, new methods like μ-synthesis based on linear matrix inequalities (LMIs) become interesting topics also for systems of higher order.

In the future, more advanced μ-synthesis algorithms capable of directly dealing with real parametric uncertainties should be developed. This would allow employment of less conservative uncertainty models and hence result in controllers with even higher performance. Furthermore, the controller design time would be shortened as the requirement for additional design iterations to compensate for problems with modeling real uncertain parameters could be eliminated.

Due to its modular structure, it should require little effort to integrate new μ-synthesis algorithms into the controller design procedure developed in this thesis.

The algorithm for identification and automated controller design has been designed to work with general rotor systems with generic performance requirements. With some adaptations, it could be employed to reconfigurable systems like tool spindles and AMB turbomachinery with changing operating conditions (e.g. pumps). In these systems, it could be used to design controllers for the various ranges of application (various tool types, different modes of operation) encountered.

For systems like tool spindles this would require extensions in the controller design part, where special criteria (in particular stiffness requirements) would have to be introduced into the automated controller design procedure. This would require modification of the rules for weighting function selection.

For pumps, adaptations and research would mainly be necessary in the area of system identification for flexible rotors. Currently, the identification algorithms are tailored to systems with free rotors. Research would have to aim at algorithm extensions for extracting the relevant model information in face of disturbances coming from the machine's operation (interaction with the medium, change of operating point). Furthermore, the new identification algorithms should be able to adequately handle altered dynamics due to the medium being processed, which might include a change of model structure and/or model order.

Finally, an interesting field for future research consists in the area of system design. It has been postulated that the control engineer must choose between two design philosophies for weighting function selection; he can either design weighting functions based on loop shaping criteria or apply a signal based scheme.

The loop shaping approach in its pure form aims at obtaining well behaved closed loop transfer functions, while ignoring any limitations imposed by hardware restrictions, e.g. actuator saturation. On the other hand, when a signal based scheme is used, hardware constraints are by definition taken into account while the closed loop transfer functions are not necessarily optimal.

In this thesis these deficiencies have been tried to overcome by application of a signal based scheme with a loop shaping flavor. However, from a practical point of view, it would be desirable to achieve *both* compliance with hardware limits and optimal closed loop behavior at the same time.

This however is not a problem of control but of adequate machinery design. In fact, this problem calls for a new concept of machinery design, in which controller design and analysis of the resulting closed loop behavior form an integral part of the design process from the very beginning when the decisions on the basic design parameters are made.

With this *design for closed loop performance* approach it will be possible to design machinery for which the above criteria *coincide*, i.e. for which the closed loop transfer functions have optimal shape and at the same time the hardware is made use of in an optimal way. This will yield systems with higher performance and lower cost.

A procedure achieving this and making use of the analysis and controller design tools developed in this thesis could work as follows: Starting with an initial sensible rotor design, a controller is designed for this model using the methods presented in this thesis (based on a signal based scheme). Then, the individual transfer functions are analyzed. If adjustments seem necessary, the weighting functions are adapted in order to achieve bet-

ter transfer functions. Since the weighting functions directly relate to the hardware due to the signal based scheme, this implies new design parameters for the non-rotating hardware (actuator dimensioning, air gap, etc.). Should the new hardware parameters appear insensible, this incurs adjustments to the rotor design. Iteration of this process will finally yield a system with both optimal closed loop performance and appropriate hardware parameters.

Appendix A

Additional Automated Features

A.1 Parameter Computation for Unbalance Compensation

Unbalance compensation, or autobalancing, is a topic of considerable interest in AMB control. By allowing the rotor to spin around its principle axis of inertia rather than its axis of symmetry, unbalance compensation helps to minimize housing vibrations and enables the operation of AMB systems at very high speeds by avoiding actuator saturation. Furthermore, displacement orbits are reduced when rigid body critical speeds are passed. Many publications have been published on the subject of unbalance compensation, the most evolved and most systematic appearing to be that by [Herzog96].

The approach taken in this paper is that of a generalized notch filter consisting of a bank of integrators and a parameter matrix $T(\Omega)$ that must be adequately chosen in order to ensure the stability of the closed loop system.

Which values for T are a good choice depends not only on the bearings, but on the closed loop configuration of bearings, controller, and rotor. As a consequence, the matrix T can only be determined after the rotor has been identified and a controller has been designed. This makes automatic

computation of stabilizing parameters for the unbalance compensation an interesting issue.

As has been elaborated in [Herzog96], a stable system configuration requires for all rotational speeds Ω that $T(\Omega)$ be chosen such that all eigenvalues of $TS(j\Omega)$ are located in the right half plane. A straightforward choice for $T(\Omega)$ is the inverse of the sensitivity function at the same frequency, $S(j\Omega)$. However, the inverse being a dense matrix, this entails considerable computational effort during operation of the system.

A more attractive solution would consist in a *diagonal* matrix T fulfilling the above requirement, leading to the problem of – given n desired eigenvalue locations (in the right half plane) $\lambda_1, ..., \lambda_n$ – determining a complex diagonal matrix $T = diag(T_1, ..., T_n)$ such that

$$eig(diag(T_1, ..., T_n)S) = \lambda_k, \quad k = 1, ..., n, \tag{A.1}$$

where S is an abbreviation for $S(j\Omega)$. This problem has been left open in [Herzog96]. A less implicit problem formulation and a solution is given in the following.

Equivalently to the above, one can consider the problem of finding solutions $T_1, .., T_n$ to the n matrix equations

$$(T \cdot S - \lambda_k I)\underline{x} = 0. \tag{A.2}$$

Considering the single plane case with $n = 2$, the problem of determining the T_k can be formulated by considering one of the above matrix equations together with the additional constraint imposed by the determinant's relation to the eigenvalues,

$$det(TS) = \prod_{k=1}^{k} \lambda_k. \tag{A.3}$$

The result is a nonlinear system of equations with three scalar equations and three unknowns (the two parameters T_1 and T_2 as well as $\underline{x}_1$ ($\underline{x}_2$ can be arbitrarily chosen)). The results for T_1 and T_2 in this case are

$$T_2 = -\frac{p}{2} \pm \sqrt{\frac{p^2}{4} - \frac{S_{1,1}}{S_{2,2}}q} \quad \text{and} \quad T_1 = \frac{q}{T_2}, \tag{A.4}$$

where

$$p = \frac{\lambda_1 + \lambda_2}{S_{2,2}} \quad \text{and} \quad q = \frac{\lambda_1 \lambda_2}{(S_{1,1}S_{2,2} - S_{2,1}S_{1,2})}. \tag{A.5}$$

This result can be used in the automated computation of unbalance compensation parameters. The computation can either be based on the identified model or on a test run during which the sensitivity function for frequency points not too far above the current rotational speed is extracted and T is computed for increasing rotation frequencies. As values for T become available, the rotational speed is successively increased, and the next values for T are computed until the maximum operating speed is reached.

It is worth noting that the case with $n = 4$ can in principle be solved in the same manner. To this end, either three matrix equations from (A.2) and the condition (A.3) can be used to obtain a nonlinear system of equations with 13 equations and unknowns, or all four matrix equations from (A.2), yielding a system of size 16. Finding solutions to these problems however is a nontrivial task that with the methods available today cannot be efficiently solved on a grid of frequencies, as would be required by the application.

However, the case with $n = 4$ is for the majority of cases satisfactorily solved by applying the solution from the single plane case ($n = 2$) to *both* planes. Typically this yields eigenvalues for the matrix TS that are not exactly equal to λ_1 and λ_2, but lie well within the right half plane, fulfilling the stability requirements from [Herzog96].

Appendix B

Signals, Norms, and Systems

Providing the theoretical background to Chapter 3, this appendix is intended for reference. It starts out with the basic definitions of norms, signals, and systems, and it contains the formal definitions of the signal spaces and system spaces encountered in robust control theory as well as information on their connection.

Towards the end of this appendix, state space systems, the term 'standard control configuration', and allpass systems are formally introduced (all of which are relevant to understanding Chapter 3), and the algorithm to compute the norm $\| \cdot \|_\infty$ is presented.

Obviously, completeness had to be traded off against brevity, therefore calculations and proofs have been omitted wherever this was possible. For a more complete treatment of the subject, the interested reader is referred to [Green95] and [Zhou96].

B.1 Norms

Given any vector space $\mathcal{V}$ defined over some algebra $\mathbb{K}$ (typically $\mathbb{K}=\mathbb{R}$ or $\mathbb{K}=\mathbb{C}$), a function $: \|.\| : \mathcal{V} \mapsto \mathbb{R}^+$ is called *norm* if it satisfies the following conditions:

1. *Positive definiteness:* $\quad ||\underline{x}|| = 0 \Leftrightarrow \underline{x} = 0$

2. *Linearity:* $\quad ||r\underline{x}|| = |r| \, ||\underline{x}|| \; \forall \, r \in \mathbb{K}, \underline{x} \in \mathcal{V}$

3. *Triangle inequality:* $\quad ||\underline{x} + \underline{y}|| \leq ||\underline{x}|| + ||\underline{y}|| \; \forall \, \underline{x}, \underline{y} \in \mathcal{V}$

A common example of a norm is the p-norm on $\mathbb{C}^n$ defined by

$$||\underline{x}||_p := \left(\sum_{i=1}^{n} |x_i|^p \right)^{1/p}, \quad 1 \leq p < \infty. \tag{B.1}$$

As a special example, any scalar product $< \cdot, \cdot >$ defined on a vector space $\mathcal{V}$ can be used to define a norm on that space by the definition

$$||\underline{x}|| := \sqrt{< \underline{x}, \underline{x} >} \tag{B.2}$$

This norm is referred to as the *norm induced by the scalar product.* Consider for example the standard scalar product on $\mathbb{R}^n$ defined by

$$< \underline{x}, \underline{y} > := \sum_{i=1}^{n} x_i y_i \tag{B.3}$$

Quite obviously, the norm induced by this scalar product is the p-norm from Equation (B.1) with $p = 2$. Any vector space equipped with a scalar product and its induced norm is called *Hilbert space* (provided it is complete with respect to the norm).

As a special type of vector space, consider now the space of complex matrices $\mathbb{C}^{n \times m}$ mapping $\mathbb{C}^m$ to $\mathbb{C}^n$. Then a norm on $\mathbb{C}^{n \times m}$ can be derived based on the norms defined on $\mathbb{C}^m$ and $\mathbb{C}^n$ as follows: For all $A \in \mathbb{C}^{n \times m}$, define

$$||A|| := \sup_{x \neq 0} \frac{||A\underline{x}||_{\mathbb{C}^n}}{||\underline{x}||_{\mathbb{C}^m}} \tag{B.4}$$

This norm is referred to as the *induced matrix norm.*

For the special case when the norm on $\mathbb{C}^m$ and $\mathbb{C}^n$ is the norm $|| \cdot ||_2$, the induced matrix norm of any $A \in \mathbb{C}^{n \times m}$ can be shown to be

$$||A||_2 := \sqrt{\lambda_{max}(A^* A)} = \bar{\sigma}(A). \tag{B.5}$$

where $\lambda_{max}(A^* A)$ is the maximum eigenvalue of the matrix $A^* A$ and $\bar{\sigma}(A)$ denotes the maximum singular value of A. From the last equality it can be seen that $\bar{\sigma}(A)$ is a measure of the maximum amplification of any vector from $\mathbb{C}^m$ by the matrix A.

B.2   Signals

The set of all signals can be formally defined as

$$\mathcal{S} = \{f : \mathbb{R} \mapsto \mathbb{R}^n, \; f \text{ Lebesgue measurable}\}.$$

This set in particular comprises all conceivable functions that can occur at the input or output of any technical system. With the pointwise addition and multiplication by real scalars, **S** can be considered an $\mathbb{R}$-vector space. Important subspaces of **S** are

$$\begin{aligned}
\mathcal{S}_+ &= \{f \in \mathcal{S} : f(t) = 0 \;\; \forall t < 0\} \qquad \text{and} \\
\mathcal{S}_- &= \{f \in \mathcal{S} : f(t) = 0 \;\; \forall t > 0\},
\end{aligned}$$

the signals of the future and those of the past.

A special class of signals is constituted by all signals of finite energy. These signals form the following function space:

$$\mathcal{L}_2(-\infty, \infty) := \{f \in \mathcal{S} : ||f||_2 < \infty\}, \quad \text{with} \quad ||f||_2 = \sqrt{\int_{-\infty}^{\infty} ||f(t)||^2 \, dt}.$$

With the scalar product

$$< f, g > := \int_{-\infty}^{\infty} f^T(t) g(t) dt \tag{B.6}$$

and the norm induced by it, $\mathcal{L}_2(-\infty, \infty)$ is a Hilbert space. By application of the projection operators P_+ and P_- to $\mathcal{L}_2(-\infty, \infty)$, one obtains $\mathcal{L}_2[0, \infty) := \mathcal{L}_2(-\infty, \infty) \cap \mathcal{S}_+$ and $\mathcal{L}_2(-\infty, 0] := \mathcal{L}_2(-\infty, \infty) \cap \mathcal{S}_-$, two orthogonal subspaces of $\mathcal{L}_2(-\infty, \infty)$.

B.2.1   Fourier Transform

Signals with finite energy can be analyzed either in the time or in the frequency domain. In the time domain these signals are elements of $\mathcal{L}_2(-\infty, \infty)$ defined above. Signals in the frequency domain are elements of the space

$$\mathcal{L}_2 := \{f : j\mathbb{R} \mapsto \mathbb{C}^n, \; \frac{1}{2\pi} \int_{-\infty}^{\infty} f^*(j\omega) f(j\omega) \, d\omega < \infty\} \tag{B.7}$$

With the scalar product

$$< f, g > := \frac{1}{2\pi} \int_{-\infty}^{\infty} f^*(j\omega) g(j\omega) \, d\omega \qquad (B.8)$$

and the induced norm

$$\|f\|_2 = \sqrt{\frac{1}{2\pi} \int_{-\infty}^{\infty} \|f(j\omega)\|^2 \, d\omega} \qquad (B.9)$$

$\mathcal{L}_2$ also is a Hilbert space.

The *Fourier transform* is defined as the following map from $\mathcal{L}_2(-\infty, \infty)$ to $\mathcal{L}_2$:

$$\hat{f}(j\omega) = \lim_{T \to \infty} \int_{-T}^{T} f(t) e^{-j\omega t} \, dt \qquad (B.10)$$

One can show that the Fourier transform is linear and bijective (one-to one), i.e. an isomorphism, which with the special choice of scalar product from above for $\mathcal{L}_2$ fulfills

$$< f, g > = < \hat{f}, \hat{g} > \quad \forall f, g \in \mathcal{L}_2(-\infty, \infty) \qquad (B.11)$$

This means that the scalar product (and hence the norm which is induced by it) is preserved under Fourier transform. Any isomorphism between two Hilbert spaces that preserves the scalar product is called an isometry. The Fourier transform hence is an isometry from $\mathcal{L}_2(-\infty, \infty)$ to $\mathcal{L}_2$.

B.2.2   Laplace Transform

The subspaces $\mathcal{L}_2(-\infty, 0]$ and $\mathcal{L}_2[0, \infty)$ of $\mathcal{L}_2(-\infty, \infty)$ can also be transformed to the frequency domain. This is done by means of the so-called *Laplace transform* which is defined as

$$\hat{f}(s) = \int_{-\infty}^{\infty} f(t) e^{-st} \, dt. \qquad (B.12)$$

The region of convergence of this integral depends on the function f. For $f \in \mathcal{L}_2[0, \infty)$, it converges on the entire open right half plane (complex plane without the imaginary axis, $Re(s) > 0$). As a consequence, the image $\hat{f}(s)$ of any $f \in \mathcal{L}_2[0, \infty)$ lies in the space $\mathcal{H}_2$. $\mathcal{H}_2$ is a so-called

Hardy space. It consists of all functions of one complex variable that are analytic in the open right half plane and for which the expression

$$sup_{\alpha>0}\sqrt{\frac{1}{2\pi}\int_{-\infty}^{\infty} f^*(\alpha+j\omega)f(\alpha+j\omega)\,d\omega} \qquad (B.13)$$

is finite. One can show [Green95] that (i) for each f in $\mathcal{H}_2$ there exists a continuous continuation $f_i(j\omega) = \lim_{\alpha\searrow 0} f(\alpha+j\omega) \in \mathcal{L}_2$, (ii) the mapping $f \mapsto f_i$ is injective (invertible). This allows us to identify each function in $\mathcal{H}_2$ uniquely with one in $\mathcal{L}_2$. As a consequence, $\mathcal{H}_2$ can be interpreted as a subspace of $\mathcal{L}_2$. Based on these considerations, one can show that the Laplace transform is an isomorphic (one to one) mapping from $\mathcal{L}_2[0,\infty)$ to $\mathcal{H}_2$.

In addition to $\mathcal{H}_2$, the space $\mathcal{H}_2^-$ is analogously introduced by replacing the right half plane by the left half plane in the above definition. In short, one can write

$$\mathcal{H}_2^- = \{f : f(-s) \in \mathcal{H}_2\}. \qquad (B.14)$$

Just like $\mathcal{H}_2$, $\mathcal{H}_2^-$ can be interpreted as a subspace of $\mathcal{L}_2$. The Laplace transform can be shown to be an isomorphism from $\mathcal{L}_2(-\infty,0]$ to $\mathcal{L}_2$. Due to the orthogonality of $\mathcal{L}_2(-\infty,0]$ and $\mathcal{L}_2[0,\infty)$, $\mathcal{H}_2$ and $\mathcal{H}_2^-$ are orthogonal as well. Figure B.1 graphically summarizes the results of this chapter [Zhou96].

B.3 Systems

Mathematically, systems are operators mapping elements of one signal space, the input space $\mathcal{S}_1$, to a second signal space, the output space $\mathcal{S}_2$.

$$\mathbf{G} \quad : \quad \mathcal{S}_1 \mapsto \mathcal{S}_2 \qquad (B.15)$$
$$: \quad w \mapsto z = \mathbf{G}w \qquad (B.16)$$

With the addition defined by parallel interconnection and the multiplication by scalars, the set of all systems becomes a vector space. From the multitude of systems, those with some specific properties are of particular interest in control theory:

Causal systems are those systems for which the output up to an arbitrary time τ only depends on inputs up to this time (and not from future inputs).
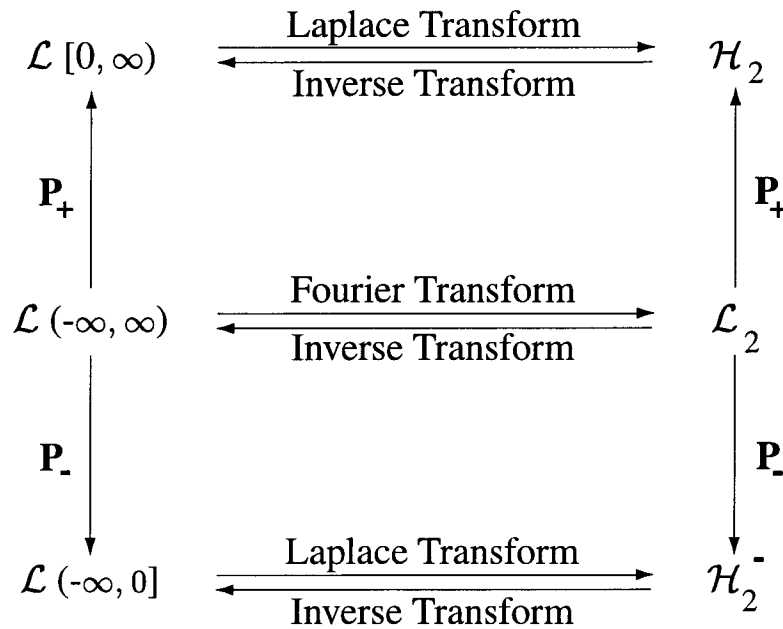
Figure B.1: *Relation of signal spaces*

Time-invariant systems always react, if the input to the system is shifted in time by an offset τ, with an output signal that is also shifted by τ.

Stable systems react to future finite energy inputs with future finite energy outputs, i.e. $z = \mathbf{G}w \in \mathcal{L}_2[0, \infty) \; \forall w \in \mathcal{L}_2[0, \infty)$.

Linear systems are all systems fulfilling
$$\mathbf{G}(rw_1 + sw_2) = r\mathbf{G}w_1 + s\mathbf{G}w_2 \; \forall w_1, w_2 \in \mathcal{S}_1, \forall r, s \in \mathbb{R}.$$

In the context of this work all problems are solved in the framework of linear, time-invariant systems. For Laplace transformable input signals $w(t)$, these systems can be represented by a convolution integral of the form

$$z(t) = \int_{-\infty}^{\infty} G(t - \tau)w(\tau)d\tau \qquad (B.17)$$

and the Laplace transform $z(s)$ of the image $z(t)$ also exists and this equation can be transformed to the frequency domain:

$$z(s) = \mathbf{G}(s)w(s) \qquad (B.18)$$

with

$$w(s) \quad = \int_{-\infty}^{\infty} w(t)e^{-st}\, dt\,, \quad \mathbf{G}(s) = \int_{-\infty}^{\infty} G(t)e^{-st}\, dt$$

$$\text{and} \qquad z(s) = \int_{-\infty}^{\infty} z(t)e^{-st}\, dt\,. \qquad \text{(B.19)}$$

In the above, $G(t)$ is a real matrix valued function and $\mathbf{G}(s)$ is a complex matrix valued function. $\mathbf{G}(s)$ is called transfer function matrix of the system. Any linear time invariant system can be represented by a transfer function matrix, and any system for which a representation as a transfer function matrix exists is linear and time invariant.

B.3.1 The Space $\mathcal{L}_\infty$

In the analysis of systems, those linear time invariant systems mapping the space $\mathcal{L}_2(-\infty, \infty)$ of finite energy signals to itself are of particular interest. It is straightforward to find a sufficient condition for a transfer function matrix to fulfill this requirement:

$$
\begin{aligned}
\|\mathbf{G}w\|_2^2 &= \frac{1}{2\pi}\int_{-\infty}^{\infty} \|\mathbf{G}(j\omega)w(j\omega)\|^2\, d\omega \\
&\leq \frac{1}{2\pi}\int_{-\infty}^{\infty} (\overline{\sigma}(\mathbf{G}(j\omega)))^2 \|w(j\omega)\|^2\, d\omega \\
&\leq \sup_\omega(\overline{\sigma}(\mathbf{G}(j\omega)))^2 \frac{1}{2\pi}\int_{-\infty}^{\infty} \|w(j\omega)\|^2\, d\omega \qquad \text{(B.20)}
\end{aligned}
$$

In the first step, the properties of the induced matrix norm $\|\cdot\|_2$ from Equation (B.5) has been used. Obviously $\|z\|_2 = \|\mathbf{G}w\|_2$ is finite for all $w \in \mathcal{L}_2(-\infty, \infty)$ if $\sup_\omega(\overline{\sigma}(\mathbf{G}(j\omega))) < \infty$ holds.

This motivates the definitions

$$\|\mathbf{G}\|_\infty := \sup_\omega \overline{\sigma}(\mathbf{G}(j\omega)) \text{ and } \mathcal{L}_\infty := \{\mathbf{G} : \|\mathbf{G}\|_\infty < \infty\}$$

$\|\cdot\|_\infty$ can be shown to be a norm on $\mathcal{L}_\infty$. Furthermore, a direct consequence from Equation (B.20) is that

$$\|\mathbf{G}w\|_2 \leq \|\mathbf{G}\|_\infty \|w\|_2 \ \forall\, w \in \mathcal{L}_2 \ \forall\, \mathbf{G} \in \mathcal{L}_\infty \qquad \text{(B.21)}$$

and one can easily show that this bound is tight, i.e.

$$\|\mathbf{G}\|_\infty = \sup_{\omega \neq 0} \frac{\|\mathbf{G}w\|_2}{\|w\|_2}, \qquad \text{(B.22)}$$

which allows interpretation of $\| \cdot \|_\infty$ as a norm induced by the signal norm $\| \cdot \|_2$. This implies that the norm $\|\mathbf{G}\|_\infty$ of a system is a measure for the worst case energy amplification of any input signal $w \in \mathcal{L}_2(-\infty, \infty)$.

B.3.2   The Hardy Space $\mathcal{H}_\infty$

Due to $\mathcal{L}_2[0, \infty)$ being isomorphic to $\mathcal{H}_2$ and the definition of stability in the last chapter, any transfer function matrix $\mathbf{G}$ of a linear, time invariant system is stable if and only if

$$z = \mathbf{G}w \in \mathcal{H}_2 \forall w \in \mathcal{H}_2.$$

Since any function must be analytic in the open right half plane in order to lie in $\mathcal{H}_2$, any stable system $\mathbf{G}$ must necessarily be analytic in the open right half plane. Checking the above stability condition

$$
\begin{aligned}
\|\mathbf{G}w\|_2^2 \;&\overset{Def.}{=}\; \sup_{\alpha>0} \frac{1}{2\pi} \int_{-\infty}^{\infty} \|\mathbf{G}(\alpha + j\omega)w(\alpha + j\omega)\|^2 \, dw \\
&\leq\; \sup_{\alpha>0} \frac{1}{2\pi} \int_{-\infty}^{\infty} \overline{\sigma}(\mathbf{G}(\alpha + j\omega))^2 \|w(\alpha + j\omega)\|^2 \, dw \\
&\overset{(B.20)}{\leq}\; \sup_{\alpha>0} \sup_{\omega} \overline{\sigma}(\mathbf{G}(\alpha + j\omega))^2 \sup_{\alpha>0} \frac{1}{2\pi} \int_{-\infty}^{\infty} \|w(\alpha + j\omega)\|^2 \, dw \\
&\overset{Def.}{=}\; \sup_{\alpha>0} \sup_{\omega} \overline{\sigma}(\mathbf{G}(\alpha + j\omega))^2 \|w\|_2^2 .
\end{aligned}
$$

implies that a sufficient condition for stability of $\mathbf{G}$ is given by

$$\sup_{\alpha>0} \sup_{\omega} \overline{\sigma}(\mathbf{G}(\alpha + j\omega)) < \infty \qquad\qquad (B.23)$$

This motivates the definition of the space $\mathcal{H}_\infty$ as the class of all systems $\mathbf{G}$ that are analytic in the open right half plane and for which the above supremum is finite.

As was the case with the embedding of $\mathcal{H}_2$ in $\mathcal{L}_2$, a linear injective mapping can be shown to exist, identifying every element $\mathbf{G}$ of $\mathcal{H}_\infty$ with its limit function for $\alpha \searrow 0$, $\mathbf{G}_b$. Additionally,

$$\sup_{\alpha>0} \sup_{\omega} \overline{\sigma}(\mathbf{G}(\alpha + j\omega)) = \sup_{\omega} \overline{\sigma}(\mathbf{G}_b(j\omega)) \qquad\qquad (B.24)$$

which implies that for any $\mathbf{G} \in \mathcal{H}_\infty$ the limit function $\mathbf{G}_b$ is an element of $\mathcal{L}_\infty$. This allows us to regard $\mathcal{H}_\infty$ as a closed subspace of $\mathcal{L}_\infty$ and to write

$$\mathcal{H}_\infty = \{\mathbf{G} : \mathbf{G} \text{ is analytic in } \operatorname{Re}(s) > 0 \text{ and } ||\mathbf{G}||_\infty < \infty\} \quad \text{(B.25)}$$

$\mathcal{H}_\infty$ is the space of all stable transfer function matrices $\mathbf{G}$. The special significance of this space in robust control theory results from the fact that it contains all desirable closed loop transfer functions. The optimal $\mathcal{H}_\infty$-algorithm introduced in chapter 3.3.1 performs a search for controllers that achieve a closed loop transfer function from $\mathcal{H}_\infty$ with minimal $|| \cdot ||_\infty$, i.e. with minimum worst case amplification of input signals.

B.3.3 State Space Systems, $\mathcal{R}\mathcal{H}_\infty$, $\mathcal{R}\mathcal{L}_\infty$

As already mentioned, the systems in this work are linear, time-invariant and causal. For any such system $\mathbf{G}$ a representation in the form

$$\begin{aligned} \underline{\dot{x}}(t) &= A\underline{x}(t) + B\underline{w}(t) \quad \text{with } \underline{x}(0) = \underline{x}_0 \quad \text{(B.26)} \\ \underline{z}(t) &= C\underline{x}(t) + D\underline{w}(t) \end{aligned}$$

with constant, real-valued matrices A, B, C, D is available. This is called a *state space representation* of $\mathbf{G}$ and often abbreviated as

$$\mathbf{G} \stackrel{s}{=} \left[\begin{array}{c|c} A & B \\ \hline C & D \end{array} \right] \quad \text{(B.27)}$$

Conversely, any system with the above representation is linear, time invariant and causal. Laplace transform of Equation (B.26) yields $\mathbf{G}(s) = C(sI - A)^{-1}B + D$, and all interconnections of state space systems can be transformed into a new state space system by simple algebraic manipulation.

Given a state space system (A,B,C,D), the state space system $(T^{-1}AT, T^{-1}B, CT, D)$ has the same input–output behavior for all invertible, real matrices T. The operation applied is called *similarity transformation*.

This implies that state space representations are not unique. Similarity transformation with a nonsingular matrix will yield an input–output equivalent but generally (in terms of matrices A, B, C, D) different state space representation. In other words, the input–output behavior of a linear, time invariant, causal system $\mathbf{G}$ can be expressed by a whole class of
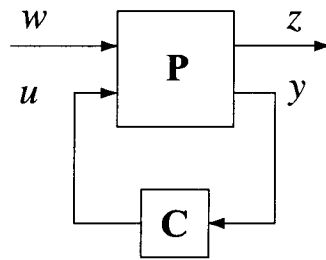
Figure B.2: *Standard control configuration*

state space systems whose matrices look very different (but are similar in the above mathematical sense).

Also, any system **G** can be represented by state space realizations of different order (size of A). However, for each **G** there exists a value m such that no state space representation with order less than m can be found. m is referred to as the McMillan degree of **G**. Any state space representation of **G** with order m is called a minimal realization of **G**. Any realization of a system is both observable and controllable if and only if it is minimal.

For state space systems as presented here the transfer function matrix **G** is a rational function of the complex variable s. The rational transfer functions of $\mathcal{H}_\infty$ and $\mathcal{L}_\infty$ form subspaces of these spaces and are denoted $\mathcal{R}\mathcal{H}_\infty$ and $\mathcal{R}\mathcal{L}_\infty$ respectively.

G $\in \mathcal{R}\mathcal{H}_\infty$ if and only if **G** has no poles in the closed right half plane. This is the basis for the standard stability check in the complex plane. Furthermore, a system **G** $\in \mathcal{R}\mathcal{H}_\infty$ is called proper if the denominator degree of **G** is larger than or equal to its numerator degree. **G** is called strictly proper if the denominator degree of **G** is larger than its numerator degree.

B.3.4   Standard Control Configuration

For a physical system there is no natural order of its inputs and outputs. However, for purposes of a structured theory and systematic controller design, it is convenient to agree on a default system setup. This setup consists of the feedback configuration from Figure B.2 where **P** represents the system resulting from the interconnection of the nominal system and all weighting functions and **C** represents the controller to be designed.

The system inputs and outputs can be differentiated and ordered based on their logical function in the system as follows [Boyd91]:

- the **control input vector** u consists of inputs (control signals) the controller gives to the nominal system.

- the **exogenous signal vector** w consists of all other input signals to the system (e.g. reference inputs, disturbances).

- the **measurement signal vector** y consists of the system's output signals that serve as inputs to the controller

- the **control objectives vector** z consists of all other output signals.

The convention in control theory is to order the inputs and outputs of $\mathbf{P}$ such that on the input side the exogenous signal vector w precedes the control input vector u and on the output side the control objectives vector z precedes the measurement vector y, see Figure B.2.

The resulting system $\mathbf{P}$ can then be partitioned according to the size of the vectors defined above and written as

$$\begin{bmatrix} \underline{\dot{x}}(t) \\ \underline{z}(t) \\ \underline{y}(t) \end{bmatrix} = \left[\begin{array}{c|cc} A & B_1 & B_2 \\ \hline C_1 & D_{11} & D_{12} \\ C_2 & D_{21} & D_{22} \end{array} \right] \begin{bmatrix} \underline{x}(t) \\ \underline{w}(t) \\ \underline{u}(t) \end{bmatrix}. \tag{B.28}$$

Furthermore, in cases when certain pairs of channels of the exogenous signal vector w and the control objectives vector z can be attributed to uncertainty modeling, the convention is to order w and z such that these channels appear first.

Another convention exists for the naming of transfer functions: Transfer function matrices are commonly named after the inputs and outputs they are associated with, which is indicated by a suffix in which the corresponding output is followed by the input. For example the name $\mathbf{T}_{zw}$ typically represents the transfer function from the inputs summarized in the vector $\underline{w}$ to the outputs summarized in $\underline{z}$.

B.3.5   Allpass Systems

Allpass systems are systems $\mathbf{G}$ with the special property

$$\|\mathbf{G}w\|_{\mathcal{S}_2} = \|w\|_{\mathcal{S}_1} \forall w \in \mathcal{S}_1 \tag{B.29}$$

i.e. the norm of the input is equal to the norm of the output. These systems are mentioned here, because the optimal solution to the $\mathcal{H}_\infty$ controller design problem presented later can be shown to yield closed loop systems with a similar property for the closed loop transfer function $\mathbf{T}_{\underline{z}w}$,

$$\bar{\sigma}(\mathbf{T}_{\underline{z}w}(j\omega)) = c \; \forall \omega \in \mathbb{R} \tag{B.30}$$

which implies that the closed loop transfer function is flat in the amplitude sense, and that $1/c \cdot \mathbf{T}_{\underline{z}w}$ is allpass. This has important consequences for the introduction of robustness and performance requirements into the controller design problem, see Chapter 3.2.2.

B.3.6   Calculation of the Norm $\|\cdot\|_\infty$

In the above, the norm $\|\cdot\|_\infty$ on $\mathcal{L}_\infty$ has been introduced as $\|\mathbf{G}\|_\infty :=$ $\sup_{\omega \in \mathbb{R}} \bar{\sigma}(\mathbf{G}(j\omega))$, and its relevance for technical problems has been outlined. In order to make use of this powerful tool, the above supremum must be evaluated. Intuitively, the solution to this problem may look simple; by defining a dense frequency grid with a finite number of frequency points ω_i and by evaluating $\max_{\omega_i} \bar{\sigma}(\mathbf{G}(j\omega_i))$ an estimate for $\|\mathbf{G}\|_\infty$ can be calculated. However, this method will only yield lower bounds for $\|\mathbf{G}\|_\infty$ and no information concerning the quality of this bound. For systems with a state space description, a better method is available [Zhou96]:

CALCULATION OF $\|\cdot\|_\infty$

Let $\gamma > 0$ and $\mathbf{G}(s) = C(sI - A)^{-1}B + D \in \mathcal{RL}_\infty$. Then the following

holds:

$$\begin{bmatrix} A + BR^{-1}D^*C & BR^{-1}B^* \\ -C^*(I + DR^{-1}D^*)C & -(A + BR^{-1}D^*C)^* \end{bmatrix}$$

with $R = \gamma^2 I - D^*D$

$\|G\|_\infty < \gamma \quad \Leftrightarrow \quad$ *has no imaginary axis eigenvalues*

and

$$\bar{\sigma}(D) < \gamma$$

Based on this theorem, an iteration can be carried out. Starting with plausible upper and lower bounds γ_u and γ_l for the norm, the above condition is evaluated for the average of these two bounds. Depending on the result, this yields a new upper or lower bound. This bisection technique brings the two bounds closer and closer together. As soon as the difference between the bounds is smaller than a predefined tolerance value, the average value of the two bounds can be used as an approximation of $\|\mathbf{G}\|_\infty$. In contrast to the grid-based approach this method gives a reliable upper bound for the maximum difference between the calculated value and the true value of $\|\mathbf{G}\|_\infty$.

Appendix C

Modeling of AMB Systems Affected by Gravity

In this chapter, the insights gained in Chapter 5.1.4 on how gravity affects the stiffness of current controlled active magnetic bearings are used to formulate a new modeling procedure for AMB systems affected by gravity. The method presented is generally valid, and the resulting models are always better[1] than models from the classical design method, while being of identical complexity.

For both the classical and the new method, the basic bearing parameter $k = \mu_0 n_c^2 A_c cos(\alpha_p)$ and the air gap s_0 are assumed to be known. Furthermore, the desired bias current i_0 is supplied by the user as an input to the algorithms.

Classical Design Method

The classical design method consists in the following two steps:

1. Calculate the force displacement and force–current factors based on

---

[1]This is a mathematical statement. For large bias currents, the classical model approaches the new model presented here asymptotically, and little is gained by using the new model. For small bias currents, however, the difference becomes very large, see Chapter 5.1.4.

the standard linearized formulae, i.e.

$$k_i = \left.\frac{\partial}{\partial i_x} f\right|_{x, i_x = 0} = k \frac{i_0}{s_0^2} \tag{C.1}$$

and

$$k_s = \left.\frac{\partial}{\partial x} f\right|_{x, i_x = 0} = k \frac{i_0^2}{s_0^3}. \tag{C.2}$$

2. Add these values to the rotor model by methods described in Chapter 2.2 and Chapter 2.3.4.

New Design Method

The new design method yields improved force–current and force–displacement factors by considering the constant set currents stemming from gravity compensating controllers. It comprises the following steps:

1. Determine the gravitational force F_g to be compensated for in the control axis under consideration. This can be done based on rigid body data and information on the orientation of the rotor.

2. Calculate the values of $\tilde{i}_{min}$ and i_Δ defined by

$$\tilde{i}_{min} = \sqrt{\frac{F_g}{k}} \cdot s_0 \quad \text{and} \quad i_\Delta = \frac{F_g \cdot s_0^2}{k \cdot i_0}. \tag{C.3}$$

3. Define the force–current and force–displacement factors as follows:

$$k_i = \begin{cases} \frac{\sqrt{k \cdot F_g}}{s_0} & : \quad i_0 \le \tilde{i}_{min} \\ k \cdot \frac{i_0}{s_0^2} & : \quad i_0 > \tilde{i}_{min} \end{cases} \tag{C.4}$$

and

$$k_s = \begin{cases} \frac{2 \cdot F_g}{s_0} & : \quad i_0 \le \tilde{i}_{min} \\ k \cdot \frac{i_0^2 + i_\Delta^2}{s_0^3} & : \quad i_0 > \tilde{i}_{min} \end{cases} \tag{C.5}$$

4. Add k_s and k_i to the rotor model as before in the classical method.

The method presented above yields *control relevant* force current and force–displacement factors, i.e. an improved model of identical complexity.

Bibliography

[Ackermann88]   J. Ackermann: *Abtastregelung*, Springer Verlag, Berlin, Heidelberg, New York, 3rd ed., 1988.

[Allaire98]   P. E. Allaire and A. Sinha: *Robust Sliding Mode Control of a Planar Rigid Rotor System of Magnetic Bearings*, in: *Proceedings of the 6th International Symposium on Magnetic Bearings*, pp. 577–586, Cambridge, MA, USA, Aug. 1998.

[Ariga00]   Y. Ariga, K. Nonami, and K. Sakai: *Nonlinear Control of Zero Power Magnetic Bearing Using Lyapunov's Direct Method*, in: *Proceedings of the 7th International Symposium on Magnetic Bearings*, pp. 293–298, ETH Zurich, Switzerland, Aug. 2000.

[Åström95]   K. J. Åström and B. Wittenmark: *Adaptive Control*, Addison-Wesley Publishing Company, Reading, MA, USA, 2nd ed., 1995.

[Åström96]   K. J. Åström: *Tuning and Adaptation*, Proceedings of the 13th Triennial World Congress IFAC, San Francisco, USA, 1996.

[Balas95a]   G. J. Balas, J. C. Doyle, K. Glover, A. K. Packard, and R. Smith: *μ-Analysis and Synthesis Toolbox*, The Mathworks, Inc., Natick, MA, USA, 1995.

[Balas95b]   G. J. Balas and P. M. Young: *Control Design for Variations in Structural Natural Frequencies*, Journal of Guidance, Control and Dynamics, vol. 18(2): pp. 325–332, 1995.

[Bartha00]   A. Bartha: *Dry Friction Backward Whirl of Rotors*, Ph.D. thesis, No. 13817, ETH Zurich, Switzerland, 2000.

[Bathe82]   K. J. Bathe: *Finite Element Procedures in Engineering Analysis*, Prentice Hall, Englewood Cliffs, NJ, USA, 1982.

[Bleuler84]   H. Bleuler: *Decentralized Control of Magnetic Rotor Bearing Systems*, Ph.D. thesis, No. 7573, ETH Zurich, Switzerland, 1984.

[Bleuler90]   H. Bleuler, D. Diez, G. Lauber, U. Meyer, and D. Zlatnik: *Nonlinear Neural Network Control with Application Example*, in: *Proceedings of INNC Paris, International Neural Network Conference*, vol. 1, pp. 201–204, Kluwer, Dordrecht, Netherlands, 1990.

[Bleuler94]   H. Bleuler, J. U. Jeon, T. Higuchi, and H. Ueyama: *Self-Tuning Control for Magnetic Bearings*, in: *Proceedings of the 4th International Symposium on Magnetic Bearings*, pp. 85–88, ETH Zurich, Switzerland, Aug. 1994.

[Boyd91]   S. P. Boyd and C. H. Barrat: *Linear Controller Design, Limits of Performance*, Prentice Hall, Information and Systems Science Series, Englewood Cliffs, NJ, USA, 1991.

[Braembussche98] P. Braembussche, van den: *Robust Motion Control of High Performance Machine Tools with Linear Motors*, Ph.D. thesis, Katholieke Universiteit Leuven, Belgium, 1998.

[Bronstein96]   I. N. Bronstein, K. A. Semendjajew, G. Grosche, V. Ziegler, and D. Ziegler: *Teubner Taschenbuch der Mathematik*, B. G. Teubner, Stuttgart, Leipzig, 1996.

[Chiang92]   R. Y. Chiang and M. G. Safonov: *Robust Control Toolbox*, The Mathworks, Inc., Natick, MA, USA, 1992.

[Costic00]   B. T. Costic, M. S. de Querioz, and D. M. Dawson: *New Learning Control Approach to the Active Magnetic Bearing Benchmark System*, in: *Proceedings of the 2000*

American Control Conference, vol. 4, pp. 2639–2643, Chicago, IL, USA, 2000.

[Cui92] W. M. Cui and K. Nonami: $\mathcal{H}_\infty$ *Control of Flexible Rotor–Magnetic Bearing Systems*, in: *Proceedings of the 3rd International Symposium on Magnetic Bearings*, pp. 505–511, Alexandria, VA, USA, Jul. 1992.

[Doyle82] J. C. Doyle: *Analysis of Feedback Systems with Structured Uncertainties*, in: *IEE Proceedings*, vol. 133, Part D, pp. 45–56, 1982.

[Doyle92] J. C. Doyle, B. A. Francis, and A. R. Tannenbaum: *Feedback Control Theory*, MacMillan Publishing Company, New York, NY, USA, 1992.

[Fahmy79] M. F. Fahmy: *Transfer Functions with Arbitrary Phase Characteristics*, *Circuit Theory and Applications*, vol. 7: pp. 21–29, 1979.

[Fittro98] R. L. Fittro and C. R. Knospe: *μ–Synthesis Control Design Applied to a High Speed Machining Spindle with Active Magnetic Bearings*, in: *Proceedings of the 6th International Symposium on Magnetic Bearings*, pp. 449–458, Cambridge, MA, USA, Aug. 1998.

[Franklin94] G. F. Franklin, J. D. Powell, and A. Emami-Naeini: *Feedback Control of Dynamic Systems*, Addison-Wesley Publishing Company, Reading, MA, USA, 3rd ed., 1994.

[Fritsche95] C. Fritsche and D. Arnold: *Rotor schweben lassen ohne Modellkenntnis*, Semesterarbeit, International Center for Magnetic Bearings, ETH Zurich, Switzerland, 1995.

[Fujita90] M. Fujita, F. Matsumura, and M. Shimizu: $\mathcal{H}_\infty$ *Robust Control Design for a Magnetic Suspension System*, in: *Proceedings of the 2nd International Symposium on Magnetic Bearings*, pp. 349–356, Tokyo, Japan, Jul. 1990.

[Gähler97] C. Gähler, M. Mohler, and R. Herzog: *Multivariable Identification of AMB Systems*, *JSME International Journal, Series C*, vol. 40(4): pp. 325–332, 1997.

[Gähler98]   C. Gähler: *Rotor Dynamic Testing and Control with Active Magnetic Bearings*, Ph.D. thesis, No. 12718, ETH Zurich, Switzerland, 1998.

[Gasch75]   R. Gasch and H. Pfützner: *Rotordynamik: Eine Einführung*, Springer Verlag, Berlin, Heidelberg, New York, 1975.

[Gasch87]   R. Gasch and K. Knothe: *Strukturdynamik Band I: Diskrete Systeme*, Springer Verlag, Berlin, Heidelberg, 1987.

[Gasch89]   R. Gasch and K. Knothe: *Strukturdynamik Band II: Kontinua und ihre Diskretisierung*, Springer Verlag, Berlin, Heidelberg, 1989.

[Geering90]   H. P. Geering: *Meß– und Regelungstechnik*, Springer Verlag, Berlin, Heidelberg, New York, 2nd ed., 1990.

[Glover91]   K. Glover, D. J. Limebeer, J. C. Doyle, E. M. Kasenally, and M. G. Safonov: *A Characterization of All Solutions to the Four Block General Distance Problem*, *SIAM Journal of Control*, vol. 29(2): pp. 283–324, Mar. 1991.

[Green95]   M. Green and D. J. Limebeer: *Linear Robust Control*, Prentice Hall, Englewood Cliffs, NJ, USA, 1995.

[Hahn90]   H. G. Hahn: *Technische Mechanik*, Carl Hanser Verlag, München, 1990.

[Hamdy97]   A. S. Hamdy: *Active Damping of Vibrations in Elevator Cars*, Ph.D. thesis, No. 12066, ETH Zurich, Switzerland, 1997.

[Haugstetter00]   C. Haugstetter: *Automated Controller Design for AMB Systems*, Semesterarbeit, International Center for Magnetic Bearings, ETH Zurich, Switzerland, Jun. 2000.

[Henk81]   T. Henk: *The Generation of Arbitrary-Phase Polynomials by Recurrence Formulae*, *Circuit Theory and Applications*, vol. 9: pp. 461–478, 1981.

[Herzog91]   R. Herzog: *Ein Beitrag zur Regelung von magnetge-
lagerten Systemen mittels positiv reeller Funktionen und*
$\mathcal{H}_\infty$*-Optimierung*, Ph.D. thesis, No. 9399, ETH Zurich,
Switzerland, 1991.

[Herzog96]   R. Herzog, P. Bühler, and R. Larsonneur: *Unbalance
Compensation Using Generalized Notch Filters in the
Multivariable Feedback of Magnetic Bearings*, *IEEE
Transactions on Control Systems Technology*, vol. 4(5):
pp. 580–586, Sep. 1996.

[IMP01]   IMPACT - Improving Machinery Performance using
Active Control Technology — Development of Diagno-
sis, Prognosis, and Correction Algorithms for Faults in
AMB and other Machinery: *BRITE/EURAM Project
No. 97-4092, Final Report*, Jan. 2001.

[Isermann92a] R. Isermann: *Identifikation Dynamischer Systeme 1:
Grundlegende Methoden*, Springer Verlag, Berlin, Hei-
delberg, 2nd ed., 1992.

[Isermann92b] R. Isermann: *Identifikation Dynamischer Systeme 2:
Besondere Methoden, Anwendungen*, Springer Verlag,
Berlin, Heidelberg, 2nd ed., 1992.

[Jarry83]   P. Jarry: *Transfer Functions Interpolating an Ideal Am-
plitude with Arbitrary Phase and Delay*, *Circuit Theory
and Applications*, vol. 11: pp. 131–140, 1983.

[Jeng99]   J. T. Jeng and T. T. Lee: *Nonlinear Adaptive Inverse
Control via the Unified Model Neural Network*, in: *Pro-
ceedings of the 2nd Conference on Applications and Sci-
ence of Computational Intelligence*, vol. 3722, pp. 153–
162, Orlando, FL, USA, 1999.

[Kellenberger87] W. Kellenberger: *Elastisches Wuchten*, Springer Ver-
lag, Berlin, Heidelberg, New York, 1987.

[Knospe97]   C. R. Knospe, S. J. Fedigan, W. R. Hope, and R. D.
Williams: *Multitasking DSP Implementation of Adap-
tive Magnetic Bearing Control*, *IEEE Transactions on
Control Systems Technology*, vol. 5(2): pp. 230–238,
Mar. 1997.

[Krämer84]   E. Krämer: *Maschinendynamik*, Springer Verlag, Berlin, Heidelberg, New York, 1984.

[Krämer93]   E. Krämer: *Dynamics of Rotors and Foundations*, Springer Verlag, Berlin, Heidelberg, New York, 1993.

[Larsonneur90] R. Larsonneur: *Design and Control of Active Magnetic Bearing Systems for High Speed Rotation*, Ph.D. thesis, No. 9140, ETH Zurich, Switzerland, 1990.

[Li01]   G. Li, Z. Lin, P. E. Allaire, B. Huang, W. Jiang, E. S. Zorzi, and R. O. Bartlett: *Stabilization of a High Speed Rotor with Active Magnetic Bearings by a Piecewise μ–Synthesis Controller*, in: *Proceedings of the 6th International Symposium on Magnetic Suspension Technology*, vol. 1, pp. 416–421, Torino, Italz, Oct. 2001.

[Lingener92]   A. Lingener: *Auswuchten – Theorie und Praxis*, Verlag Technik, Berlin, Germany, 1992.

[Lösch98]   F. Lösch, C. Gähler, and R. Herzog: *μ–Synthesis Controller Design for a 3MW Pump Running in AMBs*, in: *Proceedings of the 6th International Symposium on Magnetic Bearings*, pp. 415–428, Cambridge, MA, USA, Aug. 1998.

[Lösch00]   F. Lösch and P. Bühler: *Identification and Automated Controller Design for Rigid Rotor AMB Systems*, in: *Proceedings of the 7th International Symposium on Magnetic Bearings*, pp. 57–62, ETH Zurich, Switzerland, Aug. 2000.

[Lösch01]   F. Lösch: *Identification and Automated Controller Design – Software Tools*, Institute Report, 2001.

[Ludyk95a]   G. Ludyk: *Theoretische Regelungstechnik 1: Synthese Linearer Regelungssysteme*, Springer Verlag, Berlin, Heidelberg, 1995.

[Ludyk95b]   G. Ludyk: *Theoretische Regelungstechnik 2: Zustandsrekonstruktion, optimale und nichtlineare Regelungssysteme*, Springer Verlag, Berlin, Heidelberg, 1995.

[Mohler96]   M. Mohler: *MIMO Identifikation von Magnetlagersystemen*, Diplomarbeit, International Center for Magnetic Bearings, ETH Zurich, Switzerland, Mar. 1996.

[Morton85]   B. Morton and R. McAfoos: *A μ Test for Real Parameter Variations*, in: *Proceedings of the American Control Conference*, pp. 135–138, 1985.

[Müller76]   P. C. Müller and W. O. Schiehlen: *Lineare Schwingungen*, Akademische Verlagsgesellschaft, Wiesbaden, 1976.

[Muntwyler00]   U. Muntwyler and S. Suter: *Rotor schweben lassen ohne Modellkenntnis II*, Semesterarbeit, International Center for Magnetic Bearings, ETH Zurich, Switzerland, 2000.

[Namerikawa96]   T. Namerikawa, K. Hagiwara, M. Fujita, and F. Matsumura: *Experimental Evaluation of Gain Scheduled $\mathcal{H}_\infty$ Robust Controllers to a Magnetic Bearing*, in: *Proceedings of the 5th International Symposium on Magnetic Bearings*, pp. 137–142, Kanazawa, Japan, Aug. 1996.

[Namerikawa98]   T. Namerikawa, M. Fujita, and F. Matsumura: *Uncertainty Structure and μ–Design of a Magnetic Suspension System*, in: *Proceedings of the 6th International Symposium on Magnetic Bearings*, pp. 439–448, Cambridge, MA, USA, Aug. 1998.

[Nonami96]   K. Nonami and K. Nishina: *Discrete Time Sliding Mode Control with Simple VSS Observer of Zero-Power Magnetic Bearing System*, in: *Proceedings of the 5th International Symposium on Magnetic Bearings*, pp. 221–226, Kanazawa, Japan, Aug. 1996.

[Nordmann98]   R. Nordmann: *New Identification Techniques in Rotordynamics Using Motion and Force Control*, in: *Proceedings of the 4th International Conference on Motion and Vibration Control MOVIC*, vol. 1, pp. 33–40, Zurich, Switzerland, Aug. 1998.

[Rachline90]   M. Rachline: *La belle histoire du roulement*, SKF/Albin Michel, Paris, 1990.

[Salm88] J. Salm: *Eine aktive magnetische Lagerung eines elastischen Rotors als Beispiel ordnungsreduzierter Regelung grosser elastischer Systeme*, Tech. Rep. 1/162, VDI Fortschrittsberichte, 1988.

[Schönhoff00a] U. Schönhoff, A. Klein, and R. Nordmann: *Attitude Control of the Airborne Telescope SOFIA: µ–Synthesis for a Large Scaled Flexible Structure*, in: *Proceedings of the 39th IEEE Conference on Decision and Control*, Sydney, Australia, Dec. 2000.

[Schönhoff00b] U. Schönhoff, J. Luo, G. Li, et al.: *Implementation Results of µ–Synthesis Control for an Energy Storage Flywheel Test Rig*, in: *Proceedings of the 7th International Symposium on Magnetic Bearings*, pp. 317–322, ETH Zurich, Switzerland, Aug. 2000.

[Schweitzer94] G. Schweitzer, H. Bleuler, and A. Traxler: *Active Magnetic Bearings: Basics, Properties and Applications of Active Magnetic Bearings*, Verlag der Fachvereine, Zurich, Switzerland, 1994.

[Schweitzer98] G. Schweitzer: *Magnetic Bearings as a Component of Smart Rotating Machinery*, in: *Proceedings of the 5th International Conference on Rotor Dynamics IFToMM*, pp. 3–15, Darmstadt, Germany, Sep. 1998.

[Schweitzer01] G. Schweitzer: *What can Mechatronics do for Structural Dynamics?*, in: D. J. Ewins and D. J. Inman (Editors), *Structural Dynamics @2000: Current Status and Future Directions*, pp. 79–86, Research Studies Press, Inc., Philadelphia, PA, USA, 2001.

[Senn97] P. Senn: *MIMO Identifikation von Magnetlagersystemen*, Diplomarbeit, International Center for Magnetic Bearings, ETH Zurich, Switzerland, Jan. 1997.

[Siegwart89] R. Siegwart: *Aktive magnetische Lagerung einer Hochleistungs-Frässpindel mit digitaler Regelung*, Ph.D. thesis, No. 8962, ETH Zurich, Switzerland, 1989.

[Skogestad96]   S. Skogestad and I. Postlethwaite: *Multivariable Feedback Control*, John Wiley & Sons, Chichester, West Sussex, England, UK, 1996.

[Stein91]   G. Stein and J. C. Doyle: *Beyond Singular Values and Loop Shapes*, *Journal of Guidance*, vol. 14(1): pp. 5–16, 1991.

[Stoorvogel92]   A. A. Stoorvogel: *The $\mathcal{H}_\infty$ Control Problem: A State Space Approach*, Prentice Hall, Englewood Cliffs, NJ, USA, 1992.

[Tian94]   H. Tian and K. Nonami: *Robust Control of Flexible Rotor–Magnetic Bearing Systems Using Discrete Time Sliding Mode Control*, *JSME International Journal*, vol. 37(3): pp. 504–512, 1994.

[Wortelboer94]   P. M. R. Wortelboer: *WOR-toolbox: Toolbox for Weighted Order Reduction*, Delft University of Technology, 1994. Available via anonymous ftp: ftp-mr.wbmt.tudelft.nl/pub/wortelboer/ (outdated.).

[Wortelboer99]   P. M. Wortelboer, M. Steinbuch, and O. H. Bosgra: *Iterative Model and Controller Reduction using Closed Loop Balancing, with Application to a Compact Disc Mechanism*, *International Journal of Robust and Nonlinear Control*, vol. 9: pp. 123–142, 1999.

[Yamashita96]   K. Yamashita, P. E. Allaire, and C. R. Knospe: *Rotor Disturbance Attenuation Using an $\mathcal{H}_\infty$ Controller for Active Magnetic Bearings*, in: *Proceedings of the 5th International Symposium on Magnetic Bearings*, pp. 227–232, Kanazawa, Japan, Aug. 1996.

[Zhou96]   K. Zhou, J. C. Doyle, and K. Glover: *Robust and Optimal Control*, Prentice Hall, Upper Saddle River, NJ, USA, 1996.

[Zhou98]   K. Zhou and J. C. Doyle: *Essentials of Robust Control*, Prentice Hall, Upper Saddle River, NJ, USA, 1998.

Curriculum Vitae

I was born on February 11, 1971 in Neustadt/Weinstraße, Germany. After moving to northern Germany in the same year, I attended primary school in Halstenbek and Hetlingen from 1977 to 1981. From 1981 to 1990 I attended Johann–Rist–Gymnasium in Wedel. The academic year 1987/88 I spent in Santa Rosa, California, where I obtained an American high school diploma.

In 1991, after serving my time in the military service, I enrolled for studies in applied mathematics at the University of Kaiserslautern. After the first diploma, I started to work at the machine dynamics group of Professor Nordmann, where I was involved in an EU–funded project and several industry projects. At the same time, I continued my studies with focus on control theory, optimization, and machine dynamics. The time from August, 1994, to February, 1995, I spent in Grenoble, where I attended ENSIMAG (Ecole Nationale Supérieure d'Informatique et de Mathématiques Appliqées de Grenoble). I obtained my degree in applied mathematics from the University of Kaiserslautern with honors in October, 1997.

After working for McKinsey&Company for a short time, I joined Professor Schweitzer's International Center for Magnetic Bearings at the Institute of Robotics at ETH, the Swiss Federal Institute of Technology in Zurich, in February, 1998. During the first three years, I was involved in an EU–funded project in which I developed algorithms for fault detection and correction in Active Magnetic Bearing systems. During this time, I was also involved in teaching robotics classes, and from August, 1999, to August, 2000, I was responsible for organizing ISMB–7, the Seventh International Symposium on Magnetic Bearings at ETH with over 200 participants from 18 countries.

The vast majority of the work presented in this thesis, as well as the thesis itself, is the result of my final year at the group, from November, 2000, to November, 2001.